Synthesis, Characterization, and Functionality of Quinol-Based Superoxide Dismutase Mimics

by

Jamonica L. Moore

A dissertation submitted to the Graduate Faculty of
Auburn University
in partial fulfillment of the
requirements for the Degree of
Doctor of Philosophy of Science

Auburn, Alabama
August 6, 2022

Keywords: Reactive oxygen species, Superoxide Dismutase Mimic, Redox-responsive, Quinol

Approved by

Christian R. Goldsmith, Chair, Professor, Dept. of Chemistry and Biochemistry
Douglas C. Goodwin, Professor and Chair, Dept. of Chemistry and Biochemistry
Dean D. Schwartz, Associate Professor, Dept. of Anatomy, Physiology, and Pharmacology
Bryon H. Farnum, Assistant Professor, Dept. of Chemistry and Biochemistry
Evangelos Miliordos, Assistant Professor, Dept. of Chemistry and Biochemistry

Abstract

There is great interest in developing biopharmaceuticals that can slow or halt the effects of the primary and secondary oxidative stressors that are responsible for aging, chronic diseases, and other health disorders. A number of enzymes are capable of degrading reactive oxygen species (ROS) into less toxic H_2O and O_2. One such enzyme is superoxide dismutase (SOD), which catalyzes the conversion of superoxide ($O_2^{\cdot-}$) to H_2O_2 and O_2. Catalase is another antioxidant enzyme that instead targets H_2O_2, converting it to O_2 and H_2O. In many health conditions, the concentrations of ROS rise to levels that can overwhelm the defense system provided by SOD and other antioxidant enzymes, making the body more susceptible to oxidative stress. A therapeutic strategy to combat disorders resulting from oxidative stress would be to administer a pharmaceutical capable of catalytically degrading ROS. Consequently, small molecule mimics of SOD have been explored heavily.

Most SOD and catalase mimics derive activity from a redox-active metal cation. Unfortunately, the ligands of the most active mimetics are difficult to modify and prepare in high quantities. In this dissertation, I complex a series of highly modifiable redox-active quinol-containing organic ligands to either redox-active or redox-inactive metal ions to yield a variety of potent antioxidants that mimic either SOD or catalase. With respect to the SOD mimics, the activity can be enhanced by i) altering the coordination sphere of the metal complexes to improve the accessibility of superoxide, ii) making the overall charge more positive, iii) and stabilizing key mechanistic intermediates. Surprisingly, the complexes instead target H_2O_2 when the metal center is more positively charged; the selection of metal therefore determines whether the complex is a mimic of SOD or catalase. The ability of these ligands to allow redox-inactive metals to catalyze ROS degradation is novel, and the work in this dissertation has outlined key structure-function trends.

Acknowledgments

My life has been filled with mentors, advisors, colleagues, dear friends, and family. Each has left a unique imprint that inspires me to be the most truthful and accountable version of Jamonica possible. I am grateful to every person in my life, especially those who have influenced my pathway towards finalizing this dissertation work. Although I will never be able to acknowledge everyone, I will humbly attempt to honor as many as I can.

My parents, Jimmie and Lucille Jackson, have always encouraged me to question everything. They supported every endeavor and shared invaluable life lessons, influencing an insatiable curiosity. I thank them for being my grounding foundation, especially during the last five years. From numerous phone calls to random trips home, they continuously showered me with love, ensuring I achieved all my dreams. Every day I thank God for providing a family who loves me unconditionally. I thank my siblings, LaTonyia and Jimeriam, for being my sources of mental relaxation. From family vacations to birthday celebrations, these events provided a short break. I also thank them for forgiving me if I forgot to return their phone calls. To my niece and nephew, Hush and Louie, I am beyond blessed to have had your contagious smiles and funny colloquialisms cheer me after a long research day. I would especially like to thank Marshall Moore, you are my partner in every way and I praise the Lord that he provided you to be my soulmate, best friend, and a constant source of love. Over the past ten years, you have seen me at my highest and lowest moments, cheered and mourned with me throughout life changes, and challenged me to do more than I ever imagined. I want you to know it is because of you that I can thrive in a stressful situation because I know God provided you to be my earthly net of protection. I am excited for this next chapter of our life journey.

Professionally, many advisors, colleagues, and undergraduates have helped me grow. Initially, through the National Institute of Health (NIH) Building Infrastructure Leading to Diversity (BUILD) fellowship with Prof. Stassi DiMaggio, I acquired a deftness that allowed for facile transitioning from undergraduate endeavors to graduate-level research projects. In the past five years and under the substantial guidance of Prof. Christian R. Goldsmith, I have prepared coordination complexes that are functional mimics of either SOD or catalase. Throughout my academic research career, I have had fantastic counselors that have helped me succeed and become a well-rounded scientist. I thank both advisors for their guidance and mentorship.

To complete my projects, I also benefited from the instruction of other Auburn University professors. I thank Prof. Duin and his graduate students for their help designing, processing, and analyzing EPR measurements. Dr. Melissa Boermsa and her teaching assistants were integral in running advanced mass spectrometry experiments. I am grateful to Prof. Byron Farnum for the use of special instruments such as cyclic voltammetry and his graduate students for their troubleshooting advice. Under the supervision of Prof. Evangelos Miliordos, I acquired quantum mechanics techniques used to predict mechanistic pathways. As such, I thank Prof. Miliordos for taking the time to mentor and guide my theoretical calculations. I also thank Prof. Douglas Goodwin and his students, especially Callie Barton, for their guidance in performing catalase assay experiments. Prof. Dean D. Schwartz and Christine Camp helped immensely with antioxidant studies, advanced *in vitro* studies, and SOD mimicry analysis. I sincerely thank both for taking this humble chemist and turning me into a proficient cellular biologist. I express extreme gratitude to our collaborators for their hard work and assistance. Most importantly, I thank my current and previous group members: Tessa Hutchinson, Alexander Saunders, Sana Karbalaei, Segun Obisesan, and Hillary Polander. I also am grateful for all my prior undergraduate mentees who

helped perform experiments. Especially my mentees that have transitioned to higher learning opportunities, Kate Lightfoot, Taylor Grace Chambers, Monty Greene, Haley B. Alix, Sidney Ison, and Alisabeth Bradford, I wish you the best.

I thank Prof. Anne Gorden for encouraging me to become involved in outreach. Her encouragement helped me continue a theme of serving as a student leader that was initiated during my tenure at the Xavier University of Louisiana. At Auburn University, I have served as a graduate liaison for departmental and collegiate committees, president of the National Organization for Professional Advancement of Black Chemists and Chemical Engineers (NOBCChE), co-chair of the College of Sciences and Mathematics colloquiums, and outreach coordinator for Younger Chemist Committee of the American Chemical Society. My service through these programs promoted interactions with my fellow graduate students and opportunities to mentor young minds. I am grateful for the opportunities presented to me, especially those provided by Dr. Kimberly Mulligan-Guy and the COSAM Office of Inclusion, Equity, and Diversity.

Last but most importantly, I thank God. The year I started graduate school, I gave my life to God. I know every win and every failure has been guided by His hands to mold me into an individual who can represent Him to others. I thank God for placing these individuals in my life. Because collectively, they form my immediate village. I am eternally grateful to everyone and know I would not have completed this dissertation work without their guidance and support. Matthew 25:23, “Well done, good and faithful servant; you have been faithful over a few things, I will make you ruler over many things. Enter into the joy of your Lord.”

Table of Contents

List of Tables

List of Figures

List of Schemes

List of Abbreviations

$AgSbF_6$	Silver hexafluoroantimonate(V)
Arg	Arginine
ATR	Attenuated Total Reflectance
CAT	Catalase
CEST	Chemical Exchange Saturation Transfer
CSI-MS	Cryospray-Ionization Mass Spectrometry
Cu	Copper
CV	Cyclic Voltammetry
Cys	Cysteine
DCM	Dichloromethane (CH_2Cl_2)
DFT	Density Functional Theory
DMF	Dimethylformamide
DMSO	Dimethyl Sulfoxide
DPPH	2,2-Diphenyl-1-picryl-hydrazyl hydrate
EDTA	Ethylenediaminetetraacetic Acid
EPR	Electron Paramagnetic Resonance
ESI	Electrospray Ionization
Et3N	Triethyl Amine
Ether	Diethyl Ether
EtOAc	Ethyl Acetate
Eq.	Equation
Fe	Iron

FTIR	Fourier-Transform Infrared Spectroscopy
Ga	Gallium
Gly	Glycine
H_2O_2	Hydrogen Peroxide
H_2qp1	*N*-(2,5-dihydroxybenzyl)*N,N',N'*-tris(2-pyridinylmethyl)-1,2-ethanediamine
H_2qp3	*N*-(2,5-dihydroxybenzyl)-*N,N'*-bis(2-pyridinylmethyl)-1,2-ethanediamine
H_4qp2	*N,N'*-(2,5-dihydroxybenzyl)-*N,N'*-bis(2-pyridinylmethyl)-1,2-ethanediamine
HEPES	4-(2-hydroxyethyl)-1-piperazineethanesulfonic acid
His	Histidine
HCl	Hydrochloric acid
HO_2	Hydroperoxyl Radical
HPLC	High Performance Liquid Chromatography
Hptp1	N-(2-Hydroxy-5-methyl-benzyl)-N,N',N'-tris(2-pyridinylmethyl)-1,2-ethanediamine
HR-MS	High Resolution Mass Spectrometry
INT	Iodonitrotetrazolium Chloride
KBr	Potassium Bromide
KCl	Potassium Chloride
KO2	Potassium Superoxide
KOH	Potassium Hydroxide
Lys	Lysine
MeCN	Acetonitrile
MeOH	Methanol

Mn	Manganese
MOPS	3-(*N*-morpholino)propane sulfonic acid
MRI	Magnetic Resonance Imaging
MS	Mass Spectrometry
MTT	3-(4,5-dimethylthiazol-2-yl)-2,5-diphenyltetrazolium bromide
NADPH	Nicotinamide Adenine Dinucleotide Phosphate
NBT	4-Nitro Blue Tetrazolium Chloride
NHE	Normal Hydrogen Electrode
Ni	Nickel
NMR	Nuclear Magnetic Resonance
$O_2^{-\cdot}$	Superoxide anion
OTf_3	Triflate
pK	Dissociation Constant
q	Aquation Number
*r*1	Rate of relaxation, 1/*T1*
ROS	Reactive Oxygen Species
SOD	Superoxide Dismutase
SODm	Superoxide Dismutase Mimetic
Tyr	Tyrosine
UV/vis	Ultraviolet Visible Spectrometry
V	Volt
XOD	Xanthine Oxidase
Zn	Zinc

Chapter 1

Introduction to Superoxide Dismutase Mimics

1.1 Biological Relevance of Reactive Oxygen Species

There are both mitochondrial and non-mitochondrial sources of reactive oxygen species (ROS). In healthy cells, oxygen is consumed by the mitochondria which reduces it to H_2O as it produces chemical energy. This process is not always perfect, however, and a superoxide radical anion ($O_2^{-\cdot}$) can be produced when electrons escape the electron transport chain and bind with oxygen.[1] ROS are essential to physiology. A steady-state 0.1 nM concentration of superoxide is considered healthy for most cells.[2,3] Recent studies demonstrate that low concentrations of ROS serve as signaling agents and regulate diverse physiological processes, such as immune cell activation, gene expression, signal transduction, differentiation, metabolic adaption, and autophagy.[4-10] These oxidants, however, can react directly with a variety of biomolecules, and above 0.1 nM, the deleterious effects of ROS become more prominent. The over-production of ROS has been noted in a variety of health disorders (*vide infra*).

ROS are maintained at sub-micromolar concentrations. However, beneficial biological processes exist that result in short-term increases of $O_2^{-\cdot}$. The "respiratory burst" observed in immune responses is a heavily characterized example of stimulated ROS production. Superoxide radicals and other ROS species are generated through phagocytosis or activation of NADPH oxidase as a defense mechanism against invading microorganisms.[11] High concentrations of ROS are typically involved in oxidative stress and propagated health disorders. For instance, cancer cells generate and utilize ROS at high concentrations for cell proliferation.[12] Simultaneously the rate of ROS production is counterbalanced by stimulated production of ROS scavengers. ROS has a dualistic nature of cellular regulation and cellular cytotoxicity. Medical exploitation in form of localized induction of oxidative stress can replicate favorable effects associated with high concentrations of ROS. Specifically certain cancer treatments, use ROS generation to induce

apoptosis and eliminate malignant cells.[13] While attractive as a method of treatment, recent research indicates the beneficial role of high ROS production depends on organ type and disease progression.[14]

ROSs ability to adopt dual functionality as cellular regulators or inducers of cytotoxicity depends on concentration, location, and type of reactive intermediate produced. Enzymatic and nonenzymatic antioxidants tightly maintain superoxide levels and ensure redox homeostasis. Antioxidant enzymes include superoxide dismutase (SOD), catalase, glutathione peroxidase, and glutathione reductase. However, the failure of intracellular defenses leads to oxidative stress and ROS over-accumulation.

1.2 Oxidative stress

A marker of cardiovascular, neurological, and inflammatory diseases such as hypertension, Alzheimer's, and diabetes, oxidative stress can be viewed as the imbalance of radicals and elimination molecules. Therefore, any deviation from redox homeostasis could be interpreted as a form of "oxidative stress." Normally high concentrations of $O_2^{-\cdot}$ induce a cellular feedback loop that ensures homeostasis is maintained. Typically, antioxidant regulators are sufficient. However, when the redox balance is disrupted $O_2^{-\cdot}$ accumulation occurs which triggers a downward effect of increased production of other deleterious reactive oxygen and nitrogen species (RONS).

$O_2^{-\cdot}$ is involved in the production of other deleterious ROS and reactive nitrogen species (RNS) that further propagate oxidative damage. $O_2^{-\cdot}$ can oxidize Fe-S cluster enzymes and liberate iron – which can itself propagate oxidative stress - and halt the catalytic activity.[15] H_2O_2, a product of superoxide dismutation, can interact with liberated Fe(II) to generate hydroxyl radical and hydroxide ion via a Fenton reaction. Similar reactivity occurs with Cu(I). Hydroxyl radical is a reactive pro-oxidant that reacts with organic and inorganic molecules and causes severe damage

to cells.[16] The production of $ONOO^-$ (peroxynitrite), a highly reactive and cytotoxic secondary reactive species, is a documented consequence of the reaction between $O_2^{-\cdot}$ and NO.[17] The deleterious reactive species has been document to damage biomolecules through DNA breakage, protein carbonylation, and membrane lipid peroxidation.[12]

Despite the ambiguity in determining which ROS concentrations are ideal for cellular health and their role in cellular pathways, research has implicated excessive and/or sustained increase of ROS in the several diseases pathogenesis.[18-23] These clinical conditions are characterized by elevated ROS production and decreased function of redox-responsive regulatory mechanisms, limiting cellular ability to maintain redox homeostasis.[24]

1.3 Reactive Oxygen Species: Superoxide

Molecular oxygen is a four-electron oxidant that releases most of its oxidizing capacity following a one-electron partial reduction. This univalent reduction produces an adventitious respiratory byproduct, the highly reactive species $O_2^{-\cdot}$ (Eq. 1.1).[25] In turn, superoxide can propagate the production of even stronger oxidants and contribute to oxidative stress (vide infra).

$$O_2 + e^- \longrightarrow O_2^{-\cdot} \qquad \text{(Eq. 1.1)}$$

The O_2 consumed by respiring cells is reduced by cytochrome *c* oxidase in a four-electron/four-proton reduction process to produce two molecules of water. Although cytochrome *c* oxidase is found in complex IV of the mitochondrial respiratory chain, it's not associated with the production of $O_2^{-\cdot}$. Rather complexes I and III of the mitochondrial respiratory chain and a series of dehydrogenases (i.e. pyruvate dehydrogenase) are suspected to be the most prominent contributors to mitochondrial superoxide levels.[26,27] The production of superoxide is not limited to the mitochondria, other cellular sources include NADPH oxidases, certain nitric oxide synthases, and xanthine oxidases.[13,28-30] These sources either directly produce superoxide or initiate

enzymatic pathways that express superoxide. The superoxide radical anion can act as either a reductant or an oxidant powerful enough to oxidize ascorbic acid and tocopherol.[31] One notable reaction is when a molecule of superoxide reacts with another superoxide radical and two equiv. of H^+ in a dismutation reaction to form H_2O_2 and O_2, (Eq. 1.2).[31] This reaction is hindered by the like charges of the two $O_2^{-\cdot}$ particles.[32] The reaction is accelerated in acidic media; under these conditions, a protonated superoxide ion - a hydroperoxyl radical (HO_2) - interacts with either $O_2^{-\cdot}$ or a second equiv. of HO_2 (Eq. 1.3 and Eq. 1.4)

$$O_2^{-\cdot} + O_2^{-\cdot} + 2\ H_3O^+ \longrightarrow H_2O_2 + O_2 + 2\ H_2O \qquad \text{(Eq. 1.2)}$$

$$HO_2 + HO_2 \longrightarrow H_2O_2 + O_2 \qquad \text{(Eq. 1.3)}$$

$$HO_2 + O_2^{-\cdot} \xrightarrow{H^+} H_2O_2 + O_2 \qquad \text{(Eq. 1.4)}$$

Although H_2O_2 itself is a ROS, it can be further reduced into two H_2O molecules and O_2 by either catalase or glutathione peroxidase. Alternatively, if H_2O_2 reacts with reduced transition metals or $O_2^{-\cdot}$ it can form $OH^\cdot$ or hydroxyl anion (OH^-) via the Fenton and Haber-Weiss reactions (Eq. 1.5 and Eq. 1.6).[33]

$$H_2O_2 + Fe(II) \longrightarrow OH^\cdot + OH^- + Fe(III) \qquad \text{(Eq. 1.5)}$$

$$O_2^{-\cdot} + H_2O_2 \longrightarrow OH^\cdot + OH^- + O_2 \qquad \text{(Eq. 1.6)}$$

Under normal conditions, the dismutation of $O_2^{-\cdot}$ decreases its physiological half-life by four-fold, preventing chemical imbalance.[31,34] Due to the roles that $O_2^{-\cdot}$ has in the generation of other ROS, it is a key target for strategies to regulate the biological redox environment.

1.4 Native Regulation of Superoxide Production

A massive change occurred in the atmospheric and oceanic environment approximately 2.0 – 3.0 billion years ago which resulted in a more oxidizing environment evidenced by increased O_2 levels.[15] Research indicates the Great Oxidation Event (GOE) as one of the first major events that

induced increased atmospheric and oceanic oxygen levels. The GOE and other oxidation events contribution to enhanced levels of oxygen sequential resulted in an increased presence of ROS.[15] In response to the elevation of oxygen levels, organisms adapted by altering existing metabolic pathways to stimulate increased production of enzymes to lessen and repair the oxidative damage caused by O_2 and the ROS that derived from it. Genomic sequencing indicates that superoxide dismutase (SOD), catalase (CAT), and peroxiredoxins antioxidants evolved prior to the rise of O_2 levels.[15] SOD is an enzymatic scavenger that catalyzes the spontaneous dismutation of $O_2^{-\cdot}$ (Eq. 1.2). The consumption of H_2O_2 by either CAT or nonheme peroxidases completes the detoxification initiated by SOD and yields H_2O and oxygen.

1.4.1 Classes of Superoxide Dismutases

Three classes of SOD enzymes exist in eukaryotes. The isoenzymes ensure that redox homeostasis is tightly regulated in every cellular compartment.[25] SODs are classified by their active-site metal ion(s) and cellular location, with isoforms localized in the cytosol, mitochondrial intermembranes, mitochondrial matrices, inner membranes, and extracellular compartments.[32,35] The copper-zinc-superoxide dismutase (CuZnSOD, SOD1) was first isolated in 1969 by McCord and Fridovich, and is located in the cytosol and mitochondrial membranes.[13,36] The crystal structure of SOD1 reveals a homodimeric structure.[35] The enzyme exists in most eukaryotic life forms, and has been found in both anaerobes and aerobic organisms.

Structural characterizations and modifications have highlighted the roles of both zinc and copper cations. The redox-active portion of the molecule cycles through Cu(II/I) redox to disproportionate $O_2^{-\cdot}$. In the reduced state Cu(I) is ligated by His46, His120, His48 (Human SOD1 numbering). While in its oxidized Cu(II) state, the imidazolate of His63 bridges the two metal ions.[37] A water molecule also binds to the copper, resulting in an overall distorted square pyramidal

geometry. The Zn site maintains a nearly tetrahedral geometry in both oxidation state. The exact role of zinc has not been elucidated, however, research has proven the necessity of a second metal ion. Zinc removal enables copper to bind at the formerly zinc site, which results in a less catalytically active species.

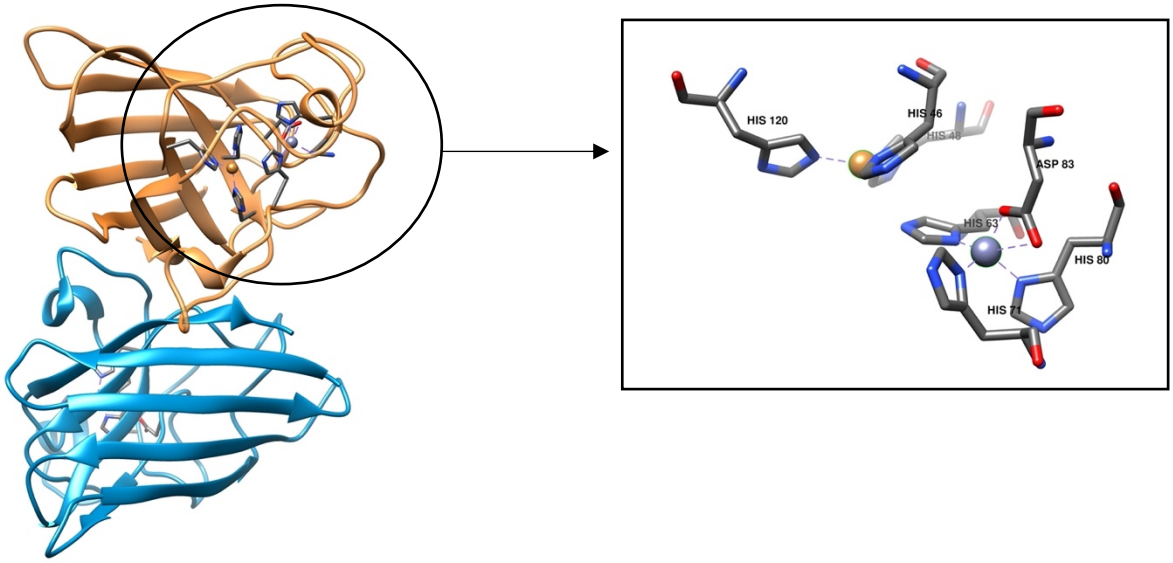

Figure 1.1 Structural representation of Human CuZnSOD (RCSB PDB: 1AZV) with inset of active site reconstructed using UCSF Chimera, developed by the Resource for Biocomputing, Visualization, and Informatics at the University of California, San Francisco, with support from NIH P41-GM103311.[43]

Shortly after the discovery of CuZnSOD, Fridovich isolated a manganese superoxide dismutase (MnSOD, SOD2).[38] The isoenzyme regulates $O_2^{\cdot-}$ levels in the mitochondrial matrix and inner membrane. Both CuZnSOD and MnSOD feature water molecules and positive electrostatic channels. Beyond these two characteristics, CuZnSOD and MnSOD share few structural features. Similar to CuZnSOD, the coordinated aqua ligand promotes catalysis through formation of a hydrogen-atom network. MnSOD exists as in both homotetrameric and homodimeric forms, with the homotetrameric belonging solely to eukaryotes.[39] This isoform is perhaps the most essential mitochondrial antioxidant enzyme due to its cellular location and proximity to the mitochondrial electron transfer chain, which greatly contributes to the production

of $O_2^{-\cdot}$.[40] The final SOD isoform found in eukaryotes is extracellular SOD (ECSOD, SOD3); to date, this enzyme is the only known extracellular scavenger of $O_2^{-\cdot}$ in the eukarya domain.[41] This isozyme is related to SOD1 in that it features zinc and copper metal ions bound in the active site of a tetrameric structure of dimers similar to dimers of human SOD1.[42]

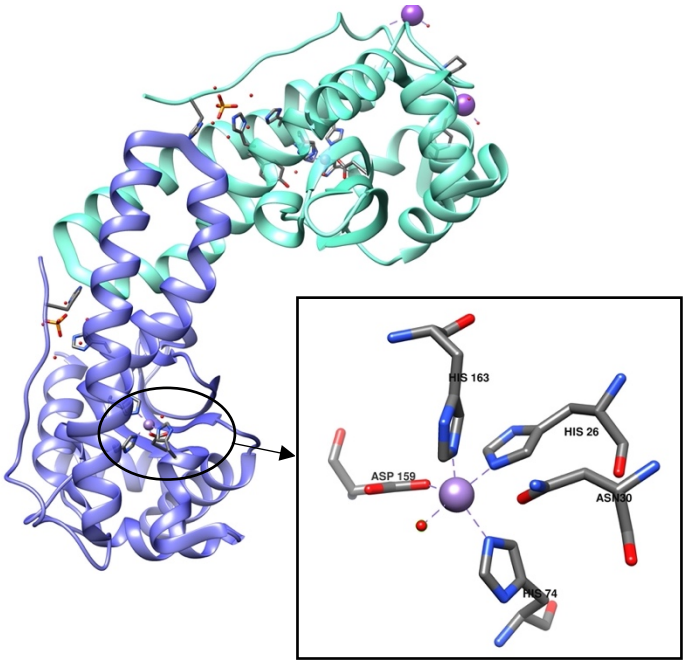

Figure 1.2 Structural adaptation of MnSOD active site (RCSB PDB : 5T30). Active depicted using UCSF Chimera, developed by the Resource for Biocomputing, Visualization, and Informatics at the University of California, San Francisco, with support from NIH P41-GM103311.[43]

Researchers have also identified an Fe-containing SOD (FeSOD) in aerobic and anaerobic bacteria, archaea protists, and eukaryotic plants.[43-45] FeSOD and MnSOD are structurally similar and operate through proton-coupled electron transfer mechanisms that use a metal-coordinated water ligand. Related to FeSOD and MnSOD are cambialistic SODs, which can function with either iron or manganese; in nature, some of these are found with both metals or with either iron or manganese exclusively.[46,47] However, truly cambialistic examples are rare, and most FeSODs

and MnSODs lose their catalytic activity when the native metal ion is replaced by the non-native one (e.g. an FeSOD with the active-site iron replaced by manganese).[48]

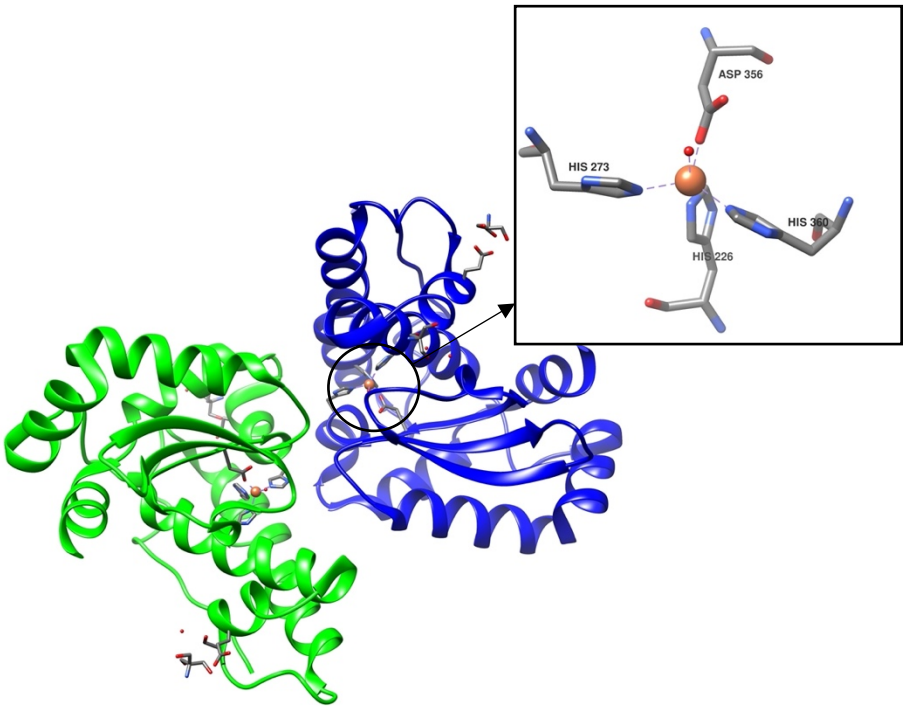

Figure 1.3 *Escherichia coli* FeSOD model isolated by X-ray diffraction (RCSB PDB: 1ZA5), reformatted to depict iron active center. Structures created using UCSF Chimera, developed by the Resource for Biocomputing, Visualization, and Informatics at the University of California, San Francisco, with support from NIH P41-GM103311.[43]

The most recently discovered class of SOD, nickel-containing SOD (NiSOD), is much different from its counterparts. Functioning as a homohexamer, the enzyme is predominantly found in bacteria and algae.[49,50] Most of its structural features have been experimentally characterized. The NiSOD isoform uses sulfur-containing ligands rather than oxygen-containing peptides. In the reduced state, nickel cation is ligated by two *cis*-cysteinate sulfurs, one amide nitrogen from a peptide backbone, and an amine nitrogen from His1. Upon oxidation the imidazole of His1 coordinates to Ni(III) producing structural changes about the active site. The as-isolated enzyme contains a roughly equivalent mix of reduced and oxidized nickel sites. Due to difficulty isolating, so far only the fully reduced enzyme has been studied.[37] Unlike the other isoforms, a

ligated thiolate adjusts reduction potential and serves as the proton donor in superoxide reduction. One structural similarity between NiSOD and MnSOD/FeSOD is the presence of a gateway tyrosine that controls access of active site.[37] Despite their diverse active-site structures, all SODs contain a single redox-active metal ion and are able to react rapidly and selectively with $O_2^{-\cdot}$.

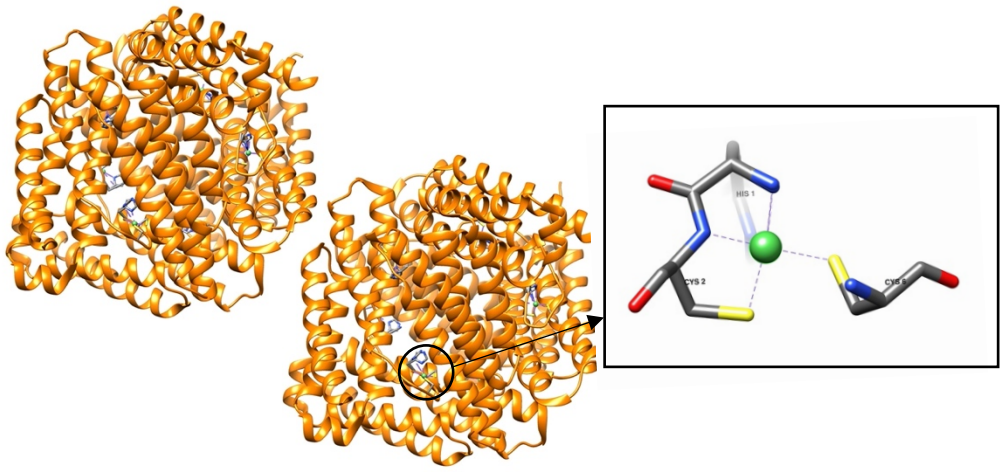

Figure 1.4 Structural modeling of *Streptomyces coelicolor* (RCSB PDB: 1T6U) with focused depiction of NiSOD active site. Image rendered using UCSF Chimera, developed by the Resource for Biocomputing, Visualization, and Informatics at the University of California, San Francisco, with support from NIH P41-GM103311.[43]

1.4.2 General Mechanism and Speed of SOD Catalysis

During catalysis, the metal ions in the enzymes cycle between two different oxidation states: Cu(II/I) (CuZnSOD), Mn(III/II) (MnSOD), Fe(III/II) (FeSOD), and Ni(III/II) (NiSOD). The oxidized form of the enzyme oxidizes $O_2^{-\cdot}$ (Eq. 1.7), whereas the reduced form of the enzyme reduces $O_2^{-\cdot}$ (Eq. 1.8).[51] ENZ represents the enzyme's environment.

$$\text{ENZ-M}^{red} + O_2^{-\cdot} + 2\,H^+ \longrightarrow \text{ENZ-M}^{ox} + H_2O_2 \qquad \text{(Eq. 1.7)}$$

$$\text{ENZ-M}^{ox} + O_2^{-\cdot} \longrightarrow \text{ENZ-M}^{red} + O_2 \qquad \text{(Eq. 1.8)}$$

More detailed studies regarding the mechanism of dismutation for each isoform is beyond the scope of this discussion. Yet, studies have shown the disproportionation can occur through either inner-sphere or outer-sphere mechanisms, depending on the metal ion center.[37] In an inner

sphere mechanism, electron transfer occurs upon direct binding of superoxide to metal (Eq. 1.8). The metal is then reduced, and oxygen molecule released. Binding of a second $O_2^{-\cdot}$ molecule to the reduced metal transfers an electron to $O_2^{-\cdot}$. Protonation of this reduced species forms hydrogen peroxide and the oxidized metal ion. An outer-sphere mechanism utilizes non-covalent interactions, such as hydrogen bonds to a ligated water molecule, to stabilize the peroxide. Superoxide oxidation reduces metal ion and forms a ligated water molecule. Another molecule of superoxide enters the outer coordination sphere and accepts a proton from the ligated water to form hydroperoxyl. The hydroperoxyl subsequently accepts an electron from the metal and a proton from nearby water molecules to yield hydrogen peroxide. In the process, the metal returns to its oxidized state with a coordinated hydroxyl.

Spontaneous dismutation of superoxide is second-order with a rate constant of 2×10^5 M^{-1} s^{-1} at neutral pH.[39] However, this reaction only represents the stoichiometric reaction of disproportionation. $O_2^{-\cdot}$ exists in a pH-dependent equilibrium with HO_2 *in vivo*. This weak acid stabilizes the peroxide product and induces fast disproportion of $O_2^{-\cdot}$, with a rate constant of 1.0×10^8 M^{-1} s^{-1}, but only when the pH < pK_a (Eq. 1.4). Otherwise, the uncatalyzed rate of dismutation is slow due to low cellular levels of superoxide. Substrate saturation in the presence of SOD yields second-order catalytic rate constants of $10^9 – 10^{10}$ M^{-1} s^{-1}.[52,53] The reduction and oxidation reactions are both first-order in [SOD] and [$O_2^{-\cdot}$] (Eq. 1.7 and 1.8)

Despite their structural dissimilarities, SOD enzymes have similar redox potentials and overall active-site charges, which in turn lead to similar reactivity with $O_2^{-\cdot}$. Efficient catalysis is performed when the optimal turnover potential is near the midpoint of the oxidation potential (-0.18 V vs. NHE) and the reduction potential (+0.91 V vs. NHE) of $O_2^{-\cdot}$. The optimal reduction potential for SOD catalysis is therefore approximately +0.36 V vs. NHE .[37]

$$O_2 + e^- \longrightarrow O_2^{-\cdot} \qquad E° = -0.18 \text{ V vs. NHE} \qquad \text{(Eq. 1.9)}$$

$$O_2^{-\cdot} + e^- + 2H^+ \longrightarrow H_2O_2 \qquad E° = +0.91 \text{ V vs. NHE} \qquad \text{(Eq. 1.10)}$$

Most SODs feature a funnel lined with positive charges that serves to guide $O_2^{-\cdot}$ into the active-site.[37] However, NiSODs lack this positively charged funnel, and the high activity is instead attributed to the more exposed nickel cation which is closer to the surface of the protein than the metals in other SODs.[37]

SODs are essential for the regulation of physiological $O_2^{-\cdot}$ levels.[37] The loss or malfunctioning of specific SODs has been associated with oxidative stress, which in turn leads to membrane lipid peroxidation, protein carbonylation, and DNA breakage.[54-57] Disruption of SOD activity could also result in accumulation of secondary toxic RONS.[58]

1.5 SOD Mimics as Supplemental Defenses against Oxidative Stress

The development of new means to control *in vivo* ROS concentrations would likely result in substantial medicinal gains. Consequently, experimental and clinical studies have sought to reduce oxidative stress by introducing inhibitors of ROS producers, inducing endogenous antioxidant production, and supplementing the body's defenses with exogenous antioxidants.[59,60] Given the ability of SOD to catalytically eliminate ROS, scientists have explored therapeutics aimed at replicating SOD catalysis to bolster the body's defenses against oxidative stress. Synthetic mimics of SOD often try to duplicate key thermodynamic and electrostatic properties that are shared by the different classes of SOD. Regardless of the metal ion, all SODs have reduction potentials near +0.36 V vs. NHE, the optimal reduction potential for SOD catalysis. This along with strategically placed active sites and rates of dismutation near diffusion-control link the three isoforms of SODs.

Evaluating the functionality of potential antioxidants is essential if one wants to develop a pharmaceutical that could convert a ROS to more innocuous molecules, such as O_2 or H_2O.

Mimicry is indirectly and directly assessed in rapid and quantitative assays that provide measures for how quickly and efficiently an antioxidant can react with biologically relevant oxidants. The *in vivo* stability and toxicity of a SOD mimic must also be carefully evaluated.

1.5.1 Indirect and Direct Methods of Evaluating SODm Activity

Small molecule models of SOD generally try to replicate the enzymatic mechanism in that they feature a metal ion that cycles through a higher and lower oxidation state as the mimic alternately oxidizes and reduces $O_2^{\cdot-}$. There are numerous ways to assess its capacity to function as antioxidant. The 2,2-diphenyl-1-picrylhydrazyl (DPPH) assay is an easy and economical method to measure the radical scavenging activity of antioxidants.[61] DPPH features a delocalized spare electron characterizing it as a stable free radical that can abstract hydrogen atoms from the antioxidant to yield an intensely colored hydrazine (Figure 1.5).[61]

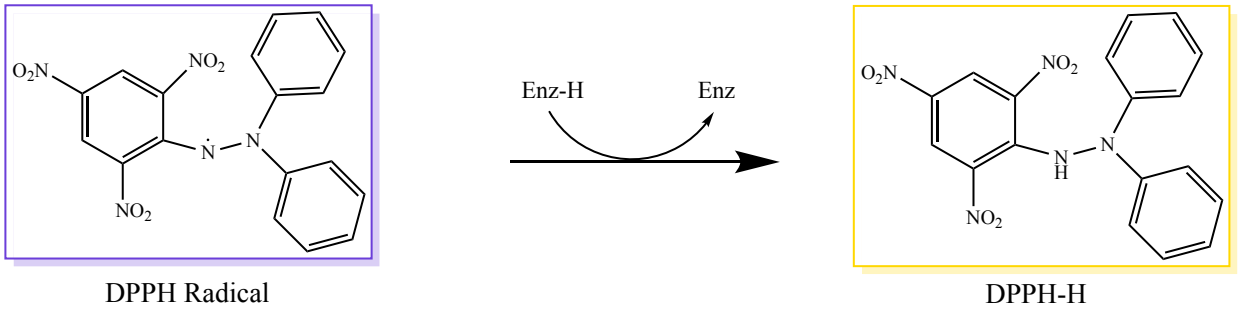

DPPH Radical DPPH-H

Figure 1.5 Diphenylpicrylhydrazyl (DPPH) free radical reaction with an enzymatic antioxidant capable of donating hydrogen atom to generate reduced DPPH, diphyenylpicrylhydrazine. Enz represents enzyme.

Although this assay qualitatively assesses the redox of a compound, it is not a measure of SOD activity. Other assays more directly assess the extent of SOD mimicry and provide quantitative measures of such activity such as experimental rate constants or IC_{50} values. These assays necessarily require a way to generate $O_2^{\cdot-}$ and a method of detection. Most reported SODm assays use steady-state concentrations of $O_2^{\cdot-}$ generated from the reaction between xanthine and xanthine oxidase (Figure 1.6).

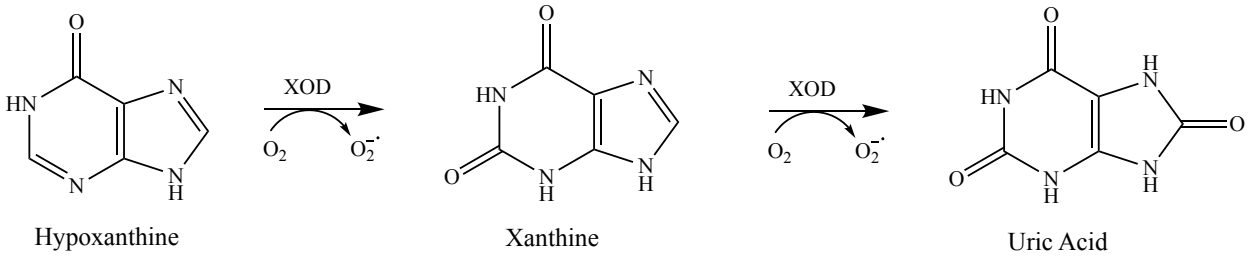

Figure 1.6 Superoxide generation system xanthine/xanthine oxidase.

This preliminary analysis method indirectly detects $O_2^{-\cdot}$ through an indicator molecule that changes its optical absorption or chemo-luminescence properties upon reaction with the analyze, allowing the reaction to be followed spectroscopically. A control experiment is needed to ensure that the photophysical properties of the SODm compound do not obscure the analysis.

The xanthine oxidase/hypoxanthine/lucigenin assay uses the reaction between xanthine oxidase and hypoxanthine to generate $O_2^{-\cdot}$; the tested antioxidant then competes with lucigenin for the ROS.[36] Lucigenin is oxidized by $O_2^{-\cdot}$ to yield a chemiluminescent species.[36] More effective antioxidants intercept the $O_2^{-\cdot}$ before it can react with lucigenin, reducing the emission.[36] One disadvantage of the lucigenin assay is that the lucigenin itself can produce $O_2^{-\cdot}$, and the assay often provides inaccurately high accounts of antioxidant activity.[62] A variation of the assay that uses cytochrome *c* as a reporter is more accurate. The use of cytochrome *c* has the advantage of being less sensitive to side-reactions propagated by radicals. Cytochrome *c* is reduced by $O_2^{-\cdot}$ to ferrocytochrome *c*, which has a detectable absorbance at 550 nm.[63] The key measure from this assay is the concentration of SODm that inhibits the rate of cytochrome *c* reduction rate by 50% (IC_{50}). The IC_{50} value can be used to estimate the catalytic rate constant (k_{cat}) for the reactions between $O_2^{-\cdot}$ and the SODm.[48] However, many chemicals and enzymes can reduce cytochrome *c* directly, making the assay a likewise imperfect gauge of activity.[63]

SOD mimics can also be assessed by more direct methods. Two widely used methods are pulse radiolysis and rapid-scan stopped-flow kinetic analysis. Analysis of a precise dismutation

rate of superoxide is visually measured using the radical's absorption properties at 250 nm. Pulse radiolysis generates a steady-state concentration of $O_2^{-\cdot}$ *in situ* when an oxygenated aqueous solution is irradiated in the presence of formate.[64] Following irradiation, e^-_{aq}, $HO^\cdot$, $H^\cdot$, H_2O_2, H_2, and H_3O^+ are produced and react directly or indirectly with O_2 to form $O_2^{-\cdot}$ and HO_2. This in turn allows rapid generation of substrate for SOD catalysis with changes monitored by UV/vis absorption. Pulse radiolysis is advantageous in that it cleanly and rapidly generates $O_2^{-\cdot}$ to allow for a large time window for kinetic measurements.[48] The inability to generate high concentrations of $O_2^{-\cdot}$ (below 50 μM) and the necessity for an accelerator limit the application of pulse radiolysis for the study of SOD mimics.[48]

Stopped-flow kinetics instrumentation is more readily accessible and can be used to directly determine k_{cat}. In a typical stopped-flow kinetics measurement, a solution of potassium hydroxide (KO_2) dissolved in dry dimethyl sulfoxide (DMSO) or acetonitrile is rapidly mixed with a solution of the SOD mimetic in a buffered aqueous solution. The loss of $O_2^{-\cdot}$ is then followed by UV/vis spectroscopy. The activity of the SOD mimic is usually determined in aqueous solutions buffered with either phosphate, MOPS, or HEPES to pH values between 7.4 and 8.1.[65-67] Presence of a first-order, as opposed to a second-order, decay of $O_2^{-\cdot}$ indicates that the mimetic is reacting directly with the superoxide and inducing a rate of decay that exceeds that of the uncatalyzed reaction.[64] Typical mixing techniques can accommodate moderate concentrations, 60 – 120 μM,[68] of superoxide but using a specialized mixer, comparable to a Berger-Ball mixer, the Ivanović-Burmazović group could initially generate 200 μM concentrations of $O_2^{-\cdot}$ in a 9:1 v/v mixture of aqueous buffer and DMSO.[65] The decay of the UV/vis feature associated with $O_2^{-\cdot}$ is fit to a model accounting for the concentrations of metal complex and $O_2^{-\cdot}$ to get k_{cat} rate constants. Initial rates

are corrected to account for uncatalyzed reaction and large excesses of $O_2^{-\cdot}$ are used to ensure pseudo-first-order conditions.

1.6 Mn-Based Redox-Active SOD Mimics

The implicated involvement of ROS in a wide array of diseases motivated efforts to develop synthetic antioxidants capable of regulating oxidative stress. Of the ROS, superoxide has emerged as the primary target of regulation, as this common denominator is prevalent in the propagation of deliberating cellular metabolism, all of which is beyond the scope of this present study. To restore redox homeostasis, synthetic antioxidants are used to supplement endogenous antioxidants. Many synthetic antioxidants are designed using principles gleaned from SOD. These mimics should i) be capable of accepting and donating electrons from superoxide, with appropriate thermodynamics defined as an approximate $E_{1/2}$ of +360 mV vs. NHE and ii) be able to attract superoxide anions towards the active site. Much like their enzymatic inspirations, SOD mimics tend to feature redox-active transition metals that can alternately oxidize and reduce $O_2^{-\cdot}$ through one-electron steps. Since the initial discovery of CuZnSOD and other SOD isoforms many mimics have been prepared, however this work will only cover a small portion. More in-depth reviews are available.[59,64,69,70]

Porphyrin-Based SOD Mimics

The earliest examples of SOD mimics include Fe- and Mn-porphyrins. The Fe porphyrin initially characterized by Pasternack and Halliwell, FeTM-4-PyP^{5+}, features positively charged, electron-withdrawing pyridyl *meso* substituents (Fig 1.3).[71] Although FeTM-4-PyP^{5+} demonstrates approximately 3% catalytical efficiency compared to CuZnSOD from bovine erythrocytes, stopped-flow kinetic analysis determined that there was a substantial drop in catalytic activity which was attributed to the formation of the catalytically inert Fe(III)-μ-oxo (hydroxo) bridged

dimer.[64] Similar to its Fe analogue, MnTM-4-PyP^{5+} has the metal bound in a square planar fashion with two exchangeable coordination sites *trans* to each other. In the cell, the positively charged metal centers coordinate strongly to the anionic phosphates of nucleic acids. The association prevents the complexes from dismutating $O_2^{-\cdot}$ within the cell and introduces toxicity.[72,73]

The ease of modifying the core structure and the stability of porphyrin ligands has enabled the synthesis of multiple SOD mimics with a range of redox-active metal centers. Batinić-Haberele is a major contributor to the field of porphyrinic SOD mimics (Fig 1.4). Study of Mn(III) complexes with derivatives of *meso*-tetrakis(*N*-methylpyridinium-2-yl)porphyrin revealed specific characteristics that govern SOD mimicry and allowed Batinić-Haberele and co-workers to optimize their catalytic activity. Weakly positive, neutral, and anionic Mn porphyrins such as MnT-2-PyP$^+$ and [Mn(TBAP)]$^{3-}$ cannot be reduced by $O_2^{-\cdot}$.[74] These complexes have $E_{1/2}$ values ranging from -280 mV vs NHE (MnT-2-PyP$^+$) to -194 mV vs NHE (MnTBAP^{3-}) which leaves the Mn(III) site too electron-rich and stable to accept electrons from $O_2^{-\cdot}$.[75-77] The lack of catalysis highlights the importance of incorporating positively charged substituents to replicate the positively charged tunnel associated with SOD enzymes and raise the Mn(III/II) reduction potential enough to allow for the facile reduction of Mn(III).

Attaching electron-withdrawing groups to *meso* or *beta* pyrrolic positions renders the metal center more electron-deficient, enhancing the affinity of the Mn site for electrons. MnTM-2-PyP^{5+} features electron-withdrawing groups in *ortho* positions closer to the metal center. *Ortho* placement yielded k_{cat} of 5.8×10^7 M^{-1} s^{-1}.[74] Substitution at the *ortho* position also introduces steric hindrance that prevents the pyridyl group from orienting co-planar with the porphyrin; this conformation places steric bulk above and below the plane of the porphyrin, hindering the coordination of nucleic acids.[74] The *meta* analogue dismutases superoxide with a rate constant of

$4.1 \times 10^6\ M^{-1}\ s^{-1}$ (cytochrome *c* assay). Although they are not as catalytically active as the *ortho* analogues, *meta N*-alkylpyridylporphyrins are more lipophilic and accumulate to higher extents in the cytosol of SOD-deficient *Escherichia coli*.[72,78-80] To date, $MnBr_8TM\text{-}3\text{-}PyP^{4+}$ has the highest reported dismutating capacity among metalloporphyrins, with a $E_{1/2}$ of +468 mV vs. NHE and a log k_{cat} exceeding 8.85.[78] However, the highly positive $E_{1/2}$ corresponds to a stabilized Mn(II) which binds to porphyrins much more weakly; this results in the dissociation of the metal, halting catalysis.[74]

The large collection of porphyrins synthesized by Fridovich, Batinić-Haberle, Spasojević, Rebouças, and coworkers have elucidated trends between ligand structure and SOD activity; in general, ligand modifications that enable the replication of the thermodynamic and electrostatic traits of native SOD enzymes tend to result in better catalysis. Although Fe porphyrin complexes can catalyze superoxide dismutation at rates that exceed those of their Mn analogues, their tendency to generate $OH^{\cdot}$ via Fenton chemistry limits their use *in vivo*.[81] Porphyrin complexes with other metals such as Cu(II), Ni(II), and Co(II) are rare but limited research indicates that these tend to be weak SOD mimics, with rate constants below $3 \times 10^7\ M^{-1}\ s^{-1}$.[59,82,83]

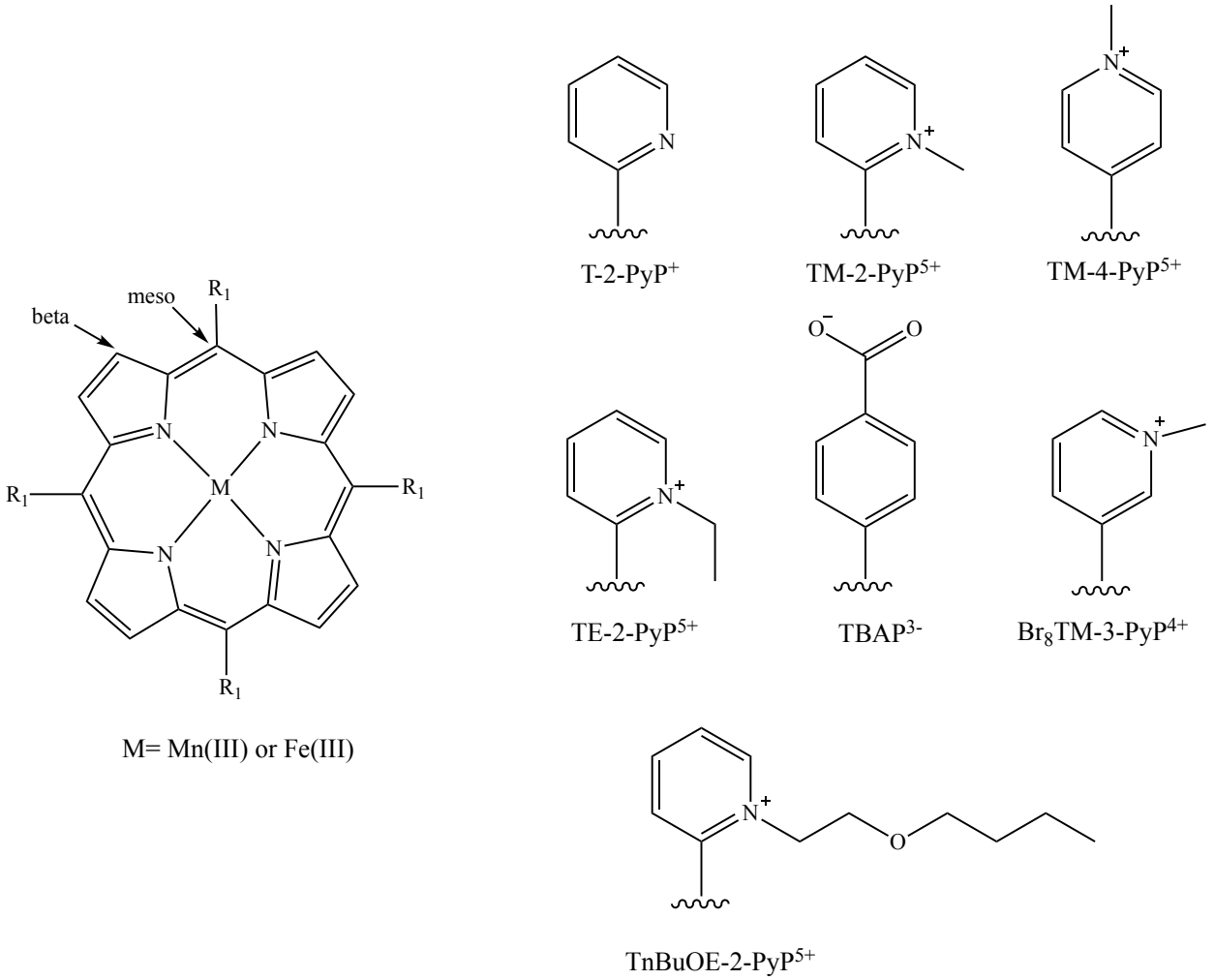

Figure 1.7 Structural representation of select Mn(III)-porphyrins characterized by Batinić-Haberle and co-workers.[59,72,82] Ligand names represent overall summarized charge of the porphyrinato ligand and coordinated Mn(III) ion or Fe(III) ion. Br_8TM-3-PyP^{4+} features 8 *beta* substituted bromines.

Out of the prepared metalloporphyrins, MnTE-2-PyP^{5+} (MnE, BMX-010) and MnTnBuOE-2-PyP^{5+} (MnBuOE, BMX-001) possess high rates of catalytic activity and lipophilicity which allow them to accumulate in cellular compartments. The combined properties along with low toxicity, has propelled these complexes into Phase II clinical trials.[75] The compounds showed promise in the treatment of sickle cell anemia as evidenced by NADPH oxidase activity, diminished leukocyte rolling, restoration of blood flow, and enhanced survival

rate in mice that exclusively express sickle hemoglobin.[84] In addition to catalyzing superoxide dismutation, Mn porphyrins can react with numerous biologically relevant molecules such as thiolates, ascorbate, hydrogen peroxide, peroxynitirite, hydrogen sulfide, and hypochlorite.[85-88] While broadly applicable, the non-specificity of Mn porphyrins has complicated clinical trials.

Other Mn- and Fe-Containing SOD mimics

Biliverdins and corroles are structurally similar to porphyrins. Mn(III) complexes with these ligands catalytic dismutate superoxide through a Mn(IV/III) redox couple rather than the Mn(III/II) couple that Mn-porphyrins commonly use.[89,90] With both biliverdins and corroles, Mn(III) reduction occurs at negative potentials outside of the optimal redox potential for superoxide, which is too thermodynamically unfavorable to be biologically relevant.[91] Biliverdins tend to form dinuclear species with two trivalent manganese (III) cations, each coordinated to four pyrrolic nitrogens and an enolic oxygen of the other monomer. [86] [Mn(BVDME)] has a Mn(IV/III) reduction potential of 450 mV vs. NHE and catalyzes superoxide dismutation with a k_{cat} ~5×10^7 M^{-1} s^{-1} in phosphate buffer, as assessed by the cytochrome *c* assay. Unfortunately, the insolubility of biliverdins in aqueous solutions has limited their study.

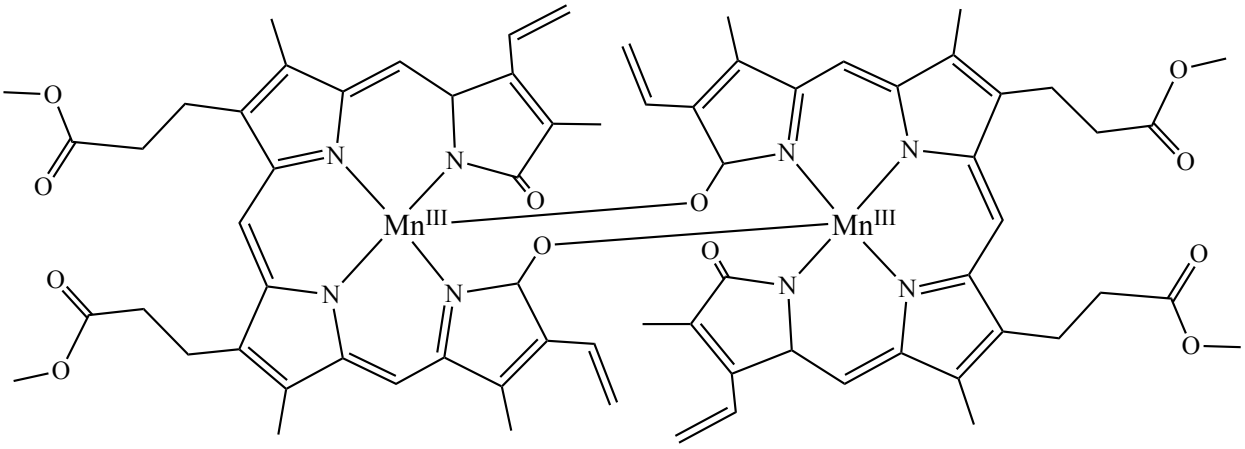

$[Mn^{III}(BVDME)]_2$

Figure 1.8 Structural representation of Mn(III) biliverdin synthesized by Spasojević *et al.*[91]

Corroles differ from porphyrins in that they have one fewer *meso* bridge and are trianionic versus dianionic poryphyrin. Gross *et al.* complexed corroles with appended sulfonates and *ortho*- or *para*-pyridinium rings to manganese; the resultant complexes display SOD activity as determined by the cytochrome *c* assay, electrochemistry, and pulse radiolysis studies.[89] An inherent positive redox potential necessitates strong electron withdrawing or positively charged substituents to electrochemical disproportionation $O_2^{-\cdot}$. The catalytic efficiency of corroles is lower than that of porphyrins, with k_{cat} of 3×10^6 M^{-1} s^{-1} for 1-Fe and k_{cat} of 7.8×10^6 M^{-1} s^{-1} for 1-Mn in phosphate buffer at pH 7.4, as measured by stopped-flow kinetics. However, these are true catalysts as porphyrins are typically indirectly assessed by indirect methods. Gross *et al.* proposed a catalytic mechanism for [Fe^{III}((tpfc)(SO_3H_2-Corrole)]. Based on the results, the rate-determining step in the catalytic cycle appears to be the reduction of $O_2^{-\cdot}$ by Fe(III). An outer-sphere oxidation of $O_2^{-\cdot}$ by the Fe(IV) form occurs much more quickly. The initial compound is reformed and can bind superoxide through an inner-sphere mechanism. Combined with superoxide dismutation, additional observations of catalase (CAT)-like activity, peroxynitrite decomposition, cellular protection against oxidative stress, and cellular accumulation for Fe and Mn corroles make the compounds attractive for further therapeutic studies. [92,93]

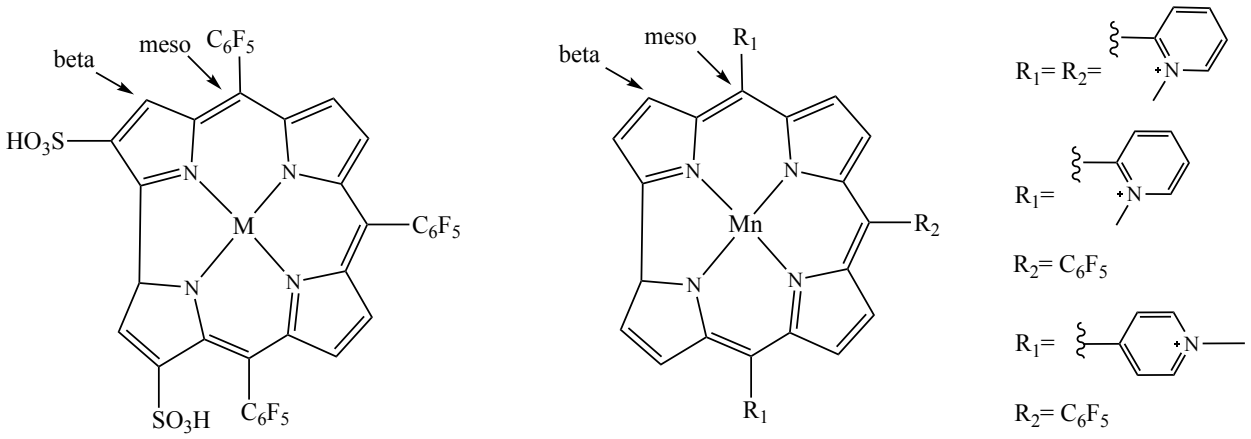

M = Mn, Fe
$[Mn^{III}((tpfc)(SO_3H)_2\text{-Corrole})]$
$[Fe^{III}((tpfc)(SO_3H)_2\text{-Corrole})]$

Pyridinium-subsituted manganese(III)corroles

Figure 1.9 Structures Mn(III) and Fe(III) corroles. Note that $[Fe^{III}(((tpfc)(SO_3H)_2\text{-Corrole})]$ features either a flouride or methoxide ligand that has been omitted for clarity.[89]

Salen-Based SOD Mimics

Various antioxidant assays initially suggested that Mn-salen complexes were competent SOD and CAT mimics. These findings were contradicted by stopped-flow kinetic analysis of the direct reactions between the compounds and the ROS performed by Riley *et al.*; the k_{cat} values for SOD activity were below 8×10^5 M^{-1} s^{-1} at pH 8.0.[64] A subsequent study of EUK-113 by Friedel *et al.* measured a k_{cat} of 1.23×10^6 M^{-1} s^{-1} in pH 8.1 HEPES solution and a k_{cat} of 1.18×10^6 M^{-1} s^{-1} in pH 7.8 phosphate solution.[65] This is just one example where the method of analysis matters for determination of superoxide activity.

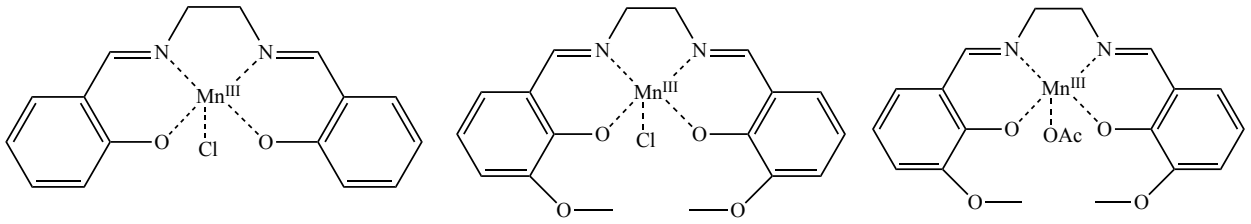

EUK-8 EUK-134 EUK-113

Figure 1.10 Schematic drawings of Mn(III)-salens.[64,65]

Synthetic modifications to EUK-8 yielded the ligand *N,N*-bis(salicyclidene)ethylendiamine chloride. The Mn(III) complex with this derivative displayed higher lipophilicity, higher aqueous stability, a greater ability to protect cells against oxidative stress, and CAT mimicry.[94] The impact of these modifications on SOD activity were not reported. Mn-salen complexes tend to be stable in aqueous solution but lose their SOD activity in the presence of EDTA; this has led to speculation that they may likewise be unstable in *in vivo* in the presence of carboxylate- and phosphate-containing cellular chelators.[77,95] Cellular studies indicate cytoprotective functionality in a range of disease models related to oxidative stress. The ambiguity regarding the extent of SOD mimicry has led many to speculate that the observed biological activity of Mn-salens may arise from alternative reactions, such as CAT mimicry.

Cyclic Polyamines

The most active SOD mimics are derived from 1,4,7,10,13-pentazacyclopentadecane ([15]aneN$_5$) ligand backbones.[48] The seven-coordinate cyclic polyamines can coordinate Mn and Fe in both the +2 and +3 oxidation states. M40403 exhibited high enough activity and thermodynamic and kinetic stability to become the first SOD mimic to enter clinical trials.[96] M40403 is a metal-based non-substituted analogue of the cyclic pentadentate polyamine ligand ([15]aneN$_5$). The design was further refined using computational molecular methods to yield a series of highly efficient SOD mimetics: M4040X (X=1-4).[97] The three complexes are stereoisomers of dimethyl derivatives of M40403 that have been functionalized with cyclohexane moieties. M40402, the *cis*-2*R*,21*S*-dimethyl complex, has a k_{cat} for superoxide dismutation of 1.57×10^6 M^{-1} s^{-1} , which is nearly identical to the 1.64×10^7 M^{-1} s^{-1} value measured for M40403.[98] Although the *trans*-2*S*,21*S*-dimethyl complex M40401 is an active catalyst, having a k_{cat} of 1.6×10^9 M^{-1} s^{-1}, the *R* isomer, M40404, is catalytically inert, as

assessed by pulse radiolysis and stopped-flow kinetics studies.[98] Regardless of the direct method used the k_{cat} values differ among the complexes.

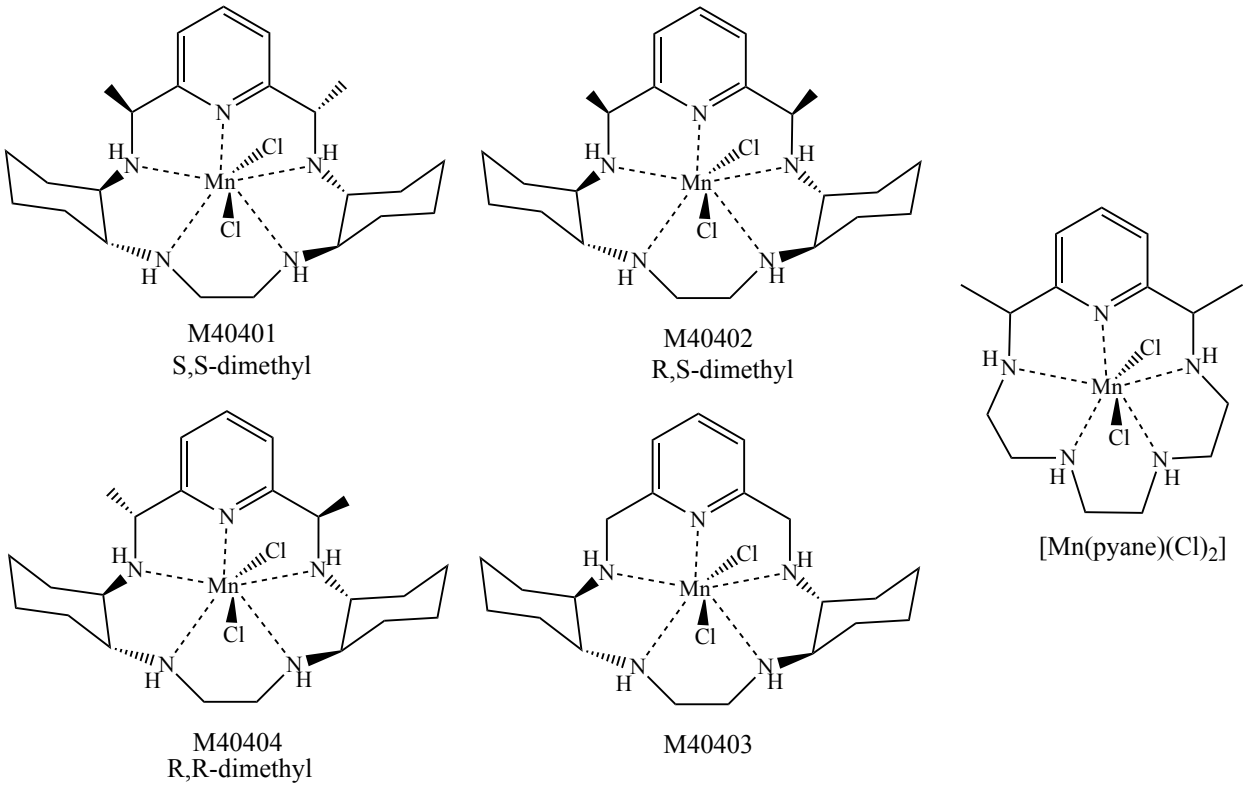

Figure 1.11 Schematic of select Mn(III)-polyamines.[65,98,99]

Despite the differing catalytic rates, the Mn(III/II) redox potentials of the three complexes are similar: 525, 464, and 452 mV vs. NHE for M40403, M40401, and M40404, respectively.[98,99] The lack of correlation between the catalytic rate and reduction potential suggests an alternative structure-activity relationship than the one proposed for metalloporpyhins. The precise mechanism for $O_2^{\cdot-}$ dismutation is still elusive and two differing catalytic cycles were proposed by Riley *et al.* and Anderson *et al.* The approach proposed by Riley involves two separate dismutation cycles, a pH-dependent outer-sphere electron transfer pathway and a pH-independent inner-sphere pathway.[99-101] For both paths, the rate-determining step is the oxidation of Mn(II) to a pseudo-

octahedral Mn(III)-OH intermediate. Anderson proposed an alternative mechanism in which the rate-limiting step is an outer-sphere electron transfer between superoxide and a Mn(III)-peroxo adduct formed from a fast inner-sphere reaction between the Mn(II) complex and superoxide.[98] Oxidation of the Mn(III)-peroxo species would form molecular oxygen and a basic Mn(II)-peroxo complex that would abstract two protons from the solvent to generate H_2O_2.

Both proposed mechanisms suggest that the conformational flexibility of the M4040X complexes is essential for their high activities. The ability of the ligand to access multiple conformations lowers the energy barrier for electron transfer and accommodates the pseudo-octahedral geometry required for the Mn(III) complex. Analysis of X-ray data for the oxidized species indicated that slight differences in the conformational flexibility could account for the differences in the catalytic activity of the isomers.

The ease of modifying the M40403 backbone inspired the design of an even more flexible ligand: *trans*-2,13-dimethyl-3,6,9,12,18-pentaazabicyclo-[12.3.1]octadeca-1(18),14,16-triene). Mn(II) complexes of this ligand are labeled as [Mn(pyane)$(Cl)_2$]. Substituent modification at the pyridine sub-moiety generated positively charged derivates or more lipophilic salens with moderate SOD activity. The pentagonal planar coordination by the pentaazamacrocycle leaves two exchangeable axial sites for the coordination of exogenous anions. Although this improves catalysis by facilitating the coordination of superoxide, it also renders this catalysis susceptible to inhibition by phosphate.

Fe(II) complexes with cyclic polyamines structurally resemble their Mn(II) analogues, being isolated as seven coordinate *trans*-dichloro complexes, but they do not dismutate superoxide as efficiently as the Mn(II) compounds.[103] The reduction of Fe(III) to Fe(II) is the rate-determining step and is believed to proceed via an inner-sphere mechanism. As such, the catalysis is constrained

by of the need to provide a vacant coordination site on Fe(III). Similar to most Fe(III) and Fe(II) complexes, they have an inherent tendency to react with H_2O_2 and generate $OH^{\cdot}$ via Fenton-like chemistry, making these less attractive as antioxidants.

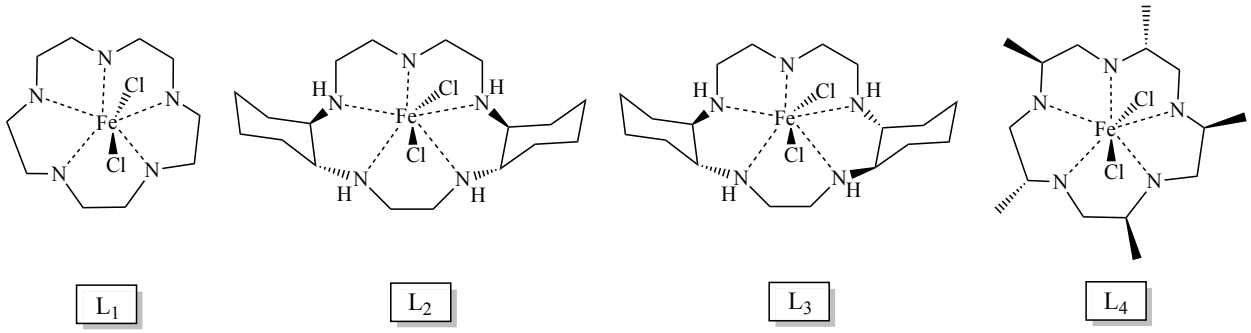

Figure 1.12 Structural representation of select Fe(III)-polyamines, L_1-L_4 containing C-substituted L by Riley *et al*.[103] L = 1,4,7,10,13-pentaazacyclopentadecane.

Flexible-Ligand Based SOD Mimics

SOD mimetics can also be prepared with acyclic polydentate ligands that consist of secondary and tertiary amines derivatized with a variety of pendent arms. The modularity of the ligands makes them highly tunable, and it is straightforward to incorporate steric bulk,[104] functional groups that target cellular structures,[105,106] and functional groups that can either stabilize particular metal oxidation states or modify the overall charge.[107-111] Research conducted by the Policar group highlights the abilities of acyclic ligands to emulate specific characteristics of SODs, such as the inclusion of an electrostatic channel composed of cationic polyarginine peptides.[105,106] Varying the ratio of N/O ligand donors assisted in replicating the N_3O_2 coordination sphere found in Fe- and Mn-containing SODs. Policar group's analysis of $[Mn^{II}(IPG)]^+$, $[Mn^{II}(BIG)]^+$, $[Mn^{II}(BMPG)]^+$, $[Mn^{III}(PI)_2]^+$, and $[Mn^{II}(TMIMA)_2]^{2+}$ demonstrated a linear correlation between Mn(III/II) redox potentials and catalytic efficiency. The compounds showed no electrocatalysis in phosphate buffer, but featured irreversible waves in pH 7.5 collidine buffer.[104] The most active and easiest to oxidize, $[Mn^{III}(PI)_2]^+$, had an electrochemical wave of 0.34 E_{pa} V vs. NHE and a catalytic rate constant of 6.6×10^6 M^{-1} s^{-1}, which was determined indirectly by the cytochrome *c*

assay.[104] Derivatives of the PI ligand overly stabilized the Mn(III) oxidation state and decreased catalysis, indicating a requirement of balanced cycling between Mn(II) and Mn(III).[112]

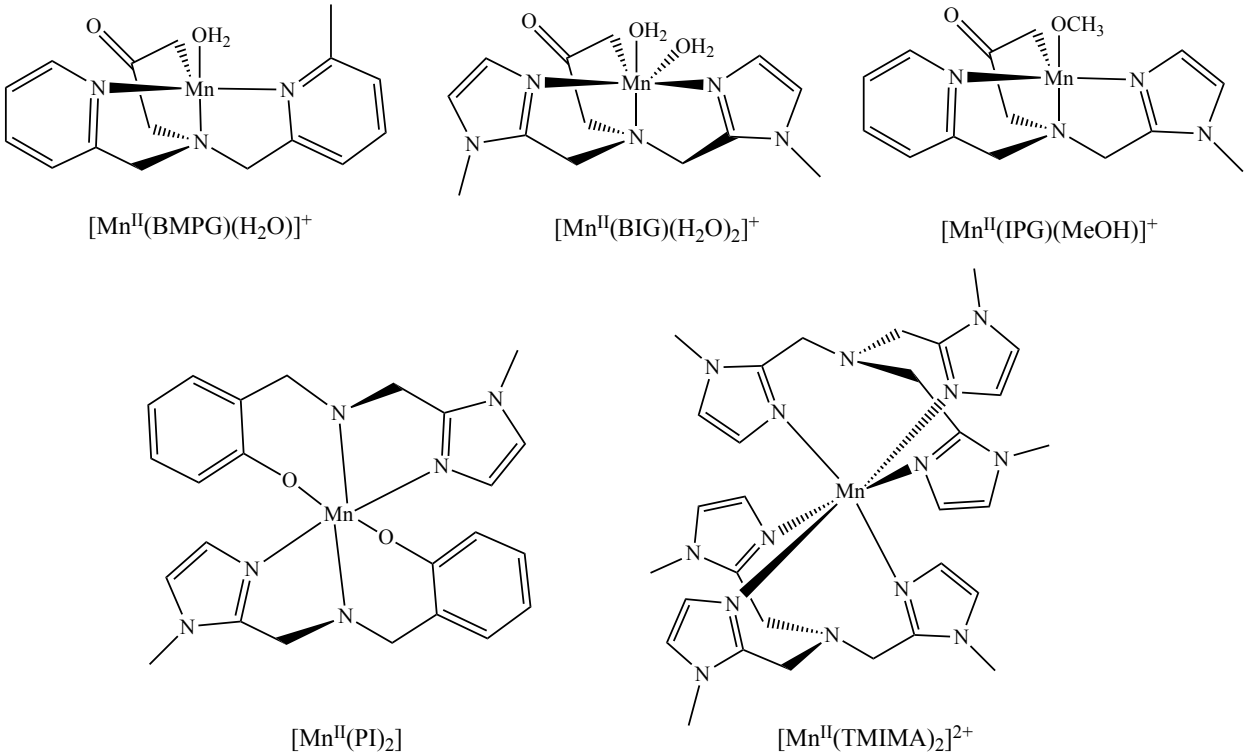

Figure 1.13 Structures of Mn(II) complexes with N-centered tridentate ligands in solution.[104]

The next highest catalytic active complexes $[Mn^{II}(BMPG)]^+$ and $[Mn^{II}(TMIMA)_2]^{2+}$. These complexes feature steric crowding of ligands and favor Mn(II) oxidation to Mn(III), the rate-limiting step of the catalytic cycle.[113] Of the complexes $[Mn^{II}(IPG)]^+$ and $[Mn^{II}(BIG)]^+$ displayed decreased activity in phosphate buffer, which can be attributed to the generation of less catalytically active Mn-phosphate intermediates; as with other Mn-containing SOD mimics, the phosphate acts as a competitive inhibitor.[65] Pulse radiolysis of $[Mn^{II}(IPG)]^+$ was consistent with a mechanistic pathway in which a transient $[Mn(IPG)(OO)]^6$ species (either a Mn(II)-peroxo or a Mn(III)-superoxo) gets protonated to release H_2O_2 and generate the $[Mn^{III}(IPG)]^{2+}$ species.[114] $[Mn^{III}(IPG)]^{2+}$ is then reduced back to $[Mn^{II}(IPG)]^+$ in the rate-limiting step as superoxide is

oxidized. $[Mn^{III}(PI)_2]^+$ is believed to react in a similar manner, and the slow reduction may explain why the complex mainly exists in the monomeric Mn(III) oxidation state.

Other examples of Mn complexes from the Policar group feature a 1,2-ethanediamine backbone with appended peptides. They added positively charged poly-arginine groups to simulate electrostatic guidance, a key feature in the areas surrounding the active sites of SOD enzymes. Stopped-flow kinetics analysis of the direct reactions between the Mn(II) complexes and superoxide revealed two trends. First, the addition of a positively charged residue in the immediate metal center environment increased the catalytical efficiency; the unsubstituted complex had a k_{cat} = 5.0 × 10^6 M^{-1} s^{-1} whereas the mono-arginine substituted complex had a k_{cat} = 6.6 × 10^6 M^{-1} s^{-1}.[115] Second, adding bulkier alkyl groups to the secondary amine worsened the catalytic efficiency and completely counteracted any benefit provided by the attached positive charges; the mono-glycine substituted complex had a k_{cat} = 4.2 × 10^6 M^{-1} s^{-1}.[115] Open chain ligands lack the rigidity associated with macrocyclic backbones; this has limited the application complexes with acyclic ligands in biological environments.

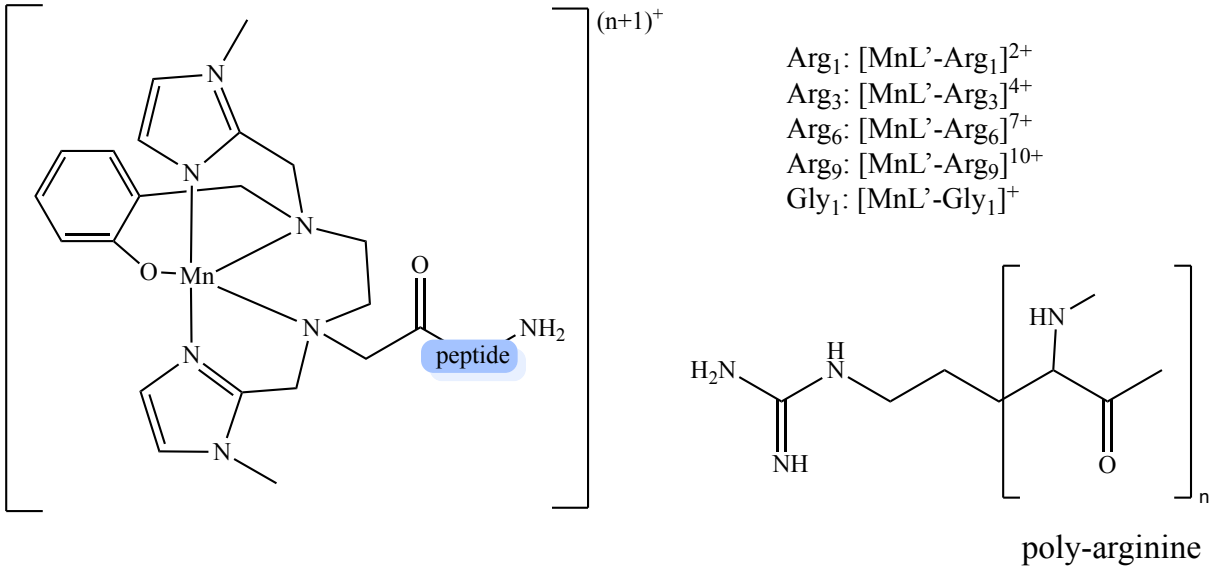

Figure 1.14 Structural depiction of peptide functionalized N-(2-oxybenzyl)-N,N′-bis[2-(N-methylimidazolyl)methyl]-ethane-1,2-diamine)maganese(II) complex.[115]

A different group of 1,2-ethanediamine derivatives were prepared by Goldsmith and co-workers. These ligands were functionalized with pyridine rings and redox-active phenolic groups: either *p*-cresol (Hptp1) or *p*-quinol (H_2qp1 and H_4qp2).[110,111,116] All three of the Mn(II) complexes are capable MRI contrast agents, with $[Mn(H_2qp1)]^{2+}$ and $[Mn(H_4qp2)]^{2+}$ exhibiting increased r_1 upon oxidation by H_2O_2. Electrochemical analysis of the quinol complexes in phosphate buffer reveals redox features of ~300 mV vs. NHE for both $[Mn(H_4qp2)]^{2+}$ and $[Mn(H_4qp2)]^{2+}$, and indirect assays of the SOD activity revealed that all three complexes were competent superoxide scavengers. The xanthine oxidase/hypoxanthine/lucigenin assay that was used to screen this activity is unfortunately subject to false positive results, and positive results need to be confirmed by more direct analytic methods, such as either stopped-flow kinetics or pulse radiolysis.

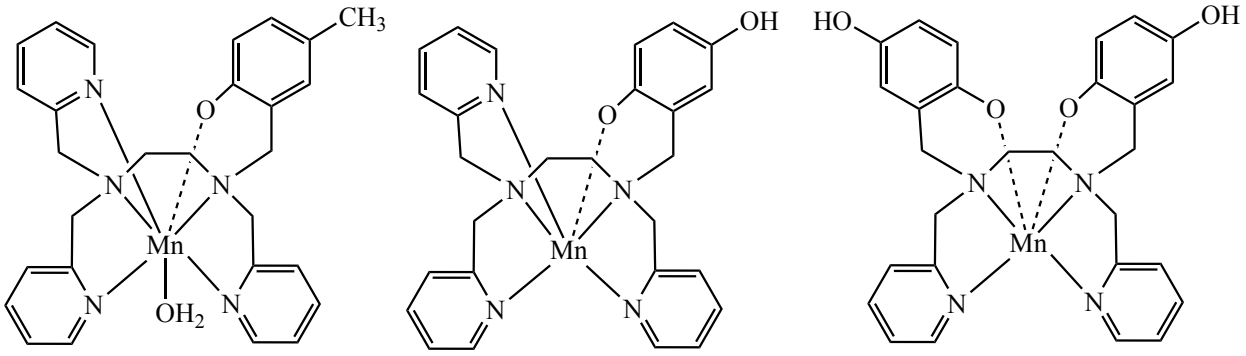

$[Mn(Hptp1)(H_2O)]^{2+}$ $[Mn(H_2qp1)]^{2+}$ $[Mn(H_4qp2)]^{2+}$

Figure 1.15 Structural depiction of 1,2-ethanediamine quinol based Mn(II) compounds.[110,111,116]

An in-depth analysis of $[Mn^{II}(Hptp1)(H_2O)]^{2+}$ using stopped-flow kinetics, ^{17}O-NMR, EPR, potentiometric pH titrations, electrochemistry, and low-temperature mass spectrometry highlighted the importance of a coordinated water molecule for inner- and outer-sphere mechanisms.[117] Above pH 6, the complex is seven-coordinate which promotes the deprotonation of *p*-cresol to form $[Mn(ptp1)(H_2O)]^{+}$. Reduction of the coordinated water molecule generates a five-coordinate species: $[Mn(ptp1)(OH)]^{+}$. It was proposed that water coordination facilitated a

proton-coupled electron transfer, which lowers the Mn(III/II) redox potential and permits the reaction to proceed through an outer-sphere mechanism.

In water, there is an equilibrium a hydrated seven-coordinate species, $[Mn^{II}(ptp1)(H_2O)]^+$ and a "water-free" six-coordinate form, $[Mn^{II}(ptp1)]^+$.[117] The water is believed to coordinate competitively with superoxide and determine the mechanism through which it gets degraded. In the absence of a water molecule, superoxide can bind to Mn(II) and get reduced through an inner-sphere mechanism. The pathway resembles superoxide reductase more than SOD activity, in that the superoxide can only be reduced by this path, not oxidized. Bound superoxide forms a Mn(III)-hydroperoxo intermediate that undergoes homolytic bond cleavage and forms a Mn(IV)-oxo intermediate and $OH^{\cdot}$. Upon oxidation via H_2O_2, $OH^{\cdot}$, or through reaction with another high-valent Mn(IV)-oxo species, the phenolic portions of two complexes oxidatively couple to yield a dimanganese structure that can continue to mimic SOD activity via the outer-sphere dismutation of superoxide. [117]

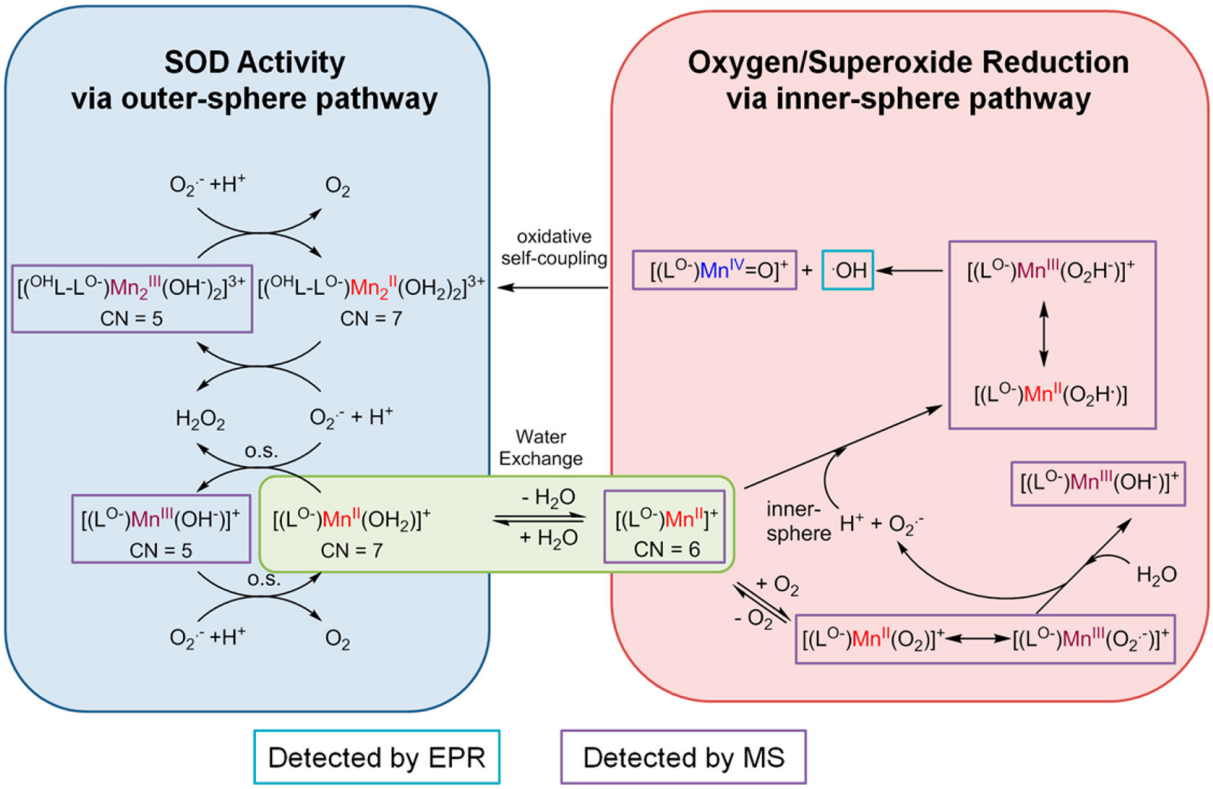

Figure 1.16 Mechanistic pathway proposed by Kenkel *et al.* Framed species are detectable by cryo-mass spectrometry.[117]

1.7 Cu-Based Redox-Active SOD Mimics

The aforementioned complexes mimic either Fe or MnSOD; however, other classes of SODs exist that contain either Cu or Ni. Copper is a trace element found in all living organisms; it is involved in diverse metabolic functions and is a key component of many metalloenzymes, including SOD1 and SOD3.[118] In SOD1 and SOD3, the active-site copper switches between Cu(I) and Cu(II). A variety of Cu complexes featuring ligand components of amino acids,[119,120] macrocycles,[89,121] commercial drugs,[122-125] and peptides[126] were designed to mimic catalytic activity of SOD1 and SOD3. Only a few of the copper mimics are illustrated here as examples.

Copper porphyrins were briefly evaluated as SOD mimics, and some demonstrate moderate SOD activity; $CuBr_8TM\text{-}4\text{-}PyP^{4+}$ has a k_{cat} of 2.9×10^6 M^{-1} s^{-1}. Metallocorroles normally feature

a copper (III) cation which renders the complexes exceptionally oxidatively stable as assessed by their Cu(III/II) reduction potentials.[89] However the reduction of superoxide requires a stable Cu(II) intermediate, making 3,17-bis-sulfonato-5,10,15(trispentafluorophenyl)corrole copper(III) a poor oxidant. Addition of formate in a pulse radiolysis study yielded a higher k_{cat} due to the formation of Cu(II) in the active site, in turn enabling the reduction of superoxide.[89] The use of a Cu(III/II) couple is more reflective of a superoxide reductase (SOR) enzyme rather than CuZnSOD which features a Cu(II/I) redox couple.

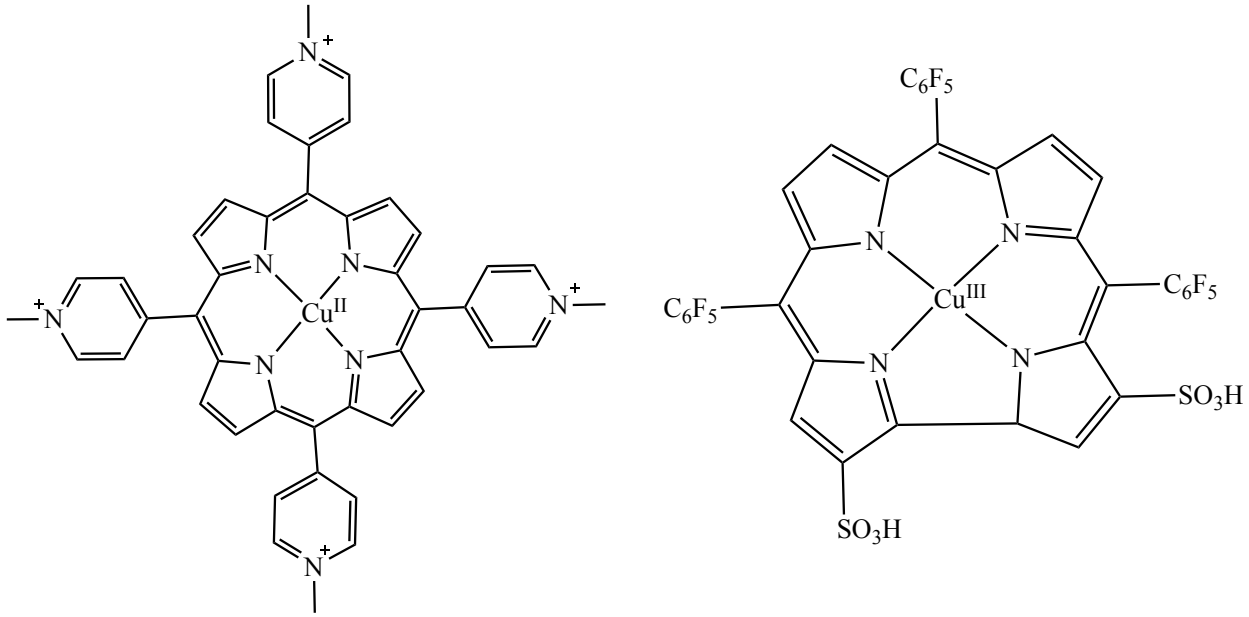

$Cu^{II}Br_8TM–4–PyP^{4+}$ $[Cu^{III}((tpfc)(SO_3H)_2\text{-Corrole})]$

Figure 1.17 Cu(II) porphyrin [$Cu^{II}Br_8$TM-4-PyP^{4+}] and Cu(III) corrole [$Cu^{II}(((tpfc)(SO_3H)_2$-Corrole].[89,121]

Simple amino acid complexes of Cu(II) such as [$Cu(tyr)_2$] and [$Cu(lys)_2$] displayed slightly above-baseline SOD mimicry, with assays providing IC_{50} values of 45 and 86 μM, respectively.[120] These values are much higher than those of a typical SOD, which would have an IC_{50} value of 0.04 μM. The addition of nanoparticles enhanced the scavenging activity of the amino acid complexes. Korschelt *et al.* synthesized a glycine functionalized cuprous hydroxide nanoparticle, [Gly-$Cu(OH)_2$]. Surprisingly, [Gly-$Cu(OH)_2$] had a 3.91×10^{10} M^{-1} s^{-1} k_{cat} according to the

iodonitrotetrazolium chloride (INT) reduction-based assay, which was over an order of magnitude greater than the 1.98×10^9 M^{-1} s^{-1} measured for CuZnSOD.[119] The INT assay is a facile colorimetric SOD assay. This method along with previously mentioned indirect methods, is vulnerable to superficial generation of superoxide. The results for [Gly-$Cu(OH)_2$] highlights the discrepancy in the catalytic values for the native enzyme on the two different assays; this suggests that the rate constants obtained from these assays are decidedly imperfect.

Many current commercially available pharmaceuticals seem to benefit from coordination to or co-administration with copper. Metal-coordinated drugs sometimes exhibit high SOD-like mimicry. [Cu(GFL)(5-nitro-1,10-phenanthroline)Cl]·$5H_2O$ has an IC_{50} of 0.5 μM measured with NADPH/PMS/NBT method.[123] GFL is the conjugate base of the fourth-generation fluoroquinolone antibacterial agent, [(±)-1-cyclopropyl-6-fluoro-1,4-dihydro-8-methoxy-7(3-methyl-1-piperazinyl)-4-oxo-3-quinoline carboxylic acid (GFLH)].[123] Non-steroidal anti-inflammatory drugs (NSAIDs) complexed with copper have lower toxicity and fewer side effects than native uncoordinated NSAIDs.[122,124] Currently, the most active is the indomethacin complex [$Cu_2(indo)_4(DMF)_2$] which has a recorded IC_{50} of 0.23 μM on the NBT assay.[125] A pulse radiolysis study reveals second-order rate constants of 6×10^9 M^{-1} s^{-1} and 1.1×10^9 M^{-1} s^{-1} in aqueous and aprotic solutions, respectively. The compound has veterinary applications, but few clinical applications have been explored.[127]

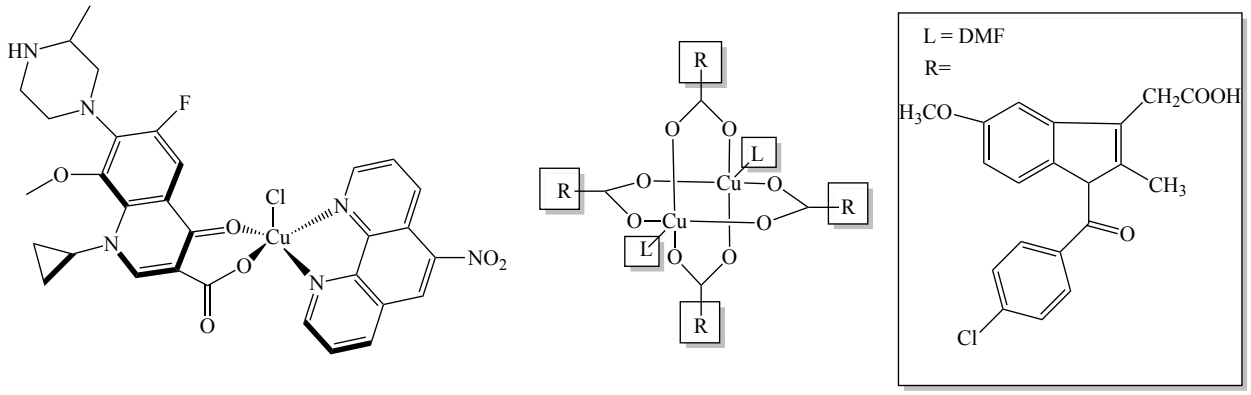

[Cu(GFL)(5-nitro-1,10-phenanthroline)Cl] $[Cu_2(indo)_4(DMF)_2]$

Figure 1.18 Copper coordinated drug-based compounds.

Although copper complexes have demonstrated therapeutic applications, limited information is available regarding its metabolic pathway of activity. Additionally, the lack of correlation between indirect methods and minimal direct analysis of Cu-SOD mimics prevents accurate recording of catalytical efficiency. As previously pointed out, indirect methods tend to record lower SOD activity than pulse radiolysis.[128] Steady-state concentrations of superoxide in indirect methods differ from those found *in vivo*, and compounds with low SOD activity are likely to be completely inefficient *in vivo.* This discrepancy may explain why several compounds show promising *in vitro* activity, but pharmaceutical applications of copper compounds are limited *in vivo*.

1.8 Ni-Based Redox-Active SOD mimics

Following the isolation and purification of NiSOD from *Streptomyces spp.,* research quickly noted key characteristics that differentiate this isoform from previously identified SOD enzymes. A few key research groups such as Shearer and Harrop synthesized nickel cation compounds to gain fundamental understanding of the governing physical properties responsible for NiSOD catalyzed disproportionation of $O_2^{\cdot-}$. The preparation of small molecule mimics of the NiSOD active site has provided insight into the electrochemical properties that support Ni(III/II)

redox,[129-131] the protection and stability of the coordinated ligands – particularly the cysteines - in the native enzyme,[132-134] the coordination geometry required for catalysis,[135-137] and probable proton sources for H_2O_2.[138-140]

Synthetic analogues of NiSOD utilize three main approaches: peptide maquettes, low molecular weight accurate models, and low molecular weight approximate models. Several groups adhere to the following three guidelines for the design and synthesis of synthetic models. First, the ligand frameworks contain a mixed N/S donor set, mimicking the primary coordination sphere in the native enzyme's active site. The coordination sphere of the Ni features two nitrogen donors, the N-terminal amine nitrogen of His1 and the amidate nitrogen of Cys2, and two cysteinate sulfur donors, Cys2 and Cys6. Second, the ligand should adopt a planar N_2S_2 arrangement and be capable of replicating the low-spin four-coordinate Ni(II) to five-coordinate Ni(III) transformation observed in the enzyme. Third, the benefits of the secondary structure, hydrogen bonding, and electrostatic interactions of the ligand frame should be replicated. It is hypothesized that cysteinates are protected from oxidative damage by electronic and structural fine-tuning, which allows NiSOD to disproportionate superoxide.[141]

Shearer and coworkers are leading contributors to the design and synthesis of maquettes. Based on the Dutton metalloprotein approach, these small metallopeptides feature protein sequences found in the parent enzyme.[142] Replicating the enzyme's biological peptide scaffold offers the advantage of closely mimicking geometric structure, electronic structure, and spectroscopic properties to gain a fundamental understanding of structural and sequence-dependent aspects of native NiSOD. The first synthetic model was designated [Ni(SOD^{M1})], where SOD^{M1} is HCDLPCGVYDPA, representing the first 12 residues of the *S. coelicolor* primary sequence.[143] The peptide coordinates in a 1:1 ratio to Ni(II) under slightly basic conditions and

adopts a square-planar Ni(II)- N_2S_2 arrangement, typical for most maquettes described *vide infra*. Modifications at the ε-nitrogen of the His1 ligand moiety provided derivatives of [Ni(SOD^{M1-X})], where X = methyl (Me), 2,4-dinitrophenyl (DNP), and tosyl (Tos).[144] These metallopeptides and a second-generation system, heptapeptide [Ni(SOD^{M2})], are all SOD active.[145] Currently, the most active maquette has a k_{cat} of 6×10^8 M^{-1} s^{-1} for the Tos substituted compound.[144]

Other peptide maquettes have been prepared using 3 – 12 amino acids with various modifications to illuminate key structural aspects of the biological Ni active site.[143,146,147] The smallest peptide maquette, [Ni(NCC)] synthesized by Laurence and coworkers is barely SOD active, with rates only slightly greater than that of the self-disproportionation of superoxide.[146] Although the synthetic analogue features peptides not employed in the immediate vicinity of the N-terminus, it is hypothesized that the surrounding environment of the native peptide may assume new configurations to remove steric hindrance that may block access to the native active site.[148] Some research has indicated that the presence of Tyr9 near the Ni active site controls access of anions similar to the tyrosine of MnSOD and FeSOD enzymes.[37]

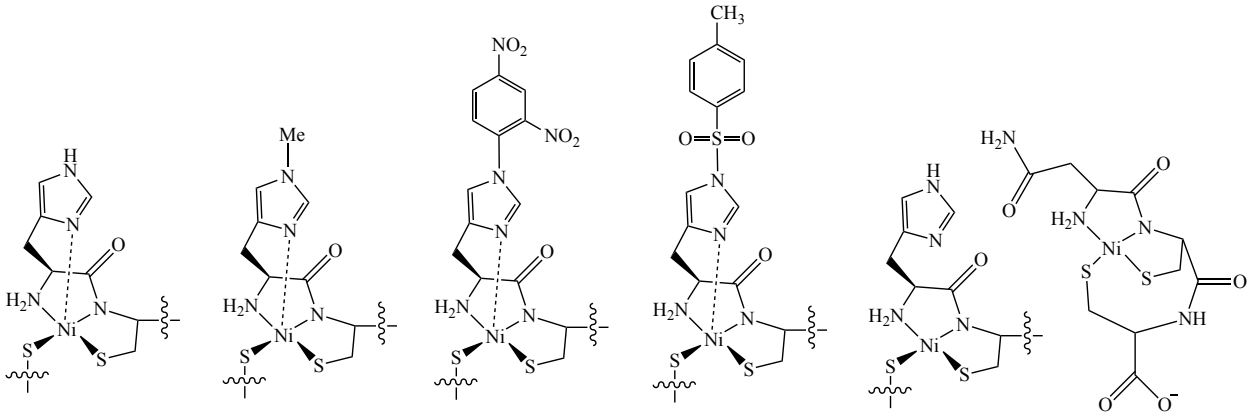

Figure 1.19 Structures of select NiSOD-maquettes.[143-146]

Complexes with maquettes have reproduced many of the spectroscopic features of NiSOD and much of the reactivity. Still, there are substantial obstacles to developing nickel-maquette

species into pharmaceuticals. Some of the maquettes formed high molecular weight polymeric species over the course of a few hours in atmospheric conditions.[143,145] Disagreement between inner- and outer-sphere mechanisms has also challenged the validity of comparing maquettes and native SOD.[3] One study suggests that synthetic analogues of the primary sequence are mechanistically distinct from native NiSOD and may only be suitable for exploring the proton source and mechanism of electron transfer.[133,149] Despite the discrepancies between studies, maquettes remain the most successful compounds for modeling NiSOD.

Small molecules with N/S or N/O ligand frameworks approximate certain aspects of the NiSOD coordination sphere. Darensbourg and coworkers synthesized the first small molecule NiSOD mimic using a 1-(2-mercapto-2-methylpropyl)methyl-1,4-diazacycloheptane (mmp-dachH) as an amine-thiol N_2S chelate; this ligand reacts with Ni(II) to form a dimeric species with the Ni(II) ions linked by a μ-thiolate bridge.[135] The dimeric species reacts with imidazole to afford two equiv. of the monomeric Ni(II) complex [Ni(mmp-mdach)-Im)]Cl with a N_3S coordination sphere.[135] The Ni(II) species features both thiolate and imidazole donors, is stable in the presence of oxygen, and can provide 40% superoxide protection against NBT scavenging.[135]

Pentadentate ligands with N_3O_2 donor sets can stabilize the Ni(III) oxidation state and oxidize superoxide. 2,6-bis{[(S)-2-(Diphenylhydroxymethyl)-1-pyrrolidinyl]methyl}pyridine (H_2BDPP) coordinates Ni(III) with one pyridine N-donor, two tertiary pyrrolidine N-donors, and two alcohol O-donors.[136] [Ni^{III}(BDPP)] adopts a distorted square-pyramidal N_3O_2 environment that replicates the five-coordinate structural arrangement found for $NiSOD_{ox}$. The Ni(III) complex reacted with excess KO_2 to yield O_2 and the Ni(II) complex, which is SOD inactive. Another functional mimic that deviates from the enzymatic N_2S_2 donor set is a sulfur-rich pseudopeptide ligand derived from nitrilotriacetic acid (NTA).[24] The ligand adopts a S_3O configuration with

thiolates originating from the three cysteinates. At physiological pH, the catalyst displays activity of 1.8×10^5 M^{-1} s^{-1} in aqueous solution. Although the catalysis does not compare to those performed by maquettes and the native enzymes, this is the first catalytically active small molecule mimic, despite the lack of N-donors.

Unlike manganese and iron complexes, Ni(II) complexes with porphyrins and macrocycles display very little SOD activity. Water-soluble Ni(II) porphyrins were not as catalytically active as peptide models.[150-152] The catalytic efficiency of the porphyrins was $\leq 6 \times 10^5$ M^{-1} s^{-1} at pH 5.6 and $\leq 8 \times 10^4$ M^{-1} s^{-1} at pH 8.0 as assessed by pulse radiolysis measurements.[150] Reaction of L = 5-amino-3-methyl-1-phenylpyrazole-4-carbaldehyde (AMPC) with Ni(II) yielded $[NiL(NO_3)_2]$.[151] The macrocyclic cationic complex performs superoxide disproportionation with an efficiency below 4.7×10^5 M^{-1} s^{-1}.

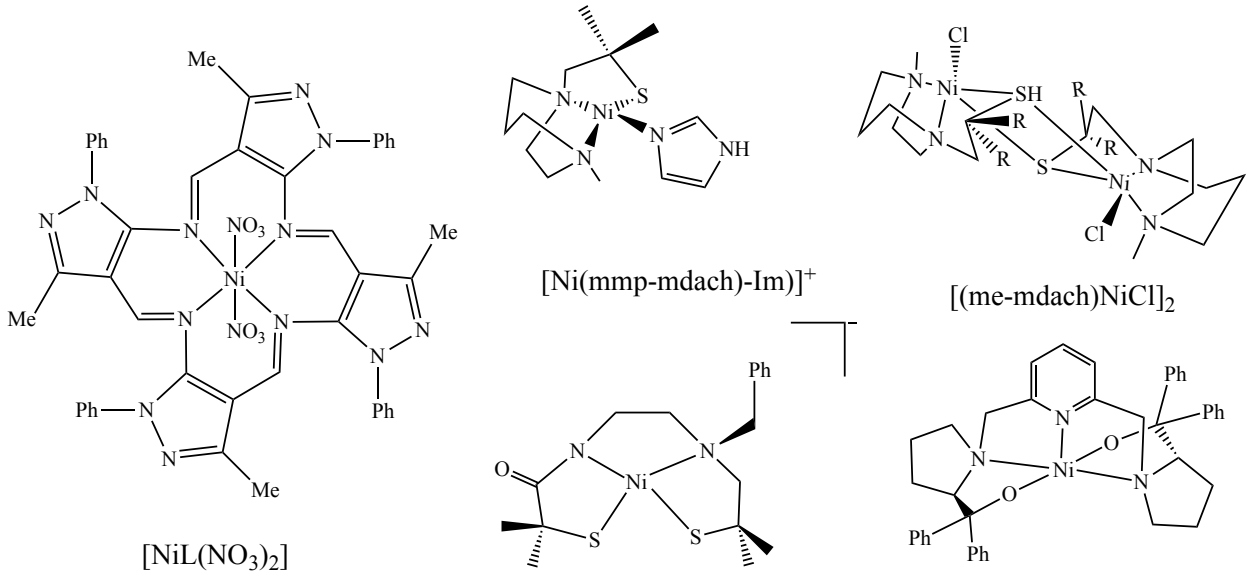

Figure 1.20 Select small molecule NiSOD mimics.

Synthetic models that replicate the structure and coordination sphere of the NiSOD active site are deemed accurate. These low-molecular-weight complexes replicate the primary coordination environment and can provide fundamental insights into NiSOD catalysis. The ligand

primarily provides either N_2S_2 or N_3S_2 coordination. The N_2S_2 ligands more accurately model the mixed-amide/bis-thiolate coordination sphere of $NiSOD_{red}$. The first accurately reproduced synthetic analogue with amide and amine ligands bound to Ni was $[Me_4N]$(Ni(BEAAM)) with a N_2S_2 ligand frame of amine nitrogen, carboxamide nitrogen, and two sulfur donors.[134] Although the compound displays an electrochemical feature of 0.120 V vs. Ag/AgCl in MeCN, a value within the SOD redox potential window, the complex does not react with superoxide.

Most [Ni(N_2S_2)]and [Ni(N_3S_2)] complexes are non-reactive or undergo sulfur oxidation when exposed to superoxide.[11,134,138] The compounds display irreversible or quasi-reversible features outside of the superoxide redox potential range. One hypothesis is that the formation of disulfide bonds diverts the superoxide from the desired dismutation reactions and precludes catalysis. A few advanced studies confirmed this hypothesis with the presence of insoluble S,S-bridged dimers.[132] Despite the lack of activity, the majority of the accurate synthetic models have nonetheless provided insight into the roles of N/S donors of the native enzyme.[129,138,153] The N/S mixed ligands can be modified to be oxidatively stable against O_2 and H_2O_2. Reproduction of the coordination environment in a non-peptide analogue has illuminated concepts such as the importance of hydrogen bonding,[132] roles of amine and amidate ligands in cysteinate protection,[141] and the requirement of a fifth axial N-donor.[129]

1.9 Alternative Approaches to SOD mimicry

Complications with metal-containing SOD mimics has prompted researchers to explore purely biochemical and organic antioxidants. Exogenous SOD, such as MnSOD, may be beneficial in terms of quantity and duration of pharmacological effect. In fact, administration of SOD *in vivo* has decreased inflammation, overcome ischemia, slowed tumor formation, and increased male fertility.[154-157] Yet, exogenous SOD as a pharmaceutical is limited to animal consumption as it

displays several side effects and is inadequately potent for human consumption.[158,159] Research also pursued a plant-based exogenous SOD, GliSODin. A wheat-gliadin encapsulated melon SOD was claimed to have promising therapeutic potential in reducing oxidative stress and preventing serve ailments. [160,161] Categorized as a supplement, the substance is neither approved nor regulated by the US Food and Drug Administration. Many studies of the benefits, the mechanism of action, and potential adverse effects are inconclusive and yet to be studied.[162]

Nonmetallic compounds were proposed to bypass the toxicity seen with "free" metals. Researchers synthesized fullerene derivatives, MitoQ, and nitroxide-based compounds as purely organic based SOD mimetics. Certain derivates can catalytically degrade $O_2^{-\cdot}$, albeit at rates far slower than those of SOD enzymes.[107,163] Although both metal-free and redox-active coordination compounds represent attractive means to catalytically degrade superoxide, both strategies have limitations that compromise their efficacy as small-molecule pharmaceuticals.

The nanozyme C_{60} fullerene was first isolated in 1985.[164] Introducing hydrophilic substituents rendered these carbon-cluster structures water-soluble and facilitated their use in biological applications. A tris-malonic acid derivative of the C_{60} fullerene (C_3) displayed SOD-like activity, with a k_{cat} of $2 \times 10^6\ M^{-1}\ s^{-1}$.[107] This complex is 100-times less active than native enzyme yet may still have therapeutic potential. It successfully prolonged the lifetimes of MnSOD knockout mice and displayed neuroprotective effects *in vitro* and *in vivo.* Detailed analysis revealed the compound interacts with superoxide through catalytic dismutation rather than stoichiometric scavenging. A mechanism was proposed where the tris-malonic acid groups electrostatically direct superoxide anions toward the electron-deficient areas on the surface of C_3.[107] Superoxide is then stabilized through hydrogen bonding until a second bound superoxide promotes dismutation assisted by protons of carboxyl groups.

Mitoquinone (MitoQ) is another metal-free organic compound that displays antioxidant activity. $MitoQ_{10}$, an extensively characterized organic SOD mimetic, targets the mitochondria through an appended cationic triphenylphosnium (TPP) ion.[165] The compound is lipophilic yet water-soluble and accumulates inside the mitochondria. The lipophilic portion allows the compound to be selectively taken up through plasma and mitochondrial membrane. Once inside the mitochondria, MitoQ adsorbs to the matrix surface of the inner membrane, and the components of the electron transport chain reduce MitoQ (quinone) to $MitoQH_2$ (quinol), which remains stable. $MitoQH_2$ can undergo oxidation by $ONOO^-$ and form MitoQH (semiquinone radical) which dismutates to MitoQ and $MitoQH_2$.[166] MitoQ reacts rapidly with $O_2^{-\cdot}$ with rate constants of 2.0×10^8 M^{-1} s^{-1} and 4.2×10^8 M^{-1} s^{-1} in water and methanol, respectively.[167] MitoQH reacts with oxygen in a reverse reaction with rate constants of 2.9×10^7 M^{-1} s^{-1} and 7.3×10^8 M^{-1} s^{-1} in water and methanol, respectively, but the forward reaction is 10-fold faster. The positive results in animal models of human diseases led to the development of MitoQ as a pharmaceutical. Phase II studies have demonstrated potential recovery from liver damage in chronic hepatitis C virus patients, but the treatment did not stop the virus from replicating.[168] In another study, MitoQ was unable to halt the progression of Parkinson's disease.[71] Additional studies are required to understand the potential uses of MitoQ as a pharmaceutical.

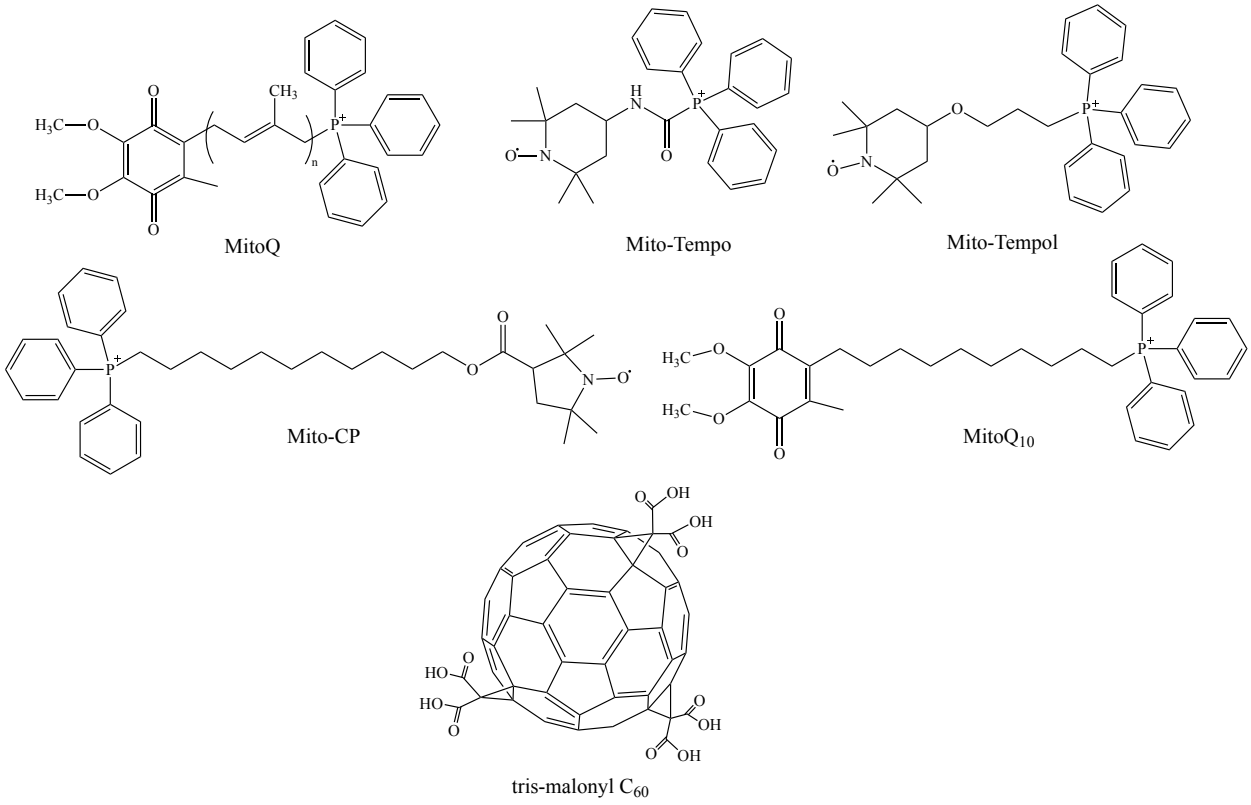

Figure 1.21 Nonmetallic SOD mimics.

Different redox-active compounds can be attached to the end of the alkyl chain to yield numerous derivatives of $MitoQ_{10}$. Nitroxides have been attached to form Mito-Tempo, Mito-Tempol, and Mito-CP, all of which display SOD mimicry in their oxidized and reduced forms.[169,170] Non-conjugated nitroxides are weaker SOD mimetics, with most reacting slowly and inefficiently with superoxide with rate constants below 10^3 M^{-1} s^{-1}. Nitroxides can react with $ONOO^-$ which forms an oxoammonium cation (RNO^+) that can subsequently react with superoxide to regenerate nitroxide (RNO^-). *In vivo* nitroxide cycles between reduced hydroxylamine (RNOH) and RNO^+, both of which act as antioxidants.[171] TEMPO (2,2,6,6-tetramethylpiperidine-1-oxyl), a nitroxide derivate, reacts with HO_2^- with a rate constant of 1.2×10^8 M^{-1} s^{-1} and forms RNO^+.[172] However, the assignment of nitroxides as SOD mimetics is controversial due their low ability to scavenge superoxide.

1.10 Thesis Overview

In this thesis, a novel strategy is proposed: using a redox-active organic molecule as a redox partner for $O_2^{-\cdot}$ and a redox-inactive metal to activate the organic component and attract $O_2^{-\cdot}$. The Goldsmith lab previously prepared Mn(II) based complexes with the quinolic ligands H_2qp1 and H_4qp2; these demonstrate SOD mimicry as confirmed by stopped-flow kinetics.[110,111] Due to the redox activity with the H_2qp1 ligand, the Goldsmith lab subsequently explored $[Zn(H_2qp1)(OTf)]^+$ and found it to be a competent functional mimic of SOD based on data from stopped-flow kinetics analysis and indirect assays.[173] Stopped-flow kinetics revealed the catalyst to be unusually active in phosphate buffer; phosphate normally inhibits the activity of manganese-based SOD mimics.[65,66,117] Based on these results, new complexes featuring Ni(II), Zn(II), and Ga(III) and redox-active ligands H_2qp1, H_4qp2, and H_2qp3 are synthesized and characterized for their capacities to act as SOD mimics. The first compounds with Ni(II) benefit from enhanced complex stability and activity in aqueous solutions. The second group of complexes with Zn(II) illustrate how ligand properties impact catalysis. The final compound explores how the use of a tricationic redox-inactive metal, Ga(III), can impact the antioxidant properties.

The majority of this text is devoted to establishing structure-activity relationships and improving the catalytic activity, particularly in phosphate buffer. The mechanism of superoxide disproportionation in solution is probed with cryo-mass spectrometry (cryo-MS). This method allows the visualization of intermediates at ambient pH. New insights into the pathway of degradation and ligand involvement in Mn(II) complexes were gained from these studies. Molecular modeling of Zn(II) complexes reveals theoretical insight into the catalytic cycle of $O_2^{-\cdot}$ degradation by polydenate quinol-containing complexes with redox-inactive metals. The theme of this text is exploring catalytical activity with redox-ligand based SOD mimics to ultimately bring

forth new knowledge, determine the relative importance of the redox-active components, and identify promising candidates for future synthesis.

References

(1) Chen, R.; Lai, U. H.*; et al. Frontiers in Cell and Developmental Biology* **2018**, *6*.

(2) Imlay, J.; Fridovich, I. *Journal of Biological Chemistry* **1991**, *266*, 6957.

(3) Poderoso, J. J.; Lisdero, C.*; et al. Journal of Biological Chemistry* **1999**, *274*, 37709.

(4) Krumova, K.; Cosa, G. In *Singlet Oxygen: Applications in Biosciences and Nanosciences, Volume 1*; The Royal Society of Chemistry: 2016; Vol. 1, p 1.

(5) Belikov, A. V.; Schraven, B.*; et al. Journal of Biomedical Science* **2015**, *22*, 85.

(6) Ray, P. D.; Huang, B. W.*; et al. Cell Signal* **2012**, *24*, 981.

(7) Redza-Dutordoir, M.; Averill-Bates, D. A. *Biochimica et Biophysica Acta* **2016**, *1863*, 2977.

(8) Sena, L. A.; Chandel, N. S. *Molecular Cell* **2012**, *48*, 158.

(9) Finkel, T. *Journal of Cell Biology* **2011**, *194*, 7.

(10) Devadas, S.; Zaritskaya, L.*; et al. The Journal of Experimental Medicine* **2002**, *195*, 59.

(11) Broering, E. P.; Truong, P. T.*; et al. Biochemistry* **2013**, *52*, 4.

(12) Schieber, M.; Chandel, N. S. *Current Biology* **2014**, *24*, R453.

(13) Bhattacharyya, A.; Chattopadhyay, R.*; et al. Physiological Reviews* **2014**, *94*, 329.

(14) Panieri, E.; Santoro, M. *Cell Death & Disease* **2016**, *7*, e2253.

(15) Case, A. J. *Antioxidants* **2017**, *6*, 82.

(16) Halliwell, B. *The FASEB Journal* **1987**, *1*, 358.

(17) Wang, Y.; Branicky, R.*; et al. Journal of Cell Biology* **2018**, *217*, 1915.

(18) Mosley, R. L.; Benner, E. J.*; et al. Clinical Neuroscience Research* **2006**, *6*, 261.

(19) Fearon, I. M.; Faux, S. P. *Journal of Molecular and Cellular Cardiology* **2009**, *47*, 372.

(20) Eskici, G. z.; Axelsen, P. H. *Biochemistry* **2012**, *51*, 6289.

(21) Gladden, J. D.; Ahmed, M. I.*; et al. The American Journal of the Medical Sciences* **2011**, *342*, 114.

(22) Roberts, C. K.; Sindhu, K. K. *Life Sciences* **2009**, *84*, 705.

(23) Clément, M.-V.; Pervaiz, S. *Redox Report* **2001**, *6*, 211.

(24) Domergue, J.; Pécaut, J.*; et al. Inorganic Chemistry* **2019**, *58*, 12775.

(25) Herb, M.; Gluschko, A.*; et al. Frontiers in Cell and Developmental Biology* **2021**, 2503.

(26) Murphy, M. P. *Biochemical Journal* **2009**, *417*, 1.

(27) Sies, H.; Berndt, C.*; et al. Annual Review of Biochemistry* **2017**, *86*, 715.

(28) Droge, W. *Physiological Reviews* **2002**, *82*, 47.

(29) Gates, K. S. In *Comprehensive Natural Products Chemistry*; Barton, S. D. N., Koji; Meth-Cohn, Otto, Ed.; Elsevier Science Ltd. : 1999; Vol. 7, p 491.

(30) Gebhart, V.; Reiß, K.*; et al. Nitric Oxide* **2019**, *89*, 14.

(31) Phaniendra, A.; Jestadi, D. B.*; et al. Indian Journal of Clinical Biochemistry* **2015**, *30*, 11.

(32) Rosa, A. C.; Corsi, D.*; et al. Molecules* **2021**, *26*, 1844.

(33) Snezhkina, A. V.; Kudryavtseva, A. V.*; et al. Oxidative Medicine and Cellular Longevity* **2019**, *2019*.

(34) Taverne, Y. J.; Bogers, A. J.*; et al. Oxidative Medicine and Cellular Longevity* **2013**, *2013*.

(35) Indo, H. P.; Yen, H.-C.*; et al. Journal of Clinical Biochemistry and Nutrition* **2015**, *56*, 1.

(36) McCord, J. M.; Fridovich, I. *Journal of Biological Chemistry* **1969**, *244*, 6049.

(37) Sheng, Y.; Abreu, I. A.*; et al. Chemical Reviews* **2014**, *114*, 3854.

(38) Keele, B. B.; McCord, J.*; et al. Journal of Biological Chemistry* **1970**, *245*, 6176.

(39) Fridovich, I. *The Journal of Experimental Biology* **1998**, *201*, 1203.

(40) Candas, D.; Li, J. J. *Antioxidants & Redox Signaling* **2014**, *20*, 1599.

(41) Yan, Z.; Spaulding, H. R. *Redox Biology* **2020**, *32*, 101508.

(42) Perry, J.; Shin, D.*; et al. Biochimica et Biophysica Acta (BBA)-Proteins and Proteomics* **2010**, *1804*, 245.

(43) Pettersen, E. F.; Goddard, T. D.*et al Journal of Computational Chemistry* **2004**, *25*, 1605.

(44) Kirby, T. W.; Lancaster Jr, J. R.*; et al. Archives of Biochemistry and Biophysics* **1981**, *210*, 140.

(45) Kwaitowski, J; Safianowska, A; *et al. European Journal of Biochemistry* **1985**, *146*, 459.

(46) Yost, F. J.; Fridovich, I. *Journal of Biological Chemistry* **1973**, *248*, 4905.

(47) Gabbianelli, R.; Battistoni, A.*; et al. Biochemical and Biophysical Research Communications* **1995**, *216*, 841.

(48) Gregory, E. M.; Dapper, C. H. *Archives of Biochemistry and Biophysics* **1983**, *220*, 293.

(49) Iranzo, O. *Bioorganic Chemistry* **2011**, *39*, 73.

(50) Barondeau, D. P.; Kassmann, C. J.*; et al. Biochemistry* **2004**, *43*, 8038.

(51) Youn, H.-D.; Kim, E.-J.*; et al. Biochemical Journal* **1996**, *318*, 889.

(52) Miller, A.-F. *Current Opinion in Chemical Biology* **2004**, *8*, 162.

(53) Getzoff, E. D.; Tainer, J. A.*; et al. Nature* **1983**, *306*, 287.

(54) Stroppolo, M.; Falconi, M.*; et al. CMLS, Cellular and Molecular Life Sciences* **2001**, *58*, 1451.

(55) Dukan, S.; Nyström, T. *Journal of Biological Chemistry* **1999**, *274*, 26027.

(56) Elchuri, S.; Oberley, T. D.*; et al. Oncogene* **2005**, *24*, 367.

(57) Van Remmen, H.; Ikeno, Y.*; et al. Physiological Genomics* **2003**, *16*, 29.

(58) Yang, W.; Li, J.*; et al. Genetics* **2007**, *177*, 2063.

(59) Pacher, P.; Beckman, J. S.*; et al. Physiological Reviews* **2007**, *87*, 315.

(60) Batinić-Haberle, I.; Rebouças, J. S.*; et al. Antioxidants & Redox Signaling* **2010**, *13*, 877.

(61) Sanchez, R. J.; Srinivasan, C.*; et al. JBIC Journal of Biological Inorganic Chemistry* **2005**, *10*, 913.

(62) Kedare, S. B.; Singh, R. *Journal of Food Science and Technology* **2011**, *48*, 412.

(63) Yamazaki, T.; Kawai, C.*; et al. Tropical Medicine and Health* **2011**, *39*, 41.

(64) Lenaz, G.; Fato, R.*; et al. Methods in Enzymology* **2004**, *382*, 3.

(65) Riley, D. P. *Chemical Reviews* **1999**, *99*, 2573.

(66) Friedel, F. C.; Lieb, D.*; et al. Journal of Inorganic Biochemistry* **2012**, *109*, 26.

(67) Lieb, D.; Friedel, F. C.*; et al. Inorganic Chemistry* **2013**, *52*, 222.

(68) Liu, G.-F.; Dürr, K.*; et al. Dalton Transactions* **2009**, 6292.

(69) Riley, D. P.; Rivers, W. J.*; et al. Analalytical Biochemistry* **1991**, *196*, 344.

(70) Batinic-Haberle, I.; Tovmasyan, A. In *Oxidative Stress and Antioxidant Protection: The Science of Free Radical Biology and Disease*; Armstrong, D., Stratton, R. D., Eds.; John Wiley & Sons: Hoboken, NJ, 2016, p 415.

(71) Liochev, S. I. *Chemical Research in Toxicology* **2013**, *26*, 1312.

(72) Pasternack, R. F.; Halliwell, B. *Journal of the American Chemical Society* **1979**, *101*, 1026.

(73) Batinic-Haberle, I.; Benov, L.*; et al. Journal of Biological Chemistry* **1998**, *273*, 24521.

(74) Pasternack, R. F.; Gibbs, E. J.*; et al. Biochemistry* **1983**, *22*, 5409.

(75) Batinic-Haberle, I.; Spasojevic, I.*; et al. Amino Acids* **2012**, *42*, 95.

(76) Batinic-Haberle, I.; Spasojevic, I. In *Porphyrin Science by Women: In 3 Volumes*; World Scientific: 2019, p 197.

(77) Rebouças, J. S.; Spasojević, I.*; et al. JBIC, Journal of Biological Inorganic Chemistry* **2008**, *13*, 289.

(78) Spasojević, I.; Batinić-Haberle, I.*; et al. Journal of Biological Chemistry* **2003**, *278*, 6831.

(79) DeFreitas-Silva, G.; Rebouças, J. S.*; et al. Archives of Biochemistry and Biophysics* **2008**, *477*, 105.

(80) Kos, I.; Benov, L.*; et al. Journal of Medicinal Chemistry* **2009**, *52*, 7868.

(81) Kos, I.; Rebouças, J. S.*; et al. Free Radical Biology and Medicine* **2009**, *47*, 72.

(82) Wolak, M.; van Eldik, R. *Chemistry - A European Journal* **2007**, *13*, 4873.

(83) Batinić-Haberle, I.; Liochev, S. I.*; et al. Archives of Biochemistry and Biophysics* **1997**, *343*, 225.

(84) Pasternack, R. F.; Skowronek Jr, W. R. *Journal of Inorganic Biochemistry* **1979**, *11*, 261.

(85) Thamilarasan, M.; Estupinan, R.*; et al. Blood Advances* **2020**, *4*, 2372.

(86) Batinic-Haberle, I.; Tome, M. E. *Redox Biology* **2019**, *25*, 101139.

(87) Batinic-Haberle, I.; Tovmasyan, A.*; et al. Antioxidants & Redox Signaling* **2014**, *20*, 2372.

(88) Batinic-Haberle, I.; Tovmasyan, A.*; et al. Antioxidants & Redox Signaling* **2018**, *29*, 1691.

(89) Batinic-Haberle, I.; Tovmasyan, A.*; et al. Redox Biology* **2015**, *5*, 43.

(90) Eckshtain, M.; Zilbermann, I.*; et al. Dalton Transactions* **2009**, 7879.

(91) Spasojević, I.; Batinić-Haberle, I.*; et al. Inorganic Chemistry* **2001**, *40*, 726.

(92) Mahammed, A.; Tumanskii, B.*; et al. Journal of Porphyrins and Phthalocyanines* **2011**, *15*, 1275.

(93) Gershman, Z.; Goldberg, I.*; et al. Angewandte Chemie* **2007**, *119*, 4398.

(94) Mahammed, A.; Gross, Z. *Angewandte Chemie* **2006**, *118*, 6694.

(95) Sharpe, M. A.; Ollosson, R.*; et al. Biochemical Journal* **2002**, *366*, 97.

(96) Archibald, F. S.; Fridovich, I. *Archives of Biochemistry and Biophysics* **1982**, *214*, 452.

(97) Cuzzocrea, S.; Riley, D. P.*; et al. Pharmacological Reviews* **2001**, *53*, 135.

(98) Aston, K.; Rath, N.*; et al. Inorganic Chemistry* **2001**, *40*, 1779.

(99) Maroz, A.; Kelso, G. F.*; et al. The Journal of Physical Chemistry A* **2008**, *112*, 4929.

(100) Riley, D. P.; Lennon, P. J.*; et al. Journal of the American Chemical Society* **1997**, *119*, 6522.

(101) Riley, D. P.; Henke, S. L.*; et al. Inorganic Chemistry* **1999**, *38*, 1908.

(102) Riley, D. P.; Weiss, R. H. *Journal of the American Chemical Society* **1994**, *116*, 387.

(103) Filipović, M. R.; Duerr, K.*; et al. Angewandte Chemie International Edition* **2008**, *47*, 8735.

(104) Zhang, D.; Busch, D. H.*; et al. Inorganic Chemistry* **1998**, *37*, 956.

(105) Durot, S.; Policar, C.*; et al.*; Wiley Online Library: 2005.

(106) Bernard, A.-S.; Giroud, C.*; et al. Dalton Transactions* **2012**, *41*, 6399.

(107) Ching, H. V.; Anxolabéhere-Mallart, E.*; et al. Chemical Science* **2014**, *5*, 2304.

(108) Ali, S. S.; Hardt, J. I.*; et al. Free Radical Biology and Medicine* **2004**, *37*, 1191.

(109) Kaizer, J.; Baráth, G.*; et al. Inorganic Chemistry Communications* **2007**, *10*, 292.

(110) Kálmán, F. K.; Tircsó, G. *Inorganic Chemistry* **2012**, *51*, 10065.

(111) Yu, M.; Ambrose, S. L.*; et al. Journal of the American Chemical Society* **2014**, *136*, 12836.

(112) Yu, M.; Ward, M. B.*; et al. Inorganic Chemistry* **2017**, *56*, 2812.

(113) Cisnetti, F.; Pelosi, G.*; et al. Inorganica Chimica Acta* **2007**, *360*, 557.

(114) Signorella, S.; Palopoli, C.*; et al. Coordination Chemistry Reviews* **2018**, *365*, 75.

(115) Durot, S.; Lambert, F.*; et al.*; Wiley Online Library: 2005.

(116) Ching, H. Y. V.; Kenkel, I.*; et al. Journal of Inorganic Biochemistry* **2016**, *160*, 172.

(117) Yu, M.; Beyers, R. J.*; et al. Inorganic Chemistry* **2012**, *51*, 9153.

(118) Kenkel, I.; Franke, A.*; et al. Journal of the American Chemical Society* **2017**, *139*, 1472.

(119) Linder, M. C. *Biochemistry of Copper*; Springer Science & Business Media, 2013; Vol. 10.

(120) Korschelt, K.; Ragg, R.*; et al. Nanoscale* **2017**, *9*, 3952.

(121) Batinic-Haberle, I; Liochev, S. I.; *et al. Archives of Biochemistry and Biophysics* **1997**, *343*, 225.

(122) Mahammed, A.; Gray, H. B.*; et al. Bioconjugate Chemistry* **2004**, *15*, 738.

(123) Beveridge, S.; Walker, W.*; et al. Journal of Pharmacy and Pharmacology* **1980**, *32*, 425.

(124) Patel, M. N.; Parmar, P. A.*; et al. Bioorganic & Medicinal Chemistry* **2010**, *18*, 1227.

(125) Sorenson, J. R. *Journal of Medicinal Chemistry* **1976**, *19*, 135.

(126) Weser, U.; Sellinger, K.-H.*; et al. Biochimica et Biophysica Acta (BBA)-General Subjects* **1980**, *631*, 232.

(127) Csire, G.; Timári, S.*; et al. Journal of Inorganic Biochemistry* **2017**, *177*, 198.

(128) Weder, J. E.; Dillon, C. T.*; et al. Coordination Chemistry Reviews* **2002**, *232*, 95.

(129) Czapski, G.; Goldstein, S. *Free Radical Research Communications* **1988**, *4*, 225.

(130) Gale, E. M.; Cowart, D. M.*; et al. Inorganic Chemistry* **2011**, *50*, 10460.

(131) Broering, E. P.; Dillon, S.*; et al. Inorganic Chemistry* **2015**, *54*, 3815.

(132) Mullins, C. S.; Grapperhaus, C. A.*; et al. Inorganic Chemistry* **2009**, *48*, 9974.

(133) Gale, E. M.; Narendrapurapu, B. S.*; et al. Inorganic Chemistry* **2010**, *49*, 7080.

(134) Shearer, J.; Peck, K. L.*; et al. Journal of the American Chemical Society* **2014**, *136*, 16009.

(135) Shearer, J.; Zhao, N. *Inorganic Chemistry* **2006**, *45*, 9637.

(136) Jenkins, R. M.; Singleton, M. L.*; et al. Inorganic Chemistry* **2009**, *48*, 7280.

(137) Lee, W. Z.; Chiang, C. W.*; et al. Chemistry–A European Journal* **2012**, *18*, 50.

(138) Nakane, D.; Kuwasako, S.-i.*; et al. Chemical Communications* **2010**, *46*, 2142.

(139) Mathrubootham, V.; Thomas, J.*; et al. Inorganic Chemistry* **2010**, *49*, 5393.

(140) Shearer, J. *Angewandte Chemie International Edition* **2013**, *52*, 2569.

(141) Tietze, D.; Voigt, S.*; et al. Angewandte Chemie International Edition* **2011**, *50*, 2946.

(142) Shearer, J. *Accounts of Chemical Research* **2014**, *47*, 2332.

(143) Robertson, D. E.; Farid, R. S.*; et al. Nature* **1994**, *368*, 425.

(144) Shearer, J.; Long, L. M. *Inorganic Chemistry* **2006**, *45*, 2358.

(145) Shearer, J.; Neupane, K. P.*; et al. Inorganic Chemistry* **2009**, *48*, 10560.

(146) Neupane, K. P.; Gearty, K.*; et al. Journal of the American Chemical Society* **2007**, *129*, 14605.

(147) Krause, M. E.; Glass, A. M.*; et al. Inorganic Chemistry* **2010**, *49*, 362.

(148) Tietze, D.; Breitzke, H.*; et al. Chemistry–A European Journal* **2009**, *15*, 517.

(149) Krause, M. E.; Glass, A. M.*; et al. Inorganic Chemistry* **2011**, *50*, 2479.

(150) Lihi, N. F., István *Insight Into the Thremodynamic and Catalytic Features of NiSOD Related Metallopeptides*; Elsevier, 2022; Vol. 79.

(151) Peretz, P.; Solomon, D.*; et al. International Journal of Radiation Biology and Related Studies in Physics, Chemistry and Medicine* **1982**, *42*, 449.

(152) Ramadan, A. E.-M. M. *Journal of Molecular Structure* **2012**, *1015*, 56.

(153) Whitburn, K. D.; Laurence, G. S. *Journal of the Chemical Society, Dalton Transactions* **1979**, 139.

(154) Gale, E. M.; Patra, A. K.*; et al. Inorganic Chemistry* **2009**, *48*, 5620.

(155) Hart, P. C.; Mao, M.*; et al. Nature Communications* **2015**, *6*, 1.

(156) Negri, L.; Benaglia, R.*; et al. Archivio Italiano di Urologia e Andrologia* **2017**, *89*, 212.

(157) Pan, X.; Qin, P.*; et al. RSC Advances* **2016**, *6*, 91141.

(158) Sibenaller, Z. A.; Welsh, J. L.*; et al. Free Radical Biology and Medicine* **2014**, *69*, 357.

(159) Jadot, G.; Vaille, A.*; et al. Clinical Pharmacokinetics* **1995**, *28*, 17.

(160) De Benito, V.; de Barrio, M.*; et al. Allergologia et Immunopathologia* **2001**, *29*, 272.

(161) Lemaire, B.; Le Quere, S.*; et al. Phytothérapie* **2016**, *v. 14*, pp. 23.

(162) Manolov, V.; Yonova, D.*; et al. J. Urology Nephrology* **2017**, *2*, 000116.

(163) Romao, S. *Nutrition* **2015**, *31*, 430.

(164) Goldstein, S.; Samuni, A.*; et al. The Journal of Physical Chemistry A* **2006**, *110*, 3679.

(165) Wei, H.; Wang, E. *Chemical Society Reviews* **2013**, *42*, 6060.

(166) James, A. M.; Cochemé, H. M.*; et al. Journal of Biological Chemistry* **2005**, *280*, 21295.

(167) Ross, M. F.; Prime, T. A.*; et al. Biochemical Journal* **2008**, *411*, 633.

(168) Maroz, A.; Anderson, R. F.*; et al. Free Radical Biology and Medicine* **2009**, *46*, 105.

(169) Batinic-Haberle, I. *Anti-Cancer Agents in Medicinal Chemistry (Formerly Current Medicinal Chemistry-Anti-Cancer Agents)* **2011**, *11*, 327.

(170) Cheng, G.; Lopez, M.*; et al. Cancer Biology & Therapy* **2011**, *12*, 707.

(171) Dessolin, J.; Schuler, M.*; et al. European Journal of Pharmacology* **2002**, *447*, 155.

(172) Trnka, J.; Blaikie, F. H.*; et al. Free Radical Research* **2009**, *43*, 4.

(173) Goldstein, S.; Merenyi, G.*; et al. Journal of the American Chemical Society* **2003**, *125*, 789.

(174) Ward, M. B.; Scheitler, A.*; et al. Nature Chemistry* **2018**, *10*, 1207.

Chapter 2

Quinol-containing Ligands Enable High Superoxide Dismutase Activity by Modulating Coordination Number, Charge, Oxidation States and Stability of Manganese Complexes Throughout Redox Cycling*

*This chapter is a revision of a published paper: Senft, Laura, Jamonica L. Moore, Alicja Franke, Katherine R. Fisher, Andreas Scheitler, Achim Zahl, Ralph Puchta, Dominik Fehn, Sidney Ison, Safaa Sader, Ivana Ivanović-Burmazović, Christian R. Goldsmith. *Chemical Science* **2021**, *12*, 10483-10500.

2.1 Introduction

High concentrations of reactive oxygen species (ROS), such as hydrogen peroxide (H_2O_2) and superoxide ($O_2^{-\cdot}$), are known to oxidatively degrade biomolecules, and their over-accumulation is believed to be involved in the pathology of several severe health conditions, including COVID-19.[1-9] The potential negative impacts of ROS overproduction on human health have motivated extensive efforts to develop methods to detect and detoxify ROS in biological environments.[10-13] One attractive antioxidant design strategy is to synthesize small molecules that resemble the enzymes that the body itself uses to regulate ROS concentrations. A small dose of such an antioxidant would alleviate oxidative stress by catalytically degrading ROS. Investigated antioxidants include functional mimics of superoxide dismutases (SODs), which are manganese-, iron-, nickel-, or copper-zinc-containing enzymes that catalyze the degradation of $O_2^{-\cdot}$ to O_2 and H_2O_2.[14-21] The enzymatic catalysis relies upon the metal center cycling between two oxidation states; there are no known SODs that instead use an organic redox partner for the disproportionation of $O_2^{-\cdot}$.

Previously, our labs developed and characterized three water- and air-stable Mn(II) complexes with redox-active organic ligands (Scheme 2.1) that respond to H_2O_2 with changes in their T_1-weighted relaxivity (r_1).[22-24] Consequently, the Mn(II) complexes can serve as redox-responsive contrast agents for magnetic resonance imaging (MRI). Notably, the MRI responses result from the oxidation of the organic component, rather than the metal, distinguishing these from redox-responsive probes developed by the Caravan group.[25-29] The first sensor, $[Mn(Hptp1)(MeCN)]^{2+}$ (**1**), reacts with H_2O_2 to form a binuclear Mn(II) species; the reaction with H_2O_2 oxidative couples the *para*-methyl phenol groups from two equiv. of the pre-activated contrast agent.[22] The other two compounds, $[Mn(H_2qp1)(MeCN)]^{2+}$ (**2**) and $[Mn(H_4qp2)Br_2]$ (**3**),

feature quinol subunits which are oxidized to *para*-quinone groups upon their reactions with H_2O_2 (Scheme 2.2).[23,24] In the reduced form of the ligands, the quinols can deprotonate and bind tightly to Mn(II) ions as quinolates; in the oxidized form, conversely, the neutral *para*-quinones have much weaker metal binding affinities and appear to be displaced by water molecules.[24] The better aquation of the Mn(II) ion is proposed to increase r_1 and thereby enhance MRI contrast.

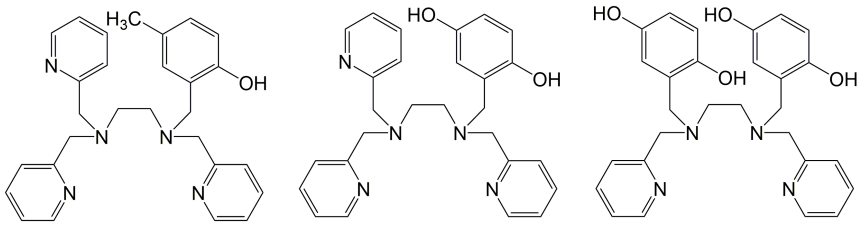

Scheme 2.1 Redox-active ligands for complex **1**, **2**, **3** and **4**.

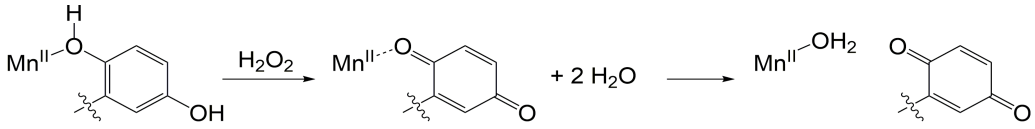

Scheme 2.2 Mechanistic MRI response to H_2O_2.

Curiously, prolonged exposure of **2** and **3** to a large excess of H_2O_2 converts only 70% of the quinols to *para*-quinones.[23,24] The existence of a possible equilibrium mixture of the reduced and oxidized forms of the ligands in the presence of excess ROS led us to speculate that the ligands were cycling between these different oxidation states; this could potentially allow **2** and **3** to catalyze ROS degradation with or without a classical metal-centered redox pathway. We initially screened the antioxidant activity of the three manganese complexes using the xanthine oxidase/hypoxanthine/lucigenin assay.[30,31] Our results suggested that **1**, **2**, and **3** all behave as SOD mimics.[23,24] The SOD activity of **1** was then confirmed using more quantitatively accurate stopped-flow kinetics measurements.[32] Comprehensive study of **1** revealed that in contrast to the majority

of non-porphyrin-based manganese-containing SOD mimics, its SOD activity mainly proceeds through an outer-sphere pathway, with additional superoxide and oxygen reductase activity operating through an inner-sphere mechanism involving a Mn(IV)-oxo intermediate and the generation of $OH^{\cdot}$ radicals.[32] As was observed with H_2O_2, these reactive species oxidatively couple the phenol groups of separate molecules to dimerize **1**. The dimerization reaction has little impact on the SOD activity and essentially protects the catalyst from inadvertently generated ROS. Much like most other non-porphyrin-based Mn SOD mimics,[14-16,33-37] **1** is more active under more acidic and phosphate-free conditions.

More recently, we found that a Zn(II) complex with the H_2qp1 ligand, [Zn(H_2qp1)(OTf)](OTf) (**4**), efficiently catalyzes the degradation of $O_2^{-\cdot}$.[38] These results demonstrate that the quinol in the H_2qp1 ligand is, by itself, a viable redox partner for superoxide dismutation. The free H_2qp1 ligand, however, cannot act as a SOD mimic, demonstrating that a metal ion is essential for the observed catalysis.

Complexes **2** and **3** contain manganese centers in addition to quinol moieties, and catalytic superoxide degradation could involve either one or both as redox partners. It is also possible that the two redox-active components may act synergistically to improve either the rate of the reactions with $O_2^{-\cdot}$ or the stability of the catalyst; the latter effect was observed with **1**, which channels other ROS towards the functionally innocuous dimerization reaction.[32] In order to determine the roles that the metal and ligand have in catalysis, we have investigated the (de)protonation equilibria, water exchange processes, and solution stability of **2** and have used stopped-flow kinetics techniques to confirm and quantitatively assess the abilities of **2** and **3** to act as SOD mimics. We have also identified several catalytically relevant intermediates by cryo-ionization mass spectrometry (CSI-MS). We observe that the ligand influences the catalysis through A) its ability

to access multiple oxidation states, B) its charge, and C) its ability to control the accessibility and rate of ligand exchange at the metal center through steric and conformational effects. Despite the high structural similarity of **1** to **2**, we find that **2** and **3** both react with $O_2^{\cdot-}$ through more efficient inner-sphere mechanisms, rather than the predominantly outer-sphere pathway observed for **1**.[32] Our results have allowed us to identify some of the key factors that modulate SOD catalysis by manganese complexes with this class of redox-active ligand.

2.2 Experimental Section

Materials

All chemicals and solvents were purchased from Sigma-Aldrich and used as received unless otherwise noted. All deuterated solvents were bought from Cambridge Isotopes. Diethyl ether (ether) and methanol (MeOH) were bought from Fisher. Methylene chloride (CH_2Cl_2) was purchased from Mallinckrodt Baker. *N*-(2,5-Dihydroxybenzyl)-*N,N',N'*-tris(2-pyridinylmethyl)-1,2-ethanediamine (H_2qp1), *N,N'*-bis(2,5-dihydroxybenzyl)-*N,N'*-bis(2-pyridinylmethyl)-1,2-ethanediamine (H_4qp2), [Mn(H_2qp1)(MeCN)](OTf)$_2$ (**2**), and [Mn(H_4qp2)Br$_2$] (**3**) were prepared through previously described procedures.[23, 24]

Instrumentation

All ^{1}H and ^{13}C NMR spectra were recorded on a 400 MHz or 600 MHz AV Bruker NMR spectrometer at 293 K. In each spectrum, the reported NMR resonance peak frequencies were referenced to internal standards. ^{17}O NMR data were collected on a Bruker AVANCE DRX 400WB spectrometer with a superconducting wide-bore magnet operating at a 54.24 MHz resonance frequency and a 9.4 T magnetic induction. A Varian Cary 50 spectrophotometer was used to collect optical data, which were then processed using software from the WinUV Analysis Suite.

Potentiometric Titrations

The speciation chemistry of **2** in water was assessed using a METROHM 765 Dosimat with a jacketed, airtight glass titration vessel. A Fisher Scientific Accumet Research AR15 pH meter was used to determine the pH of the sample solutions during the titrations. The electrode was calibrated before each titration using commercially available standard solutions buffered to pH 4.0, 7.0, and 10.0. All samples were purged with argon prior to analysis and subsequently analyzed under an argon atmosphere at 25 °C. All solution samples were prepared in solutions of 100 mM KCl in deionized Millipore water. The titrations investigating metal-ligand speciation were run with solutions that contained a 1:1 molar mixture of the ligand and $MnCl_2 \cdot (4H_2O)$. Carbonate-free solutions of 0.10 M KOH and 0.10 M HCl were prepared using argon-saturated deionized Millipore water. These data were analyzed and fit to speciation models using the Hyperquad2006 program.[39]

^{17}O NMR Measurements of Aquation Numbers (q) and Water Exchange Processes

^{17}O NMR spectra were recorded on a Bruker AVANCE DRX 400WB spectrometer equipped with a spectrospin superconducting widebore magnet operating at a resonance frequency of 54.24 MHz at a magnetic induction of 9.4 T. The measurements at atmospheric pressure were performed with a commercial 5 mm Bruker broad band probe thermostated with a Bruker B-VT 3000 variable temperature unit. Relaxation rates were measured for both the paramagnetic solutions and metal-free aqueous buffer solutions. The line widths at half the maximum height of the signal were determined by a deconvolution procedure on the real part of the Fourier transformed spectra with a Lorentzian shape function in the data analysis module of Bruker Topspin 1.3 software. Pressure-dependent measurements were done with a custom-made

thermostated high-pressure probe. The sample was measured in a standard 5 mm NMR tube cut to a length of 50 mm. To enable pressure transmittance to the solution, the NMR tube was closed with a moveable Macor piston. The advantage of this method is that oxygen-sensitive samples can be easily placed in the NMR tube and sealed with the Macor piston under an argon atmosphere. The pressure was applied to the high-pressure probe via a perfluorinated hydrocarbon (hexafluoropropylene oxide, Hostinert 175, Hoechst) and measured by a VDO gauge with an accuracy of ±1%. The temperature was adjusted with circulating, thermostated water (Colora thermostat WK 16) to ±0.1 K of the desired value and monitored before each measurement with an internal Pt-resistance thermometer with an accuracy of ±0.2 K. Enriched (10%) ^{17}O-labeled water (D-Chem Ltd. Tel Aviv, Israel) was used for the ^{17}O NMR water exchange experiments. Samples were prepared by dissolving solid Mn(II) complexes in MeCN and refilling the sample with degassed buffer solution (60 mM acetate buffered to pH 4.0 or 60 mM HEPES buffered to pH 7.4 or 7.0) to get a 4–5 mM solution of the complex containing 10% MeCN. 10%-Enriched ^{17}O-labeled water was added to the solution (1 : 10 v/v) which was then transferred to a NMR tube. The temperature-dependence of the ^{17}O-line broadening was studied from 274.2 to either 343.2 or 348.2 K. A detailed description of the experiments and general data treatment can be found in Appendix A.

Aquation numbers (q) were calculated from the maximum ^{17}O transverse relaxivity, $r^{\circ}_{2\,max}$, and the equation: $q = r^{\circ}_{2\,max}/510$; Gale, Zhu, and Caravan previously used this relationship to estimate the inner-sphere hydration state of Mn(II) in coordination complexes.[40] Relaxation rates were measured both for aqueous solutions containing **2** and for metal-free solutions buffered to pH 4.0 and 7.4.

Cryospray-Ionization Mass Spectrometry

Cryospray-ionization mass spectrometry (CSI-MS) measurements were performed on a UHR-TOF Bruker Daltonik maXis plus, an ESI-quadrupole time-of-flight (qToF) mass spectrometer capable of a resolution of at least 60.000 (FWHM), which was coupled to a Bruker Daltonik Cryospray unit. Detection was in positive ion mode, with a source voltage of 3.5 kV and a flow rate of 240 μL per hour. The temperatures of the spray gas (N_2) and the dry gas used for solvent removal were maintained at –40 °C and –35 °C, respectively. The mass spectrometer was calibrated prior to every experiment *via* direct infusion of an Agilent ESI-TOF low concentration tuning mixture, which provided a *m/z* range of singly charged peaks up to 2700 Da in both ion modes. For the reactions with $O_2^{\cdot-}$, 1 mM solutions of either **2** or **3** in MeCN (1 % DMF) were cooled to –40 °C and mixed with excess solid KO_2. The mixture was diluted to roughly 1×10^{-5} M and quickly injected into the mass spectrometer. Applied solvents were not extra dry in order to provide a source of protons. The measured data were processed and analyzed with Bruker Data Analysis. The complete CSI-MS spectra recorded for the reactions of **2** and **3** with excess superoxide are shown in Figure A1 and A2, respectively, in Appendix A.

Determination of the SOD Activity

We previously assessed the abilities of **2** and **3** to catalytically degrade superoxide using the xanthine oxidase/hypoxanthine/lucigenin assay.[23,24,31] Each assay was carried out in a total volume of 1 mL containing 50 mM tris (pH 8.0), 50 μM hypoxanthine, 0.005 U mL^{-1} xanthine oxidase (Calbiochem), and 5 μM dark adapted lucigenin in the presence of either 0.1 nM or 10 μM of the Mn(II) complex or its vehicle.

The ability of the Mn(II) complexes to catalytically degrade superoxide was tested by a direct method using stopped-flow techniques as described elsewhere.[34] Experiments were carried

out using syringes 1, 2, and 3 on a Biologic SFM-400 instrument that was equipped with an Energetiq LDLS ENQ EQ-99-FC laser driven light source and a J&M TIDAS diode array detector (integration time = 0.5 ms, λ = 180 – 724 nm). The source of superoxide was commercially available KO_2 dissolved in dry and non-buffered DMSO ($[O_2^{\cdot-}] \approx 1 – 2$ mM). Complexes **2** and **3** were each tested at four different concentrations between 0.9 and 9 μM in aqueous solutions buffered with HEPES or sodium phosphate to either pH 7.4 or pH 8.1. The ionic strength of all solutions was 111 mM. The aqueous solution containing the studied Mn(II) complex was mixed in a 9:1 ratio with the superoxide solution in DMSO using a high-density mixer. In each experiment, the concentration of superoxide exceeded that of the metal-containing catalyst by at least ten-fold to ensure catalytic conditions. Millipore water was used for the preparation of the buffer solutions. All of the prepared buffers were treated with Chelex 100 sodium exchange resin for at least 12 h before use in order to remove adventitious metal ions. The data analysis was performed using the BioKine V4.66 software. Each reported k_{obs} value is the average of at least 10 measurements. The reported k_{cat} values were determined from the slope of the k_{obs} vs. [SODm] plot. The presence of H_2O_2 was qualitatively confirmed using Baker Testrips for Peroxides.

Cryo UV/vis Spectroscopy Measurements

Cryo UV/vis experiments were performed with the use of low temperature stopped-flow technique involving a biologic cryo SFM-4000 four-syringe stopped-flow combined with a 150 W xenon lamp and a J&M TIDAS diode array detector (200−724 nm) with an integration time of 0.5 ms. A Huber C-905 cryostat filled with silicon oil was used to cool the samples. Specfit, Global Analysis System (Version 3.0.38 for 32-bit Windows system) was used to analyze the spectral changes and perform a global analysis of kinetic traces at various wavelengths.

EPR Spectroscopy Measurements

EPR spectra were recorded on a JEOL continuous wave spectrometer JES-FA200, equipped with an X-band Gunn diode oscillator bridge, a cylindric mode cavity, and a helium cryostat. The samples were measured in the solid state in quartz glass EPR tubes at 95 K and 7 K. The spectra shown were measured using the following parameters: microwave frequency = 8.959 GHz, modulation width 1.0, and 0.5 mT, microwave power 1.0 mW, modulation frequency 100 kHz, and time constant of 0.1 s.

DFT Calculations

All calculations were done by applying the B3LYP functional[41-43] in combination with the def2svp basis set.[44-46] The characterization as minima or transition states was done by computation of vibrational frequencies at the same level. All wavefunctions were tested successfully for stability.[47-49] Relative energies were corrected for zero-point vibrational energies (ZPE). All calculations were performed using the Gaussian 16 program package.[50]

2.3 Results and Discussion

Before one can identify the factors that govern the ability of manganese complexes with polydentate ligands (Scheme 2.1) to catalytically decompose superoxide, one needs to understand how they behave in water. We have therefore characterized the pH-dependent speciation, stability, and water exchange kinetics of $[Mn(H_2qp1)(MeCN)](OTf)_2$ (**2**) in aqueous solutions using potentiometric and spectrophotometric pH titrations and vari-able temperature and pressure ^{17}O NMR spectroscopy. We previously reported analogous studies for $[Mn(Hptp1)(MeCN)]^{2+}$ (**1**) and $[Mn(H_4qp2)Br_2]$ (**3**).[24,32] The new data enable us to fully compare the aqueous chemistries of **1**, **2**, and **3**. Further, we determined catalytic rate constants for superoxide dismutation by **2** and **3** using the same techniques that were used for **1**, again enabling the three to be compared.[32] Mechanistic

insights were gained by characterizing reactive intermediates using low-temperature UV/vis and EPR spectroscopies and CSI-MS.

Protonation Equilibria and Solution Stability

Potentiometric and spectrophotometric pH titration data were collected to assess the stability and ligand protonation states of **2** in water. Previously, we found that the H_2qp1 ligand itself undergoes two ionization events consistent with pK_L values of 7.24 and 4.72 which were assigned to the (de)protonation of one of the tertiary amines (H_3qp1$^+$) and one of the pyridine rings (H_4qp1^{2+}), respectively.[38] We observed precipitation upon raising the pH above 10; consequently, we were unable to measure pK_a values for the quinolic O-H groups of H_2qp1, which likely fully deprotonate at pH values higher than 10. Similar ligand instability above pH 9 was observed for H_4qp2.[24]

By comparison, complex 2 displays ionization events with pK_a values of 6.3 and 3.1 (Figure A3, Figure A4, Table 2.1). The pK_a value of 6.3 for the Mn(II) complex is consistent with the (de)protonation of a M(II)-bound phenolate.[26,51] The assignment of the 6.3 pK_a value to the (de)protonation of a metal-bound quinol is supported by spectrophotometric pH titration data. At pH 6.0 and above, there is a strong peak at 305 nm; the energy of this band is consistent with an intraligand electronic transition for a phenolate, rather than a phenol (Figure A5).[24,26] As the pH drops below 6, this band disappears and is replaced by a prominent shoulder at 295 nm, an energy which is more consistent with the conjugate acid phenol. At physiologically relevant pH 7.4, 93% of the complex has a [Mn(Hqp1)]$^+$ core, with the other 7% existing as the dicationic [Mn(H_2qp1)]$^{2+}$ (Figure 2.1). Additional aquation number (q) measurements were performed to fully describe the water speciation (*vide infra*).

Table 2.1 p*K* and pMn values related to the protonation and stability constants of Hptp1, H_2qp1, and H_4qp2 and their respective Mn(II) complexes **1**, **2**, and **3** as determined by potentiometric titration at 25 °C.

Hptp1		**1**	
pK_{L1}[a]	4.11	$pK_a(Mn(H_2ptp1)^{3+})$[b]	3.93
pK_{L2}[a]	10.01	$pK_a(Mn(Hptp1)^{2+})$[b]	6.16
		pMn (pH 7.4)[c]	5.40
H_2qp1		**2**	
pK_{L1}[a]	4.72 (±0.08)	$pK_a(Mn(H_3qp1)^{3+})$[b]	3.1
pK_{L2}[a]	7.24 (±0.03)	$pK_a(Mn(H_2qp1)^{2+})$[b]	6.3
		pMn (pH 7.4)[c]	7.25
H_4qp2		**3**	
pK_{L1}[a]	4.47 (±0.08)	$pK_a(Mn(H_5qp2)^{3+})$[b]	5.53
pK_{L2}[a]	7.18 (±0.03)	$pK_a(Mn(H_4qp1)^{2+})$[b]	5.82
		$pK_a(Mn(H_3qp1)^{+})$[b]	7.14
		pMn (pH 7.4)[c]	5.36

[a]Ligand pK_a values correspond to the following equilibrium constants:

Hptp1 $K_{L1} = [Hptp1][H^+]/[H_2ptp1^+]$[32]
$K_{L2} = [ptp1^-][H^+]/[Hptp1]$[32]

H_2qp1 $K_{L1} = [H_3qp1^+][H^+]/[H_4qp1^{2+}]$[38]
$K_{L2} = [H_2qp1][H^+]/[H_3qp1^+]$[38]

H_4qp2 $K_{L1} = [(H_5qp2)^+][H^+]/[(H_6qp2)^{2+}]$[24]
$K_{L2} = [(H_4qp2)][H^+]/[(H_5qp2)^+]$[24]

[b]Metal complex pK_a values correspond to the following equilibrium constants:

1 $K_a(Mn(H_2ptp1)^{3+}) = [Mn(Hptp1)^{2+}][H^+]/[Mn(H_2ptp1)^{3+}]$[32]
$K_a(Mn(Hptp1)^{2+}) = [Mn(ptp1)^+][H^+]/[Mn(Hptp1)^{2+}]$[32]

2 $K_a(Mn(H_3qp1)^{3+}) = [Mn(H_2qp1)^{2+}][H^+]/[Mn(H_3qp1)^{3+}]$
$K_a(Mn(H_2qp1)^{2+}) = [Mn(Hqp1)^+][H^+]/[Mn(H_2qp1)^{2+}]$

3 $K_a(Mn(H_5qp2)^{3+}) = [Mn(H_4qp2)^{2+}][H^+]/[Mn(H_5qp2)^{3+}]$[24]
$K_a(Mn(H_4qp2)^{2+}) = [Mn(H_3qp2)^+][H^+]/[Mn(H_4qp2)^{2+}]$[24]
$K_a(Mn(H_3qp2)^{+}) = [Mn(H_2qp2)][H^+]/[Mn(H_3qp2)^+]$[24]

[c]pMn = -log$[Mn(II)]_{free}$ calculated for [Mn(II)] = 1.0 mM and [L] = 1.0 mM at 25 °C and pH 7.4.

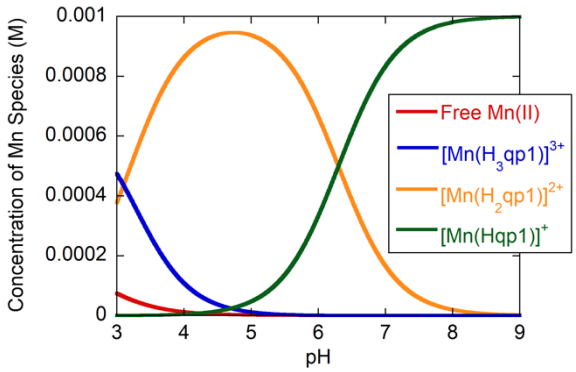

Figure 2.1 Species distribution for solutions of 1:1 H_2qp1/$MnCl_2$·($4H_2O$) in water containing 100 mM KCl as a function of pH at 25 °C and [H_2qp1] and [$MnCl_2$·($4H_2O$)] both equal to 1.0 mM.

Analogous studies for **1**, which features a *para*-methyl phenol group in place of the quinol, revealed that **1** is slightly more acidic, and the metal-bound phenol has a pK_a value of 6.16.[32] Consequently, the conjugate base phenolate should be a slightly weaker base and electron pair donor than the quinolate in **2**. To our initial surprise, **2** is much more stable in water than **1** as evidenced by their respective pMn[52] values of 7.25 and 5.40 (Table 2.1).[32] A *priori*, the hydroxyl group *para* to the coordinating O atom in H_2qp1 would be anticipated to be a better electron donor than the methyl group in Hptp1,[53] possibly explaining why H_2qp1 coordinates more tightly to Mn(II) than Hptp1. We recently found that *N,N′*-bis(2,5-dihydroxybenzyl)ethanediamine-*N,N′*-diacetic acid formed a more stable Mn(II) complex than *N,N′*-bis(2-hydroxybenzyl)ethylenediamine-*N,N′* -diacetic acid, providing another example of a quinol-for-phenol substitution improving complex stability.[54] That quinols/quinolates are indeed better ligands than phenols/phenolates is sup-ported by previously obtained crystallographic data. In the structures of **1** and **2** obtained from MeCN, Hptp1 and H_2qp1 remain protonated and coordinate to the Mn(II) centers in a hexadentate fashion.[22,23] The Mn-OH(quinol) bond (2.319 Å) in $[Mn(H_2qp1)(MeCN)]^{2+}$ is markedly shorter than the Mn-OH(phenol) bond (2.366 Å) in $[Mn(Hptp1)(MeCN)]^{2+}$,[22,23] demonstrating that quinol binds to Mn(II) more tightly than *para*-methyl phenol.

At pH 7.4, the H_2qp1 ligand is also found to coordinate Mn(II) more tightly than H_4qp2. The pMn value of **3** was determined to be 5.36.[24] Although over 99% of both the H_2qp1 and H_4qp2 ligands are bound to the Mn(II) above pH 7.0 (Figure 2.1),[24] H_4qp2 protonates and dissociates from the metal ion to a greater extent than H_2qpl under acidic conditions. Less than 10% of the Mn(II) is ligand-free at pH 3 with 1.0 mM amounts of metal and H_2qpl; conversely, over 80% of the Mn(II) dissociates from H_4qp2 under the same conditions.[24] The pK_a values of the first and the

second Mn(II)-quinol groups in **3** were found to be 5.82 and 7.14, respectively, resulting in 66% of species with a doubly deprotonated [Mn(H_2qp2)] core and 33% of species with a singly deprotonated [Mn(H_3qp2)]$^+$ core at pH 7.4.[24] The crystallographic data that we have obtained thus far with the H_2qpl and H_4qp2 ligands suggest that protonated quinols bind less avidly to metal ions than pyridine rings.[23, 24, 38]Whenever these ligands have not been fully coordinated to the metal centers in the solid-state structures, it is always the quinol groups that are not ligated. The stronger metal-binding affinity of H_2qpl relative to H_4qp2 is therefore likely a consequence of replacing one of the H_4qp2 quinols with a pyridine. The singly deprotonated H_3qp2$^-$ thereby acts more like a pentadentate ligand at physiological pH; Hqp1$^-$, conversely, behaves more fully like a hexadentate ligand.

Aquation and Water Exchange Processes

The aquation number (q) and rate of water exchange at 298 K (k_{ex}^{298}) for **2** were determined from variable temperature ^{17}O NMR data at pH 4.0 and 7.4 using a protocol developed by Gale *et al.* (Figure 2.2).[40]

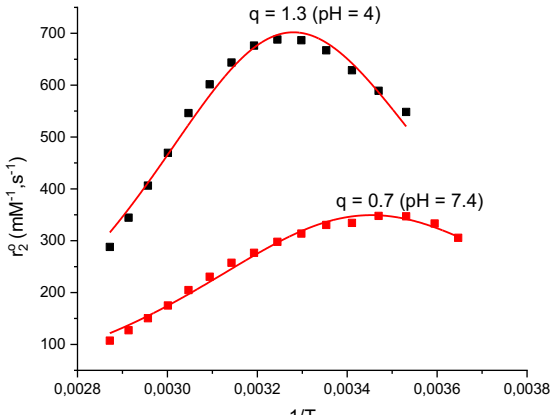

Figure 2.2 Plots of $r_2°$ as a function of temperature for 2 at pH = 4 (black squares) and pH = 7.4 (red squares). Experimental conditions: [2] = 4.0 mM in 60 mM acetate buffer (pH = 4.0) or in 60 mM HEPES buffer (pH = 7.4) with 10% (v/v) of 10% $^{17}OH_2$, B = 9.4 T.

The aquation of **2** is not as extensive as it is for either **1** or **3** (Table 2.2). The simplest interpretation of the 0.7 value of I at pH 7.4 for **2** suggests that approximately 70% of the Mn(II)

binds a single water molecule, with the other 30% without coordinated water molecules. The overall composition of the major component is therefore proposed to be $[Mn(Hqp1)(OH_2)]^+$. The pH 7.4 solutions structures of **1**, **2**, and **3** are depicted on Scheme 2.3. The metal center in this species could be heptacoordinate; this is plausible since the previously obtained crystal structure of $[Mn(H_2qp1)(MeCN)]^{2+}$ contains a seven-coordinate metal center.[23] The minor component, $[Mn(Hqpl)]^+$, most likely features a hexacoordinate metal center. Complexes **1** and **3**, which respectively exist as $[Mn(ptp1)]^+$ or a mixture of $[Mn(H_2qp2)]$ and $[Mn(H_3qp2)]^+$ at pH 7.0-7.4, have higher aquation numbers (Table 2.2).[24,32] That the aquation number for **2** is lower than it is for **1** and **3** under similar conditions may suggest that the monoaqua species for **2** is thermodynamically favored to a lesser degree than the analogous species for the Hptpl and H_4qp2 ligands. Between pH 7.0 and 7.4, H_2qpl appears to be more strongly electron-donating than the other two ligands, as evident from its stronger chelating ability, *vide supra*. The more electron-rich metal center in **2** may thereby have a weaker affinity for the additional aqua ligand.

Table 2.2 Water exchange activation parameters obtained for complexes **1**, **2**, and **3**.

Parameter	**1** (pH 4.8)[a]	**1** (pH 7.4)[a]	**2** (pH 4.0)	**2** (pH 7.4)	**3** (pH 7.0)[b]
q	1	1	1.3 (±0.3)	0.7 (±0.2)	0.9 (±0.2)
k_{ex}^{298} (s^{-1})	1.9×10^7	1.3×10^8	$2.9\ (\pm 0.2) \times 10^7$	$1.1\ (\pm 0.1) \times 10^8$	$4.9\ (\pm 1.4) \times 10^6$
$\Delta H^{\ddagger}$ (kJ mol^{-1})	26.4 (±0.2)	26.6 (±0.5)	13.6 (±0.9)	28.7 (±0.7)	22.0 (±1.7)
$\Delta S^{\ddagger}$ (J K^{-1} mol^{-1})	-17.0 (±0.7)	-0.65 (±1.68)	-56.3 (±3.3)	+5.4 (±2.2)	-41.0 (±2.0)
$\Delta V^{\ddagger}$ (cm^3 mol^{-1})	−10.9 (± 0.4)	+8.1 ± (0.4)	−15.2 (± 0.9)	+10.9 (± 0.6)	nd

[a]From reference 32. [b]From reference 24.

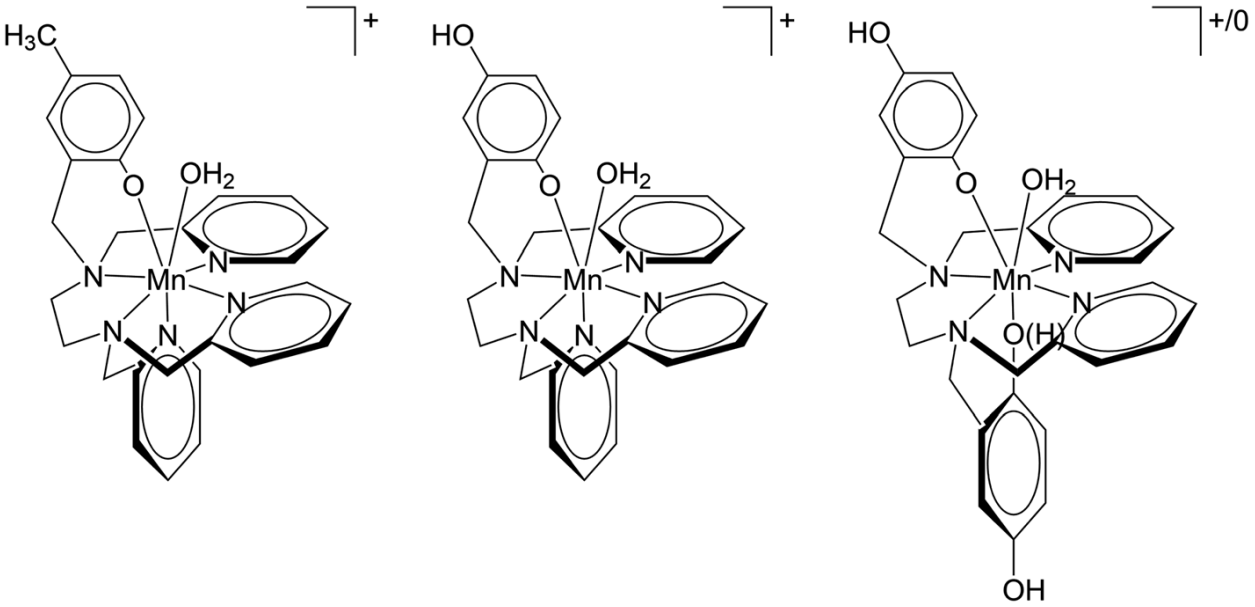

1 **2** **3**

Scheme 2.3 Proposed solution structures of **1**, **2**, and **3** at pH 7.4 based on titration and ^{17}O NMR data. Note that **3** exists as a mixture of $[Mn(H_2qp2)(OH_2)]$ and $[Mn(H_3qp2)(OH_2)]^+$.

That less of the Mn(II) in **2** is heptacoordinate suggests that water exchange proceeds through a dissociative mechanism (D), which is supported by the highly positive activation volume of +10.9 (±0.6) cm^3 mol-1 as well as a positive activation entropy (Figure A6, A7, and Table 2.2). These temperature- and pressure-dependent ^{17}O NMR data confirm that $Hqpl^-$ labilizes the coordinated water molecule. They also explain the co-existence of the seven-coordinate $[Mn(Hqp1)(OH_2)]^+$ and the six-coordinate $[Mn(Hqp1)]^+$ species at pH 7.4, with the latter being the intermediate for the dissociative water exchange mechanism. DFT calculations (B3LYP/def2svp; Figure 2.3) support the operation of a D mechanism and predict that the energy difference between $[Mn(Hqpl)(OH_2)]^+$ and $[Mn(Hqpl)]^+$ is only 2.2 kJ mol^{-1}, with the seven-coordinate structure being slightly more stable. These calculations also predict a low activation barrier for ligand exchange (8.6 kJ mol^{-1}, Figure 2.3), explaining the high experimentally observed lability of $[Mn(Hqp1)(OH_2)]^+$.

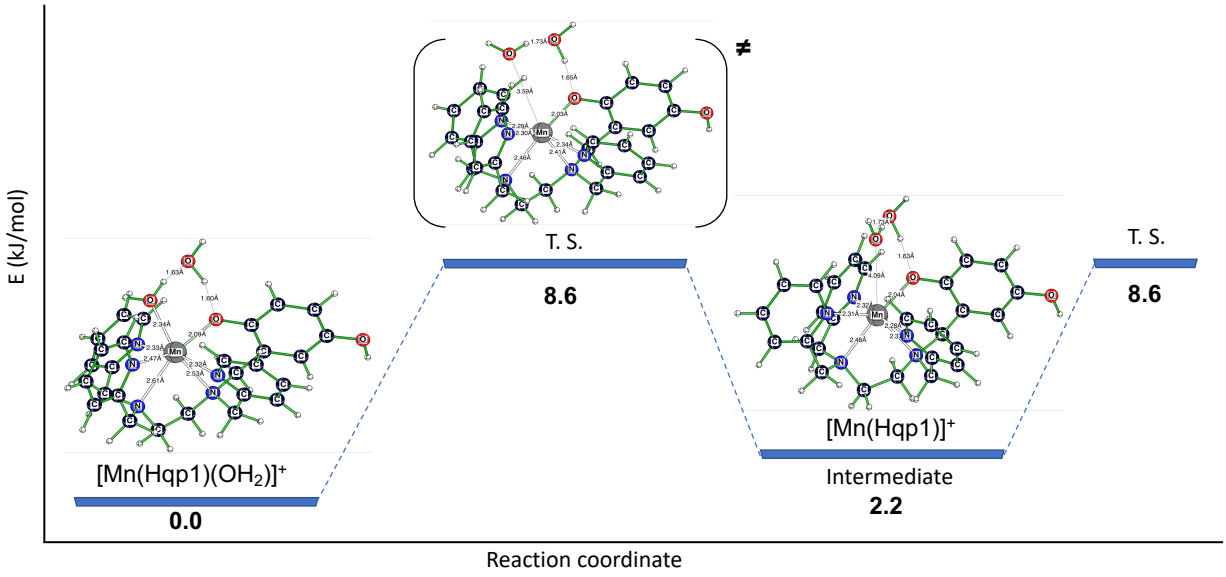

Figure 2.3 Energy profile for water exchange on seven-coordinate $[Mn(Hqp1)(OH_2)]^+$ with six-coordinate $[Mn(Hqp1)]^+$ as an intermediate species (relative energies: B3LYP\def2svp).

At pH 4.0, the number of coordinated water molecules is higher (q = 1.3), suggesting an equilibrium between two Mn(II) species: $[Mn(H_3qp1)(H_2O)_2]^{3+}$ and $[Mn(H_2qp1)(H_2O)]^{2+}$. The corresponding values of $\Delta S^{\ddagger}$ and $\Delta V^{\ddagger}$ become substantially more negative with a concomitant decrease in k_{ex}^{298} (Table 2.2, Figure A8 and A9). The same trends were seen for complex 1 at pH = 4.8.[32] The substantially more negative values for the activation entropy and activation volume at pH 4 than at pH 7.4 indicate an associative mechanism of water exchange, consistent with both $[Mn(H_3qp1)(H_2O)_2]^{3+}$ and $[Mn(H_2qp1)(H_2O)]^{2+}$ being hexacoordinate; the lower coordination numbers would be more amenable to associative pathways for water exchange. Water exchange for **2** is almost four-fold faster at pH 7.4 than at pH 4.

The more positive charges of $[Mn(H_3qp1)(H_2O)_2]^{3+}$ and $[Mn(H_2qp1)(H_2O)]^{2+}$ relative to $[Mn(Hqp1)(H_2O)]^+$ also contribute to the slower rate of water exchange at the lower pH. The faster rate and a dissociative character of the exchange mechanism under more basic conditions suggest

that the coordination of quinolate groups increases the kinetic lability of the Mn(II) center. The higher ligand substitution reactivity of **2** at pH 7.4, may be beneficial for catalytic activity involving an inner-sphere mechanism.

*SOD Activity of Complexes **2** and **3***

The SOD activities of complexes **2** and **3** were initially assessed using an established procedure that uses xanthine oxidase and hypoxanthine to produce $O_2^{-\cdot}$ and a subsequent reaction with lucigenin to detect it.[23,24,30,31]The concentrations at which half of the sensing reaction was blocked (IC_{50}) were found to be 11.3 nM (**2**) and 18.2 nM (**3**). Based on the IC_{50} values and the 7.7×10^5 M^{-1} s^{-1} rate constant reported for the reaction between $O_2^{-\cdot}$ and lucigenin,[55] one would estimate k_{cat} values of 3.4×10^8 M^{-1} s^{-1} (**2**) and 2.1×10^8 M^{-1} s^{-1} (**3**) from these data.

Side reactions between the various components of the assays have been hypothesized to influence the measured IC_{50}, and these assays frequently provide inaccurate accounts of antioxi-dant activity. [17,34,56-59] In order to obtain the best possible assessment of the SOD mimicry of **2** and **3**, we performed an extensive kinetic analysis of the reactions between $O_2^{-\cdot}$ and the complexes in aqueous solutions buffered to pH 7.4 and 8.1 (Table 2.3). We recently reported similar studies for complexes **1** and **4**, the latter being the Zn(II) complex $[Zn(H_2qp1)(OTf)]^+$.[32,38] The H_2qp1 ligand by itself was previously tested and found to be inactive as a catalyst for the decomposition of $O_2^{-\cdot}$ at either pH 7.4 or 8.1.[38] The degradation of superoxide is second-order in $O_2^{-\cdot}$ in the absence of added catalyst, confirming that treatment of the solutions through a Chelex exchange matrix successfully removed all potentially catalytic metal impurities. The decomposition of $O_2^{-\cdot}$ in solutions containing either **2** or **3**, conversely, were found to be first-order with respect to both $O_2^{-\cdot}$ and the manganese catalyst. The k_{cat} values for **2** and **3** are both within the

ranges seen for manganese-containing SOD mimics, with the most efficient of the complexes having k_{cat} values ranging from 10^7 to 10^8 M^{-1} s^{-1}.[15,18,19,30,32,33,35,60-70]

Table 2.3 Catalytic rate constants, k_{cat} (M^{-1} s^{-1}), for the reactions of **1**, **2**, and **3** with superoxide.

Buffer, pH	**1**[a]	**2**	**3**
60 mM HEPES, 8.1	6.2 (±0.5) × 10^5	2.2 (±0.08) × 10^7	9.6 (±0.03) × 10^6
60 mM HEPES, 7.4	3.6 (±0.1) × 10^6	9.7 (±0.04) × 10^7	1.2 (±0.19) × 10^7
50 mM Phosphate, 7.4	1.1 (±0.02) × 10^6	8.0 (±0.03) × 10^6	1.0 (±0.12) × 10^7

[a]Data from reference 32.

Complex **2** is especially effective in HEPES buffer, with a catalytic activity (log k_{cat} = 7.99) that rivals those of cationic porphyrin complexes.[18,19] One particularly effective porphyrin-based SOD mimic is $Mn^{II}Br_8$TM-4-PyP^{4+}, which has both a highly positive charge and a large catalytic rate constant (log k_{cat} = 8.34, determined by the cytochrome *c* assay) that approaches the 8.84-9.30 values measured for SODs.[71-73] However, $Mn^{II}Br_8$TM-4-PyP^{4+}, is unstable at neutral pH and releases free manganese; approximately 30% of the Mn is estimated to be lost.[74] The decomposition of the complex has a substantial impact on the reactivity; if the $Mn^{II}Br_8$TM-4-PyP^{4+}, catalyst were fully intact, its estimated log k_{cat} value would exceed 8.67.[74] The release of neurotoxic Mn(II) ions would severely limit the ability of this and similarly unstable complexes to serve as pharmaceuticals.[71] Complex **2** also compares well to manganese complexes with pentaazamacrocyclic ligands, which comprise the other major class of highly active SOD mimetics. Arguably the best of these mimics is M40401, which has a catalytic rate of approximately 1.5 × 10^9 M^{-1} s^{-1}.[68,69] As with $Mn^{II}Br_8$TM-4-PyP^{4+}, M40401 is markedly less stable in water than **2**, with a pMn = 4.7 versus the 7.25 value measured for **2**.[75] Although complex **2** is about an order of magnitude less active than M40401, its much greater aqueous stability may allow it to engage in longer-lived catalysis.

Much like most other manganese-containing SOD mimics, complex **2** displays lesser activity at pH 8.1 and in phosphate buffer. [14-16,32-37] The inhibition of the SOD activity by phosphate through its competitive binding to the metal center[34] is usually indicative of an inner-sphere

pathway for superoxide decomposition.[14] The activity of complex **3**, conversely, is less sensitive to the composition of the solution; despite this, the data suggest that **3** likewise reacts with superoxide through inner-sphere pathways. The second quinol in **3** does not enhance the catalysis. To the contrary, **2** is a superior catalyst to **3** in two of the investigated aqueous solutions and is approximately equivalent to **3** in phosphate buffer. The second quinol in **3** partly deprotonates to a quinolate, which reduces the overall charge of the complex in water. Complex **2** largely exists as $[Mn(Hqp1)(H_2O)]^+$ with some $[Mn(H_2qp1)]^{2+}$ at pH 7.4, whereas complex **3** is a mixture of 32% $[Mn(H_3qp2)(H_2O)]^+$ and 66% $[Mn(H_2qp2)(H_2O)]$.[24] The lesser average positive charge on the H_4qp2 complexes is anticipated to weaken their abilities to attract and bind anions, both slowing the rate of superoxide complexation and decomposition and attenuating the inhibitory effect of phosphate. The lessened positive charge for **3** also accounts for its slower rate of water exchange which unlike **2**, appears to proceed through an associative mechanism on the basis of its highly negative entropy of activation.[24] These results and the intermediate species characterized within the catalytic cycles (*vide infra*) are consistent with both **2** and **3** degrading $O_2^{\cdot-}$ through inner-sphere pathways.

Despite its strong structural similarity to **2**, complex **1** exhibits much lower SOD activity than either **2** or **3** and catalytically degrades $O_2^{\cdot-}$ through mostly outer-sphere pathways.[32] These differences can be rationalized by considering the Mn(III/II) reduction potentials. Engagement of the coordinated water molecule in proton coupled electron transfer (PCET) lowers the Mn(III/II) reduction potential (466 mV vs. Ag/AgCl)[32] and allows an outer-sphere reduction of $O_2^{\cdot-}$, yielding a Mn(III)-OH species that can then oxidize superoxide to O_2 and regenerate the Mn(II)-OH_2 complex. The calculated structure of the Mn(III) form of **1**, $[Mn^{III}(ptp1)(OH)]^+$, features a strong bond between the OH and the metal center. Although the Mn(III) center in $[Mn^{III}(ptp1)(OH)]^+$ is

predicted to be pentacoordinate with three neutral N-donors and an anionic O-donor from the ptp1$^-$ ligand and a second anionic O-donor from the hydroxide, its distorted square pyramidal structure, the diamine backbone of the ligand, and the negatively charged phenolate and hydroxide groups block access to the only accessible coordination site for potential sixth ligands.[32] Therefore, our calculations suggest that the Mn(III) form of **1** is inaccessible to $O_2^{-\cdot}$ and cannot oxidize it through an inner-sphere mechanism. Conversely, the Mn(III/II) reduction potentials of **2** (645 mV vs. Ag/AgCl)[23] and **3** (725 mV vs. Ag/AgCl)[24] are both too high to support efficient reduction of $O_2^{-\cdot}$ through an outer-sphere catalytic pathway; **2** and **3** are instead proposed to catalyze superoxide degradation through inner-sphere pathways that involve the oxidation and reduction of the quinol/*para*-quinone groups (*vide infra*). Complexes **2** and **3** differ from **1** in that the stabilizations of their Mn(III) forms do not require additional anionic ligands. The Mn(III) state of **3** is stabilized by the deprotonation of the second quinol group, which yields species **b** in Scheme 2.4, The Mn(III) form of **2** can be stabilized via inner-sphere electron transfer from the quinolate to the Mn(III) center, yielding the Mn(II)-quinoxyl radical valence tautomer which can then undergo deprotonation of the unbound OH group to produce species **d** in Scheme 2.4. The additional acid/base and redox transformations available to quinols are important factors that allow **2** and **3** to perform efficient catalytic inner-sphere decomposition of superoxide.

Observation of Reaction Intermediates and Mechanistic Analysis of SOD Mimicry Based on the CSI-MS Results

The reactions between KO_2 and the manganese complexes were probed by cryo-MS, rapid-scan stopped-flow and cryo UV/vis techniques, and EPR spectroscopy. Based on our results, we propose a detailed common mechanism for complexes **2** and **3** (Scheme 2.4).

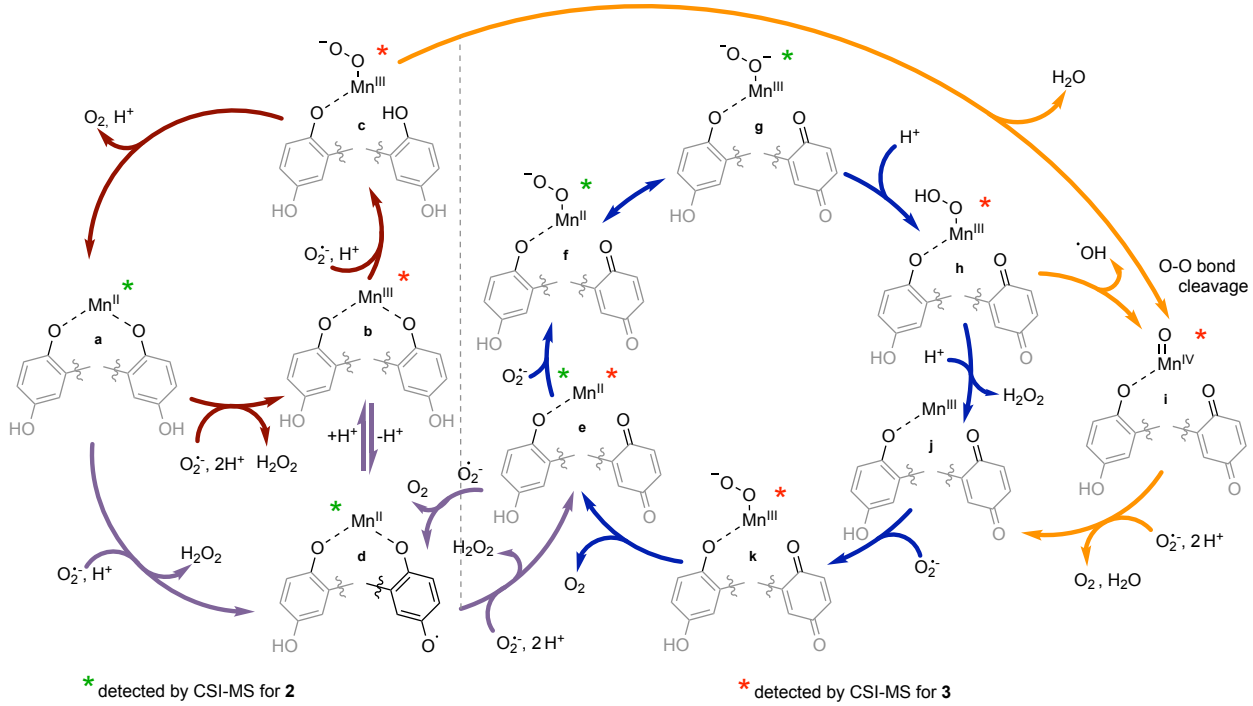

Scheme 2.4 Proposed mechanism of catalytic superoxide removal by **2** and **3**. Depicted are two quinol moieties of H_4qp2 within the structure of **3** (the rest of the pyridylamine ligand is omitted for clarity). In the case of **2**, the leftmost quinol moiety is replaced by a pyridine ring from the ligand. Within the cycle of **3**, the intermediates marked with * could not be observed by CSI-MS due to their neutral charge. Note that species presented as Mn-O-O$^-$ refer to formally coordinated superoxide and those presented as Mn-O$^-$-O$^-$ to formally coordinated peroxide.

We were able to identify most of the reactive and volatile intermediates participating in redox catalysis during the reac-tions between **2** and **3** with excess superoxide (species **a**-**k** in Scheme 2.4) by analyzing these reactions in MeCN at -40 °C with ultra-high resolution cryo-mass spectrometry. The initial reaction between the starting Mn(II) species with the ligand in a fully reduced state (**a**) and $O_2^{\cdot-}$ oxidizes the metal center to Mn(III) (**b**, Figure 2.4), with concomitant reduction of $O_2^{\cdot-}$ to H_2O_2. For compound **3**, the presence of two negative charges from the two quinolates in the coordination sphere stabilizes the +3 oxidation state of the metal. Since an external anion, such as OH^-, is not needed to stabilize the complex, the metal center remains accessible to additional equivalents of $O_2^{\cdot-}$, unlike the Mn(III) form of **1**.[32] Species **b** can therefore coordinate $O_2^{\cdot-}$ (**c**, Figure Al0 in appendix A) and continue to participate in inner-sphere catalytic

cycles (red cycle in Scheme 2.4). This type of reactivity is well-established for many Mn-containing SOD mimics with redox-innocent polydentate ligands.[15-17,30,61] However, the introduction of redox-active, non-innocent ligands enables more versatile reactivity, introducing pathways involving ligand oxidation and reduction (**d** and **e**) in addition to traditional metal-based redox catalysis.

The inclusion of redox-active ligands also appears to allow the generation of a higher-valent Mn(IV)-oxo intermediate (**i**). The observation of this species would imply that the Mn(III)-superoxo species formed with **3** (**c**) can itself undergo heterolytic O-O bond cleavage, with a two-electron oxidation of the hydroquinone ligand to a *para*-quinone and loss of water. Similar reactivity was recently reported for an iron porphyrin complex with a pendant quinol group; in this work, an Fe(III)-superoxo reacts to form a ferryl species (Fe(IV)-oxo) with an oxidized *para*-quinone moiety.[76] The reaction goes through an Fe(III)-semiquinone (quinoxyl radical) species as an interme-diate.[76] This path (upper orange arrow in Scheme 2.4) might contribute to our detection of a quinoxyl-radical by the UV/vis spectroscopy (*vide infra*) during the catalytic degradation of $O_2^{-\cdot}$ by **3**.

In the case of **2**, the initial oxidation by $O_2^{-\cdot}$ appears to generate a Mn(II)-quinoxyl radical species (**d**) through tautomerization of Mn(III)-quinolate since one quinolate anion is not sufficient to stabilize the formally +3 oxidation state of the metal center. The quinoxyl radical is a stronger acid than quinolate, which facilitates its deprotonation (**d**, Figure 2.5). Thus, **2** probably does not enter the metal-only cycle observed for **3** (red cycle), and its SOD activity relies more on the ligand's ability to undergo redox transformation. Although intermediate **d** was not directly observed for **3**, it too may be capable of forming a Mn(II) intermediate with a quinoxyl radical through either a valence tautomerism or direct oxidation of the quinols. We find this likely since

Mn(II)-*para*-quinone species (**e** in Figure 2.4 and A11) are observed with both **2** and **3**; the *para*-quinone results from further oxidation of the quinoxyl radical in species **d**.[38]

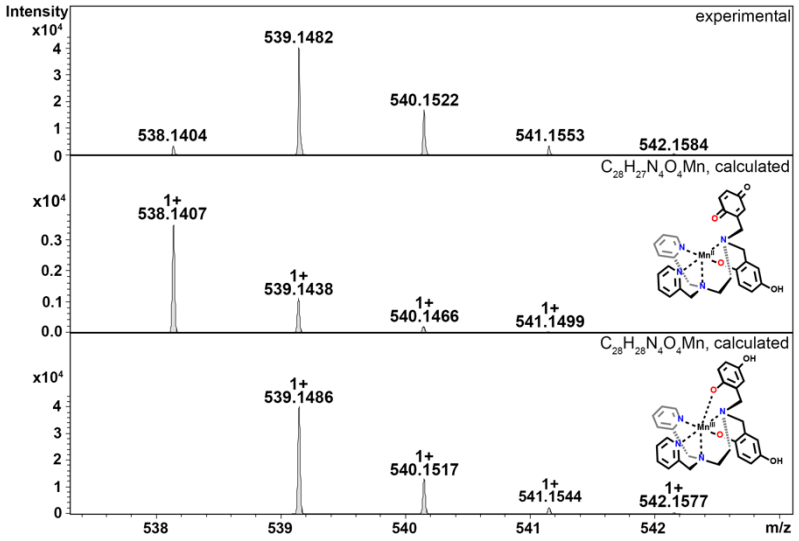

Figure 2.4 CSI-MS spectrometry of **3** upon reaction with KO_2. The graphics depict possible structures; we cannot preclude other modes of ligand coordination. The *m/z* = 538.1404 feature is assigned to the Mn(II)-quinol-quinone intermediate (**e** in Scheme 2.4). The other *m/z* peaks for e, overlap with those of the Mn(III)-diquinolate species **b**, such as the one at 539.1482. The *m/z* = 542.1584 feature is unique for species **b**. Experimental conditions: 1 mM solutions of **3** in MeCN (1% DMF) were cooled to -40 °C and then mixed with an excess of solid KO_2. Subsequently, the mixture was diluted in a pre-cooled syringe with pre-cooled MeCN to approximately 1×10^{-5} M and quickly injected into the mass spectrometer.

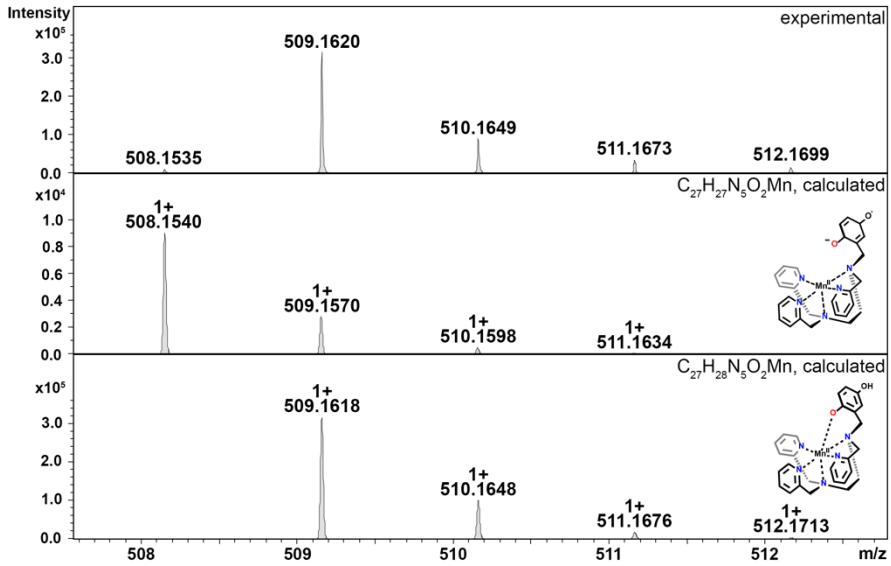

Figure 2.5 CSI-MS of **2** upon reaction with KO_2. The graphics depict possible structures; we cannot preclude other modes of ligand coordination. The *m/z* = 508.1535 peak is assigned to the Mn(II)-quinoxyl radical species (**d**). The other *m/z* peaks for **d** overlap with those of the initial Mn(II)-quinolate complex (**a**), such as that at 509.1620. The *m/z* = 512.1699 feature is unique to a. Experimental conditions: 1 mM solutions of **2** in MeCN (1% DMF) were cooled to -40 °C and then mixed with an excess of solid KO_2. Subsequently, the mixture was diluted in a pre-cooled syringe with pre-cooled MeCN to approximately 1×10^{-5} M and quickly injected into the mass spectrometer.

Cycling between a metal-coordinated quinolate, quinoxyl radical, and *para*-quinone (violet cycle) was the sole possible mechanism for the SOD activity of the Zn(II) complex with H_2qpl (**4**). With **2** and **3**, however, the ligand-only redox cycle is not likely to be a major contributor to the overall superoxide degradation since the catalysis exhibited by **4** is much slower ($k_{cat} = 3.4 \times 10^6$ M^{-1} s^{-1} for **4** at pH 7.4 in HEPES)[38] than what was detected for **2** and **3**. The Mn(II)-quinone species of **2** and **3** (**e**) can enter alternative metal-based catalytic cycles for superoxide degradation (blue cycle; for CSI-MS spectra of **f**/**g** see Figure A11). We speculate that these pathways are more efficient than those with the reduced ligands for two reasons. First, the oxidized *para*-quinone forms of the ligands, qpl and H_2qp2, are effectively pentadentate ligands, with either N5 or N4O donor sets respectively. The removal of a chelating arm improves the accessibility of the metal center to $O_2^{\cdot-}$ in both the Mn(II) and Mn(III) states. The N5 coordination provided by qpl is stronger than that of the N4O coordination by H_2qp2,

maintaining the higher stability of **2** under catalytic conditions (*vide infra*) and bolstering its SOD activity. Second, the transformation of the quinolate to a neutral *para*-quinone increases the overall positive charge of the catalyst, which would more readily attract and bind $O_2^{\cdot-}$.

An intermediate that is noticeably unobservable during the catalysis is the Mn(III)-*para*-quinone species **j**, which is either tricationic (for **2**) or dicationic (for **3**). We believe that **j** rapidly reacts with $O_2^{\cdot-}$ to yield species **k** (Figure A12), which then oxidizes $O_2^{\cdot-}$ to O_2 and regenerates the Mn(II) species **e**. The heightened positive charges of **j** species would attract $O_2^{\cdot-}$ more efficiently and enable its stronger coordination to the metal center due to the stronger coulombic interactions. The inability to detect intermediates **j** with cryo-MS would be consistent with the heightened positive charge increasing the rate of reactivity to the extent that these species are too reactive to observe by CSI-MS. The ability of **2** to attain a tricationic form would partially explain its high activity, particularly relative to that of **3**. Notably, the most active reported manganese-containing SOD mimic M40401 (based on the catalytic rate constants deter-mined by direct stopped-flow measurements)[68,69] features the neutral N5 pentaazamacrocyclic ligand. M40401 likewise has a +2 or +3 overall charge depending on the manganese redox state during the catalytic cycling and predominantly exists as a pentacoordinate species in solution, supporting our observed correlations between catalyst charge, the accessibility of the metal center for superoxide binding, and the rate of superoxide decomposition.

The hydroperoxo species **h** from the blue cycle in Scheme 2.4 can either get protonated to release H_2O_2 or undergo homolytic cleavage to generate a high-valent Mn(IV)-oxo species **i** (Figure 2.6) and a hydroxyl radical. The ability of the H_4qp2 to provide a dianionic coordination sphere in its reduced form (H_2qp2^{2-}) and a monoanionic one in its two-electron oxidized form (Hqp2^{-}) allows this ligand system to better stabilize the higher-valent intermediate than H_2qp1. We

can therefore observe **i** for **3**, but not **2**, using CSI-MS. We note that Mn(IV)-oxo interme-diates could also form directly from the Mn(III)-superoxo species **c** (*vide supra*; orange paths). Although **i** could not be detected under CSI-MS experimental conditions in the reaction with **2**, perpendicular EPR measurements suggest that this species is formed transiently with the H_2qp1 system (*vide infra*). The end-products of the reactions between **2** and $O_2^{\cdot-}$ provide further, but indirect, evidence for the generation of the $OH^{\cdot}$ by-products anticipated from the formation of Mn(IV)-oxo species.

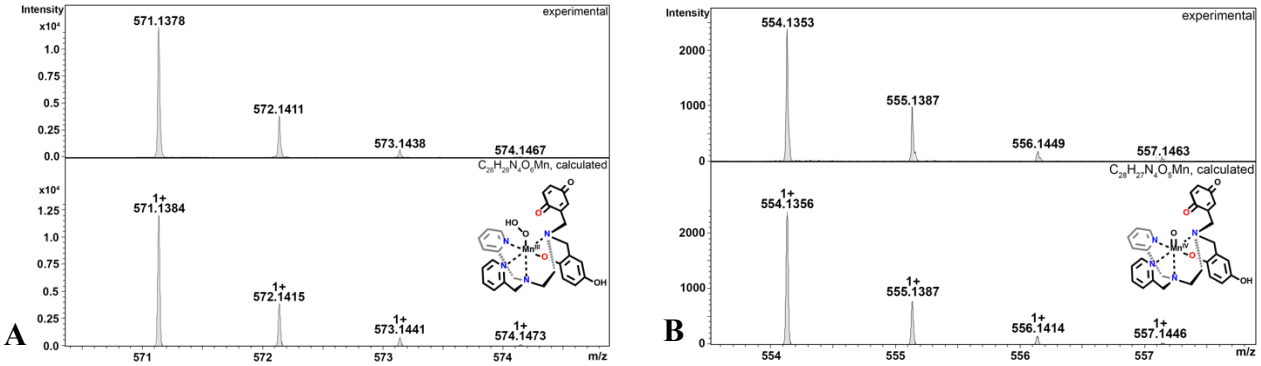

Figure 2.6 CSI-MS of **3** upon reaction with KO_2. Observed products include: (A) the Mn(III)-hydroperoxo-*para*-quinone complex **h** for **3**, which has a *m/z* = 571.1378, and (B) the Mn(IV)-oxo species **i** for **3**, which has a *m/z* = 554.1353. Experimental conditions: 1 mM solutions of **3** in MeCN (1% DMF) were cooled to -40 °C and then mixed with an excess of solid KO_2. Subsequently, the mixture was diluted in a pre-cooled syringe with pre-cooled MeCN to approximately 1×10^{-5} M and quickly injected into the mass spectrometer.

Upon prolonged reaction times, we observe Mn(II) complexes with oxygenated ligand backbones and missing quinol/*para*-quinone groups by CSI-MS (Figure 2.7). We believe that $O_2^{\cdot-}$ will normally intercept and react with Mn(IV)-oxo and $OH^{\cdot}$ oxidants quickly enough to prevent them from oxidizing the organic ligands. When the catalysis has depleted the $O_2^{\cdot-}$, however, this protective benefit is lost, resulting in ligand oxidation. The benzylic carbons that connect the quinols/*para*-quinones to the rest of the ligand are particularly susceptible to oxidation due to their weak C-H bonds.[38,78] With **3**, the long-term decomposition renders the ligand tetradentate. In water, neutral and acyclic N4 coordination environments cannot out-compete water molecules as

ligands; consequently, the end-products of the reactions between **3** and $O_2^{-\cdot}$ consist of a mixture of organic ligand fragments and no distinct Mn(II) or Mn(III) species. With **2**, the loss of a quinol group from H_2qp1 yields a pentadentate ligand with a N5 coordination environment. This decomposition product can still bind Mn(II) tightly enough to allow us to observe discrete Mn(II) complexes with the degraded ligand by CSI-MS (Figure 2.7). The *m/z* features of the decomposition products are less prominent for **2** than those for **3**; this is consistent with the H_2qp1 system generating fewer Mn(IV)-oxo and $OH^{\cdot}$ species during catalysis. Importantly, the species with the oxygenated H_2qp1 ligand could still be catalytically active even without its quinol/*para*-quinone group (*vide supra*). Lastly, we also detect a Mn(II) species with an oxygenated benzylic carbon of H_2qp1 where the quinol is still attached to the framework (Figure 2.7B). The quinol is in its reduced form, which suggests that the ligand indeed cycles between its quinol and *para*-quinone oxidation states during catalysis (purple pathway) in parallel with the metal redox cycling (red and blue cycles).

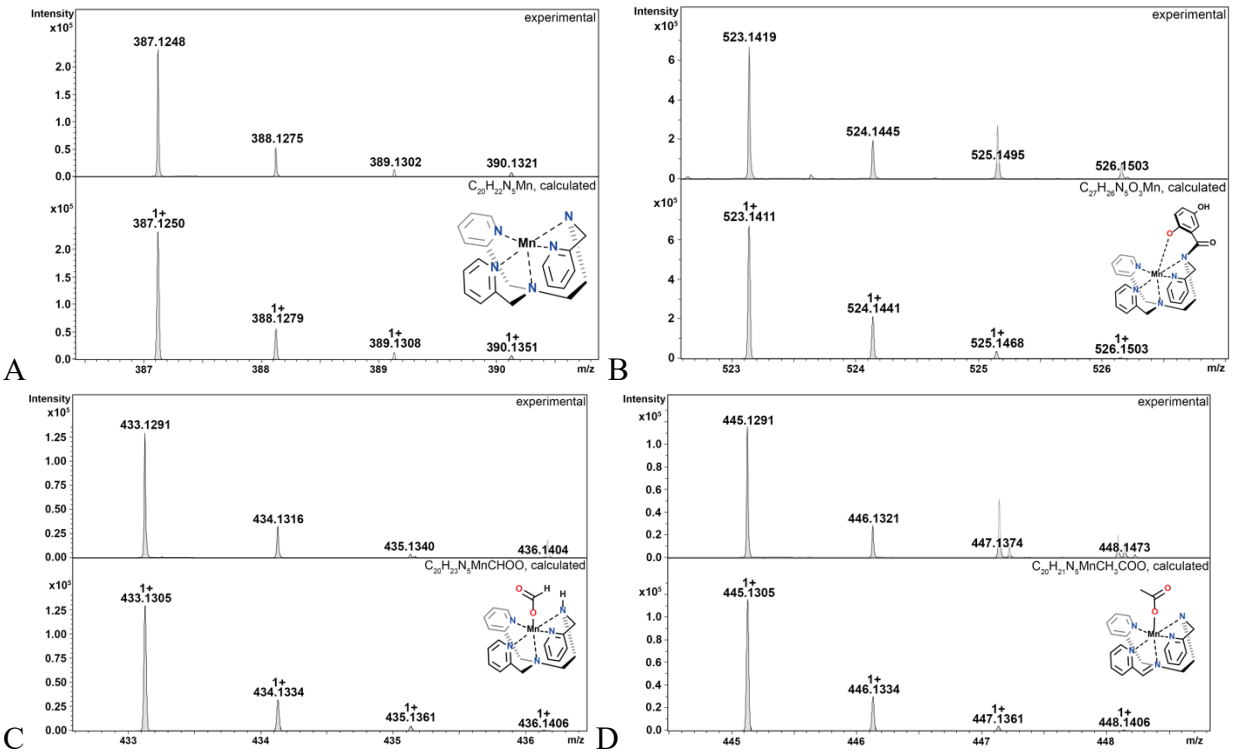

Figure 2.7 CSI-MS spectra of end-products of **2** after reaction with $O_2^{\cdot-}$. Species **A** (*m/z* = 387.1248), **C** (*m/z* = 433.1305) and **D** (*m/z* = 445.135) show a complete loss of the quinol/*para*-quinone moiety. Species **B** (*m/z* = 523.1411) shows an oxygenated ligand backbone.

Although parallel MS experiments using a ^{18}O-labeled source of superoxide would be invaluable for corroborating the identities of many of the detected intermediates, such studies were impractical due to the nature of the available resources. We were unable to find a reliable and economic source of ^{18}O-labeled KO_2 but were previously able to synthesize this reagent.[79] Regrettably, the synthetic procedure contaminates the product with substantial amounts of basic impurities that have proven to be difficult to remove. These basic impurities are not present in commercially available $K^{16}O_2$. In prior studies, we found that the buffer solutions used under the required CSI-MS experimental conditions cannot sufficiently mitigate the added basicity. As a consequence of the more basic conditions that arise from the use of the ^{18}O-labeled oxidant, the data are dominated by metal-OH species which yield *m/z* features that overlap with and obscure the regions corresponding to the target intermediates.[38]

Observation of Reaction Intermediates by Low-Temperature UV/vis and EPR

When 0.1 mM **2** is rapidly mixed with excess of superoxide (0.5-1 mM) in MeCN at -40 °C, three bands at 422, 448, and 595 nm appear within 3 s (Figure 2.8, green line). Over the next 30 s, the features at 422 and 448 nm begin to diminish while the broad band at 595 nm continues to intensify (Figure 2.8, blue line). The appearance of an isosbestic point at 474 nm indicates that the observed spectral changes can be ascribed to two distinct species that are formed as intermediates in the reaction between **2** and $O_2^{-\cdot}$ at low temperature. When the reaction is monitored at -40 °C for 1200 s, the 595 nm band slowly disappears as the absorbance below 400 nm increases without the formation of distinct peaks (Figure A13 in Appendix A). The long-term spectra likely correspond to a complex mixture of products (*vide supra*).

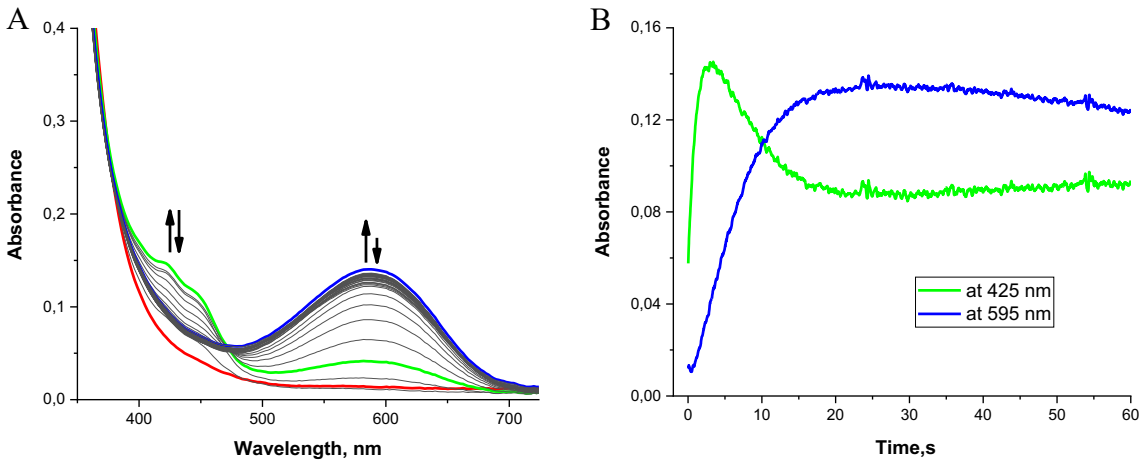

Figure 2.8 (A) Time-resolved UV/vis spectra measured after stopped-flow mixing 0.1 mM **2** with 0.5 – 1 mM KO_2 in MeCN at -40 °C. 1 equiv. of dibenzo-18-crown-6 was added to solubilize the KO_2. Red line: the first spectrum observed after mixing **2** and $O_2^{-\cdot}$.Green and blue lines: spectra recorded 3 s and 30 s after mixing, respectively. (B) Kinetic traces recorded for this reaction within the first 60 s depicting the formation of two reaction intermediates.

Although absorption bands above 400 nm may be consistent with higher-valent manganese intermediates formed from the oxidation of the metal center in **2** by $O_2^{-\cdot}$, the energies and

characteristic shapes of the features at 422 and 448 nm resemble those found in the spectrum of the semiquinone radical anion.[80, 81] When the H_2qpl ligand by itself is allowed to react with an excess of $O_2^{-\cdot}$ in MeCN, we observe similar bands by UV/vis (Figure A14), confirming that the species observed as the first intermediate in the low-temperature reaction between **2** and $O_2^{-\cdot}$ is best interpreted as a Mn(II) complex with a semiquinone radical anion ligand. The UV/vis changes observed at low temperature therefore result from ligand-centered, rather than metal-centered, oxidation. The UV/vis data corroborate the identity of species **d** (Scheme 2.4 and Figure 2.5).

The formation of the semiquinone radical anion is accompanied by an additional process that produces the species associated with the broad band centered at 595 nm. This secondary reaction is also observed in the reaction between $O_2^{-\cdot}$ and the free H_2qpl ligand; the peak at 595 nm therefore cannot be ascribed to a low-energy charge transfer band between the metal and the ligand. The most probable expla-nations for the 595 nm absorbance band involve the occurrence of either intermolecular self-association between semiquinone radicals or an electron transfer equilibrium between semiquinone radical electron donors and *para*-quinone electron acceptors to form corresponding π-dimers. Such π-association charge transfer equilibria of organic radical ions have been the subject of many investigations.[82,83] They have been shown to be thermochromic systems which display a strong absorption band at ~600 nm at lower temperatures. Unfortunately, these intermolecular self-association processes could not be observed with the extremely dilute solutions and low-pressure conditions associated with the CSI-MS experiments.

Mn(III)-peroxo complexes with amino-pyridine ligands have been documented to have UV/vis bands between 550 and 600 nm.[84-86] We cannot preclude the possibility that these are partly contributing to the 595 nm band observed for **2**. To further investigate the potential contribution of multiple species to the 595 nm band, we compared the kinetic traces for the reaction between

KO_2 and the H qpl ligand and that between KO_2 and complex **2** (Figure A15). Although the kinetic trace obtained for the ligand reaction can be satisfactorily fit to a one-exponential function, the kinetic trace for the reaction with complex **2** cannot, suggesting that more than one process is contributing to the increased absorbance at ~600 nm.

The subsequent slow disappearance of the 595 nm band over 10 min at -40 °C indicates that further oxidation processes occur. Unfortunately, these processes cannot be well resolved from the UV/vis data since (A) the more intense absorption bands of the oxidized ligands dominate the spectra and (B) the high reactivities of higher-valent manganese intermediates preclude their accumulation to concentrations high enough to be clearly observed by UV/vis spectroscopy under the experimental conditions. In the reactions between **2** and $O_2^{\cdot-}$, we observe a small but significant increase in the absorbance at 700 nm that is not duplicated in the reactions between free H_2qpl and $O_2^{\cdot-}$ (Figure A16). This may be consistent with the presence of a small amount of a higher-valent manganese species, but the data do not unambiguously support this.

Additional evidence of high-valent manganese species in the reaction cycles of **2** was provided by EPR analysis of freeze-quenched samples. To prepare the samples, an MeCN solution of **2** was rapidly mixed with an excess of $O_2^{\cdot-}$ at 233 K and then rapidly cooled to 9 K after 30 s. The X-band EPR spectrum recorded in frozen MeCN at 9 K in the perpendicular mode displays the characteristic features of the high-spin d^3 electronic configuration anticipated for a monomeric Mn(IV) complex, with a strong signal at $g \sim 2$ and weak broad signals at $g \sim 4$ and $g \sim 1.23$ (Figure A17). The EPR spectra of most Mn(IV) complexes tend to follow one of two patterns, depending on the magnitude of the zero-field splitting. When the axial parameter D is much larger than the energy provided by the spectrometer (0.31 cm^{-1} with X-band), a weak signal is found at $g \sim 2$ and a strong signal is observed at $g \sim 4$. When D is much smaller than the excitation energy, the

predominant peak instead occurs at $g \sim 2$ with weaker features at $g \sim 4$; this tends to occur in high symmetry environments.[87-93] With complex **2**, the more intense signal at $g \sim 2$ indicates that the Mn(IV) species has a small zero-field splitting, with $2|D| << h\nu$.

The spectrum shown in Figure A17 was analyzed and fitted using EasySpin in MATLAB®[94] and the values of the obtained parameters are given in Table A3. The linewidth (fitted using a Gaussian distribution) is relatively large, most probably due to unresolvable hyperfine coupling between the manganese nucleus and nitrogen atoms in the surrounding ligand. The magnitude of the D value was determined to be 0.048 cm^{-1} (note: the sign of D is unknown), hence confirming that $2|D| << h\nu$. The E/D is approximately equal to zero (0.05), showing that there is negligible rhombicity in the system. These values suggest that the effective electronic environment of the Mn(IV) closely approximates an ideal octahedral configuration. The N5 core of the two electron-oxidized *para*-quinone form of the ligand (qp1) and the oxo group would provide such a coordination environment.

It should be noted that it is theoretically possible to model the spectrum for **2** as a Mn(II) species. However, although residual Mn(II) species, superoxide, and/or ligand radicals could contribute to the strong signal at $g \sim 2$, our control experiments analyzing the EPR spectra of MeCN solutions of **2**, the semiquinone radical ligand, and $O_2^{\cdot-}$ (Figure A18) demonstrate that none of these three species can account for the feature at $g \sim 2$ shown in Figure A17. The vast majority of the superoxide has been consumed by the 30 s timepoint. In principle, the broad feature at $g \sim 2$ can also be ascribed to another Mn(II) species generated in the catalytic cycle (Scheme 2.4). This species should display high symmetry, regardless of whether the spectrum is simulated as a Mn(II) or as a Mn(IV) species, since the magnitude of the E/D ratio is small. The only plausible candidate with these characteristics would be a Mn(II) intermediate bearing a quinone ligand (species **e**

shown in Scheme 2.4). Although we cannot preclude this possibility, we believe that the UV/vis data taken during the catalysis performed by **2** is indicative of a transient high-valent manganese intermediate, and consequently, we assign the feature at g ~ 2 to a Mn(IV) species. Although the zero-field splitting parameters obtained in the present study are in line with those observed for other Mn(IV) centers,[92] the *D* parameter is significantly smaller than those reported for other Mn(IV)-oxo adducts. . The *D* values for other reported Mn(IV)-oxo complexes are usually much larger than the microwave frequency, resulting in a more intense EPR signal situated near *g* ~ 4. A rare counterexample of a Mn(IV)-oxo species with a more prominent signal at *g* ~ 2 was described by van Eldik et al. for the oxidation of $[Mn^{II}(bpy)_2Cl_2]$ by H_2O_2.[95] Although the authors did not perform explicit calculations to reveal the value of *D* for this system, limiting direct comparison, the formation of a Mn(IV)-oxo complex was supported by UV/vis spectroscopy. Consequently, the features at *g* ~ 2 observed in the present study could plausibly be assigned to high-valent manganese-oxo intermediates. Very recently, an unprecedented signal at *g* ~ 1.8 was observed during water oxidation reactions involving manganese-containing heterogeneous catalysts; the feature was assigned to a low-spin Mn(IV)-oxo species with $S = 1/2$.[96] Although the signal at ~2 described in the present work could be also generally ascribed to a low-spin Mn(IV)-oxo species, we could not adequately fit the data using a $S = 1/2$ model; a $S = 3/2$ model provides a superior fit.

When UV/vis is used to analyze a rapidly mixed MeCN solution containing 0.1 mM **3** and 0.5-1.0 mM $O_2^{\cdot-}$ at -40 °C, we observe bands similar to those found for analogous reactions with **2**: sharp features at 423 and 448 nm and a much broader band centered at 595 nm (Figure 2.9, green and blue lines). Over longer periods of time, however, a new band appears at 520 nm as the 595 nm feature vanishes, resulting in the solution changing color from blue to purple (Figure 2.9,

magenta line). Since a 520 nm band was not observed for **2**, this suggests that **3** proceeds through an additional intermediate. The 520 nm peak is also observed when the free H_4qp2 ligand is oxidized by $O_2^{-\cdot}$ under similar reaction conditions, suggesting that this new feature corresponds to a purely ligand-derived electronic tran-sition (Figure A19).

As with the other bands, the 520 nm peak observed during oxidation of both **3** and H_4qp2 cannot correlate to a charge transfer process between the ligand and the metal center but must instead be associated with a redox process on the ligand itself. The purple color of the solution is reminiscent of the charge-transfer complex quinhydrone, which consists of a reduced quinone interacting with an oxidized *para*-quinone through ring stacking.[96-98] In the presence of light, an electron from the reduced hydroquinone donor transfers to the oxidized benzoquinone acceptor, accounting for the characteristic purple hue of quinhydrone.[99,100] This charge-transfer complex can only form when both redox forms of the quinol group - the two-electron oxidized *para*-quinone and fully reduced quinol - exist in the solution at the same time. That a similar complex is not observed during the oxidation of either H_2qp1 or **2** suggests that this is an intramolecular, rather than an intermolecular, process that requires the molecule to have two redox-active quinol/*para*-quinone subunits. Although the existence of this species cannot be clearly resolved from the UV/vis data due to interference from the strong absorbance bands of the semiquinone radicals, the cryo-MS data demonstrate that a Mn(II)-quinol-*para*-quinone intermediate **e** is produced during the oxidation of **3** by $O_2^{-\cdot}$ (Scheme 2.4, the *m/z* = 538.1404 species in Figure 2.4). In intermediate **e**, the quinhydrone would form from intramolecular ring stacking interactions between the quinol and *para*-quinone groups in the coordination sphere.

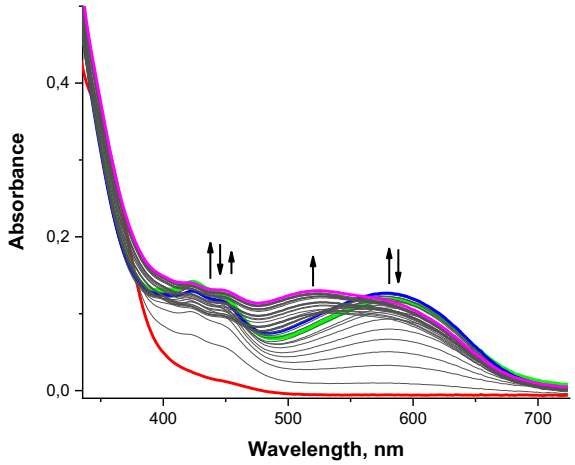

Figure 2.9 Time-resolved UV/vis spectra acquired during the reaction between 0.1 mM **3** and excess (0.5 – 1 mM) $O_2^{\cdot-}$ in MeCN at -40 °C. Red line: the spectrum taken immediately after mixing the solutions of **3** and $O_2^{\cdot-}$. Green, blue and magenta lines: spectra recorded at 30, 60, and 375 s after mixing, respectively.

Since the UV/vis data recorded during the oxidation of **3** by $O_2^{\cdot-}$ are dominated by the strong absorption bands assigned to semiquinone radical anions (422 and 448 nm),[79,80] quinhydrone (520 nm),[96-98] and also partially to π-association charge transfer equilibria (the red shifted band at 595 nm),[81,82] it is difficult to identify additional intermediates using these data by themselves (Figure A20). With this system, the CSI-MS results are quite helpful to understanding the overall mechanism (Scheme 2.4) and, concerning their complexity, are rare for SOD catalytic cycles.[38] Lastly, we note that the UV/vis data suggest that the H_4qp2 ligand in **3** undergoes secondary oxidation reactions, specifically oxygenation of the methylene positions and cleavage of the quinol groups from the 1,2-ethanediamine backbone, more slowly than the H_2qp1 ligand in **2**. This can be rationalized by the much higher SOD activity of **2**, which more quickly decomposes the $O_2^{\cdot-}$ that could sufficiently scavenge reactive Mn(IV)-oxo and hydroxyl radicals (*vide supra*).

The reaction between **3** and $O_2^{\cdot-}$ was also characterized by EPR. In these experiments, MeCN solutions of **3** were rapidly mixed with an excess of $O_2^{\cdot-}$ at 233 K, and the resulting mixtures were frozen at 9 K after 30 s and analyzed by X-band EPR (Figure A21). Similar to the reactivity of complex **2**, the vast majority of the superoxide has been consumed by the 30 s time point. When the reaction is quenched at 10 s, however, we observe an additional sharp signal that can be attributed to residual superoxide (Figure A22). The 9 K spectrum obtained at 30 s (Figure A21) is complicated and suggests the presence of multiple species. The intense signal centered at $g \sim 2.0$ with the partially resolved hyperfine splitting from the manganese nucleus (I= 5/2) is most likely a Mn(II) species. In addition, the spectrum exhibits multiple low-field components below 2000 G and high-field components above 4000 G. These features probably result from the superposition of signals from one or more distinct S = 3/2 species, with the S value being characteristic of a mononuclear Mn(IV) species with $D > h\nu$.[86-92] Using EasySpin,[93] it was possible to simulate the spectrum with two components: a Mn(IV) species (S = 3/2) and a Mn(II) species (S = 5/2) (Figure A21). Fitting this spectrum was not trivial due the multiple components and many parameters needed for optimization. As a result, the obtained fit, although reasonable, is not as accurate as that for complex **2**. Nevertheless, the model still accounts for the main features and reproduces most of the features observed for a highly complicated spectrum. According to our model, the Mn(II) and Mn(IV) species are present in an approximately 1 : 1 ratio (Table A3). The Mn(IV) complex has a D value of magnitude 0.323 cm^{-1}, which is slightly greater than $h\nu$. The E/D ratio for the Mn(IV) species generated from **3** is small suggesting that this species, like the one generated from **2**, is slightly axially distorted with negligible rhombicity.

An alternative EasySpin model that also provided a reasonable fit to the data included two Mn(IV) species: one with $2|D| << h\nu$ and another with a D value greater than $h\nu$ (Figure A23 and

Table S3). Although there is little difference between the two models used to fit **3**, we believe that, though possible, it is unlikely for two different reactive Mn(IV) species to coexist together under these conditions. As previously mentioned, the hyperfine splitting observed around the central g ~ 2 feature suggests that a Mn(II) species is more likely, although we were unable to simulate these features using either model. Irrespective of which model is correct, both give evidence for the existence of a Mn(IV) species. It should be noted that other models were also tested that consisted of one or two Mn(IV) species with $2|D| << h\nu$, but these did not yield accurate simulations representative of our spectrum for **3**. Models involving Mn(II) alone were also tested, but they likewise did not replicate as many of the spectral features.

2.4 Conclusions

Although complexes **1** and **2** are structurally similar, with the only difference being the identity of the *para* substituent in the phenolic portion of the ligand, the two compounds display markedly different activities with $O_2^{\cdot-}$. The *para*-methyl group in **1** provides a Mn(III/II) reduction potential that is low enough to enable outer-sphere electron transfer; whereas the *para*-hydroxyl group in 2 increases this reduction potential enough to make this pathway energetically non-competitive with inner-sphere oxidation. The hydroxyl-for-methyl substitution on the phenol also increases the catalytic rate, with 2 displaying activity comparable to those of cationic porphyrin manganese complexes[62,71] and potent pentaazamacrocyclic MnSOD mimetics that have entered clinical trials, but with superior aqueous stability to the latter.[101-103] The inclusion of a second quinol in **3** was found to destabilize the Mn(II) complex in water and reduce both the catalytic activity and its substitution reactivity. Both effects are proposed to result from a lesser overall charge on the manganese complex, which should weaken the ability of the complex to attract both $O_2^{\cdot-}$ and competitive inhibitors, such as phosphate. Although a typical counter-ion inhibition is not

observed, **3** catalytically degrades $O_2^{\cdot-}$ through an inner-sphere mechanism. The CSI-MS and time resolved UV/vis data provide evidence for a host of reaction intermediates that demonstrate the inner-sphere nature of the catalysis and reveal that both the manganese centers and the ligands are oxidatively active during catalysis. Though involvement of high-valent manganese species is well documented in the catalase-like activity of porphyrin- and non-porphyrin-based enzyme mimetics,[67,104] generation of Mn(IV)-oxo in a direct reaction between a monomeric Mn(II) complex and superoxide within a SOD catalytic cycle had not been documented prior to this report.

In the case of a polymeric mixed valence Mn(III)/Mn(II) complex, Mn(III)-O-Mn(IV) was identified as an intermediate in a reaction with superoxide by EPR spectroscopy.[105] Our explicit observation of Mn(IV)-oxo intermediates generated from mononuclear Mn(III) SOD mimetics by CSI-MS, UV/vis and EPR spectra is unique. Using the SOD activity of the Zn(II) analogue of **2** (**4**) as an estimate for the ligand-only contribution to the reactivity, we conclude that the metal-based inner-sphere SOD mechanism provides the more efficient pathway for superoxide degradation in Mn-quinol/phenol-based systems. The steric/ conformational features enabling stable pentacoordination upon ligand oxidation and higher overall positive charges of **2** allow it to efficiently bind $O_2^{\cdot-}$. The oxidation of the $Hqp1^-$ ligand to neutral qp1 also limits the accumulation of a potentially deleterious Mn(IV)-oxo species, relative to the H_4qp2 system. These aforementioned factors combine to make **2** arguably the most effective reported Mn SOD mimic when one accounts for its higher stability. The results here demonstrate that the concerted/complementing redox-activity of manganese and organic ligands can be a highly effective strategy for developing small molecule antioxidants.

Appendix A

Experimental Details:

In the case of pH 4.0, a buffer was selected that displays the smallest effect of pressure on the pK_a value for the studied pH range. In this context, 60 mM acetate buffer was used and its pressure dependence of pK_a ($\Delta V_a° = -11.2$ cm^3 mol^{-1}),[106] was considered in the calculation of the activation volume for the water exchange reaction at the Mn center of complex **2** at pH = 4.0 (for detailed description of the data treatment see below). The temperature-dependence of the ^{17}O-line broadening was studied from 274.2 to 348.2 K. The pressure-dependent experiments were performed at 288 K or 303 K for pH 4.0 or pH 7.4, respectively, at ambient, 2, 30, 60, 90, 120, and 150 MPa pressures. The number of coordinated water molecules was determined via a method described by Gale *et al.*[40]

General Data Treatment:

The exchange rates of the bound water molecules were determined by the line-broadening technique developed by Swift and Connick.[107] This approach makes use of the relationship between the reduced transverse relaxation rate ($1/T_{2r}$) and the mean lifetime of the coordinated solvent (τ_m), (see Eq. A1),

$$\pi \cdot 1/P_m(\Delta\nu_{obs} - \Delta\nu_{solvent}) = 1/T_{2r}$$
$$= 1/\tau_m\{(T_{2m}^{-2} + (T_{2m}\tau_m)^{-1} + \Delta\omega_m^2)/(T_{2m}^{-1} + \tau_m^{-1})^2 + \Delta\omega_m^2)\ \} + 1/T_{2os} \quad \text{(Eq. A1)}$$

where T_{2m} describes the transverse relaxation time of coordinated water in the inner sphere of the complex in the absence of chemical exchange, ω_m is the difference in resonance frequency of bulk solvent and solvent in the first coordination sphere, $\Delta\nu_{obs}$-$\Delta\nu_{solvent}$ is the difference between the full line widths at half height of the ^{17}O NMR signal of the bulk solvent in the presence ($\Delta\nu_{obs}$) and absence ($\Delta\nu_{solvent}$) of the paramagnetic compound, P_m is the mole fraction of bound water ($P_m = n_{H2O} \times$ [complex]/55.56), and T_{2os} represents an outer-sphere contribution to T_{2r} that arises from long-range interactions of the paramagnetic unpaired electrons of the metal complex with water molecules outside the first coordination sphere. The exchange rate constant between coordinated and bulk solvent, k_{ex}, can accordingly be expressed as the reciprocal residence time of the bound solvent molecule $k_{ex} = 1/\tau_m$. The line-broadening experiments were performed at complex

concentrations which assured a reasonable broadening compared to the aqueous reference ($\Delta\nu_{obs}$-$\Delta\nu_{solvent}$ > 20 Hz). The separation of the contributing factors in Eq. A1 is achieved by measuring the temperature dependence of the reduced transverse relaxation rate ($1/T_{2r}$). These measurements are, in principle, restricted to a rather small kinetic window between the boiling and freezing points of water. For the studied systems, temperature range from 274.2 to 348.2 K was selected. A contribution of $1/T_{2os}$ to the reduced transverse relaxation rate that would be clearly visible by a changeover to a positive slope at low temperatures (very slow exchange domain, I) was not observed in the available temperature range, and therefore, this term can be neglected in the treatment of the data. Depending on the selected reaction conditions (on pH value), the studied system operated in different exchange regimes (in different exchange domains). In this context, different contributions to the overall Swift – Connick equation must be taken into consideration.

pH 4.0

The dependence of $\ln(1/T_{2r})$ on 1/T clearly shows that under condition of pH = 4.0 the studied system operates in the slow exchange regime (domain II, where $1/T_{2r} \cong 1/\tau_m$) with significant contribution from $1/T_{2m}$ at elevated temperatures (Figure A6).

In that case, the values of $1/T_{2r}$ are best described by Eq. A2 and an exponential Arrhenius-type temperature dependence can be applied in the treatment of the bound water relaxation rate $1/T_{2m}$ as given by Eq. A3.

$$1/T_{2r} = 1/\tau_m\{(T_{2m}^{-2} + (T_{2m}\tau_m)^{-1}+\Delta\omega_m^2)/(T_{2m}^{-1}+\tau_m^{-1})^2+\Delta\omega_m^2)\} \quad \text{(Eq. A2)}$$

$$1/T_{2m} = 1/T_{2m}^{0} \exp(E_m/RT) \quad \text{(Eq. A3)}$$

$$k_{ex} = 1/\tau_m = (k_b/hT) \exp\{(\Delta S^{\neq}/R) - (\Delta H^{\neq}/RT)\} \quad \text{(Eq. A4)}$$

The dependence of the exchange rate constant (k_{ex}) on temperature variation can be derived from the Eyring equation (Eq. A4). Here the reciprocal residence time, or k_{ex}, depends on the activation parameters for the water exchange process, viz. the activation enthalpy, $\Delta H^{\neq}$ and activation entropy, $\Delta S^{\neq}$. For ω_m, a reciprocal temperature dependence was applied. The hyperfine coupling constant (A/h) serves as a proportionality factor and defines the relationship between temperature variation and chemical shift of the bound water molecule. Eq. A5 gives the

mathematical treatment that describes the temperature dependence of ω_m involving (A/*h*) as proportionality constant.

$$\omega_m = (2\pi g_L \mu_B S(S+1)B)(A/h)/(3k_B T) \quad \text{(Eq. A5)}$$

To clarify unambiguously the detailed mechanism of the studied exchange process, ln $(1/T_{2r})$ was measured as a function of pressure at a constant temperature of 288 K as shown in Figure A7. A study of the pressure dependence is principally advisable in the slow exchange domain (II), because of $1/T_{2r} \cong k_{ex}$. The relationship between the applied pressure and the exchange rate constant at a fixed temperature T is described by Eq. A6, where P = pressure.

$$k_{ex} = k_{ex}^0 \exp\{(-\Delta V^{\neq}/RT)\, P\} \quad \text{(Eq. A6)}$$

In view of the fact that the acetate buffer used for the measurements at pH 4.0 shows pressure dependent value of pK_a ($\Delta V_a^{\circ} = -11.2$ cm^3 mol^{-1}),[1] the appropriate changes in pH and with them associated changes in the concentration of $[Mn(H_2qp1)(H_2O)]^{2+}$ on going from 2 to 90 MPa were taken into consideration for the calculation of the corresponding values of $\ln(1/T_{2r})$ according to the Table A1.

pH 7.4

Under conditions of higher pH (7.4), the temperature dependence for $1/T_{2r}$ revealed a changeover to the fast exchange regime (III) as compared to the system studied at pH 4.0. In this case, the relative long T_{1e} for Mn(II) complexes causes T_{2m} contributions to dominate in Eq. A2 with negligible contributions from ω_m. The values of $1/T_{2r}$ were calculated with the assumption of 1 water molecule exchanging at manganese(II) center. The relevant contributions to T_{2r} under such conditions is adequately described by Eq. A7.

$$1/T_{2r} = 1/\{(\tau_m + 1/C(\tau_m^{-1}+T_{1e}^{-1})\} \quad \text{(Eq. A7)}$$

$$C = 4/3\pi^2 S(S+1)(A/h)^2 \quad \text{(Eq. A8)}$$

Where, T_{1e} is the electronic spin relaxation mainly governed by the transient zero field splitting (ZFS) mechanism. From the nonlinear fit of experimental data to Eq. A4 and Eq. A7 (Figure A4), activation enthalpy and activation entropy were determined. To clarify unambiguously the detailed

mechanism of the water exchange processes at higher pH, k_{ex} values were measured as a function of pressure. The pressure experiments were performed by measuring the reduced transverse relaxation rates at different pressures and at a constant temperature of 303 K. The exchange rate constants, k_{ex}, at different pressures were obtained as a solution to the reduced Swift-Connick equation (Eq. A7), which is quadratic function with respect to k_{ex}. On the assumption that pressure dependence of the exchange rate constant is described by Eq. A6, the activation volume, $\Delta V^{\neq}$, can be calculated from the slope of the resulting straight line P versus $\ln(k_{ex})$ (Figure A5).

Determination of the Number of Coordinated Waters

In order to determine the inner-sphere hydration state of manganese(II) center, a method described by Gale *et al*.[40] was employed. They have shown that at field strengths commonly utilized for NMR spectroscopy (B ≥ 7 T) the maximum ^{17}O relaxivity, r_{2max}^{o}, is directly proportional to the number of inner sphere water ligands (n_{H2O}) according to Eq. A9.

$$n_{H2O} = r_{2max}^{o}/510 \qquad \text{(Eq. A9)}$$

Based on the plot of r_2^o as a function of temperature determined for the studied system (Figure 2.2) and Eq. A9, the number of water coordinated to the Mn(II) center was estimated to be 1.3 and 0.7 for pH = 4.0 and pH = 7.4, respectively.

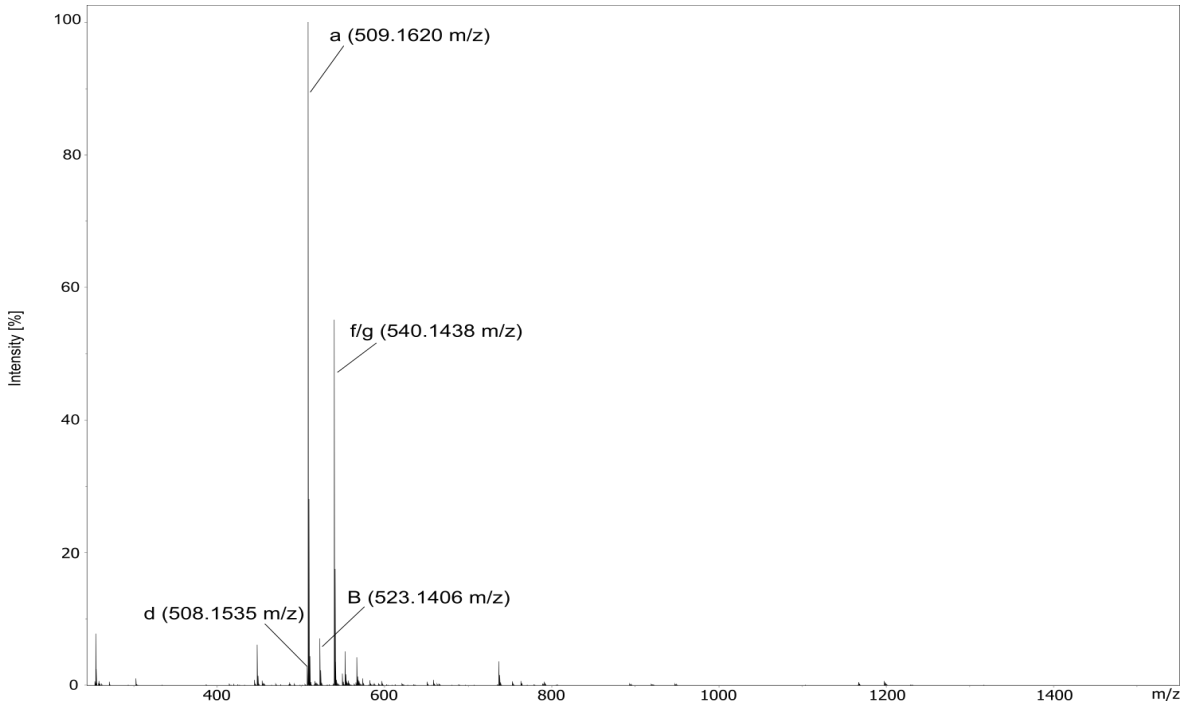

Figure A1. Full CSI-MS spectrum obtained after mixing of 1 mM solution of **2** in MeCN (1 % DMF) with an excess of solid KO_2 at -40 °C. The mixture was diluted with additional MeCN to approximately 1×10^{-5} M and quickly injected into the mass spectrometer.

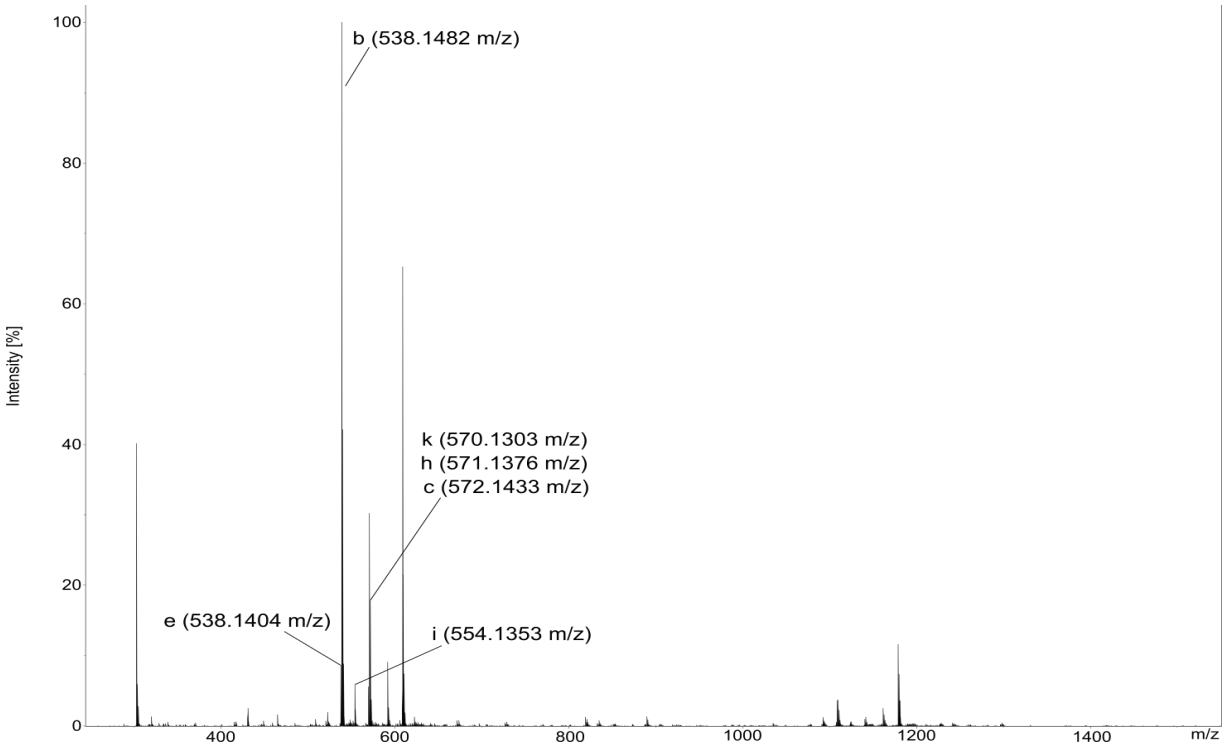

Figure A2. Full CSI-MS spectrum obtained after mixing of 1 mM solution of **3** in MeCN (1 % DMF) with an excess of solid KO_2 at -40 °C. The mixture was diluted with MeCN to approximately 1×10^{-5} M and quickly injected into the mass spectrometer.

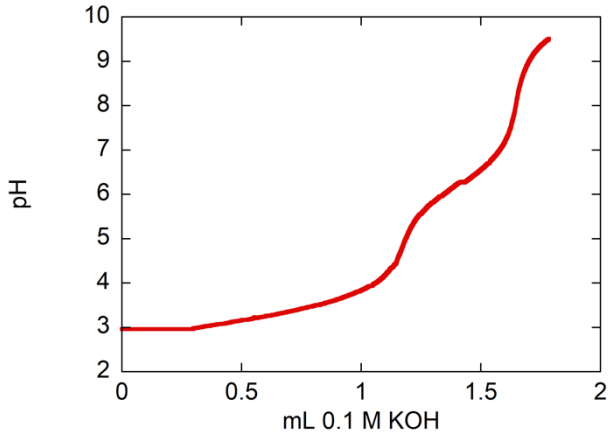

Figure A3. Raw potentiometric pH titration data for the addition of 0.10 M KOH to acidic aqueous solutions containing 100 mM KCl, 1.0 mM H_2qp1, and 1.0 mM $MnCl_2 \cdot (4H_2O)$. Each titration was performed at 25 °C under an argon atmosphere.

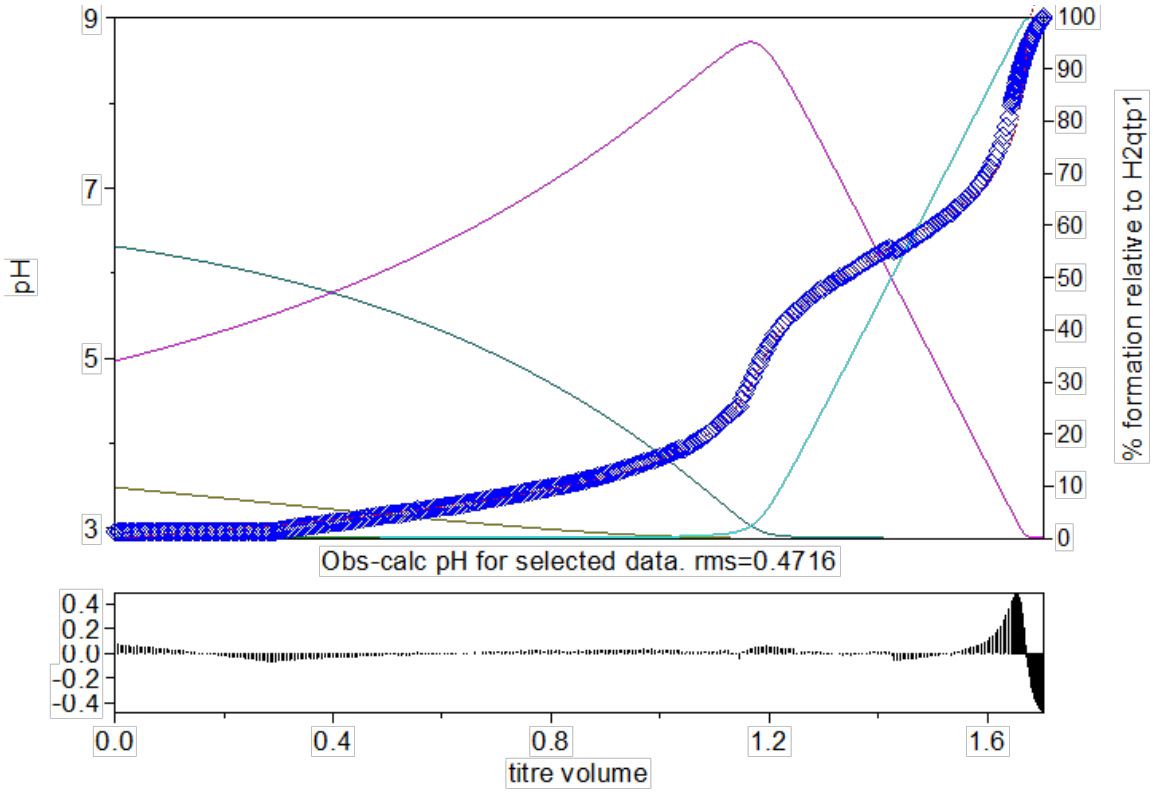

Figure A4. Hyperquad model (red line) overlaid on the experimental data from Figure A3 (blue). The data above pH 8 have been excluded from the calculations since precipitation was observed above this value. The parameters for the Hyperquad model are provided on Table A2. The residuals for the fit are provided below. The curves represent the formation of various species including $[Mn(Hqp1)]^{+}$ (light blue), $[Mn(H_2qp1)]^{2+}$ (purple), $[Mn(H_3qp1)]^{3+}$ (pine green), free Mn(II) (olive green).

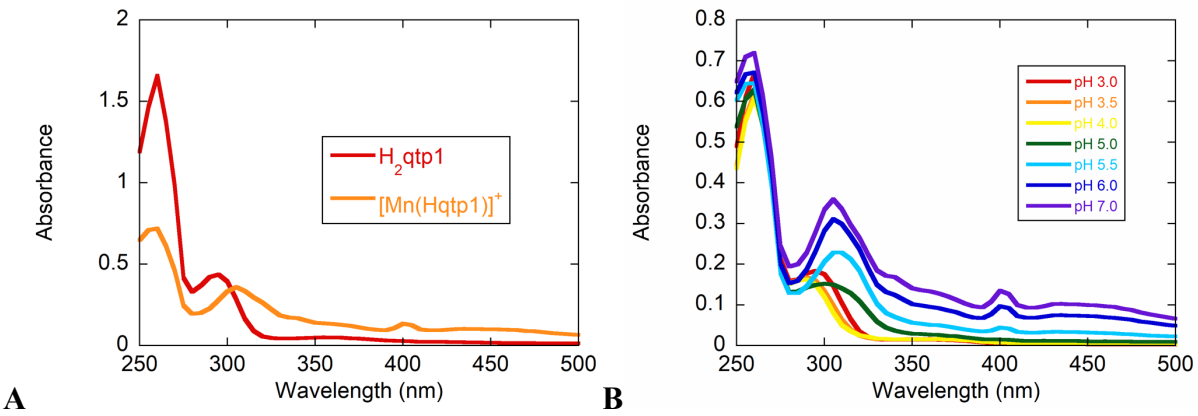

Figure A5. UV/vis data for H_4qp2 and **2** in aqueous solutions. All spectra were obtained at 298 K under air using a 1.0 cm pathlength cuvette. A) UV/vis spectra of 0.10 mM solutions of H_2qp1 and **2** in aqueous solutions containing 50 mM HEPES buffered to pH 7.00. B) UV/vis spectra of a 0.10 mM solution of **2** in water adjusted to various pH values between 7.0 and 3.0. through the addition of either KOH or HCl.

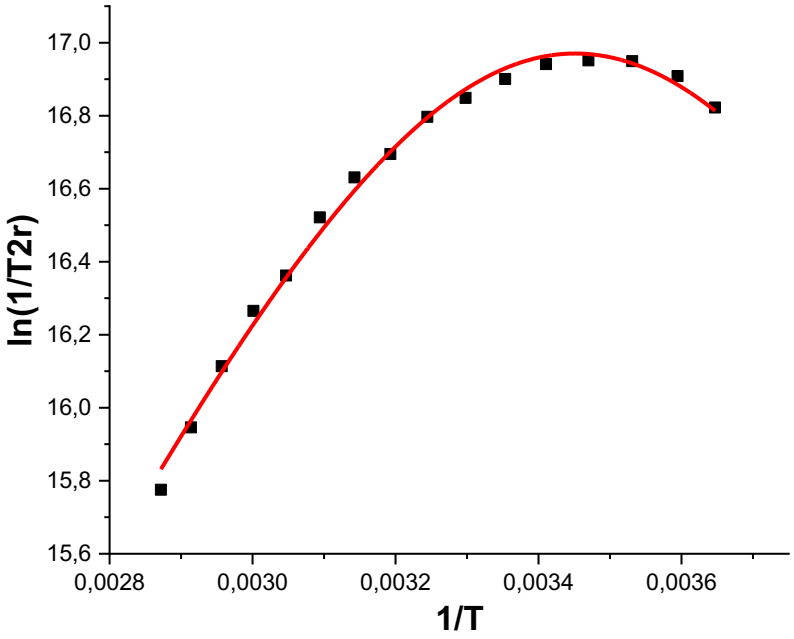

Figure A6. Temperature dependence of the reduced transverse relaxation rate ($\ln(1/T_{2r})$) for complex **2** in an aqueous 60 mM HEPES solution buffered to pH 7.4 (see Eq. A4, A7, and A8).

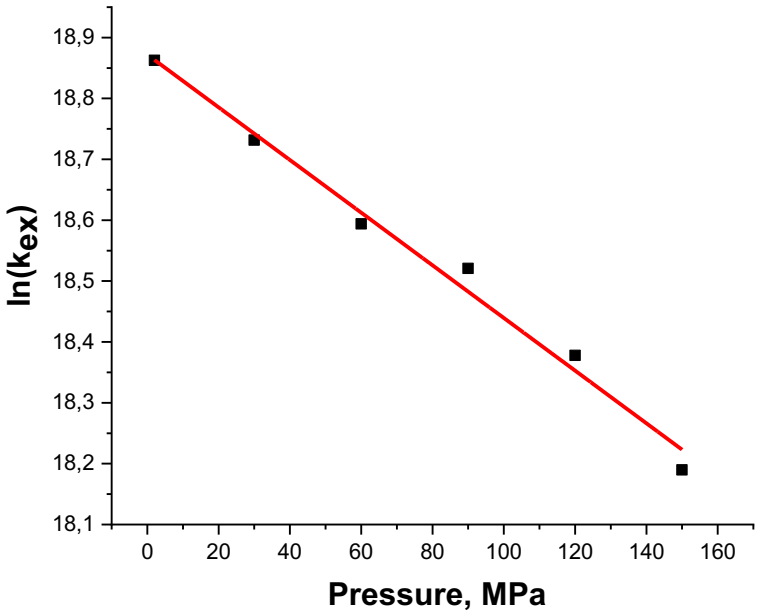

Figure A7. Pressure dependence of ln(k_{ex}) at pH 7.4 and 303 K for complex **2** in an aqueous 60 mM HEPES solution buffered to pH 7.4 (see Eq. A6).

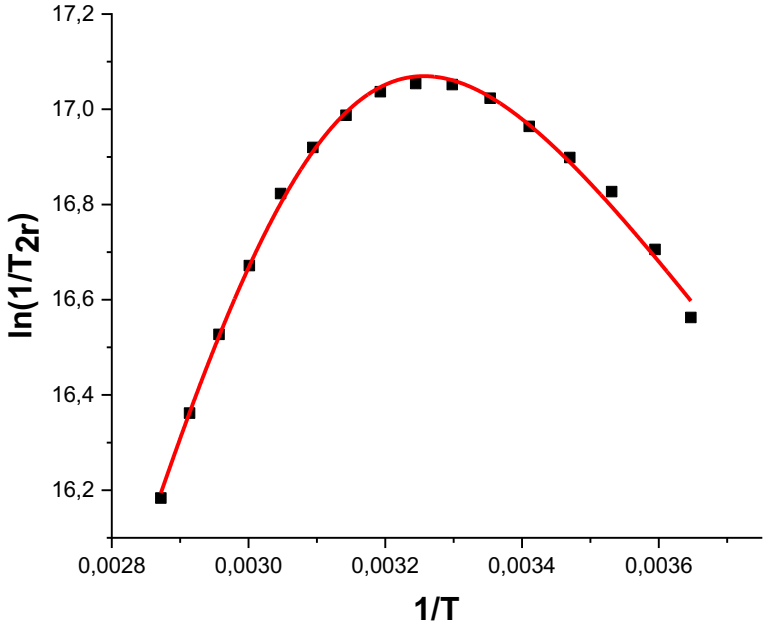

Figure A8. Temperature dependence of the reduced transverse relaxation rate (ln ($1/T_{2r}$)) for complex **2** in 60 mM acetate solution buffered to pH 4.0. The solid line is the result of the nonlinear fit using the reduced Swift-Connick equation (see Eq. A2 – A5).

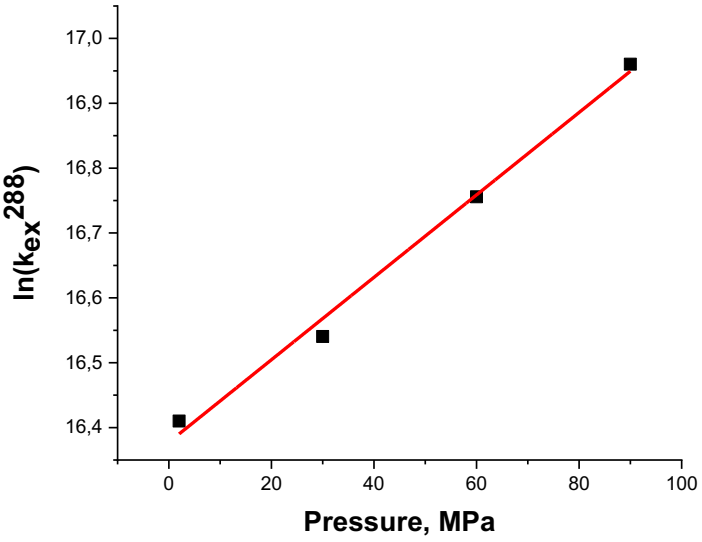

Figure A9. Pressure dependence of $\ln(k_{ex}^{288})$ at pH 4.0 and 288 K for complex **2** in 60 mM acetate buffer (see Eq. A6).

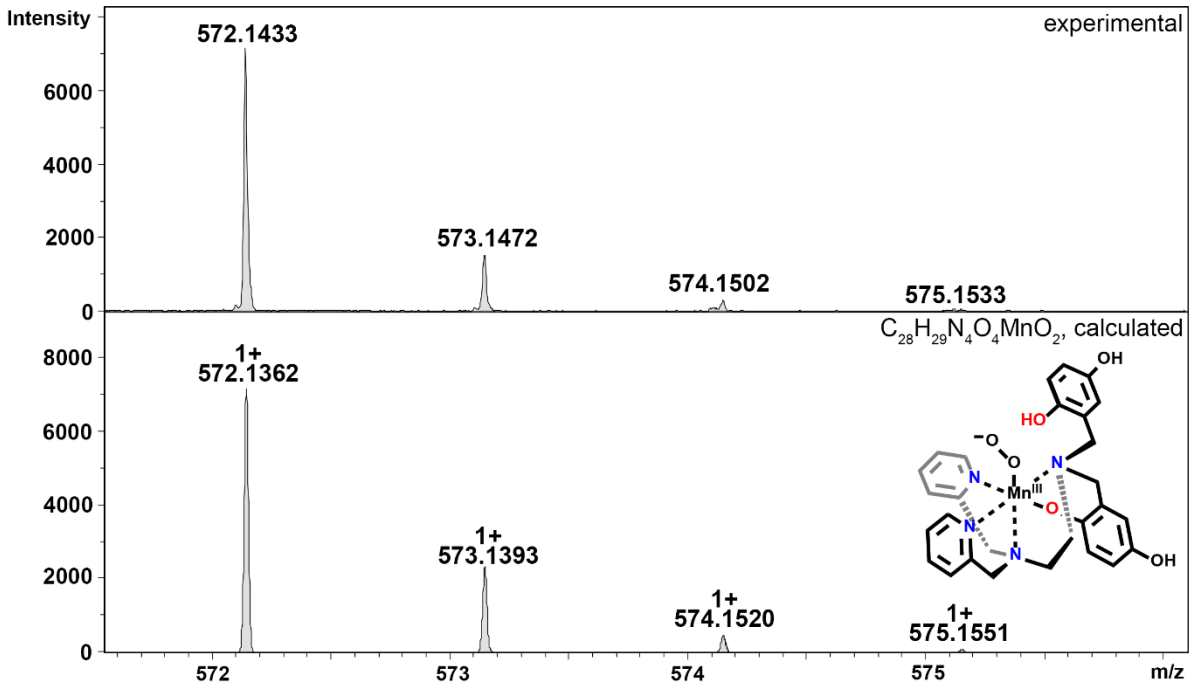

Figure A10. CSI-MS spectrum of **3**. The signal at *m/z* = 572.1433 is assigned to species **c**, which is $O_2^{\cdot-}$ coordinated to species **b**.

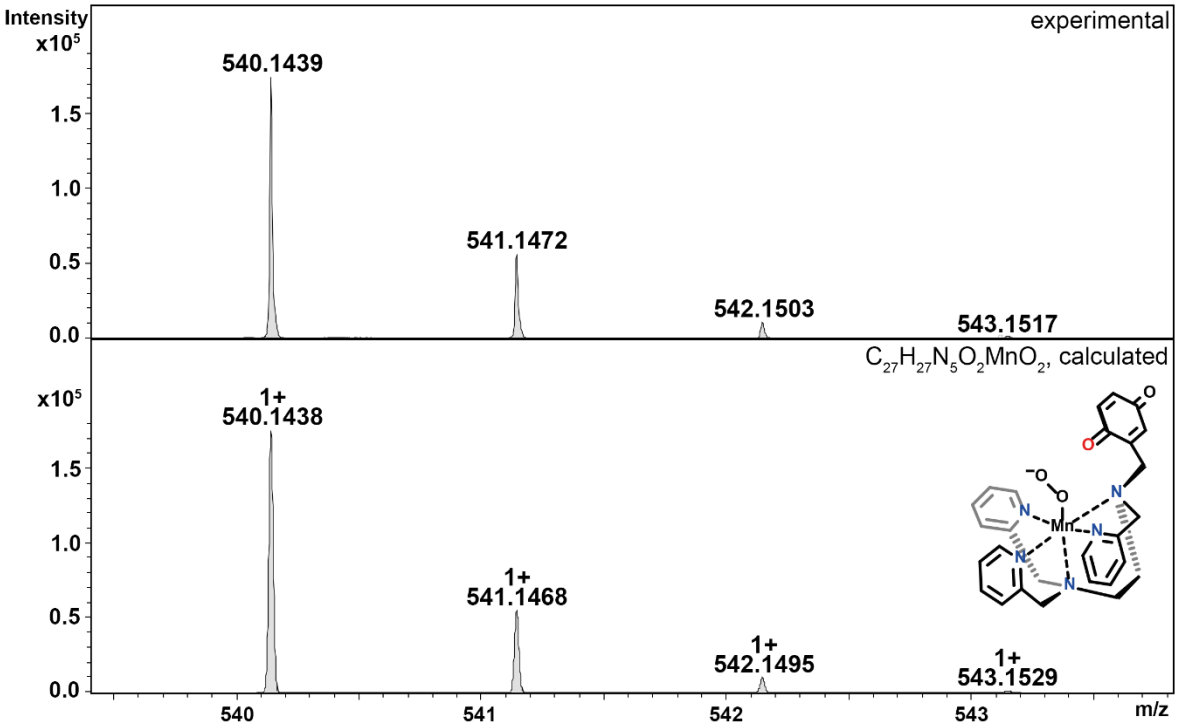

Figure A11. CSI-MS spectrum of the quinone ligand species with Mn(II)- $O_2^{\cdot-}$ ↔ Mn(III)-O_2^{2-} observed for **2** (**f**/**g**) at *m/z* = 540.1439.

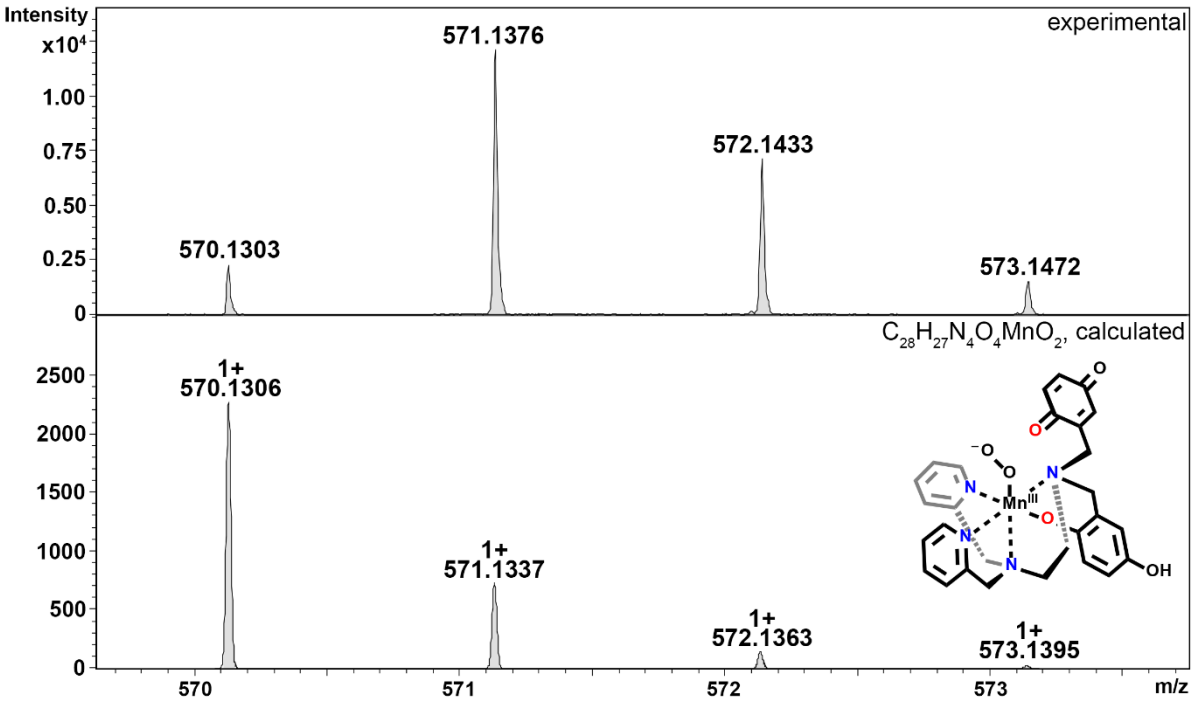

Figure A12. CSI-MS spectrum of **3**. The species at *m/z* = 570.1303 is assigned to species **k**, which is the Mn(III)-quinone complex coordinated to $O_2^{\cdot-}$.

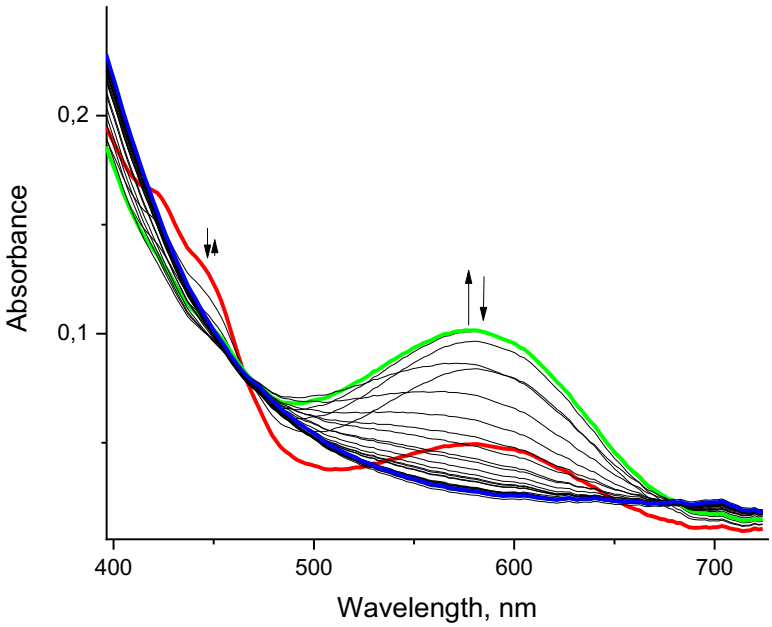

Figure A13. Spectral changes recorded up to 1240 s for the reaction between 1×10^{-4} M **2** and an excess of superoxide in MeCN at -40 °C. Red line: the spectrum recorded immediately after mixing; green and blue lines: the spectra recorded after 30 s and 1240 s, respectively.

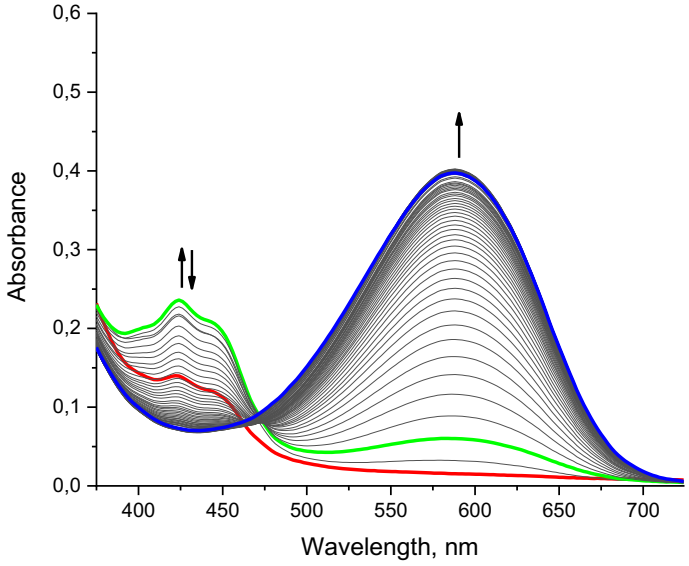

Figure A14. Spectral changes recorded for the reaction between 2×10^{-4} M H_2qp1 ligand and an excess of superoxide in MeCN at -40 °C. Red line: the spectrum recorded immediately after mixing; green and blue lines: the spectra recorded after 2 and 62 s, respectively.

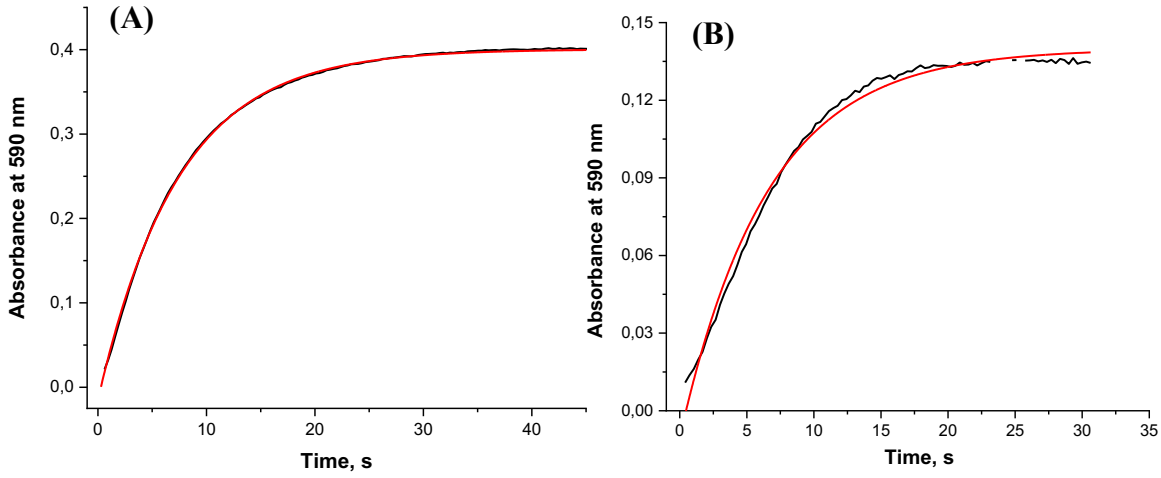

Figure A15. Kinetic traces recorded at 590 nm for the reaction of an excess of superoxide with (A) 2×10^{-4} M H_2qp1 ligand or (B) 1×10^{-4} M complex **2** in MeCN at -40 °C. The black and red lines correspond to the experimental data and one-exponential fit to the experimental data, respectively.

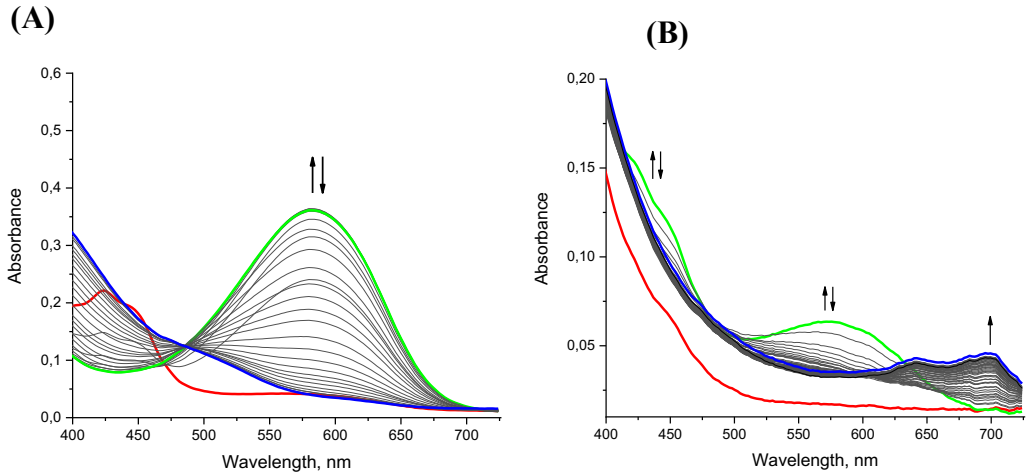

Figure A16. Comparison of the spectral changes recorded for the reaction of an excess of superoxide with (**A**) 2×10^{-4} M H_2qp1 ligand (red line: spectrum taken immediately after mixing; green and blue lines: spectrum recorded after 47 and 1240 s, respectively) and (**B**) 1×10^{-4} M **2** (red line: spectrum taken immediately after mixing; green and blue lines: spectra recorded after 25 and 1240 s, respectively) in MeCN at -30 °C.

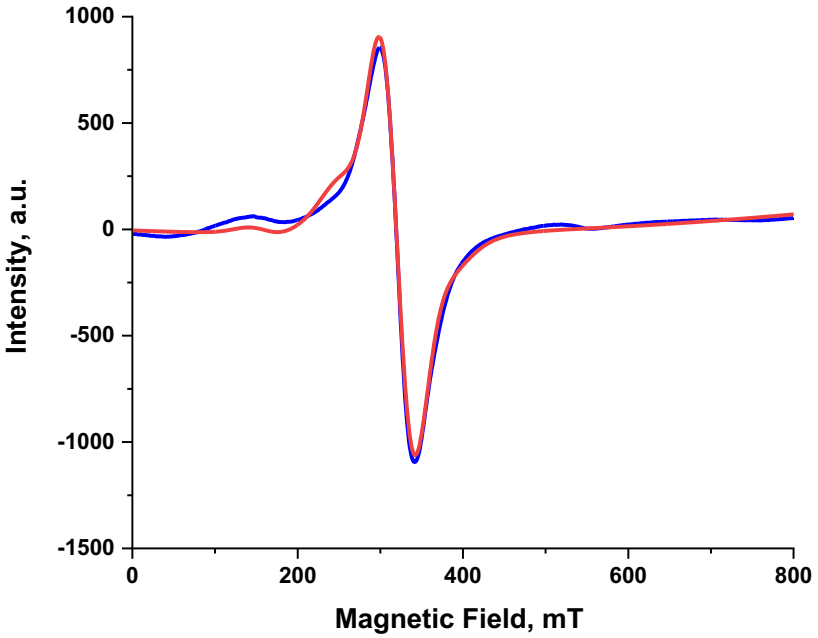

Figure A17. X-band EPR spectrum recorded at 9 K after rapid mixing of 1 mM **2** in CH_3CN with an excess of $O_2^{\cdot-}$ at 233 K. 1 equiv. of dibenzo-18-crown-6 was added to solubilize the KO_2 in MeCN. Blue line: experimental data; red line: spectrum simulated using EasySpin program[4] (see Table A3 for the values of fit parameters). Experimental conditions: microwave frequency ν = 8.959 GHz, modulation width = 0.5 mT, microwave power = 1.0 mW, modulation frequency = 100 kHz, time constant = 0.1 s.

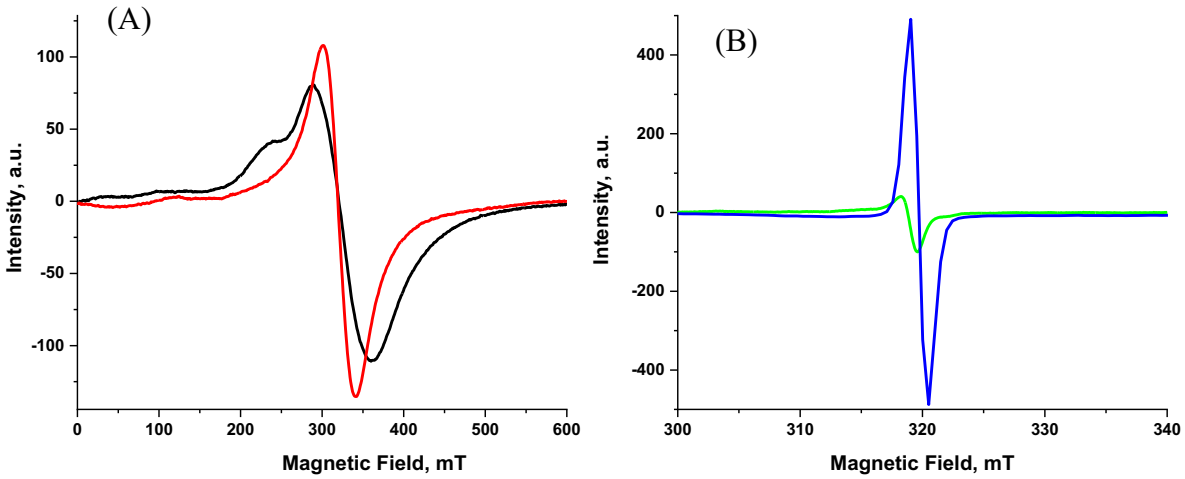

Figure A18. X-band EPR spectra of (A) 0.5 mM **2** in CH_3CN (black line) and 0.5 mM **2** after addition of excess $O_2^{\cdot-}$ (red line) and (B) 0.5 mM H_2qp1 after addition of an excess of $O_2^{\cdot-}$ (blue line) and $O_2^{\cdot-}$ in CH_3CN (green line) recorded at 95 K. Experimental conditions: microwave frequency ν = 8.959 GHz, modulation width = 0.5 mT, microwave power = 1.0 mW, modulation frequency = 100 kHz, time constant = 0.1 s.

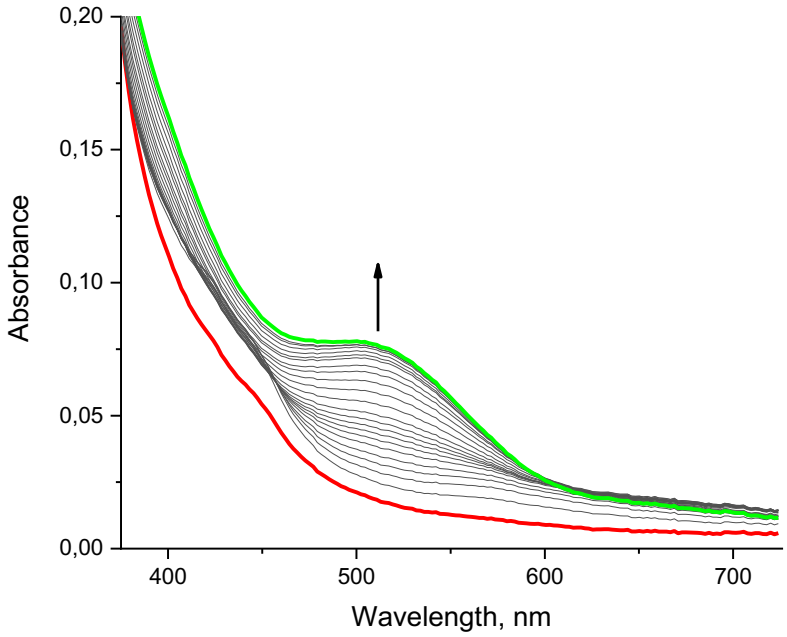

Figure A19. Spectral changes recorded for the reaction between 2×10^{-4} M H_4qp2 ligand and an excess of superoxide in MeCN at -40 °C. Red line: the spectrum recorded immediately after mixing; green line: the spectrum recorded after 62 s.

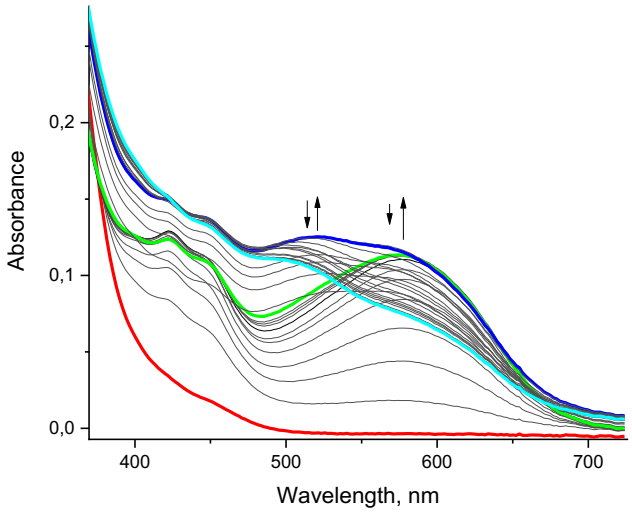

Figure A20. Spectral changes recorded up to 1240 s for the reaction between 1×10^{-4} M **3** and an excess of superoxide in MeCN at -40 °C. Red line: the spectrum recorded immediately after mixing; green, blue, and cyan lines: the spectra recorded after 60 s, 400 s, and 1240 s, respectively.

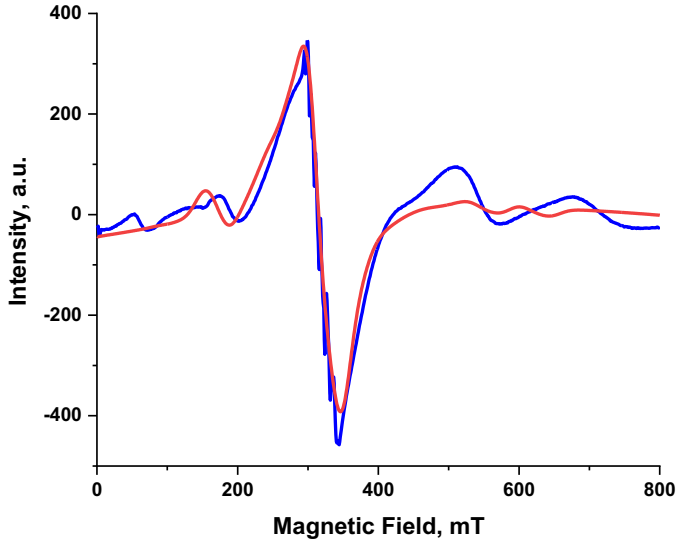

Figure A21. X-band EPR spectrum recorded at 9 K after rapid mixing of 1 mM **3** in CH_3CN with an excess of $O_2^{\cdot-}$ in CH_3CN (1 equiv. of dibenzo-18-crown-6 was added to solubilize the KO_2 in MeCN) at 233 K. The reaction was provided 30 s to complete. Blue line: experimental data; red line: spectrum simulated using EasySpin program[4] applying the model with two components, an Mn(IV) species (S=3/2) and an Mn(II) species (S=5/2) (see Table A3 for the values of fit parameters). Experimental conditions: microwave frequency ν = 8.959 GHz, modulation width = 0.5 mT, microwave power = 1.0 mW, modulation frequency = 100 kHz, time constant = 0.1 s.

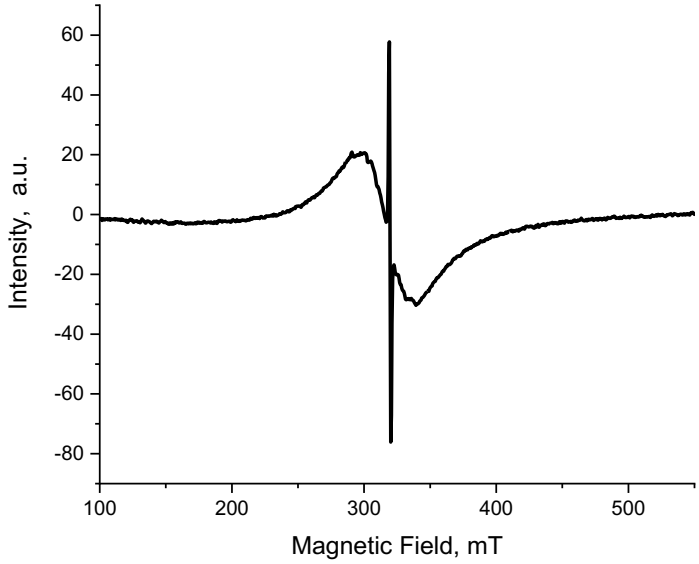

Figure A22. X-band EPR spectrum recorded at 9 K after rapid mixing of 1 mM **3** in CH_3CN with an excess of $O_2^{\cdot-}$ at 233 K and then cooled to 9 K after delay of 10 s. The intense, sharp signal centered at g ~ 2 can be attributed to the presence of superoxide that was not consumed within 10 s of the catalytic cycle. Experimental conditions: microwave frequency ν = 8.959 GHz, modulation width = 0.5 mT, microwave power = 1.0 mW, modulation frequency = 100 kHz, time constant = 0.1 s.

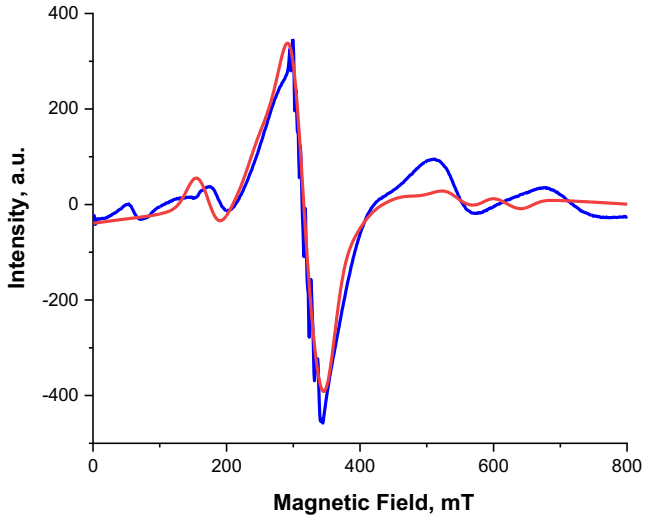

Figure A23. X-band EPR spectrum recorded at 9 K after rapid mixing of 1 mM **3** in CH_3CN with an excess of $O_2^{\cdot-}$ at 233 K. The reaction was provided 30 s to complete. Blue line: experimental data; red line: spectrum simulated using EasySpin program[4] applying the model with two components being two Mn(IV) species: one with a $2|D| << h\nu$ and another with a D value greater than $h\nu$ (see Table A3 for the values of fit parameters). Experimental conditions: microwave frequency ν = 8.959 GHz, modulation width = 0.5 mT, microwave power = 1.0 mW, modulation frequency = 100 kHz, time constant = 0.1 s.

Table A1. Changes in pH, concentration of Mn complex and corresponding $\ln(1/T_{2r})$ induced by pressure increase.

Pressure MPa	pH	Conc. of $[Mn(H_2qp1)(H_2O)]^{2+}$ mM	$\ln(1/T_{2r})$
2	4.0	3.00	16,626
30	3.95	2.77	16,906
60	3.91	2.59	17,179
90	3.86	2.36	17,449

Table A2. Parameters for the Hyperquad model used in Figure A4.

Species	Mn^{2+}	H_4qp2	H^+	log(β)	Derived Values
H_2qp1	0	1	0	0.00	
$\mathbf{H_3}qp1^+$	0	1	1	7.24	$pK_{L2} = 7.24$[a]
$\mathbf{H_4}qp1^{2+}$	0	1	2	11.96	$pK_{L1} = 4.72$[a]
$[Mn(\mathbf{H}qp1)]^+$	1	1	-1	4.2	
$[Mn(\mathbf{H_2}qp1)]^{2+}$	1	1	0	10.5	$pK_a(Mn(H_2qp1)^{2+}) = 6.3$[b]
$[Mn(\mathbf{H_3}qp1)]^{3+}$	1	1	1	13.6	$pK_a(Mn(H_3qp1)^{3+}) = 3.1$[c]

Due to the instability of the ligand at high pH values, we were unable to obtain log(β) values for the $Hqp1^-$ and $qp1^{2-}$ species.

[a]Ligand pK_a values corresponding to the (de)protonation of the free ligand amine and pyridine groups. $K_{L1} = [H_3qp1^+][H^+]/[H_4qp2^{2+}]$, $pK_{L1} = \log\beta_{012} - \log\beta_{011}$. $K_{L2} = [H_2qp1][H^+]/[H_3qp1^+]$, $pK_{L2} = \log\beta_{011} - \log\beta_{010}$.

[b]$K_a(Mn(H_2qp1)^{2+}) = [Mn(Hqp1)^+][H^+]/[Mn(H_2qp1)^{2+}]$, corresponds to the (de)protonation of the quinol. $pK_a(Mn(H_2qp1)^{2+}) = \log\beta_{110} - \log\beta_{11\text{-}1}$.

[c]$K_a(Mn(H_3qp1)^{3+}) = [Mn(H_2qp1)^{2+}][H^+]/[Mn(H_3qp1)^{3+}]$, corresponds to the (de)protonation of a pyridine group. $pK_a(Mn(H_3qp1)^{3+}) = \log\beta_{111} - \log\beta_{110}$.

Table A3. The values of parameters obtained from the simulations of experimental data to models with either one or two components (see Figures A17, A21, and A23) using the program EasySpin.[93]

Complex	Component	S	g	A_{iso} (MHz)	Line width (MHz)	D (cm^{-1})	E/D	$\sigma_{E/D}$	Percen-tage
2	1	3/2	1.921, 2.101, 2.027	138.9	36.4	0.048	0.05	0.03	100%
3	1	5/2	1.939, 2.162, 2.000	225.5	23.2	0.032	0.171	0.041	49%
	2	3/2	2.005, 2.005, 2.004	221.8	30.8	0.323	0.031	0.122	51%
3	1	3/2	1.933, 2.146, 1.995	221.5	32.4	0.041	0.160	0.122	58%
	2	3/2	2.001, 2.001, 2.001	224.8	32.6	0.323	0.031	0.122	42%

References

(1) Mosley, R. L.; Benner, E. J.; *et al. Clinical Neuroscience Research* **2006**, *6*, 261.

(2) Fearon, I. M.; Faux, S. P. *Journal of Moleuclar and Cellular Cardiology* **2009**, *47*, 372.

(3) Roberts, C. K.; Sindhu, K. K. *Life Sciences* **2009**, *84*, 705.

(4) Eskici, G.; Axelsen, P. H. *Biochemistry* **2012**, *51*, 6289.

(5) AbdulSalam, S. F.; Thowfeik, F. S.*; et al. Biochemistry* **2016**, *55*, 5341.

(6) Ahmed, M. I.; Gladden, J. D.*; et al. Journals of the American College of Cardiology* **2010**, *55*, 671.

(7) Kinnula, V. L. *Current Drug Targets Inflammation & Allergy* **2005**, *4*, 465.

(8) Abouhashem, A. S.; Singh, K.*; et al. Antioxidants & Redox Signaling* **2020**, *33*, 59.

(9) Laforge, M.; Elbim, C.*; et al. Nature Reviews Immunology* **2020**, *20*, 515.

(10) Chang, M. C. Y.; Pralle, A.*; et al. Journal of the American Chemical Society* **2004**, *126*, 15392.

(11) Miller, E. W.; Albers, A. E.*; et al. Journal of the American Chemical Society* **2005**, *127*, 16652.

(12) Koide, Y.; Urano, Y.*; et al. Journal of the American Chemical Society* **2007**, *129*, 10324.

(13) Maeda, H.; Yamamoto, K.*; et al. Journal of the American Chemical Society* **2005**, *127*, 68.

(14) Riley, D. P.; Weiss, R. H. *Journal of the American Chemical Society* **1994**, *116*, 387.

(15) Riley, D. P.; Schall, O. F. *Advances in Inorganic Chemistry* **2006**, *59*, 233.

(16) Riley, D. P.; Lennon, P. J.*; et al. Journal of the American Chemical Society* **1997**, *119*, 6522.

(17) Riley, D. P. *Chemical Reviews* **1999**, *99*, 2573.

(18) Tovmasyan, A.; Carballal, S.*; et al. Inorganic Chemistry.* **2014**, *53*, 11467.

(19) Batinic-Haberle, I.; Reboucas, J. S.*; et al. Antioxidants & Redox Signaling* **2010**, *13*, 877.

(20) Batinic-Haberle, I.; Rajic, Z.*; et al. Free Radical Biology & Medicine* **2011**, *51*, 1035.

(21) Abreu, I. A.; Cabelli, D. E. *Biochimica et Biophysica Acta* **2010**, *1804*, 263.

(22) Yu, M.; Beyers, R. J.*; et al. Inorganic Chemistry.* **2012**, *51*, 9153.

(23) Yu, M.; Ambrose, S. L.*; et al. Journal of the American Chemical Society* **2014**, *136*, 12836.

(24) Yu, M.; Ward, M. B.*; et al. Inorganic Chemistry.* **2017**, *56*, 2812.

(25) Loving, G. S.; Mukherjee, S.*; et al. Journal of the American Chemical Society* **2013**, *135*, 4620.

(26) Gale, E. M.; Mukherjee, S.*; et al. Inorganic Chemistry.* **2014**, *53*, 10748.

(27) Gale, E. M.; Jones, C. M.*; et al. Journal of the American Chemical Society* **2016**, *138*, 15861.

(28) Wang, H.; Jordan, V. C.*; et al. Journal of the American Chemical Society* **2019**, *141*, 5916.

(29) Wahsner, J.; Gale, E. M.*; et al. Chemical Reviews* **2019**, *119*, 957.

(30) Iranzo, O. *Bioorganic Chemistry* **2011**, *39*, 73.

(31) McCord, J. M.; Fridovich, I. *Journal of Biological Chemistry* **1969**, *244*, 6049.

(32) Kenkel, I.; Franke, A.*; et al. Journal of the American Chemical Society* **2017**, *139*, 1472.

(33) Lieb, D.; Friedel, F. C.*; et al. Inorganic Chemistry.* **2013**, *52*, 222.

(34) Friedel, F. C.; Lieb, D.*; et al.* J*ournal of Inorganic Biochemistry* **2012**, *109*, 26.

(35) Ivanović-Burmazović, I. *Advances in Inorganic Chemistry* **2008**, *60*, 59.

(36) Weekley, C. M.; Kenkel, I.*; et al. Inorganic Chemistry.* **2017**, *56*, 6076.

(37) Riley, D. P.; Henke, S. L.*; et al. Inorganic Chemistry.* **1996**, *35*, 5213.

(38) Ward, M. B.; Scheitler, A.*; et al. Nature Chemistry* **2018**, *10*, 1207.

(39) Gans, P.; Sabatini, A.*; et al. Talanta* **1996**, *43*, 1739.

(40) Gale, E. M.; Zhu, J.*; et al. Journal of the American Chemical Society* **2013**, *135*, 18600.

(41) Becke, A. D. *Journal of Chemical Physics* **1993**, *98*, 5648.

(42) Lee, C.; Yang, W.*; et al. Physical Review B* **1988**, *37*, 785.

(43) Stephens, P. J.; Devlin, F. J.*; et al. The Journal of Physical Chemistry* **1994**, *98*, 11623.

(44) Weigend, F.; Ahlrichs, R. *Physical Chemistry Chemical Physics* **2005**, *7*, 3297.

(45) Eichkorn, K.; Treutler, O.*; et al. Chemical Physics Letters* **1995**, *240*, 283.

(46) Eichkorn, K.; Weigend, F.*; et al. Theoretical Chemistry Accounts* **1997**, *97*, 119.

(47) Seeger, R.; Pople, J. A. *Journal of Chemical Physics* **1977**, *66*, 3045.

(48) Bauernschmitt, R.; Ahlrichs, R. *Journal of Chemical Physics* **1996**, *104*, 9047.

(49) Schlegel, H. B.; McDouall, J. J. In *Computational Advances in Organic Chemistry*; Ögretir, C., Csizmadia, I. G., Eds.; Kluwer Academic: The Netherlands, 1991, p 167.

(50) Frisch, M. J.; Trucks, G. W.*; et al.*; Gaussian, Inc: Wallingford, CT, 2016.

(51) Sahoo, S. C.; Dubey, M.*; et al. Inorganica Chimica Acta* **2010**, *363*, 3055.

(52) Drahoš, B.; Kotek, J.*; et al. Inorganic Chemistry.* **2010**, *49*, 3224.

(53) Hansch, C.; Leo, A.*; et al. Chemical Reviews* **1991**, *91*, 165.

(54) Hutchinson, T. E.; Bashir, A.*; et al. Inorganica Chimica Acta* **2019**, *496*, 119045.

(55) Taubert, D.; Breitenbach, T.*; et al. Free Radical Biology & Medicine* **2003**, *35*, 1599.

(56) Fridovich, I. *Journal of Biological Chemistry* **1997**, *272*, 18515.

(57) Liochev, S. I. *Chemical Research Toxicology* **2013**, *26*, 1312.

(58) Riley, D. P.; Rivers, W. J.*; et al. Analytical Biochemistry* **1991**, *196*, 344.

(59) Liochev, S. I.; Fridovich, I. *Archives of Biochemistry and Biophysics* **1997**, *337*, 115.

(60) Dees, A.; Zahl, A.*; et al. Inorganic Chemistry.* **2007**, *46*, 2459.

(61) Ivanović-Burmazović, I.; Filipović, M., R. *Advances in Inorganic Chemistry* **2012**, *64*, 53.

(62) Batinic-Haberle, I.; Tovmasyan, A. In *Oxidative Stress and Antioxidant Protection: The Science of Free Radical Biology and Disease*; Armstrong, D., Stratton, R. D., Eds.; John Wiley & Sons: Hoboken, NJ, 2016, p 415.

(63) Palopoli, C.; Ferreyra, J.*; et al. ACS Omega* **2019**, *4*, 48.

(64) Vincent, A.; Thauvin, M.*; et al. Journal of Inorganic Biochemistry* **2021**, *219*, 111431.

(65) Mathieu, E.; Bernard, A.-S.*; et al. Chemical Communications* **2020**, *56*, 7885.

(66) Ching, H. Y. V.; Kenkel, I.*; et al. Journal of Inorganic Biochemistry* **2016**, *160*, 172.

(67) Ledesma, G. N.; Eury, H.*; et al. Journal of Inorganic Biochemistry* **2015**, *146*, 69.

(68) Salvemini, D.; Wang, Z.-Q.*; et al. Science* **1999**, *286*, 304.

(69) Aston, K.; Rath, N.*; et al. Inorganic Chemistry.* **2001**, *40*, 1779.

(70) Policar, C. In *Redox-Active Therapeutics. Oxidative Stress in Applied Basic Research and Clinical Practice.*; Batinić-Haberle, I., Rebouças, J.*; et al.*, Eds.; Springer, Cham: 2016.

(71) Batinic-Haberle, I.; Spasojevic, I. In *Porphyrin Science by Women: In 3 Volumes*; World Scientific: 2019, p 197.

(72) Batinic-Haberle, I.; Tovmasyan, A.*; et al. Antioxidants & Redox Signaling* **2018**, *29*, 1691.

(73) Batinić-Haberle, I.; Liochev, S. I.*; et al. Archives of Biochemistry and Biophysics* **1997**, *343*, 225.

(74) DeFreitas-Silva, G.; Rebouças, J. S.*; et al. Archives of Biochemistry and Biophysics* **2008**, *477*, 105.

(75) Lieb, D., Ph.D thesis, University of Erlangen-Nuremberg, 2013.

(76) Singha, A.; Dey, A. *Chemical Communications* **2019**, *55*, 5591.

(77) Zhang, Q.; Bell-Taylor, A.*; et al. Inorganic Chemistry.* **2017**, *56*, 773.

(78) Duerr, K.; Olah, J.*; et al. Dalton Transactions* **2010**, *39*, 2049.

(79) Swallow, A. J. In *Functions of Quinones in Energy Converting Systems*; Trumpower, B. L., Ed.; Elsevier, Inc.: New York, NY, 1982, p 59.

(80) Zhao, X.; Imahori, H.*; et al. The Journal of Physical Chemistry A* **1997**, *101*, 622.

(81) Small, D.; Zaitsev, V.*; et al. Journal of the American Chemical Society* **2004**, *126*, 13850.

(82) Lü, J.-M.; Rosokha, S. V.*; et al. Journal of the American Chemical Society* **2003**, *125*, 12161.

(83) Geiger, R. A.; Leto, D. F.*; et al. Inorganic Chemistry* **2011**, *50*, 10190.

(84) Groni, S.; Blain, G.*; et al. Inorganic Chemistry.* **2007**, *46*, 1951.

(85) Ching, H. Y. V.; Anxolabéhère-Mallart, E.*; et al. Chemical Science* **2014**, *5*, 2304.

(86) Leto, D. F.; Massie, A. A.*; et al. Inorganic Chemistry.* **2016**, *55*, 3272.

(87) Gupta, R.; Taguchi, T.*; et al. Inorganic Chemistry.* **2013**, *52*, 12568.

(88) Duboc, C. *Chemical Society Reviews* **2016**, *45*, 5834.

(89) Duboc, C.; Collomb, M.-N. *Chemical Communications* **2009**, 2715.

(90) Zlatar, M.; Gruden, M.*; et al. Inorganic Chemistry.* **2016**, *55*, 1192.

(91) Weyhermüller, T.; Paine, T. K.*; et al. Inorganica Chimica Acta* **2002**, *337*, 344.

(92) Dave, B. C.; Czernuszewicz, R. S. *Journal of Coordination Chemistry* **1994**, *33*, 257.

(93) Stoll, S.; Schweiger, A. *Journal of Magnetic Resonance* **2006**, *178*, 42.

(94) Rothbart, S.; Ember, E.*; et al. Dalton Transactions* **2010**, *39*, 3264.

(95) Park, S.; Jin, K.*; et al. Nature Communications* **2020**, *11*, 5230.

(96) Slifkin, M. A. *Charge Transfer Interactions of Biomolecules*; Academic Press: London, 1971.

(97) González Moa, M. J.; Mandado, M.*; et al. The Journal of Physical Chemistry A* **2007**, *111*, 1998.

(98) Regeimbal, J.; Gleiter, S.*; et al. Proceedings of the National Academy of Sciences, U. S. A.* **2003**, *100*, 13779.

(99) Li, N.; Wang, J. *The Journal of Physical Chemistry A* **2008**, *112*, 6281.

(100) Tong, L.; Chen, Q.*; et al. Physical Chemistry Chemical Physics* **2017**, *19*, 31684.

(101) Anderson, C. M.; Allen, B. G.*; et al. International Journal of Radiation Oncology, Biology, Physics* **2016**, *94*, 869.

(102) Bonetta, R. *Chemistry-A European Journal.* **2018**, *24*, 5032.

(103) The two clinical trials involving M40403 have been suspended (NCT00033956) or terminated (NCT00101621).

(104) Chino, M.; Leone, L.*; et al. Biopolymers* **2018**, *109*, e23107.

(105) Costa, R. O.; Ferreira, S. S.*; et al. Frontiers in Chemistry* **2018**, *6*, Article 491.

(106) Neuman, R. C.; Kauzmann, W.; *et al. Journal of Physical Chemistry* **1973**, *77*, 2687.

(107) Swift, T. J.; Connick, R. E. *Journal of Physical Chemistry* **1964**, *41*, 2553.

Chapter 3

Nickel(II) Complexes with Quinol-Containing Ligands as Highly Functional Mimics of Superoxide Dismutase

*This chapter is a revision of a manuscript under preparation by the following authors: Robert Boothe[1], Jamonica L. Moore[1], Julian Oppelt[1], Alisabeth Bradford, Dean D. Schwartz, Ivana Ivanović-Burmazović, and Christian R. Goldsmith.

[1] *Authors contributed equally*

3.1 Introduction

The over-production of reactive oxygen species (ROS) has been linked to a wide array of cardiovascular,[1,2] neurological,[3] and inflammatory disorders[4] as well as tumorigenesis.[5] Understanding when and where ROS concentrations spike during the progression of these pathologies could lead to improved ways to diagnose and treat these conditions. These potential benefits have motivated efforts by us and others to develop redox-responsive probes capable of investigating the involvement of ROS in normal and aberrant physiology in conjunction with non-invasive magnetic resonance imaging (MRI) instrumentation.[6-14] The links between oxidative stress and the aforementioned health conditions have also motivated efforts to develop small molecule antioxidants that could potentially slow or even reverse disease progression. Many of these antioxidants are functional mimics of superoxide dismutases (SODs), which are enzymes that catalyze the degradation of $O_2^{-\cdot}$ to O_2 and H_2O_2 (Eq. 3.1).[15-22]

$$2\ O_2^{-\cdot} + 2\ H^+ \rightarrow O_2 + H_2O_2 \qquad \text{(Eq. 3.1)}$$

Our laboratory has recently developed a series of Mn(II)-containing contrast agents for magnetic resonance imaging (MRI) that display changes to their T_1-weighted relaxivity (r_1) upon reaction with H_2O_2.[23-25] The more recent of these contrast agents feature ligands that contain quinol groups (Scheme 3.1).[24,25] Upon oxidation by H_2O_2, these convert to *para*-quinones (Scheme 3.2). Conversely, the Mn(II)-containing probes display a negligible response to O_2 at neutral pH. The manganese complexes with both H_2qp1 and H_4qp2 were also found to be catalysts for $O_2^{-\cdot}$ decomposition, as assessed by the commonly used hypoxanthine/xanthine oxidase/lucigenin assay and subsequent stopped-flow kinetics analysis of the direct reactions between the compounds[26,27] and superoxide.[24,25,28] A Zn(II) complex with H_2qp1 can also catalyze $O_2^{-\cdot}$ degradation, indicating

that the redox activity of the ligand can allow even a redox-inactive metal ion to catalyze SOD-like reactivity.[29]

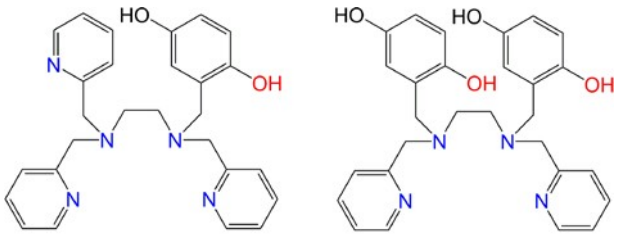

H_2qp1 H_4qp2

Scheme 3.1 Redox-active ligands for complex **1** and **2**.

The use of Mn(II) poses a problem for both MRI and SOD mimicry in that this metal ion tends to bind to ligands more weakly than most other transition metal ions.[30,31] The affinity of this metal ion for water is great enough to destabilize Mn(II) complexes with acyclic tetradentate linear ligands in aqueous solutions. When we partially oxidized the H_4qp2 complex with H_2O_2, we measured an aquation number that was difficult to reconcile unless at least some of the metal ion were released and complexed as $[Mn(H_2O)_6]^{2+}$.[24] Although "free" Mn(II) is not as toxic as unchelated iron or copper, it is still harmful and has been documented to cause neurological problems.[32] Most reported manganese-containing MRI contrast agents and SOD mimics have ligands that use macrocycles and/or a large number of anionic coordinating groups to stabilize the complexin water, but even these measures are insufficient to ensure long-term stability.[20,21,33,34]

The use of another transition metal ion could potentially relax these requirements due to the intrinsically greater complex stability.[31] We initially decided to investigate Ni(II)complexes with H_2qp1 and H_4qp2 as redox-responsive MRI contrast agents that would operate through a chemical exchange saturation transfer (CEST) pathway involving bulk water exchanging ^{1}H nuclei with the quinolic OH groups (Scheme 3.2).[35,36] Although these complexes did not give rise to a

practical and readily replicable CEST response to H_2O_2, we found that the Ni(II)-for-Mn(II) substitution did indeed stabilize the complexes in water and decided to investigate whether these compounds could serve as antioxidants.

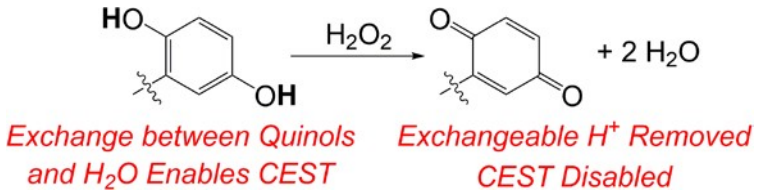

Scheme 3.2 Mechanistic MRI response to H_2O_2.

The manganese and zinc SOD mimics prepared with quinolic ligands have provided two different sets of benefits. The Mn(II) complex with H_2qp1 is highly active in HEPES buffer and appears to rely mostly on metal-centered redox processes for its SOD mimicry.[28] The zinc complexes with H_2qp1 and H_4qp2, conversely, are more stable than their Mn(II) analogues but are less effective as SOD mimics in HEPES solution.[29,37] In phosphate solution, however, the Zn(II) complexes gain enough activity to overtake the Mn(II)-H_2qp1complex as a catalyst under these conditions. That these Zn(II)-containing catalysts are not inhibited by phosphate is noteworthy since most manganese-containing SOD mimics lose substantial catalytic ability in this media.[38-40] Given the high levels of phosphate in mammalian cells,[41,42] this represents a substantial advantage for the Zn(II) complexes. We attributed the lack of phosphate inhibition to the smaller size of Zn(II) – when coordinatedby H_2qp1, the metal ion can accommodate an $O_2^{-\cdot}$ but not a bulkier phosphate anion. Ni(II) is even smaller than Zn(II),[43] and there could be a similar, if not more pronounced, phosphate-induced enhancement. Ni(II), unlike Zn(II), is redox-active, and additional redox cycles involving the metal ion could also improve the activity.

We find that the use of nickel results in catalysts that exhibit both high stability and high

activity. The activity is diminished by phosphate, but not to the same extent as most manganese-containing SOD mimics. The nickel complex with H_4qp2 is the more active of the two catalysts, and it is the most highly functioning SOD mimic in phosphate solution.

3.2 Experimental Section

Materials

Most of the chemical precursors and solvents were bought from Sigma-Aldrich and used as received. 2,2-Diphenyl-1-picryl-hydrazyl hydrate (DPPH) was bought from EMD Millipore. All deuterated solvents were purchased from Cambridge Isotopes. Fisher supplied the diethyl ether (ether) and methanol (MeOH). Methylene chloride (CH_2Cl_2) was acquired from Mallinckrodt Baker. The ligands *N*-(2,5-Dihydroxybenzyl)-*N,N',N'*-tris(2- pyridinylmethyl)-1,2-ethanediamine (H_2qp1) and *N,N'*-bis(2,5-dihydroxybenzyl)-*N,N'*-bis(2-pyridinylmethyl)-1,2-ethanediamine (H_4qp2) were prepared as previously described.[24,25]

Instrumentation

All ^{1}H and ^{13}C NMR spectra were recorded on a 400 MHz or 500 MHz AV Bruker NMR spectrometer. All reported NMR resonance peak frequencies were referenced to internal standards. Optical data were collected on a Varian Cary 50 spectrophotometer and analyzedusing software from the WinUV Analysis Suite. Electron paramagnetic resonance (EPR) spectra were collected using a Bruker EMX-6/1 X-band EPR spectrometer operated in the perpendicular mode and analyzed with the program EasySpin. Each EPR sample was run as a frozen solution in a quartz tube. High-resolution mass spectrometry (HR-MS) data were obtained at the Mass Spectrometer Center at Auburn University on a Waters Q-ToF Premier mass spectrometer via electrospray operated in the positive ion mode. Infrared spectroscopy (IR) data were obtained with a Shimadzu IR Prestige-21 FTIR spectrophotometer. A Johnson Matthey magnetic susceptibility balance

(model MK I#7967) was used to measure the magnetic properties of the Ni(II) complexes; the reported μ_{eff} values are the average of two independent measurements, each of which corresponded to a unique solid sample. Atlantic Microlabs (Norcross, GA) performed the elemental analyses (C, H, N). All samples submitted for elemental analysis were dried under vacuum prior to their shipment.

X-Ray Crystallography

Crystals were mounted in paratone oil on a glass fiber and aligned on a Bruker SMART APEX CCD X-ray diffractometer. Intensity measurements were performed using graphite monochromated Mo Kα radiation (λ = 0.71073 Å) from a sealed tube and monocapillary collimator. SMART (v 5.624) was used to determine the preliminary cell constants and regulate the data acquisition. The intensities of reflections of a sphere were collected through the compilation of three sets of exposures (frames). Each set had a different ϕ anglefor the crystal, with each exposure spanning a range of 0.3° in ω. A total of 1800 frames were collected with exposure times of 40 s per frame. The data were corrected for Lorentzand polarization effects. Structures were solved using direct methods and expanded using Fourier techniques. All non-hydrogen atoms were refined anisotropically. Hydrogen atomswere included at idealized positions 0.95 Å from their parent atoms prior to the final refinement. Further details regarding the data acquisition and analysis are included in Tables 3.1 and 3.2.

Potentiometric Titrations

The speciation chemistry of the Ni(II) complexes in water was probed using a METROHM 765 Dosimat with a jacketed, airtight glass titration vessel. A Fisher Scientific Accumet Research AR15 pH meter was used to determine the pH of the sample solutions during the titrations. The electrode was calibrated before each titration using commercially available standard solutions

buffered to pH 4.0, 7.0, and 10.0. All samples were purged with argon prior to analysis and subsequently analyzed under an argon atmosphere at 25 °C. All solution samples were prepared in solutions of 100 mM KCl in deionized Millipore water. The titrations investigating metal-ligand speciation were run with solutions that contained a 1:1 molar mixture of the ligand and $Ni(OTf)_2$. Carbonate-free solutions of 0.10 M KOH and 0.10 M HCl were prepared using argon-saturated deionized Millipore water. We attempted to analyze and fit the data to speciation models using the Hyperquad2006 software. [44]

Analysis of the Antioxidant Properties of the Coordination Complexes

We initially assessed the antioxidant activities of the Ni(II) complexes through the DPPH assay (DPPH = 2,2-diphenyl-1-picrylhydrazyl radical hydrate).[45-47] In this assay, potential antioxidants are tested for their abilities to donate hydrogen atoms to the radical to generate the corresponding hydrazine. Aqueous solutions of either **1**, **2**, or ascorbic acid were added to a solution of 0.10 mM DPPH in MeOH, such that the final reaction volume was 0.2 mL. Samples were incubated in the dark for 30 min at room temperature before being spectrophotometrically analyzed on a Molecular Devices Spectramax Plus. The absorbance at 517 nm, the λ_{max} of the hydrazine product, was recorded. Experiments were performed in triplicate.

Determination of in vitro SOD Activity via Stopped-Flow Technique

The ability of **1** and **2** to catalytically degrade superoxide was more thoroughly tested by a direct method using stopped-flow techniques that has been more fully described in prior work from one of our laboratories.[39] Stopped-flow measurements were performed on a Biologic SFM-400 four syringe stopped-flow system using only the first three syringes and a Berger Ball mixer to minimize mixing effects between aqueous buffered solutions and DMSO solutions of KO_2. A J&M

TIDAS S MMS UV/VIS diode array detector (integration time 0.5 ms, 180 nm – 720 nm wavelength) and an Energetiq LDLS ENQ EQ-99-FC laser driven light source were used.

Superoxide solutions were prepared by suspending 220 – 240 mg KO_2 in 20 mL dry DMSO. The suspension was stirred for at least 30 min under inert atmosphere before the suspension was filtered through a PTFE syringe filter (Ø = 0.45 µm) to give a saturated KO_2 solution, which was transferred to the stopped flow setup. The potential SOD mimics (SODm) were dissolved in aqueous solutions buffered to either pH 7.4 or 8.1. The buffers were prepared from Millipore water and either 4-morpholinepropanesulfonic acid (MOPS) or sodium dihydrogen phosphate. The concentration of the buffer was 60 mM, and the ionic strength was adjusted to 150 mM for each solution through the addition of NaCl. All of the buffered solutions were treated with Chelex 100 sodium exchange resin for at least 24 h before use in order to remove adventitious metal ions. Stock solutions containing 0.10 mM of each tested SODm were prepared in each buffer; if necessary, the stock solution contained 10% DMSO to ensure that the complexes dissolved fully. The stock solutions were diluted in buffer to give a series of SODm concentrations suitable for the stopped-flow experiments.

Kinetic measurements were performed adding a large excess of superoxide to the putative SOD mimetic: $[O_2^{-\cdot}]$ = 100 – 200 µM, [SODm] = 0.25 – 4.5 µM. The aqueous solution containing the studied Ni(II) complex was mixed in a 9:1 ratio with the superoxide solution in DMSO using a high-density mixer. In each experiment, the concentration of superoxide exceeded that of the zinc-containing catalyst by at least ten-fold to ensure catalytic conditions. All kinetic data were fit with the program Biokine 32 V4.80. Each k_{obs} value represents an average of at least nine measurements. Each k_{cat} was determined from the slope of k_{obs} vs. [SODm]. All measurements were performed at 21 °C. Kinetic measurements and analysis was performed by Julian Oppelt.

Syntheses

Acetonitrilo(*N*-(2,5-Dihydroxybenzyl)-*N,N',N'*-tris(2-pyridinylmethyl)-1,2-ethanediamine) nickel(II) triflate ([Ni(H_2qp1)(MeCN)]($OTf)_2$, 1).

The H_2qp1 ligand (105 mg, 0.230 mmol) and nickel(II) triflate ($Ni(OTf)_2$, 83 mg, 0.23 mmol) were dissolved in 3 mL of acetonitrile (MeCN) under air. The solution was stirred for 30 min at room temperature (RT). The solvent was removed to yield an oily reddish solid. The crude was recrystallized from a mixture of MeCN and ether to yield the product as dark red crystals that were suitable for single crystal X-ray diffraction (179 mg, 89%). ^{1}H NMR (500 MHz, CD_3CN, 294 K): 51.9, 45.9, 15.2, 14.3, 8.8, 6.7 (quinol O-H) 4.9. Optical spectroscopy (MeCN): 256 nm (6810 M^{-1} cm^{-1}), 299 nm (3430 M^{-1} cm^{-1}), 453 nm (273 M^{-1} cm^{-1}), 513 nm (175 M^{-1} cm^{-1}). Solid-state magnetic susceptibility (294 K): μ_{eff} = 3.4 μ_B. IR (KBr, cm^{-1}): 3529 (s), 3289 (s), 2286 (m), 1608 (s), 1574 (m), 1463 (s), 1364 (m), 1278 (s), 1256 (s), 1226 (s), 1158 (s), 1073 (w), 1056 (w), 1029 (s), 949 (w),824 (m), 766 (s), 730 (w), 639 (s), 573 (w), 517 (m), 429 (w). Elemental analysis (crystals): Calcd for $C_{31}H_{32}N_6F_6O_8S_2Ni$•$2H_2O$: C, 41.86%; H, 4.08%; N, 9.45%; Found: C, 41.76%; H, 3.91%; N, 9.38%.

***cis*-Diacetonitrilo(*N,N'*-bis(2,5-dihydroxybenzyl)-*N,N'*-bis(2-pyridinylmethyl)-1,2-ethanediamine)nickel(II) triflate ([Ni(H_4qp2)($MeCN)_2$]($OTf)_2$, 2).**

The H_4qp2 ligand (152 mg, 0.312 mmol) and $Ni(OTf)_2$ (114 mg, 0.319 mmol) were dissolved in 3 mL of MeCN under N_2. The solution was stirred for 30 min at RT. Ether was gradually added to the reaction mixture to yield large, purple crystals of the product that were suitable for single crystal X-ray diffraction (95 mg, 42%). ^{1}H NMR (400 MHz, CD_3CN, 294 K): 54.9, 41.1, 16.3, 9.7, 6.7 (quinol O-H), 4.9, 3.3. Optical spectroscopy (MeOH): 298 nm (7750 M^{-1} cm^{-1}), 449 nm (589 M^{-1} cm^{-1}), 516 nm (306 M^{-1} cm^{-1}). Solid-state magnetic susceptibility (294 K): μ_{eff} = 3.4 μ_B. IR (KBr, cm^{-1}): 3371 (s),

1610 (s), 1574 (m), 1509 (s), 1454 (s), 1252 (s), 1201 (s), 1173 (s), 1107 (w), 1029 (s), 948 (w), 879 (w), 818 (m), 761 (s), 729 (w), 639 (s), 578 (w), 519 (m), 422 (m). Elemental analysis: Calcd for $C_{34}H_{36}N_6F_6O_{10}S_2Ni•2H_2O$ C, 42.47%; H, 4.19%; N, 8.74%; Found: C, 42.13%; H, 3.98%; N, 8.32%.

3.3 Results

Synthesis and Characterization

The Ni(II) complexes were initially prepared by Robert Boothe in a facile reaction where both complexes form upon simply mixing the ligand and $Ni(OTf)_2$ in a common solvent (MeCN) under N_2. Pure $[Ni(H_2qp1)(MeCN)](OTf)_2$ (**1**) and $[Ni(H_4qp2)(MeCN)_2](OTf)_2$ (**2**) can be crystallized in approximately 90% and 40% yields, respectively. The yield of **2** is substantially lower than the ~75% values typical for $[Mn(H_4qp2)Br_2]$.[24] We speculate that the greater solubility of **2** in MeCN reduces the amount of material that we can cleanly precipitate and crystalize from this solvent. Elemental analysis indicates that both **1** and **2** are hygroscopic, which was also observed for the Mn(II) complex with H_2qp1.[25]

The nickel remains in the +2 oxidation state upon complexation by either quinol-containing ligand. For both **1** and **2**, the solid-state magnetic susceptibility measurements are consistent with μ_{eff} values of 3.4 μ_B; these are in the middle of the 2.8-4.0 μ_B range reported for previously characterized Ni(II) complexes.[48] The complexes display paramagnetic ^{1}H NMR spectra that features spectroscopic characteristics likewise consistent with the assignment of $S = 1$ systems. Upon adding D_2O to the NMR samples, the peaks at 6.7 ppm for both **1** and **2** vanish, leading us to assign these to quinolic O-H resonances.

Complexes **1** and **2** are readily crystallized from mixtures of MeCN and ether (Table 3.1). The crystal structures show that the H_2qp1 and H_4qp2 ligands are bound to the metal center in

pentadentate and tetradentate fashions, respectively, through their amine and pyridine groups (Figure 3.1). None of the quinols are bound to the Ni(II) in either structure. Each Ni(II) center is coordinated by a distorted octahedral array of donor atoms,with either one (**1**) or two (**2**) MeCN molecules occupying the remaining coordination sites. The metal-ligand bond distances corroborate the assignment of a +2 oxidation state for the nickel (Table 3.2).[43] The C-O bond distances average 1.37 Å, demonstrating that the quinols are both in their reduced state and protonated.[25,49]

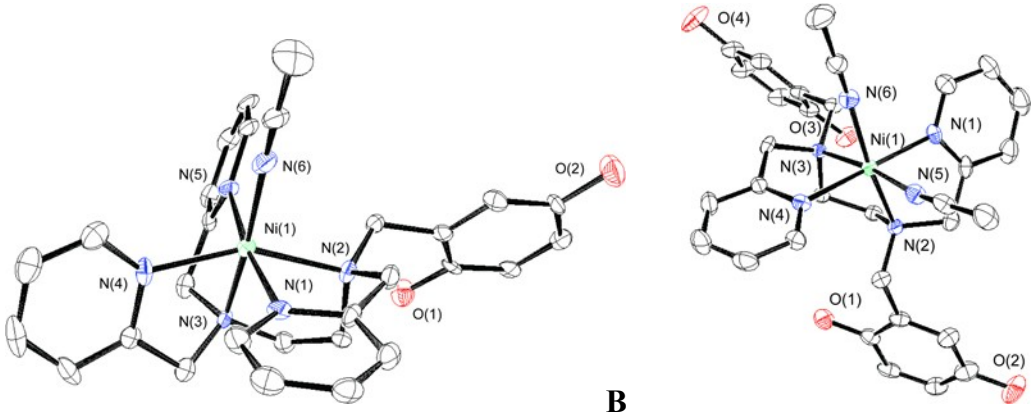

A **B**

Figure 3.1 ORTEP representations of (A) $[Ni(H_2qp1)(MeCN)]^{2+}$ (**1**) and (B) $[Ni(H_4qp2)(MeCN)_2]^{2+}$ (**2**). All hydrogen atoms, triflate counteranions, and solvent molecules have been removed for clarity. All ellipsoids are at 50% probability.

Table 3.1 Selected crystallographic data for $[Ni(H_2qp1)(MeCN)]^{2+}$ (**1**) and $[Ni(H_4qp2)(MeCN)_2]^{2+}$ (**2**).

Parameter	$[Ni(H_2qp1)(MeCN)](OTf)_2$ (**1**)	$[Ni(H_4qp2)(MeCN)_2](OTf)_2$ (**2**)
Formula	$C_{31}H_{34}F_6N_6NiO_9S_2$	$C_{38}H_{42}F_6N_8NiO_{10}S_2$
MW	871.47	1007.62
Crystal system	Orthorhombic	Orthorhombic
Space group	*Pca2₁*	*P2₁2₁2₁*
a (Å)	16.662(2)	12.8113(6)
b (Å)	12.3619(16)	17.4024(9)
c (Å)	17.649(2)	20.1442(10)
α (°)	90	90
β (°)	90	90
γ (°)	90	90
V (Å^3)	3635.2(8)	4491(4)
Z	4	4
Crystal color	Clear light purple	Clear violet
T (K)	180	180
Reflns collected	29809	105753
Unique reflns	3992	9748
R1 (F, I > 2σ(I))	0.0620	0.0730
wR2 (F^2, all data)	0.1175	0.1496

$R1 = \Sigma \big| |F_o| - |F_c| \big| / \Sigma |F_o|$; $wR2 = [\Sigma w(F_o^2 - F_c^2)^2 / \Sigma w(F_o^2)^2]^{1/2}$.

Table 3.2 Selected bond lengths (Å) for complexes $[Ni(H_2qp1)(MeCN)]^{2+}$ (**1**) and $[Ni(H_4qp2)(MeCN)_2]^{2+}$ (**2**).

Bond	**2**	**3**
Ni-N(1)[a]	2.150(7)	2.079(3)
Ni-N(2)[b]	2.140(8)	2.125(3)
Ni-N(3)[b]	2.101(7)	2.137(4)
Ni-N(4)[a]	2.077(8)	2.078(3)
Ni-N(5)[c]	2.100(8)	2.110(4)
Ni-N(6)[d]	2.062(8)	2.067(4)
C-O(1)	1.369(11)	1.369(6)
C-O(2)	1.381(12)	1.370(6)
C-O(3)		1.375(6)
C-O(4)		1.372(7)

[a]Bond between Ni(II) and pyridine nitrogen. [b]Bond between Ni(II) and amine. [c]Bond between Ni(II) and pyridine nitrogen for **1** and MeCN nitrogen in **2**. [d]Bond between Ni(II) and a MeCN molecule. The atoms in **1** and **2** have been relabeled to facilitate comparisons of the structures.

Characterization of the Aqueous Chemistry of the Ni(II) Complexes

Potentiometric pH titration data suggest that the quinols readily deprotonate and bind to the Ni(II) centers in anaerobic aqueous solutions, contrary to what is observed in the crystal structures. The H_2qp1 ligand by itself was previously found to undergo two ionization events with pK_a values of 4.72 and 7.24,[29] these are consistent with the protonation of a pyridine ring and the tertiary amines, respectively.[30] Due to the precipitation of the ligands under basic conditions, we were unable to measure the pK_a values of the O-H protons, which are estimated to be about 10.[50] Intramolecular hydrogen bonding was observed in the crystal structure of the ligand, which we believe renders it unavailable for further protonation.[29]

Our best fits to the data collected for complex **1** suggest that free ligand is not present to an appreciable degree between pH 2.5 and 9.0. Since we do not observe dissociation of the ligand, we cannot calculate formation constants for either the $[Ni(Hqp1)]^+$ or $[Ni(H_2qp1)]^{2+}$ species. We observe an ionization event consistent with a pK_a value of 6.33 (±0.05), which is assigned to the (de)protonation of a M(II)-bound phenolate.[9,51,52] Consequently, we believe that the predominant species between pH 7.0 and 7.4 is $[Ni(Hqp1)]^+$.

The Ni(II) complex with H_4qp2 also appears to be fully stable in water, and the lack of free ligand under even the most acidic of conditions tested again precluded us from calculating stability constants. The H_4qp2 ligand was previously observed to display two ionization events upon either basification of an acidic solution or acidification of a basic solution. The corresponding pK_a values of 4.47 and 7.18 were assigned to the (de)protonation of a pyridine and tertiary amine, respectively.[24] When complex **2** is subjected to the same conditions, two clear ionization events are observed between pH 3 and 10. The corresponding pK_a values of 5.99 (±0.05) and 8.24 (±0.05) are assigned to the (de)protonation of metal-bound quinols. Consequently, we believe that the complex is

predominantly $[Ni(H_3qp2)]^+$ between pH 7.0 and 7.4, with H_3qp2^- being the monodeprotonated form of the ligand.

The assignments are supported by spectrophotometric pH titrations in aqueous solutions. The UV/vis spectra of both **1** and **2** at pH 7.0 feature bands at 313 nm, consistent with metal-bound quinolate ligands.[24] Upon acidification, these bands disappear, and new peaks appear at 294 and 293 nm for **1** and **2**, respectively. Similar changes were observed for the protonation of $[Mn(H_3qp2)]^+$ and $[Zn(Hqp1)]^+$ in water.[24,29] Given the noted tendency of Ni(II) to avoid heptacoordination, even transiently,[53,54] it is unlikely that water molecules are directly coordinated to the metal center in **1** when it is dissolved in water. Since the quinols are relatively poor ligands for metal ions, a water molecule could conceivably enter the coordination sphere in **2**, yielding $[Ni(H_3qp2)(H_2O)]^+$.

Antioxidant Activity

Complexes **1** and **2** were initially screened for antioxidant activity using two common assays. The xanthine oxidase/hypoxanthine/lucigenin assay is frequently used to probe the ability of an antioxidant to decompose superoxide.[24-27] Unfortunately, we were unable to obtain reliable data from this method. We believe that the photophysical properties of the Ni(II) complexes are disrupting the analysis. Lucigenin needs to absorb light at 460 nm to produce a chemiluminescent signal, but both **1** and **2** absorb strongly in this region as well.

The DPPH assay tests the ability of antioxidants to donate hydrogen atoms to 2,2-diphenyl-1-picrylhydrazyl radical hydrate (DPPH).[45-47,55] Hydrogen atom transfer to DPPH yields a distinctly colored hydrazine product which can be quantified by UV/vis. Both **1** and **2** are strong antioxidants by this measure, with 12.5 μM (**1**) and 6.3 μM (**2**) being sufficient to convert half the radical to the hydrazine (Figure B8). 21.9 μM of ascorbic acid was needed to elicit a similar response. Other divalent metal complexes with the H_2qp1 and H_4qp2 ligands likewise

outperformed ascorbic acid in these measurements by approximately the same extent.[24,25,29] The high sensitivity of the DPPH assay precludes us from drawing more quantitative conclusions regarding the relative reactivities of the H_2qp1 and H_4qp2 complexes.

The aforementioned assays are imperfect measures of the actual reactivity with superoxide due to the possibility of competing side-reactions between the various components in the reaction mixtures.[18,38,56-59] In order to more thoroughly and accurately gauge the antioxidant activity, we followed the direct reactions between the Ni(II) compounds and KO_2 using stopped-flow kinetics methods. These studies confirm that both **1** and **2** are highly capable SOD mimics (Figure 3.2, Figures B15-B18, Table 3.3). The H_4qp2 complex is the more active of the two in all three studied aqueous media, being approximately 6 to 8-fold more active than **1**. The activity is highest in MOPS buffered to pH 7.4 and lowest in pH 7.4 phosphate solutions. Approximately half of the activity is lost going from MOPS to phosphate buffer.

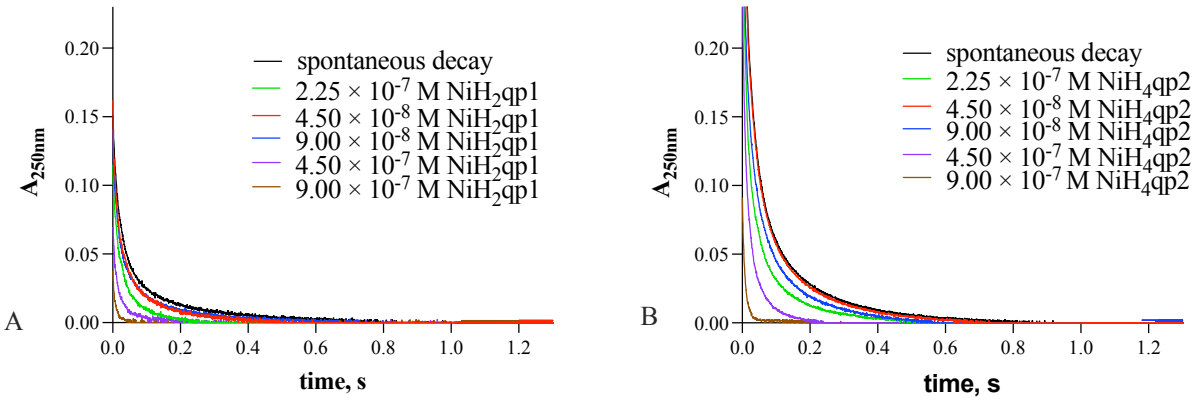

Figure 3.2 Kinetic traces of superoxide decomposition at 250 nm in 60 mM MOPS buffer, pH 7.4 for **1** (A) and **2** (B), respectively.

MS reveals that the end-products of the reactions between the Ni(II) compounds and KO_2 include Ni(II) complexes with oxidized forms of the ligands (Figures B9-B14). With a small excess of KO_2, the ligands are primarily oxidized to *para*-quinone compounds: qp1 for **1** and a mixture

of H_2qp2 and qp2 for **2** (Scheme 3.3). When larger amounts of KO_2 are added, additional *m/z* features appear that are consistent with secondary ligand oxidation processes, such as the installation of O atoms onto the ligand and the detachment of quinol/*para*-quinone or picolyl groups.

Table 3.3 Catalytic rate constants, k_{cat} (M^{-1} s^{-1}), measured by stopped-flow kinetics for the direct reactions of **1** and **2** with superoxide.

Buffer, pH	**1**	**2**
60 mM MOPS, 7.4	1.75×10^7	12.8×10^7
60 mM MOPS, 7.8	1.18×10^7	9.74×10^7
50 mM Phosphate, 7.4	1.08×10^7	6.21×10^7

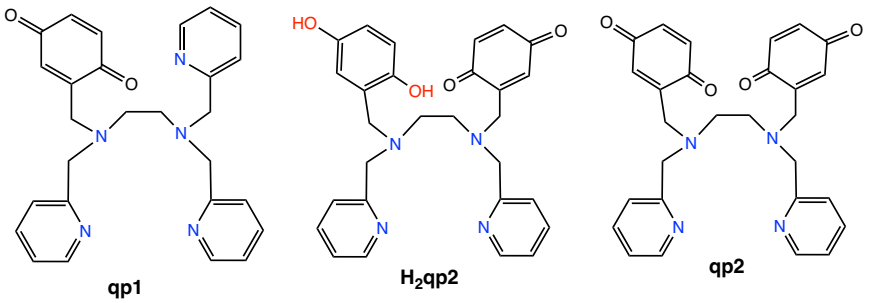

Scheme 3.3 Oxidized versions of the H_2qp1 and H_4qp2 ligands.

EPR Analysis of Viable Intermediates for SOD Mimicry

In order to look at possible intermediates relevant to the SOD mimicry, we reacted **1** and **2** with stoichiometric amounts of $AgSbF_6$ and Et_3N in H_2O (Figure 3.3). We previously ran analogous studies with a Zn(II) complex with H_2qp1 to demonstrate that Zn(II)-quinoxyl radical species were viable intermediates in its catalytic cycle for superoxide dismutation.[29]

EPR analysis of the reaction mixtures indicates that at least some of the nickel has been oxidized to the +3 oxidation state for both **1** and **2** and that this oxidation state is potentially accessible for the catalysis. For complex **1**, two small features appear with $g = 2.22$ and $g = 2.00$. The intensities of the features maximize by 45 min. Although the $g = 2.00$ feature resembles that

found for the aforementioned Zn(II)-quinoxyl radical species and resembles features seen for previously reported Ni(II) complexes with organic radicals,[60,61] it is unlikely that such a species would persist for 45 min. We therefore believe that both features correspond to Ni(III) species.[62]

Complex **2** gives rise to a stronger feature at $g = 2.22$ upon reaction with the Ag(I) oxidant and base. No features that can be unambiguously distinguished from noise are seen around $g = 2.00$. On the basis of the heightened intensity of the $g = 2.22$ feature, it would seem that the additional quinol/quinolate in the H_4qp2 framework stabilizes Ni(III) species.

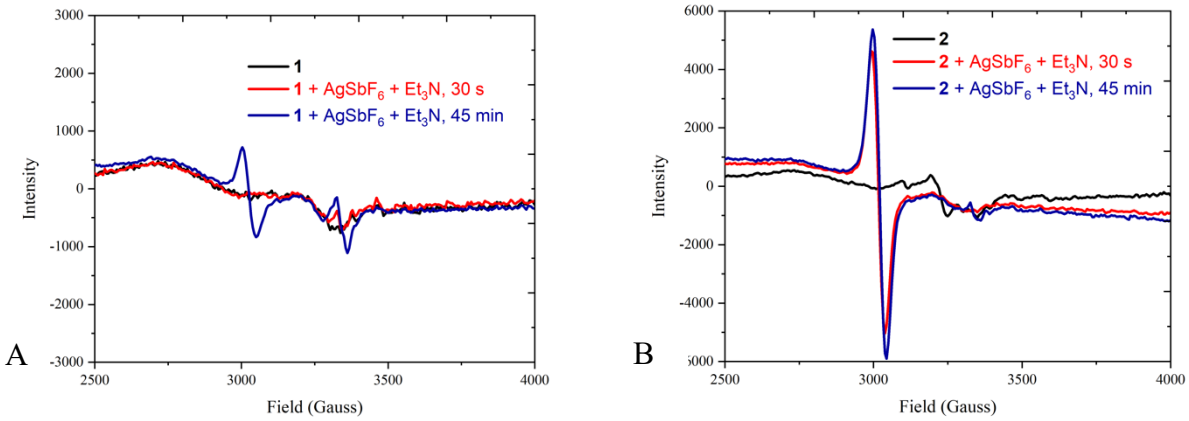

Figure 3.3 X-band EPR data for the reactions between A) 1.0 mM **1**, 2.35 mM $AgSbF_6$, and 235 mM Et_3N in H_2O and B) 1.0 mM **2**, 2.35 mM $AgSbF_6$, and 235 mM Et_3N in H_2O. At the given time points, aliquots were rapidly filtered and frozen at 77 K.

3.4 Discussion

The ligands *N*-(2,5-Dihydroxybenzyl)-*N,N',N'*-tris(2-pyridinylmethyl)-1,2-ethanediamine (H_2qp1) and *N,N'*-bis(2,5-dihydroxybenzyl)-*N,N'*-bis(2-pyridinylmethyl)-1,2-ethanediamine (H_4qp2) were previously used to prepare complexes with Mn(II) and Zn(II), and precipitation from organic solvents enabled us to obtain $[Mn(H_2qp1)(MeCN)](OTf)_2$, $[Mn(H_4qp2)Br_2]$, $[Zn(H_2qp1)(OTf)](OTf)$, and $[Zn(H_2qp1)(MeCN)](OTf)_2$ in moderately high yields ranging from 70% to 90%.[24,25,29] The syntheses of Ni(II) complexes with these ligands likewise proceed smoothly,

and crystalline samples of both [Ni(H_2qp1)(MeCN)](OTf)$_2$ (**1**) and [Ni(H_4qp2)(MeCN)$_2$](OTf)$_2$ (**2**) can be obtained in yields exceeding 40%.

In the crystal structures of [Mn(H_4qp2)Br$_2$], [Zn(H_2qp1)(OTf)](OTf), and [Zn(H_2qp1)(MeCN)](OTf)$_2$ which were obtained from MeCN/ether solutions, the protonated quinols do not bind to the metal center.[24,29] In the structures of **1** and **2**, the quinolic portions of the ligands likewise do not coordinate to the Ni(II) (Figure 3.1). With the aforementioned Mn(II) and Zn(II) complexes, however, the solid-state structures do not appear to be maintained in water.[24,29] UV/vis measurements show that at pH 7.0, a quinol from each complex has deprotonated to a quinolate, which serves as a better ligand for cationic metal centers. The pK_a values obtained from potentiometric pH titrations range from 5.8-7.1; these are more consistent with M(II)-phenol complexes than free phenols. [9,51,52] The pH titration data for **1** and **2** likewise demonstrate that a quinol from each ligand has deprotonated at pH 7.0. Given that Ni(II) ions are rarely more than six-coordinate,[53,54] the major aqueous cations at this pH are likely [Ni(Hqp1)]$^+$ and [Ni(H_3qp2)]$^+$, although the second quinol in the H_3qp$^-$ complex interacts weakly with the metal center and could be displaced by water to yield [Ni(H_3qp2)(H_2O)]$^+$.

Although there is a class of SODs that naturally contain nickel, neither **1** nor **2** resemble these either structurally or spectroscopically. Nickel- containing SODs cycle between five-coordinate Ni(III) and four-coordinate Ni(II) species.[62] The coordination spheres of the enzymes include two cysteinate, an amidate backbone and a N-terminal amine, with an imidazole ligand completing the coordination of the Ni(III) form. Instead of an S_2N_3 or S_2N_2 coordination sphere, **1** and **2** have N_5O and N_4O_2, respectively.

Despite their lack of resemblance to the active sites in nickel SODs, both **1** and **2** are functional mimics of these enzymes. Complexes **1** and **2** are highly capable antioxidants as assessed

by both assays and stopped-flow kinetics analysis of the direct reactions between the Ni(II) complexes and KO_2. The SOD mimicry exhibited by **1** and **2** is noteworthy since nickel has rarely supported this sort of reactivity in small molecule complexes. Complexes with short peptide chains, or maquettes, have been able to reproduce many of the spectroscopic features of nickel-containing SODs and much of the reactivity,[63-65] but we were able to locate only one instance where a nickel complex with a non-peptide-derived ligand acted as a functional mimic.[66] This mimic made use of a tripodal trithiolate ligand and had a $k_{cat} = 1.8 \times 10^5$ M^{-1} s^{-1} in 60 mM HEPES solution buffered to pH 7.75. Complexes **1** and **2** are approximately 70 and 540 times more active, respectively, under similar conditions (Table 3.3) with the caveat that we use MOPS instead of HEPES.

That **1** and **2** catalyze superoxide disproportionation at rates that rival those found for the best nickel-maquette species is a significant development since there are substantial obstacles for developing the latter into pharmaceuticals. Peptide-based therapeutics tend to be metabolized quickly within the body and display a limited ability to traverse epithelial barriers.[67] Further, peptide synthesis is generally inefficient and often requires extensive labor and chemical resources in order to obtain sufficient amounts of the products.[68]

The activities of the nickel complexes, particularly that of **2**, compare well to those of manganese-containing SOD mimics.[15,18,20,40,69-72] The k_{cat} measured for **2** in pH 7.4 MOPS buffer exceeds the 9.7×10^7 M^{-1} s^{-1} value measured for $[Mn(H_2qp1)(MeCN)]^{2+}$ in pH 7.4 HEPES.[28] The cationic porphyrin complex $MnBr_8TM\text{-}4\text{-}PyP^{4+}$ may be faster, but the k_{cat} of 21.9×10^7 M^{-1} s^{-1} was measured through an assay rather than stopped-flow kinetics.[73] The manganese- pentaazamacrocycle M40401 is unambiguously more active, with a $k_{cat} = 1.5 \times 10^9$ M^{-1} s^{-1} in pH 7.4 HMES buffer,[74,75] but is markedly less stable in water than both $[Mn(H_2qp1)(MeCN)]^{2+}$ and **2**.[28]

Another notable feature about the catalysis performed by both **1** and **2** is that they only lose

about 50% of their activity upon switching from a sulfonic acid-based buffer to phosphate buffer (Table 3.3). Most manganese complexes, conversely, lose 75% or more of their activity upon such a switch,[28,38,40,76] and the rare examples that retain most of their activity, such as [Mn(H_4qp2)Br_2], tend to be poorer catalysts under all conditions.[28,38] The Zn(II) complex with H_2qp1, [Zn(H_2qp1)(OTf)]$^+$, conversely, displays enhanced SOD mimicry in phosphate buffer.[29] Phosphate is generally believed to inhibit activity by acting as a competitive inhibitor that blocks the coordination of superoxide to the metal center. The lack of phosphate inhibition seen for the Zn(II) complex was attributed to the smaller size of this metal ion relative to Mn(II). The combination of relatively small metal ion and a sterically bulky ligand disfavors the coordination of bulky phosphate ions. With respect to its size, Ni(II) is slightly smaller than Zn(II),[43] and it is not immediately apparent why phosphate inhibition is still seen, albeit to a smaller extent than for most manganese complexes.

That **2** is more catalytically active than **1** is initially surprising since the Mn(II) complex with H_4qp2 is much less active than the one with H_2qp1 in HEPES solution (although the catalysts are approximately equivalent in phosphate buffer).[28] With Mn(II), the ligands fully deprotonate to Hqp1$^-$ and H_2qp2^{2-}, rendering their complexes monocationic and neutral, respectively. Higher positive charges on SOD mimics tends to lead to faster catalysis, explaining the higher k_{cat} for the H_2qp1 complex. With Ni(II), conversely, the H_4qp2 does not fully deprotonate, and **1** and **2** both form predominantly monocationic species in water between pH 7 and 7.8. Unless they are deprotonated, quinols have tended to be poor ligands for metal center, as seen in Figure 3.1.[29] We speculate that the second quinol in **2** can be more readily displaced from the metal center by $O_2^{\cdot-}$, enabling more ready access and faster SOD mimicry.

The mechanism of superoxide dismutation, like that observed for the manganese complexes

with H_2qp1 and H_4qp2, involves changes to the oxidation states of both the ligands and the metal center.[28] The quinols within the ligand oxidize to *para*-quinones, as evidenced by MS. The oxidation of the nickel is confirmed by EPR (Figure 3.3). Notably, Ni(III) has been found to be capable of directly oxidizing quinols.[77]

3.5 Conclusions

We find that polydentate ligands with redox-active quinols can enable nickel to catalytically degrade superoxide at rates that are highly competitive with those of the most active reported manganese-containing SOD mimics. Although phosphate can inhibit the catalysis, this effect is not as severe as seen for other highly active antioxidants. The ligand design has a noticeable impact on the reactivity. The complex with a second quinol is much more active, which we attribute to the superoxide being better able to access the metal center. The catalysis involves both ligand- and metal-centered redox cycles.

Appendix B

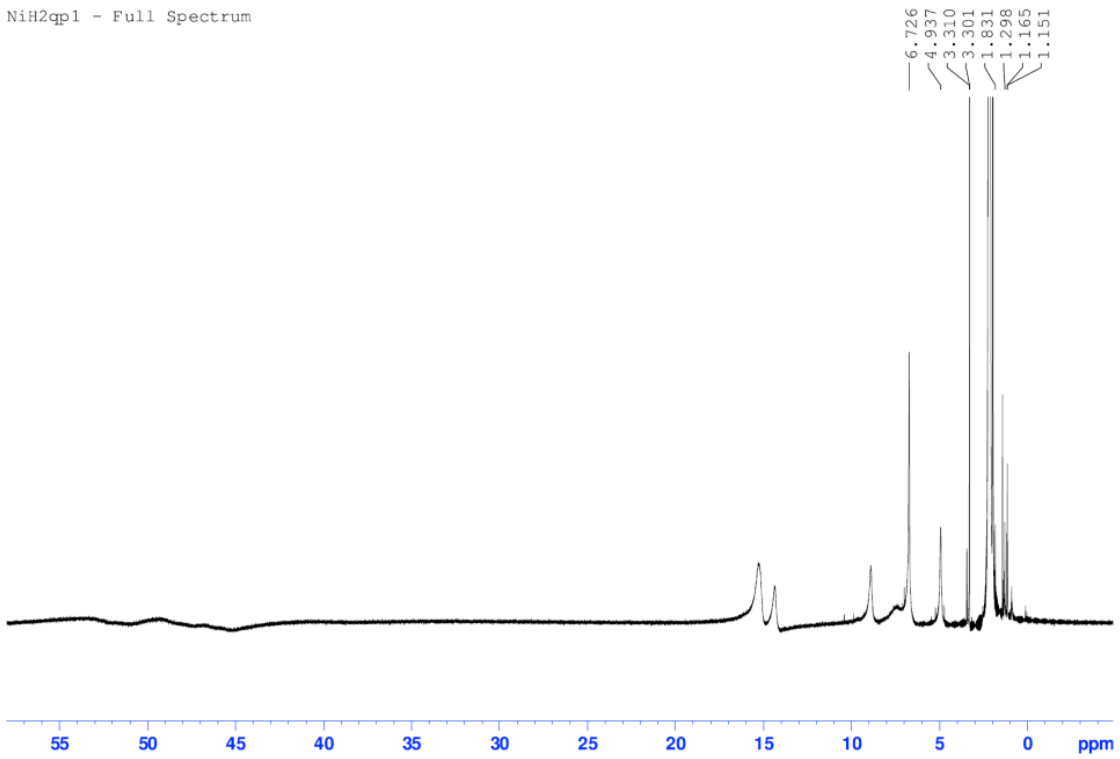

Figure B1. ^{1}H NMR data (500 mHz, 294 K) for a sample of **1** in CD_3CN. The feature at 6.7 ppm vanishes when D_2O is added to the sample, suggesting that it results from the O-H resonances.

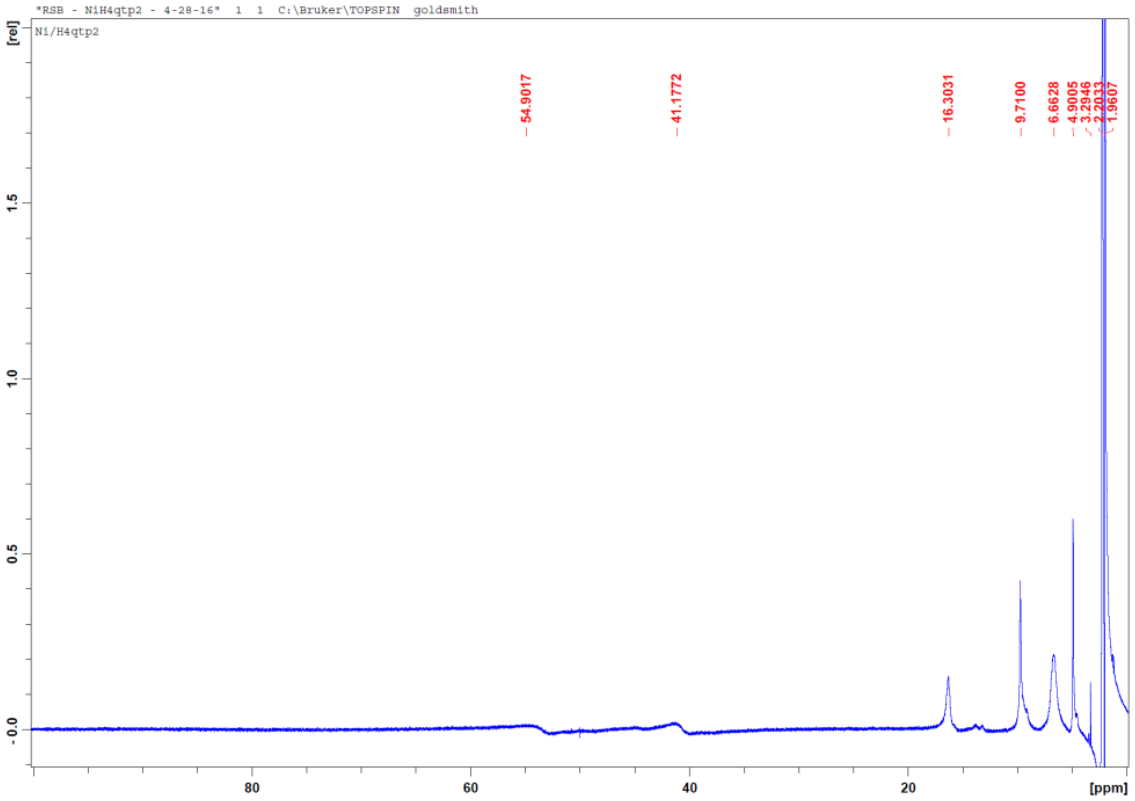

Figure B2. ^{1}H NMR data (400 mHz, 294 K) for a sample of **2** in CD_3CN. The feature at 6.7 ppm vanishes when D_2O is added to the sample, suggesting that it results from the O-H resonances.

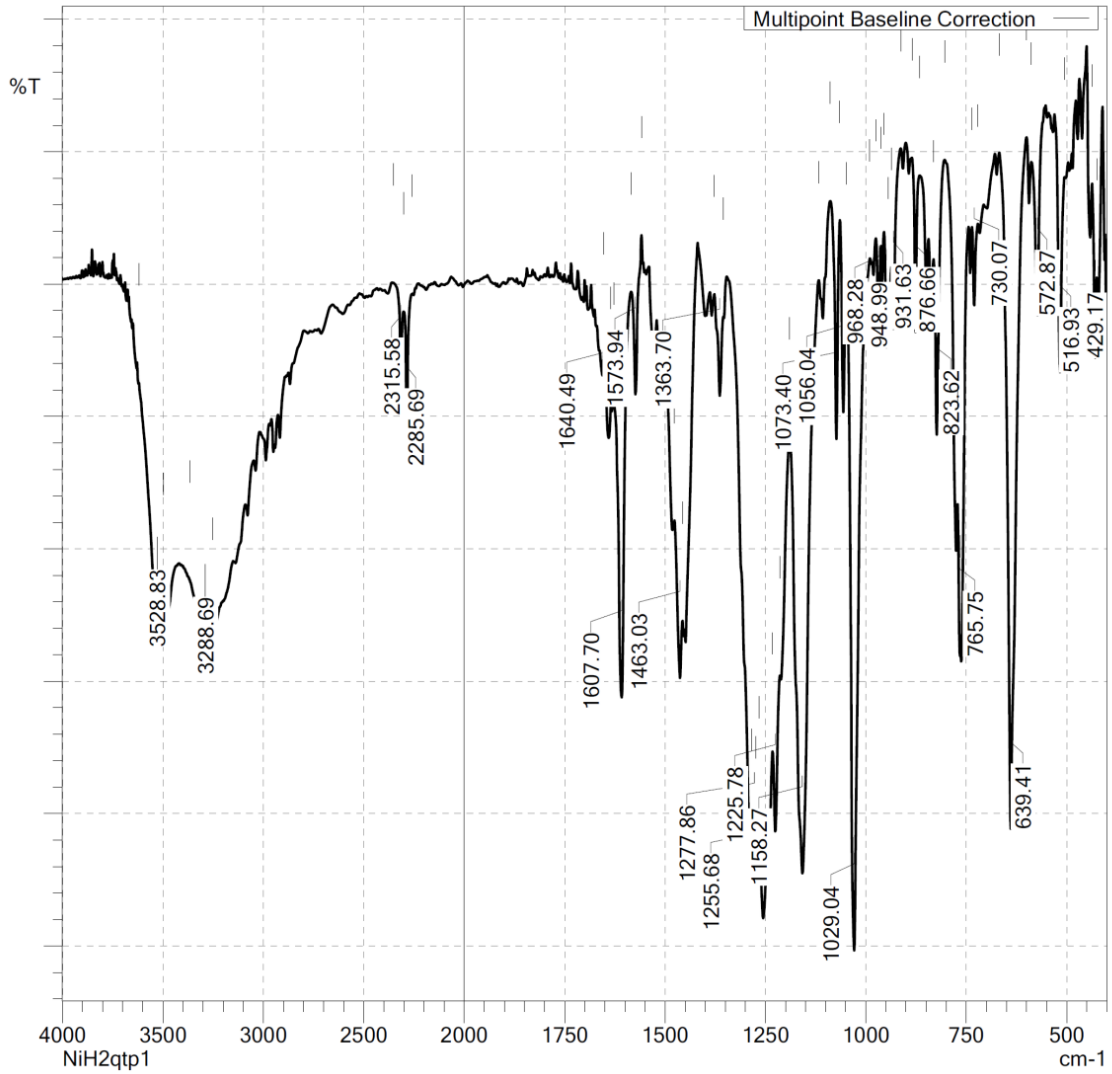

Figure B3. IR data (KBr) for [Ni(H_2qp1)(MeCN)](OTf)$_2$ (**1**).

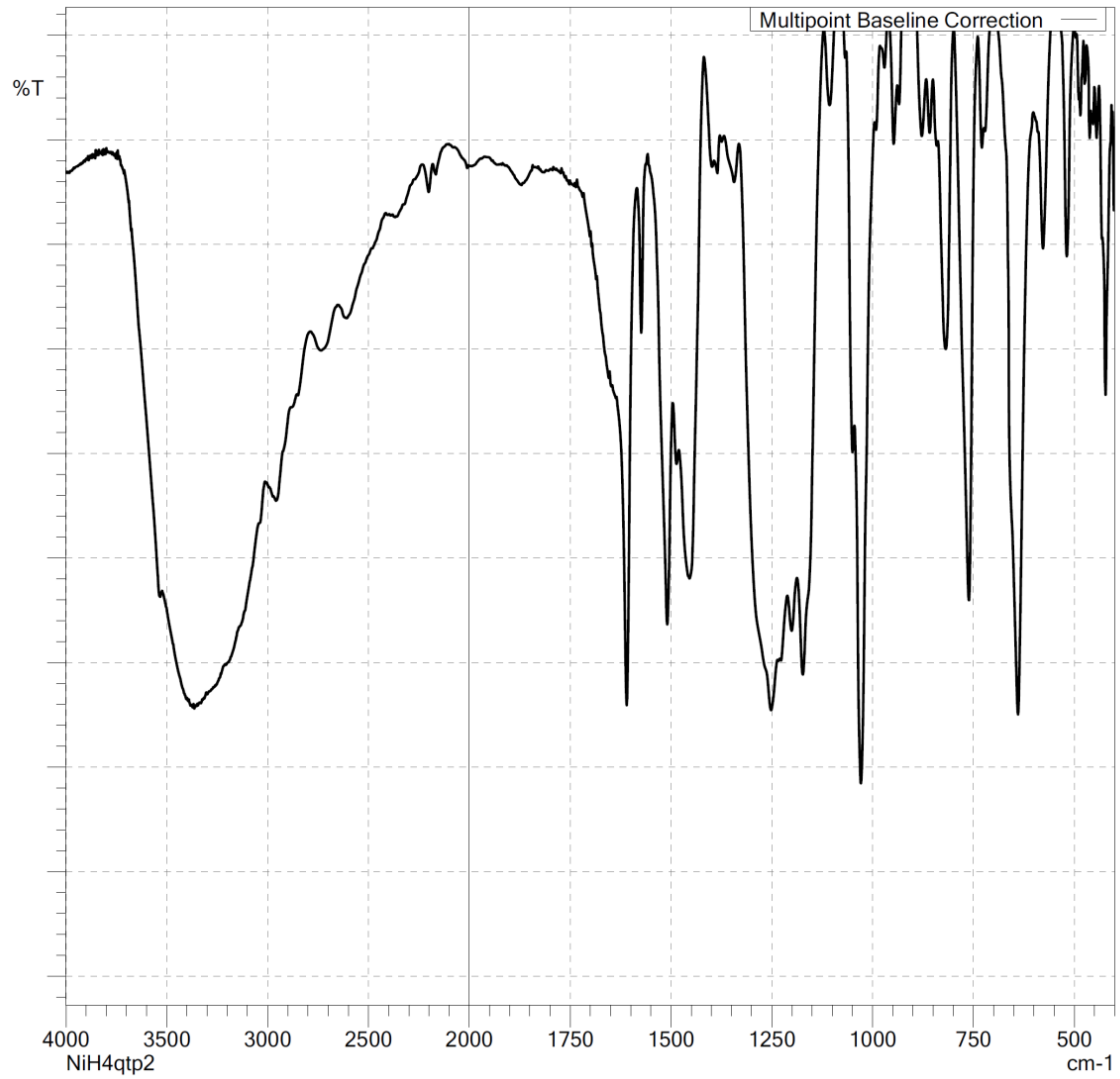

Figure B4. IR data (KBr) for $[Ni(H_4qp2)(MeCN)_2](OTf)_2$ (**2**).

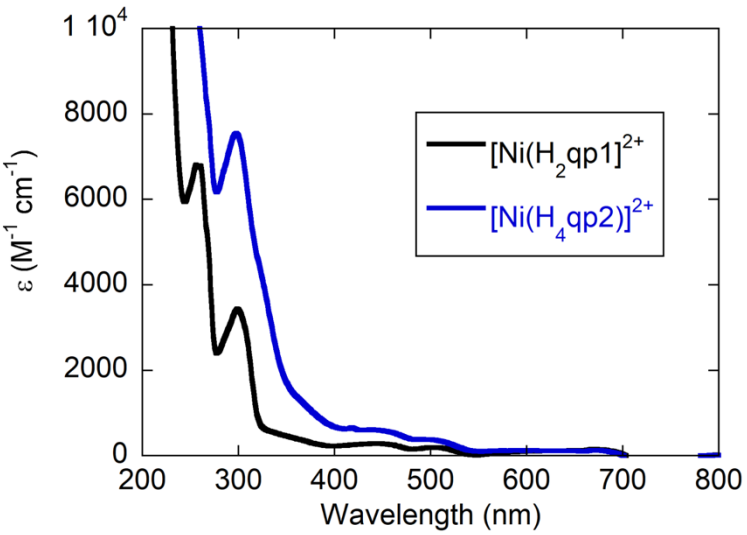

Figure B5. UV/vis data for **1** and **2**. The data for **1** were acquired for a 0.1 mM solution of the Ni(II) complex in MeOH whereas those for **2** were obtained using a 0.1 mM solution of the complex in MeCN. Both sets of data were obtained at 298 K using a 1.0 cm quartz cuvette. Observed peaks:

1 - 255 nm (6810 M^{-1} cm^{-1}), 299 nm (3430 M^{-1} cm^{-1}), 453 nm (273 M^{-1} cm^{-1}), and 513 nm (175 M^{-1} cm^{-1})

2 - 298 nm (7750 M^{-1} cm^{-1}), 449 nm (589 M^{-1} cm^{-1}), and 516 nm (306 M^{-1} cm^{-1})

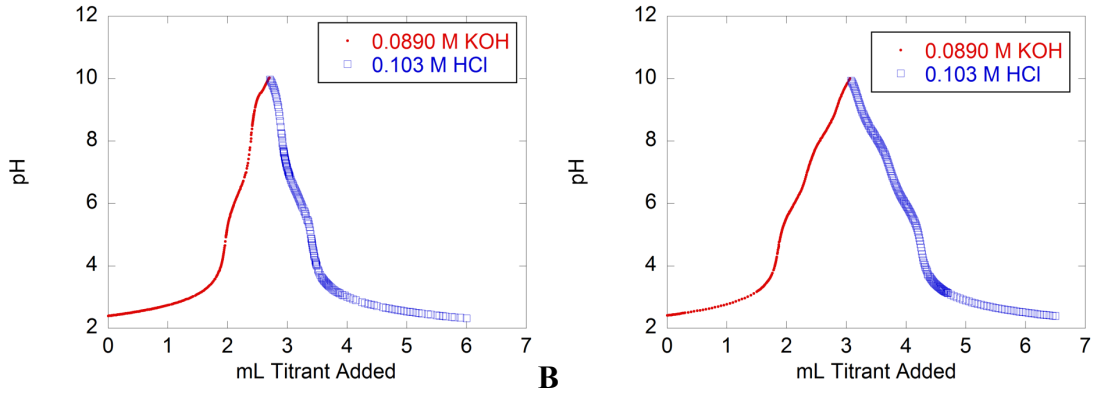

Figure B6. Potentiometric pH titration data for A) **1** and B) **2** in aqueous 100 mM KCl solutions. For the analysis of **1**, 0.10 mmol of H_2qtp1 and Ni(OTf)$_2$ were added to 48 mL of the KCl solution. 2.0 mL of 0.1018 M HCl was added to make the solution acidic, and the resultant mixture was subsequently titrated with 0.1008 M KOH (red data points). After 2.700 mL of KOH solution were added, the mixture was titrated with 0.1018 M HCl (blue data points). For the analysis of **2**, 0.10 mmol of H_4qtp2 and Ni(OTf)$_2$ were added to 50 mL of the KCl solution. 2.0 mL of 0.1018 M HCl was added to make the solution acidic, and the resultant mixture was subsequently titrated with 0.1008 M KOH (red data points). After 3.060 mL of KOH solution were added, the mixture was titrated with 0.1018 M HCl (blue data points). Analyses of the data confirm a pK_a value of 6.33 (±0.05) for **1** and pK_a values of 5.99 (±0.05) and 8.24 (±0.05) for **2**.

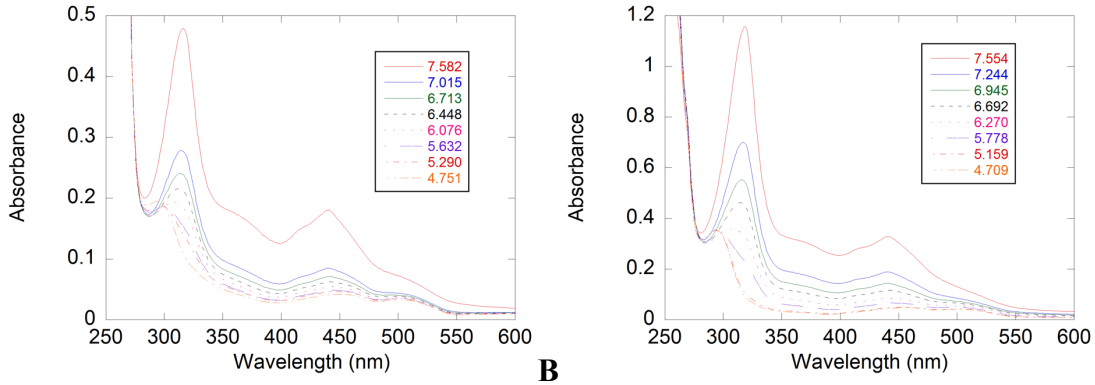

Figure B7. Spectrophotometric pH titration data for A) **1** and B) **2** in aqueous solutions. The data were acquired at 294 K with a 1.0 cm pathlength. The concentrations of Ni(II) and ligand in each sample were 0.10 mM. The pH was controlled through the addition of KOH and HCl. The peaks at 313 nm correspond to deprotonated quinols, whereas the peaks at 293-294 nm correspond to protonated quinols.

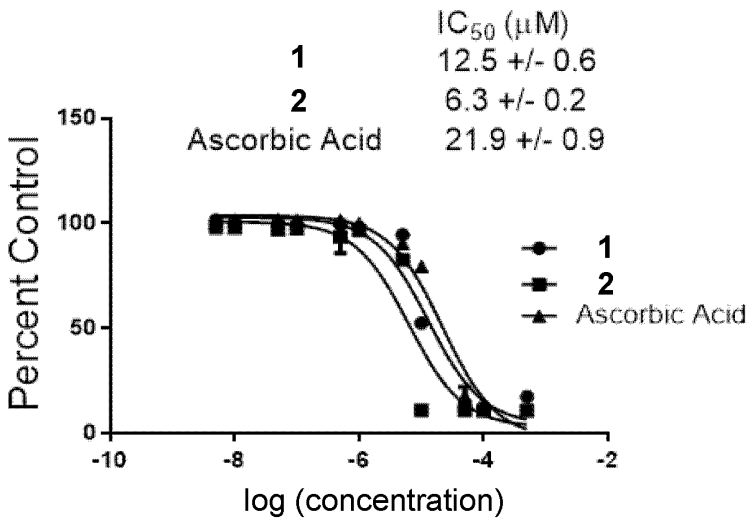

Figure B8. DPPH free radical scavenging assay of **1**, **2**, and ascorbic acid. The antioxidants were added to a DPPH solution and incubated in the dark for 30 min at 298 K. Spectroscopic measurements were performed at 517 nm. The data were normalized to the absorbance in the presence of vehicle. All experiments were performed in triplicate and repeated twice.

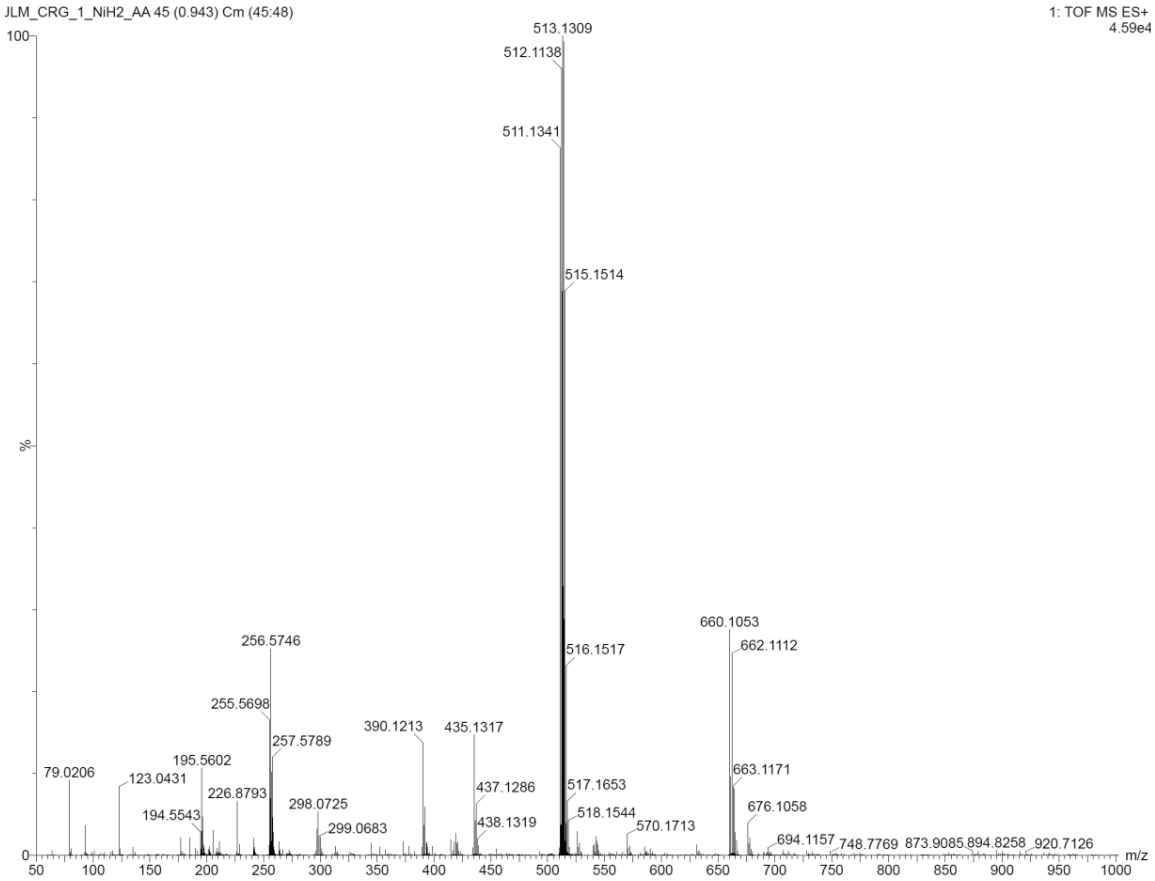

Figure B9. Mass spectrometry (ESI) of the products of the reaction between 0.10 mM **1** and 0.10 mM KO_2 in water containing 10 mM acetate buffered to pH 7.0. The reaction was allowed to proceed for 30 s. The following *m/z* features were assigned to oxidation products:

660.1053: $[Ni(qp1)(OTf)]^+$ (calculated *m/z* = 660.1044)

511.1341: $[Ni(qp1)]^+$ (calculated *m/z* = 511.1518)

390.1213: $[Ni(H_2qp1\text{-quinol-H})]^+$ (calculated *m/z* = 390.1229)

255.5698: $[Ni(qp1)]^{2+}$ (calculated *m/z* = 255.5671)

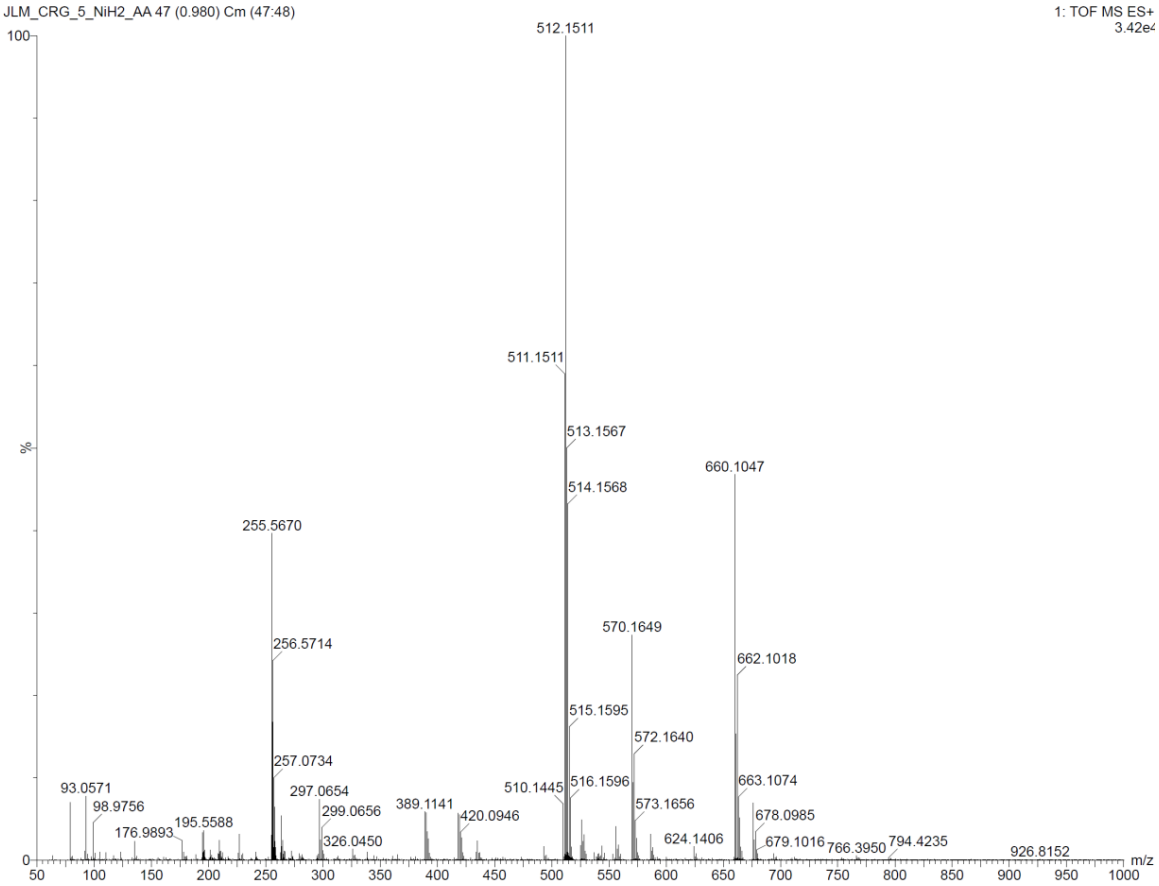

Figure B10. Mass spectrometry (ESI) of the products of the reaction between 0.10 mM **1** and 0.50 mM KO_2 in water containing 10 mM acetate buffered to pH 7.0. The reaction was allowed to proceed for 30 s. The following *m/z* features were assigned to oxidation products:

660.1047: $[Ni(qp1)(OTf)]^+$ (calculated *m/z* = 660.1044)
570.1649: $[Ni(qp1)(OAc)]^+$ (calculated *m/z* = 570.1657)
511.1511: $[Ni(qp1)]^+$ (calculated *m/z* = 511.1518)
420.0946: $[Ni(qp1\text{-picolyl})]^+$ (calculated *m/z* = 420.1096)
389.1141: $[Ni(H_2qp1\text{-quinol-2H})]^+$ (calculated *m/z* = 389.1151)
255.5670: $[Ni(qp1)]^{2+}$ (calculated *m/z* = 255.5671)

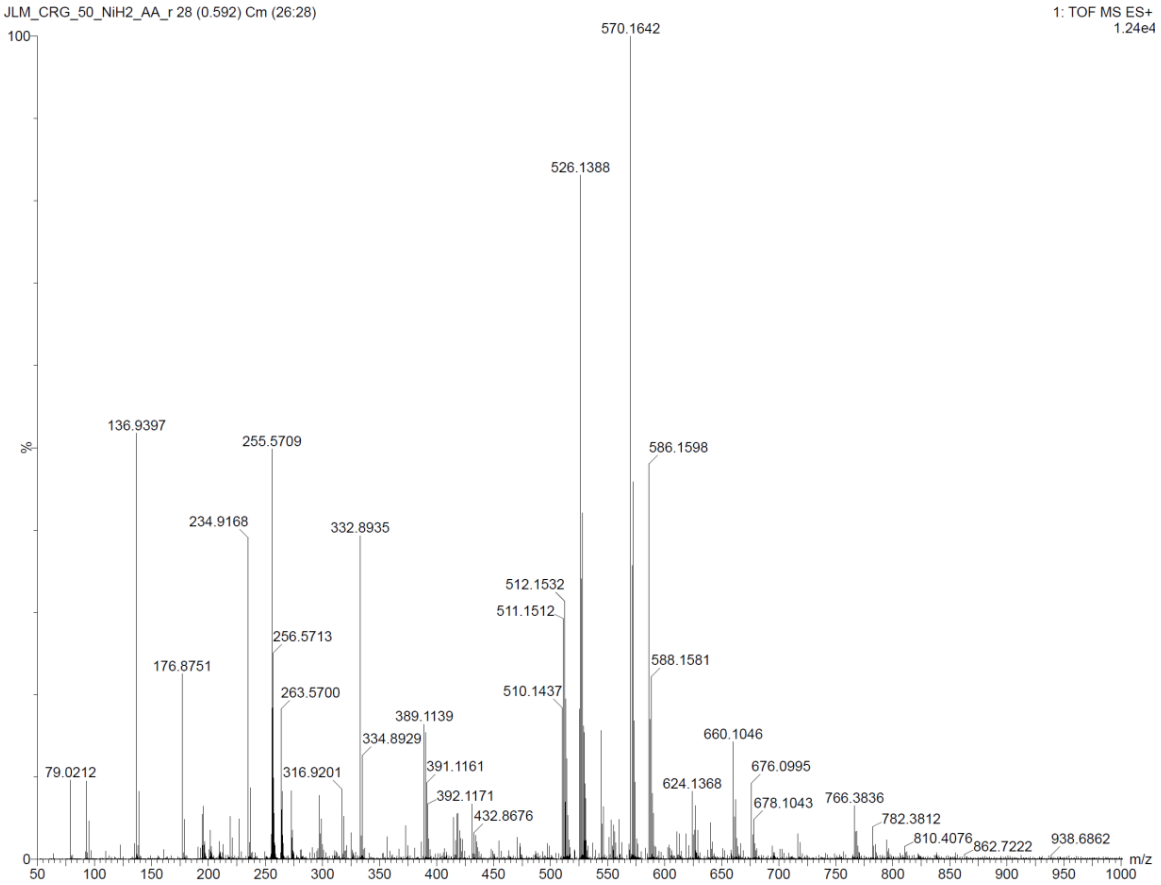

Figure B11. Mass spectrometry (ESI) of the products of the reaction between 0.10 mM **1** and 5.0 mM KO_2 in water containing 10 mM acetate buffered to pH 7.0. The reaction was allowed to proceed for 30 s. The following *m/z* features were assigned to oxidation products:

660.1046: $[Ni(qp1)(OTf)]^+$ (calculated *m/z* = 660.1044)
586.1598: $[Ni(qp1+O)(OAc)]^+$ (calculated *m/z* = 586.1601)
570.1642: $[Ni(qp1)(OAc)]^+$ (calculated *m/z* = 570.1657)
526.1388: $[Ni(qp1-H+O)]^+$ (calculated *m/z* = 526.1389)
511.1512: $[Ni(qp1)]^+$ (calculated *m/z* = 511.1518)
389.1139: $[Ni(H_2qp1\text{-quinol-}2H)]^+$ (calculated *m/z* = 389.1151)
255.5709: $[Ni(qp1)]^{2+}$ (calculated *m/z* = 255.5671)

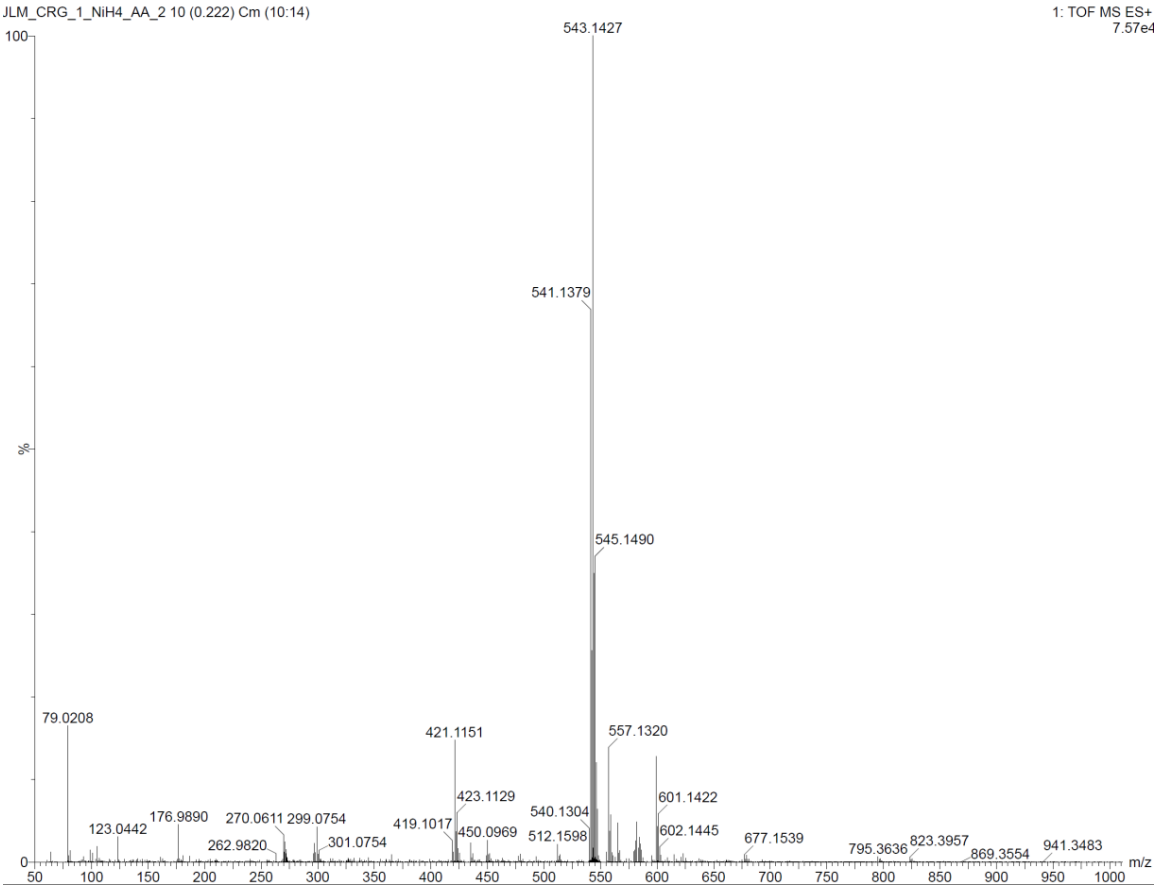

Figure B12. Mass spectrometry (ESI) of the products of the reaction between 0.10 mM **2** and 0.10 mM KO_2 in water containing 10 mM acetate buffered to pH 7.0. The reaction was allowed to proceed for 30 s. The following *m/z* features were assigned to oxidation products:

601.1422: $[Ni(H_2qp2)(OAc)]^+$ (calculated *m/z* = 601.1598)
557.1320: $[Ni(Hqp2+O)]^+$ (calculated *m/z* = 557.1335)
541.1379: $[Ni(Hqp2)]^+$ (calculated *m/z* = 541.1386)
540.1304: $[Ni(qp2)]^+$ (calculated *m/z* = 540.1308)
450.0969: $[Ni(Hqp2\text{-picolyl})]^+$ (calculated *m/z* = 450.0964)
421.1151: $[Ni(H_3qp2\text{-quinol})]^+$ (calculated *m/z* = 421.1175)
270.0611: $[Ni(qp2)]^{2+}$ (calculated *m/z* = 270.0653)

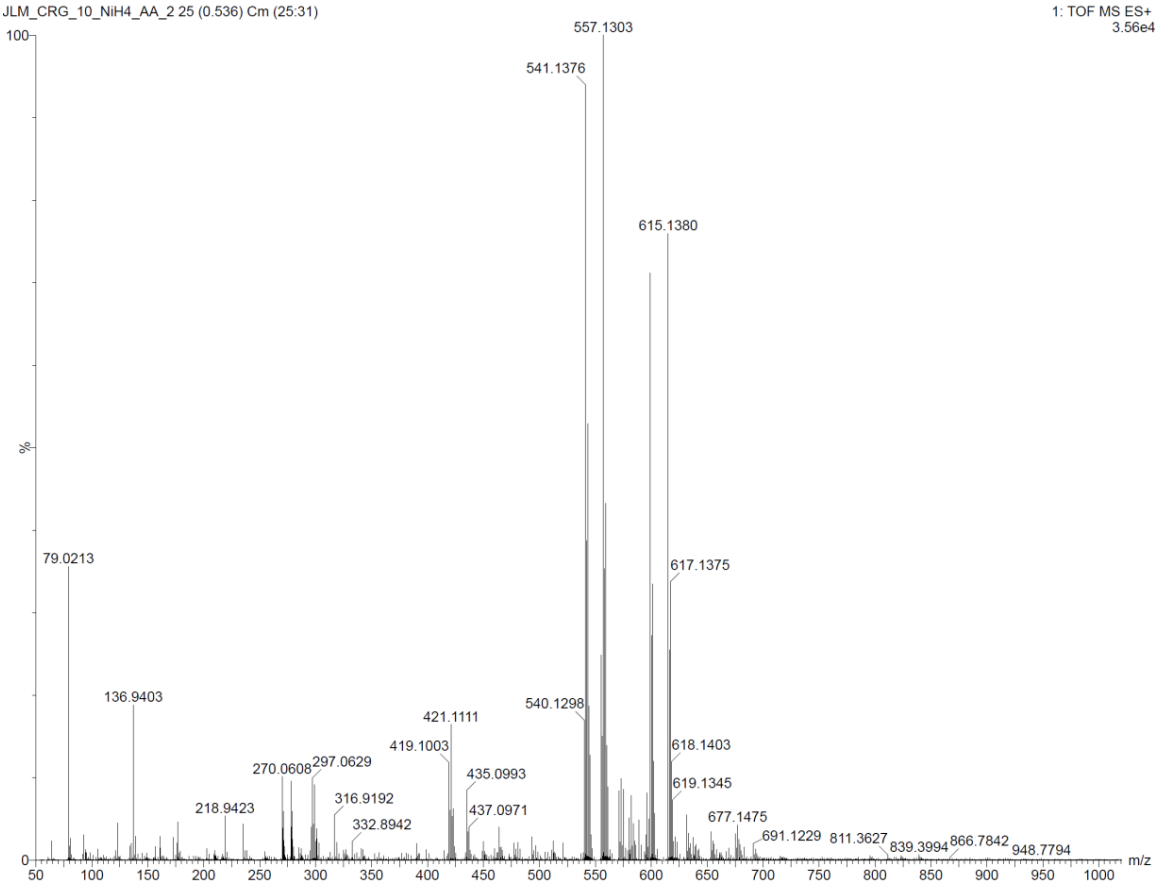

Figure B13. Mass spectrometry (ESI) of the products of the reaction between 0.10 mM **2** and 1.0 mM KO_2 in water containing 10 mM acetate buffered to pH 7.0. The reaction was allowed to proceed for 30 s. The following *m/z* features were assigned to oxidation products:

615.1380: $[Ni(Hqp2\text{-}H+O)(OAc)]^+$ (calculated *m/z* = 615.1390)
557.1303: $[Ni(Hqp2+O)]^+$ (calculated *m/z* = 557.1335)
541.1376: $[Ni(Hqp2)]^+$ (calculated *m/z* = 541.1386)
540.1298: $[Ni(qp2)]^+$ (calculated *m/z* = 540.1308)
421.1111: $[Ni(H_3qp2\text{-quinol})]^+$ (calculated *m/z* = 421.1175)
419.1003: $[Ni(qp2\text{-quinol-H})]^+$ (calculated *m/z* =419.1018)
270.0608: $[Ni(qp2)]^{2+}$ (calculated *m/z* = 270.0653)

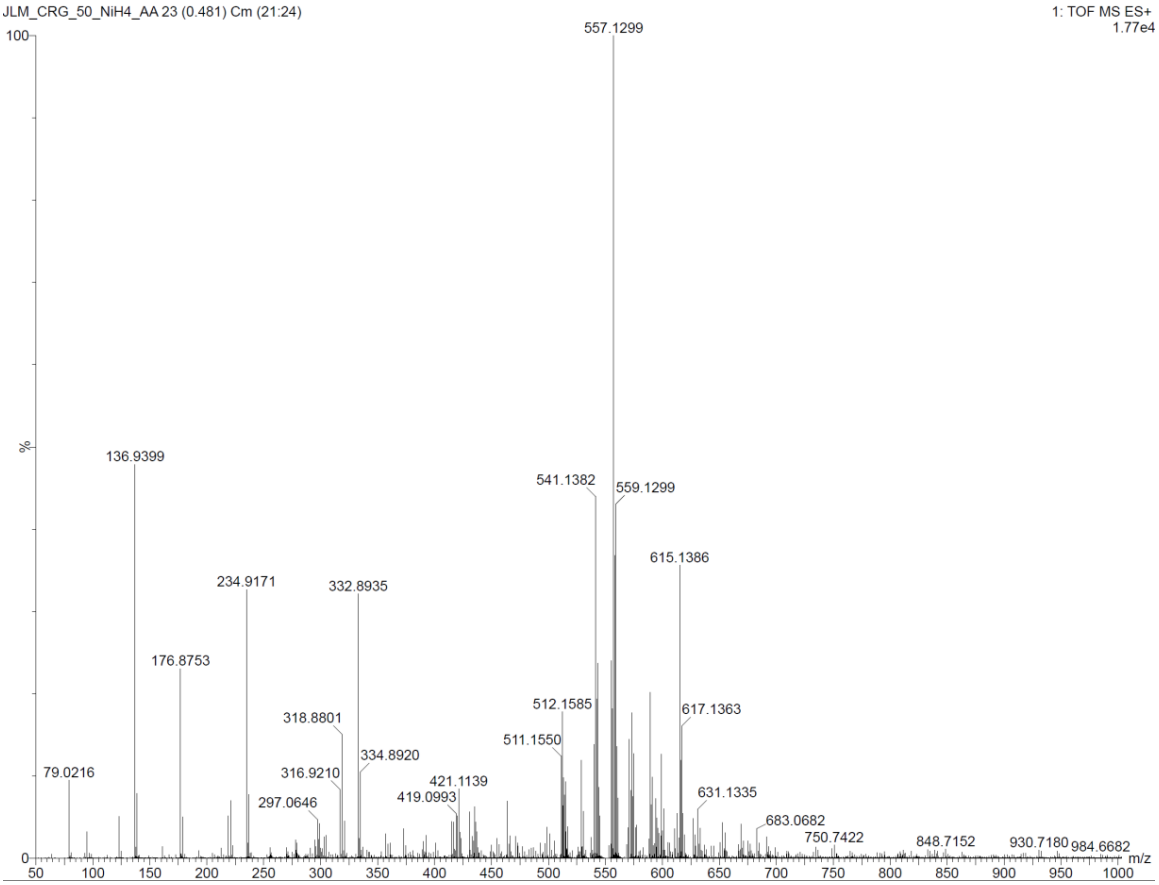

Figure B14. Mass spectrometry (ESI) of the products of the reaction between 0.10 mM **2** and 5.0 mM KO_2 in water containing 10 mM acetate buffered to pH 7.0. The reaction was allowed to proceed for 30 s. The following *m/z* features were assigned to oxidation products:

615.1386: $[Ni(Hqp2\text{-}H+O)(OAc)]^+$ (calculated *m/z* = 615.1390)
557.1299: $[Ni(Hqp2+O)]^+$ (calculated *m/z* = 557.1335)
541.1382: $[Ni(Hqp2)]^+$ (calculated *m/z* = 541.1386)
421.1139: $[Ni(H_3qp2\text{-quinol})]^+$ (calculated *m/z* = 421.1175)
419.0993: $[Ni(qp2\text{-quinol-H})]^+$ (calculated *m/z* =419.1018)

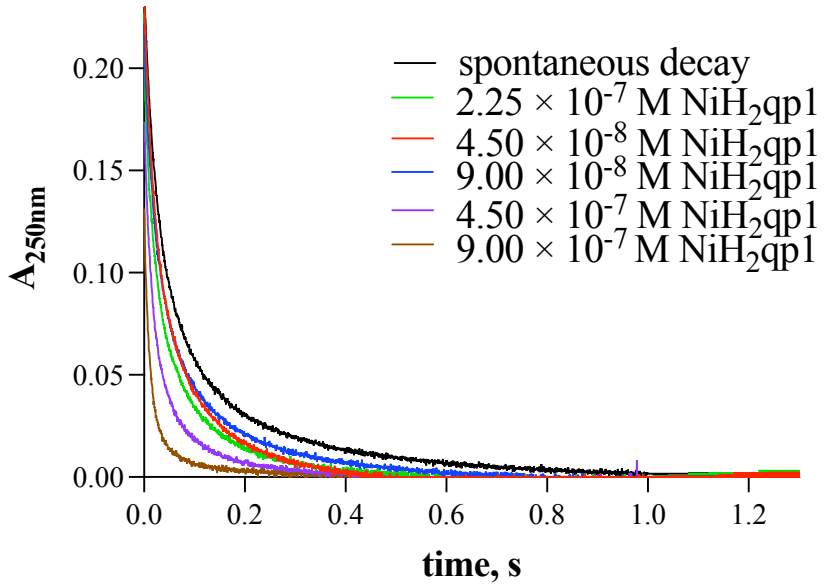

Figure B15. Kinetic traces of superoxide decomposition at 250 nm (60 mM MOPS buffer, pH 7.8 ionic strength of 150 mM) by **1**.

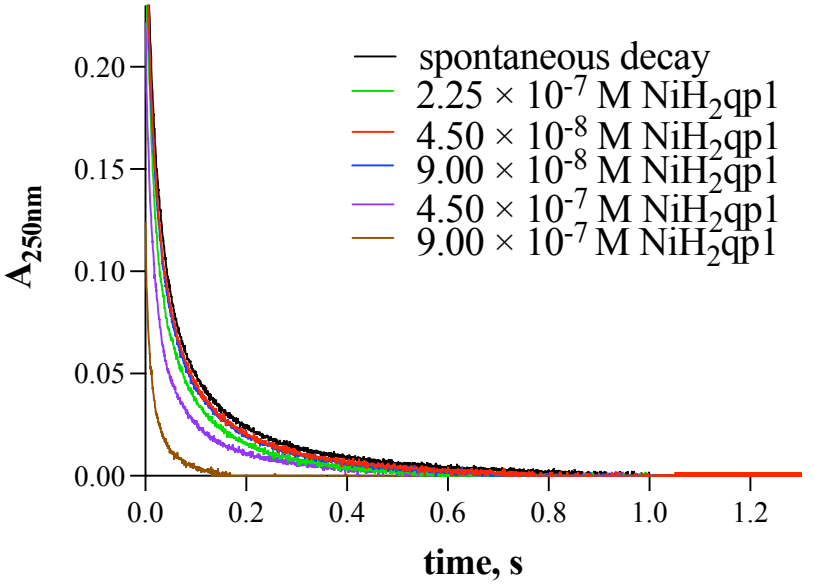

Figure B16. Kinetic traces of superoxide decomposition at 250 nm (50 mM phosphate buffer, pH 7.4 ionic strength of 150 mM) by **1**.

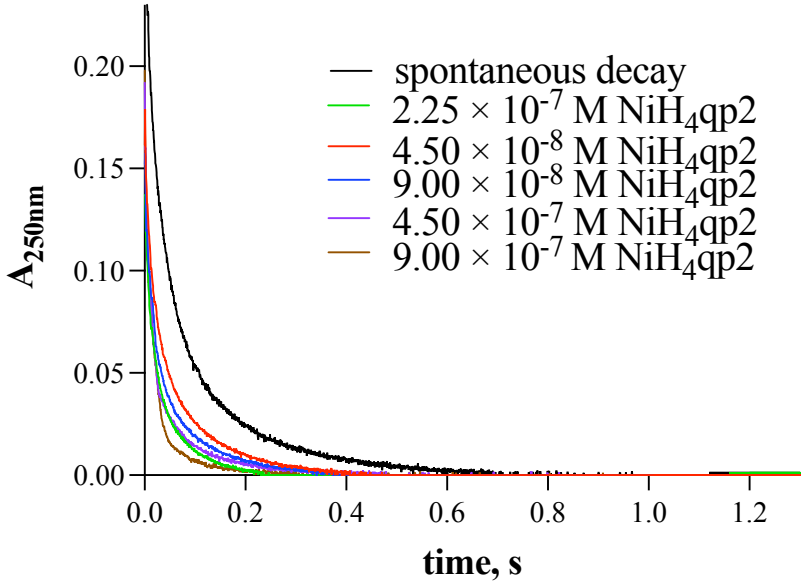

Figure B17. Kinetic traces of superoxide decomposition at 250 nm (60 mM MOPS buffer, pH 7.8 ionic strength of 150 mM) by **2**.

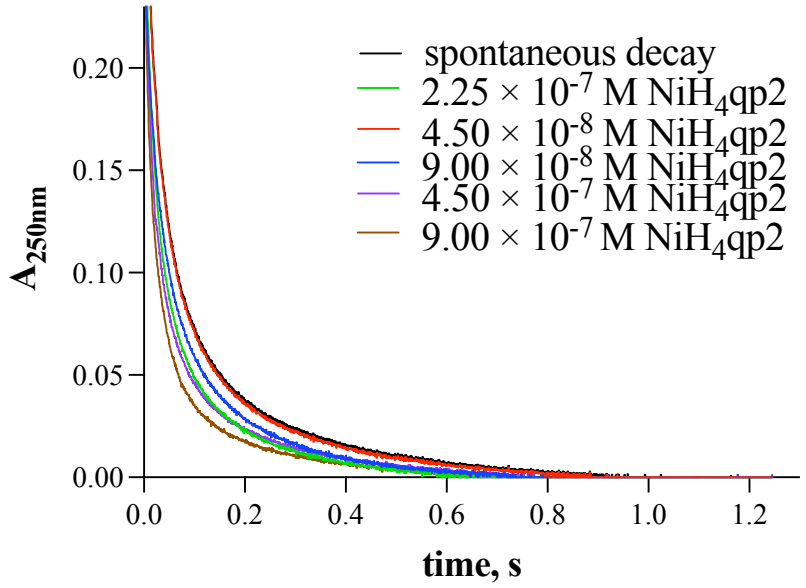

Figure B18. Kinetic traces of superoxide decomposition at 250 nm (50 mM phosphate buffer, pH 7.4 ionic strength of 150 mM) by **2**.

References

(1) Ahmed, M. I.; Gladden, J. D.*; et al. Journal of the American College of Cardiology* **2010**, *55*, 671.

(2) Fearon, I. M.; Faux, S. P. *Journal of Molecular and Cellular Cardiology* **2009**, *47*, 372.

(3) Eskici, G. z.; Axelsen, P. H. *Biochemistry* **2012**, *51*, 6289.

(4) Kinnula, V. L. *Current Drug Targets Inflammation & Allergy* **2005**, *4*, 465.

(5) AbdulSalam, S. F.; Thowfeik, F. S.*; et al. Biochemistry* **2016**, *55*, 5341.

(6) Do, Q. N.; Ratnakar, J. S.*; et al. ChemMedChem* **2014**, *9*, 1116.

(7) Lou, Z.; Li, P.*; et al. Accounts of Chemical Research* **2015**, *48*, 1358.

(8) Loving, G. S.; Mukherjee, S.*; et al. Journal of the American Chemical Society* **2013**, *135*, 4620.

(9) Gale, E. M.; Mukherjee, S.*; et al. Inorganic Chemistry* **2014**, *53*, 10748.

(10) Gale, E. M.; Jones, C. M.*; et al. Journal of the American Chemical Society* **2016**, *138*, 15861.

(11) Song, B.; Wu, Y.*; et al. Dalton Transactions* **2013**, *42*, 8066.

(12) Ratnakar, S. J.; Viswanathan, S.*; et al. Journal of the American Chemical Society* **2012**, *134*, 5798.

(13) Tsitovich, P. B.; Spernyak, J. A.*; et al. Angewandte Chemie* **2013**, *125*, 14247.

(14) Tsitovich, P. B.; Burns, P. J.*; et al. Journal of Inorganic Biochemistry* **2014**, *133*, 143.

(15) Riley, D. P.; Weiss, R. H. *Journal of the American Chemical Society* **1994**, *116*, 387.

(16) Riley, D. P.; Schall, O. F. *Adv. Inorganic Chemistry* **2006**, *59*, 233.

(17) Riley, D. P.; Lennon, P. J.*; et al. Journal of the American Chemical Society* **1997**, *119*, 6522.

(18) Riley, D. P. *Chemical Reviews* **1999**, *99*, 2573.

(19) Tovmasyan, A.; Carballal, S.*; et al. Inorganic Chemistry* **2014**, *53*, 11467.

(20) Batinić-Haberle, I.; Rebouças, J. S.*; et al. Antioxidants & Redox Signaling* **2010**, *13*, 877.

(21) Batinic-Haberle, I.; Rajic, Z.*; et al. Free Radical Biology and Medicine* **2011**, *51*, 1035.

(22) Abreu, I. A.; Cabelli, D. E. *Biochimica et Biophysica Acta* **2010**, *1804*, 263.

(23) Yu, M.; Beyers, R. J.*; et al. Inorganic Chemistry* **2012**, *51*, 9153.

(24) Yu, M.; Ward, M. B.*; et al. Inorganic Chemistry* **2017**, *56*, 2812.

(25) Yu, M.; Ambrose, S. L.*; et al. Journal of the American Chemical Society* **2014**, *136*, 12836.

(26) Iranzo, O. *Bioorganic Chemistry* **2011**, *39*, 73.

(27) McCord, J. M.; Fridovich, I. *Journal of Biological Chemistry* **1969**, *244*, 6049.

(28) Senft, L.; Moore, J. L.*; et al. Chemical Science* **2021**, *12*, 10483.

(29) Ward, M. B.; Scheitler, A.*; et al. Nature Chemistry* **2018**, *10*, 1207.

(30) Martell, A. E.; Smith, R. M. *Critical Stability Constants*; Springer, 1974; Vol. 1.

(31) Irving, H.; Williams, R. *Journal of the Chemical Society (Resumed)* **1953**, 3192.

(32) Chen, P.; Chakraborty, S.*; et al. Journal of Neurochemistry* **2015**, *134*, 601.

(33) Drahoš, B.; Kotek, J.*; et al. Inorganic Chemistry* **2010**, *49*, 3224.

(34) Aitken, J. B.; Shearer, E. L.*; et al. Inorganic Chemistry* **2013**, *52*, 4121.

(35) Van Zijl, P. C.; Yadav, N. N. *Magnetic Resonance in Medicine* **2011**, *65*, 927.

(36) Zhang, S.; Merritt, M.*; et al. Accounts of Chemical Research* **2003**, *36*, 783.

(37) Moore, J. L.; Scheitler, A.*; et al. Thesis Work Chapter 4* **2022**.

(38) Friedel, F. C.; Lieb, D.*; et al. Journal of Inorganic Biochemistry* **2012**, *109*, 26.

(39) Lieb, D.; Friedel, F. C.*; et al. Inorganic Chemistry* **2013**, *52*, 222.

(40) Kenkel, I.; Franke, A.*; et al. Journal of the American Chemical Society* **2017**, *139*, 1472.

(41) Bergwitz, C.; Jüppner, H. *Advances in Chronic Kidney Disease* **2011**, *18*, 132.

(42) Bevington, A.; Mundy, K. I.*; et al. Clinical Science* **1986**, *71*, 729.

(43) Shannon, R. D. *Acta Crystallographica Section A: Crystal Physics, Diffraction, Theoretical and General Crystallography* **1976**, *32*, 751.

(44) Gans, P.; Sabatini, A.*; et al. Talanta* **1996**, *43*, 1739.

(45) Blois, M. S. *Nature* **1958**, *181*, 1199.

(46) Kedare, S. B.; Singh, R. *Journal of Food Science and Technology* **2011**, *48*, 412.

(47) Milaeva, E. R.; Shpakovsky, D. B.*; et al. Dalton Transactions* **2013**, *42*, 6817.

(48) Drago, R. S. *Physical Methods for Chemists*; 2 ed.; Surfside Scientific Publishers: Gainesville, FL, 1992.

(49) Chan, T.-L.; Mak, T. C. W. *Journal of the Chemical Society, Perkin Transactions 2* **1983**, 777.

(50) Quan, M.; Sanchez, D.*; et al. Journal of the American Chemical Society* **2007**, *129*, 12847.

(51) Sahoo, S. C.; Dubey, M.*; et al. Inorganica Chimica Acta* **2010**, *363*, 3055.

(52) Iitaka, Y.; Koike, T.*; et al. Inorganic Chemistry* **1986**, *25*, 402.

(53) Casanova, D.; Alemany, P.*; et al. Chemistry–A European Journal* **2003**, *9*, 1281.

(54) Cotton, F. A.; Wilkinson, G.; Wiley-Interscience, New York: 1988.

(55) Ancerewicz, J.; Migliavacca, E.*; et al. Free Radical Biology and Medicine* **1998**, *25*, 113.

(56) Fridovich, I. *Journal of Biological Chemistry* **1997**, *272*, 18515.

(57) Liochev, S. I. *Chemical Research in Toxicology* **2013**, *26*, 1312.

(58) Riley, D. P.; Rivers, W. J.*; et al. Analytical Biochemistry* **1991**, *196*, 344.

(59) Liochev, S. I.; Fridovich, I. *Archives Biochemistry and Biophysics* **1997**, *337*, 115.

(60) Kunert, R.; Philouze, C.*; et al. Inorganic Chemistry* **2019**, *58*, 8030.

(61) Manuel, T. D.; Rohde, J.-U. *Journal of the American Chemical Society* **2009**, *131*, 15582.

(62) Barondeau, D. P.; Kassmann, C. J.*; et al. Biochemistry* **2004**, *43*, 8038.

(63) Shearer, J. *Accounts of Chemical Research* **2014**, *47*, 2332.

(64) Shearer, J.; Long, L. M. *Inorganic Chemistry* **2006**, *45*, 2358.

(65) Schmidt, M.; Zahn, S.*; et al. ChemBioChem* **2008**, *9*, 2135.

(66) Domergue, J.; Pécaut, J.*; et al. Inorganic Chemistry* **2019**, *58*, 12775.

(67) Bruno, B. J.; Miller, G. D.*; et al. Therapeutic Delivery* **2013**, *4*, 1443.

(68) Isidro-Llobet, A.; Kenworthy, M. N.*; et al. The Journal of Organic Chemistry* **2019**, *84*, 4615.

(69) Batinic-Haberle, I.; Spasojevic, I. In *Porphyrin Science by Women: In 3 Volumes*; World Scientific: 2019, p 197.

(70) Liu, G.-F.; Dürr, K.*; et al. Dalton Transactions* **2009**, 6292.

(71) Riley, D. P.; Henke, S. L.*; et al. Inorganic Chemistry* **1996**, *35*, 5213.

(72) Policar, C. In *Redox-Active Therapeutics. Oxidative Stress in Applied Basic Research and Clinical Practice.*; Batinić-Haberle, I., Rebouças, J.*; et al.*, Eds.; Springer, Cham: 2016.

(73) Batinić-Haberle, I.; Liochev, S. I.*; et al. Archives of Biochemistry and Biophysics* **1997**, *343*, 225.

(74) Aston, K.; Rath, N.*; et al. Inorganic Chemistry* **2001**, *40*, 1779.

(75) Salvemini, D.; Wang, Z.-Q.*; et al. Science* **1999**, *286*, 304.

(76) Lieb, D., University of Erlangen-Nuremberg, 2013.

(77) Brodovitch, J. C.; McAuley, A.*; et al. Inorganic Chemistry* **1982**, *21*, 3442.

Chapter 4

Probing the Mechanism of a Redox-Active Metal-Free Superoxide Dismutase Mimic through the Study of Zinc(II) Complexes with Quinol-Containing Ligands

*This chapter is a revision of a manuscript under preparation by the following authors: Jamonica L. Moore, Andreas Scheitler, Meghan B. Ward, Haley B. Alix, Alexander C. Saunders, D. Schwartz, Ivana Ivanović-Burmazović, and Christian R. Goldsmith.

4.1 Introduction

The over-production of reactive oxygen species (ROS), such as superoxide ($O_2^{-\cdot}$) and hydrogen peroxide (H_2O_2), has been associated with a wide array of health conditions.[1-7] Although the exact contributions of ROS to these disorders remain unresolved, the development of antioxidants capable of correcting aberrant oxidative activity within the body would greatly benefit modern medicine.[8] One attractive antioxidant design strategy is to synthesize small molecules that resemble the enzymes that the body itself uses to regulate ROS concentrations. A small dose of such an antioxidant would alleviate oxidative stress by catalytically degrading one or more sort of ROS. Investigated antioxidants include functional mimics of superoxide dismutases (SODs), which are manganese-, iron-, nickel-, or copper-containing enzymes that catalyze the degradation of $O_2^{-\cdot}$ to O_2 and H_2O_2 (Eq. 4.1).[9-16] In these enzymes, the metal cycles between two oxidation states, with the oxidized form oxidizing $O_2^{-\cdot}$ to O_2 and the reduced partner reducing $O_2^{-\cdot}$ to H_2O_2. The copper-containing SODs usually, but not always,[17] contain a Zn(II) ion in the active site. The role of the Zn(II) appears to be to stabilize the enzyme and facilitate release of the H_2O_2 product, but some catalysis is retained if the zinc is removed.[18,19]

$$2\ O_2^{-\cdot} + 2\ H^+ \rightarrow O_2 + H_2O \qquad \text{(Eq. 4.1)}$$

Our laboratory has recently found that three Mn(II)-containing magnetic resonance imaging contrast agent sensors for H_2O_2 can also serve as catalysts for $O_2^{-\cdot}$ degradation.[20-23] The organic ligands of two of these probes contain quinol groups, which reversibly oxidize to *para*-quinones upon reaction with excess $O_2^{-\cdot}$ or H_2O_2 (Scheme 4.1).[21,22] These catalysts differ from other SOD mimics in that the organic ligand can potentially serve as a redox partner for the oxidation and reduction of $O_2^{-\cdot}$; normally, the transition metal is the sole oxidant and reductant. Although metal-free *N*-(2,5-dihydroxybenzyl)*N,N',N'*-tris(2-pyridinylmethyl)-1,2-ethanediamine (H_2qp1, Scheme 4.2) cannot catalyze superoxide degradation by itself, $[Zn(H_2qp1)(OTf)]^+$ (**1**) is a viable catalyst, with activity

comparable to those of manganese-containing SOD mimics.[24] The activity is further notable since it is amplified in phosphate buffer; phosphate anions competitively inhibit most manganese-containing SOD mimics.[23,25,26] Since Zn(II) cannot readily change oxidation states, the H_2qp1 ligand was proposed to be the relevant redox partner for $O_2^{\cdot-}$ and cycle through three different forms, containing either a quinol, a quinoxyl radical, or a *para*-quinone (Scheme 4.1). The catalytic activity of this compound demonstrates that the dual roles of the transition metal ion in traditional SOD mimicry – electrostatically attracting $O_2^{\cdot-}$ and transferring electrons to or from the substrate – can instead be fulfilled by a complex consisting of a redox-inactive metal ion and a redox-active ligand.

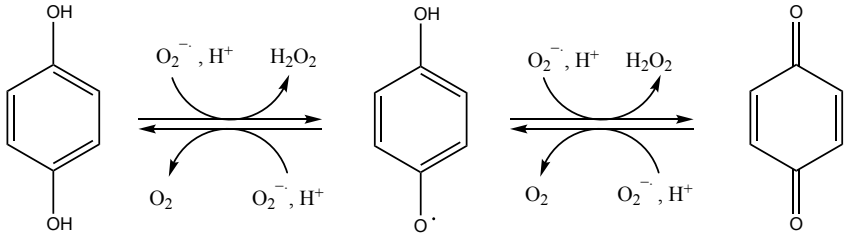

Scheme 4.1 Redox-reaction for quinols.

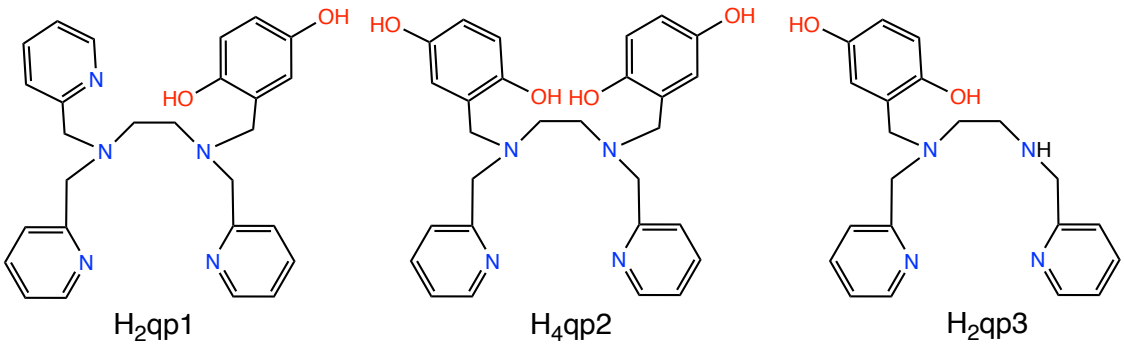

Scheme 4.2 Redox-active ligands used in this study for **1**, **2**, and **3**.

There are several benefits to such an approach. First, it allows more innocuous metal ions to be used in place of toxic redox-active transition metals, such as iron and manganese. Second, Zn(II) complexes tend to be more stable than their Mn(II) and Fe(II) analogs,[27,28] which should prolong

catalysis. Due to these first two factors, the study of manganese-containing SOD mimics has been heavily centered around complexes with macrocyclic ligands, which can be difficult to synthesize and modify; even then, these compounds have limited stability in aqueous solutions.[29-31] A third, and unanticipated, benefit is the aforementioned enhanced activity of **1** in phosphate solution. This is a significant advantage since mammalian cells contain high levels of phosphate.

The development of additional complexes is essential to determining how molecular structure impacts function, and even subtle changes to the ligand may substantially alter the activity. The H_2qp1 ligand is hexadentate and is capable of fully coordinating the Zn(II) by itself.[24] Previously obtained mass spectrometry data suggest that **1** reacts with $O_2^{\cdot-}$ through an inner-sphere mechanism. Replacing H_2qp1 with a pentadentate ligand could potentially improve the activity by introducing a more accessible site for superoxide coordination. The structural and potentiometric pH titration data that we have previously obtained for Mn(II) and Zn(II) complexes suggest that quinols are poor ligands but that deprotonation to the quinolate form markedly improves their metal-binding affinity.[21,24] The installation of a second redox-active quinol into the ligand may improve the activity either by better ensuring that a quinol remains bound to the Zn(II) at all times or by providing a donor atom that is easier to displace if one of the quinols remains protonated. Further, the additional quinol may serve to protect the catalyst from inadvertent oxidation and deactivation by ROS by providing a sacrificial reductant; complex **1** does degrade when the concentrations of H_2O_2 are too high.[24] In order to develop structure-function relationships for this new class of SOD mimic, we have therefore prepared Zn(II) complexes with *N,N'*-(2,5-dihydroxybenzyl)-*N,N'*-bis(2-pyridinylmethyl)-1,2-ethanediamine (H_4qp2) and *N*-(2,5-dihydroxybenzyl)-*N,N'*-bis(2-pyridinylmethyl)-1,2-ethanediamine (H_2qp3, Scheme 4.2). The former ligand was previously used in a redox-responsive MRI contrast agent; whereas, the potentially pentadentate H_2qp3 was the immediate precursor in its synthesis.[21]

$[Zn(H_4qp2)]^{2+}$ (**2**), is more active than **1** and likewise displays improved catalytic activity in phosphate buffer, whereas $[Zn(H_2qp3)(H_2O)]^{2+}$ (**3**) does not noticeably hasten $O_2^{\cdot-}$ degradation beyond the uncatalyzed reaction. Simply mixing zinc salts and quinols together is therefore not sufficient to achieve SOD mimicry. The relative activities of the three Zn(II)-quinol complexes can be rationalized by their speciation of the complexes in water and the observed oxidation products.

4.2 Experimental Section

Materials

All chemicals and solvents were purchased from Sigma-Aldrich and used as received unless otherwise noted. 2,2-Diphenyl-1-picryl-hydrazyl hydrate (DPPH) was supplied by EMD Millipore. All deuterated solvents were bought from Cambridge Isotopes. Diethyl ether (ether) and methanol (MeOH) were bought from Fisher. Methylene chloride (CH_2Cl_2) was purchased from Mallinckrodt Baker. *N,N'*-Bis(2,5-dihydroxybenzyl)-*N,N'*-bis(2-pyridinylmethyl)-1,2-ethanediamine (H_4qp2) and *N*-(2,5-dihydroxybenzyl)-*N,N'*-bis(2-pyridinylmethyl)-1,2-ethanediamine (H_2qp3) were previously prepared.[21]

Instrumentation

All ^1H and ^{13}C NMR spectra were recorded on a 400 MHz, 500 MHz, or 600 MHz AV Bruker NMR spectrometer. In each spectrum, the reported NMR resonance peak frequencies were referenced to internal standards. Optical data were collected on a Varian Cary 50 spectrophotometer and analyzed using software from the WinUV Analysis Suite. High-resolution mass spectrometry (HR-MS) data were obtained at the Mass Spectrometer Center at Auburn University on a Waters Q-ToF Premier or ThermoFisher Orbitrap Exploris 120 mass spectrometer via electrospray operated in the positive ion mode. Infrared spectroscopy (IR) data were obtained with a Shimadzu IR Prestige-21 FTIR spectrophotometer. Cyclic voltammetry (CV) was performed under N_2 at 294 K using an Epsilon

electrochemistry workstation (Bioanalytical System, Inc.), a gold working electrode, a platinum wire auxiliary electrode, and a silver/silver(I) chloride reference electrode. All elemental analyses (C, H, N) were performed by Atlantic Microlabs (Norcross, GA); crystalline samples were dried under vacuum and placed under a N_2 atmosphere prior to shipment.

X-Ray Crystallography

Structural data on single crystals were collected using a Bruker D8 VENTURE κ-geometry diffractometer system equipped with an Incoatec IμS 3.0 microfocus sealed tube (Mo Kα, λ = 0.71073 Å) and a multilayer mirror monochromator. SMART (v 5.624) was used to determine the preliminary cell constants and control data acquisition. The Bruker SAINT software package was used to determine integrated intensities; the data were corrected for absorption effects using the multi-scan method (SADABS). The structure was solved and refined using the Burker SHELXTL software package. All non-hydrogen atoms were refined anisotropically. Hydrogen atoms were included at idealized positions 0.95 Å from their parent atoms prior to the final refinement. Further details regarding the data acquisition and analysis are included in Appendix C as well as Table 4.1.

Potentiometric Titrations

The speciation chemistry of the Zn(II) complexes in water was assessed using a METROHM 765 Dosimat with a jacketed, airtight glass titration vessel. A Fisher Scientific Accumet Research AR15 pH meter was used to determine the pH of the sample solutions during the titrations. The electrode was calibrated before each titration using commercially available standard solutions buffered to pH 4.0, 7.0, and 10.0. All samples were purged with argon prior to analysis and subsequently analyzed under an argon atmosphere at 25 °C. All solution samples were prepared in solutions of 100 mM KCl in deionized Millipore water. The titrations investigating metal-ligand speciation were run with solutions that contained a 1:1 molar mixture of the ligand and $Zn(OTf)_2$. Carbonate-free solutions

of 0.10 M KOH and 0.10 M HCl were prepared using argon-saturated deionized Millipore water. Initially, we estimated pK_a values through visual inspection of the data plotted in KaleidaGraph v. 4.0. We subsequently attempted to analyze and fit the data to speciation models using the Hyperquad2006 program.[32]

Analysis of the Antioxidant Properties of the Coordination Complexes

We previously screened the abilities of other coordination complexes to catalytically degrade superoxide using the xanthine oxidase/hypoxanthine/lucigenin assay.[21,22,33] Superoxide was generated *in situ* from a reaction between xanthine and xanthine oxidase. A subsequent reaction between $O_2^{-\cdot}$ and lucigenin provides a spectroscopic signal that can be used to quantify an antioxidant's ability to degrade $O_2^{-\cdot}$. The copper/zinc superoxide dismutase isolated from bovine erythrocytes (0.001-100 U/ml, Calbiochem) served as a positive control. Each assay was carried out in a total volume of 1 mL containing 50 mM tris (pH 8.0), hypoxanthine (50 μM), xanthine oxidase (0.005 U/ml, Calbiochem) and dark-adapted lucigenin (5 μM) in the presence of either the studied Zn(II) complex (0.1 nM – 10 μM) or its vehicle. Reactions were carried out at room temperature and were initiated by the addition of xanthine oxidase to the hypoxanthine-containing solution. Luminescence was measured using a TD-20/20 (Turner Designs) luminometer and expressed as relative light units (RLU). Luminescence was measured for ten 10 s integrations after an initial delay of 3 s. The ten RLU values were averaged, and each concentration was expressed as a percent of that produced in the presence of vehicle. Each assay data point was performed in triplicate and each assay was repeated three times.

We also assessed the antioxidant activities of the Zn(II) complexes through the DPPH assay (DPPH = 2,2-diphenyl-1-picrylhydrazyl radical hydrate).[34-36] In this assay, potential antioxidants are tested for their abilities to donate hydrogen atoms to the radical to generate the corresponding hydrazine. Aqueous solutions of either **2**, **3**, or ascorbic acid were added to a solution of 0.10 mM

DPPH in MeOH, such that the final reaction volume was 0.2 mL. Samples were incubated in the dark for 30 min at room temperature before being spectrophotometrically analyzed on a Molecular Devices Spectramax Plus. The absorbance at 517 nm, the λ_{max} of the hydrazine product, was recorded. Experiments were performed in triplicate and repeated three times.

Determination of in vitro *SOD Activity via Stopped-Flow Technique*

The ability of the Zn(II) complexes to catalytically degrade superoxide was more thoroughly tested by a direct method using stopped-flow techniques that has been more fully described in prior work from one of our laboratories.[25] Stopped-flow measurements were performed on a Biologic SFM-400 four syringe stopped-flow system using only the first three syringes and a Berger Ball mixer to minimize mixing effects between aqueous buffered solutions and DMSO solutions of KO_2. A J&M TIDAS S MMS UV/VIS diode array detector (integration time 0.5 ms, 180 nm – 720 nm wavelength) and an Energetiq LDLS ENQ EQ-99-FC laser driven light source were used.

Superoxide solutions were prepared by suspending 220 – 240 mg KO_2 in 20 mL dry DMSO. The suspension was stirred for at least 30 min under inert atmosphere before the suspension was filtered through a PTFE syringe filter (Ø = 0.45 μm) to give a saturated KO_2 solution, which was transferred to the stopped flow setup. The potential SOD mimics (SODm) were dissolved in aqueous solutions buffered to pH 7.4. The buffers were prepared from Millipore water and either 4-morpholinepropanesulfonic acid (MOPS) or sodium dihydrogen phosphate. The concentration of the buffer was 60 mM, and the ionic strength was adjusted to 150 mM for each solution through the addition of NaCl. All of the buffered solutions were treated with Chelex 100 sodium exchange resin for at least 24 h before use in order to remove adventitious metal ions. Stock solutions containing 1.00×10^{-4} M of each tested SODm were prepared in each buffer; if necessary, the stock solution

contained 10% DMSO to ensure that the complexes dissolved fully. The stock solutions were diluted in buffer to give a series of SODm concentrations suitable for the stopped-flow experiments.

Kinetic measurements were performed adding a large excess of superoxide to the putative SOD mimetic: $[O_2^{\cdot-}]$ = 100 – 200 μM, [SODm] = 0.25 – 4.5 μM. The aqueous solution containing the studied Zn(II) complex was mixed in a 9:1 ratio with the superoxide solution in DMSO using a high-density mixer. In each experiment, the concentration of superoxide exceeded that of the zinc-containing catalyst by at least ten-fold to ensure catalytic conditions. All kinetic data were fitted with the program Biokine 32 V4.80. Each k_{obs} value represents an average of at least nine measurements. Each k_{cat} was determined from the slope of k_{obs} vs. [SODm]. All measurements were performed at 21 °C.

Syntheses

(*N,N'*-Bis(2,5-dihydroxybenzyl)-*N,N'*-bis(2-pyridinylmethyl)-1,2-ethanediamine)zinc(II) triflate ([Zn(H$_4$qp2)](OTf)$_2$, 2).

The H$_4$qp2 ligand (213 mg, 0.434 mmol) and Zn(OTf)$_2$ (159 mg, 0.434 mmol) were dissolved in 3 mL of MeCN under N_2. The solution was stirred for 16 h at 60 °C. After the solution was cooled to room temperature (RT), ether was gradually added to precipitate the product as a white powder (264 mg, 71%). CH_2Cl_2 was gradually added to a saturated solution of the product in MeOH to yield crystals suitable for single-crystal X-ray diffraction. ^{1}H NMR (400 MHz, CD_3CN, 293 K): δ 8.73 (d, J = 5.4 Hz, 2H), 7.92 – 8.03 (m, 3H), 7.54 (t, J = 6.4 Hz, 2 H), 7.32 – 7.45 (m, 5H), 4.39 (d, J = 16.4 Hz, 2H), 4.09 – 4.27 (m, 1H), 3.72 – 3.91 (m, 6H), 3.43 (d, J = 13.6 Hz, 2H), 3.22 (s, 1H), 2.75 (d, J = 10.9 Hz, 2H), 2.60 (d, J = 11.1 Hz, 2H). ^{13}C NMR (100 MHz, CD_3CN, 293 K): δ 155.11, 150.56, 147.86, 147.83, 141.11, 132.30, 131.29, 128.73, 125.01, 124.94, 57.38, 52.87. Optical spectroscopy (MeCN, 293 K): 298 nm (ε = 2400 M^{-1} cm^{-1}), 262 nm (ε = 2500 M^{-1} cm^{-1}). IR (KBr, cm^{-1}): 3406 (m), 3144 (m),

1653 (w), 1612 (m), 1576 (w), 1508 (w), 1458 (w), 1400 (s), 1385 (s), 1252 (m), 1157 (m), 1101 (w), 1032 (s), 943 (w), 920 (w), 878 (w), 824 (m), 766 (s), 638 (s), 577 (m), 517 (s), 419 (m). MS (ESI): Calcd for $[Zn(H_3qp2)]^+$, 549.1481, $[Zn(H_4qp2)(OTf)]^+$, 699.1079; Found, 549.1415, 699.1237. Elemental analysis: Calcd for $C_{30}H_{30}N_4F_6O_{10}S_2Zn \cdot H_2O$: C, 41.51%; H, 3.72%; N, 6.45%; Found: 41.30%; H, 3.37%; N, 6.32%.

Aqua(*N*-(2,5-dihydroxybenzyl)-*N,N'*-bis(2-pyridinylmethyl)-1,2-ethanediamine)zinc(II)] triflate ($[Zn(H_2qp3)(H_2O)](OTf)_2$, 3).

The H_2qp3 ligand (166 mg, 0.456 mmol) and zinc(II) triflate ($Zn(OTf)_2$, 166 mg, 0.456 mmol) were dissolved in 3 mL of acetonitrile (MeCN) under N_2. The solution was stirred for 16 h at 60 °C. Ether was added to the solution as it cooled to RT to deposit the product as a white crystalline powder (267 mg, 78% yield). Gradually adding ether to a saturated MeCN solution resulted in crystals that were suitable for single-crystal X-ray diffraction. ^{1}H NMR (400 MHz, CD_3CN, 293 K): δ 8.84 (d, J = 4.8 Hz, 1H) 8.56 (d, J = 4.4 Hz, 1H), 8.39 – 7.98 (m, 4 H), 7.64 – 7.35 (m, 6H), 4.54 – 4.48 (m, 2H), 4.28 (d, J = 16.4 Hz, 2H), 3.73 (t, J = 13.2 Hz, 2H), 3.54 (d, J = 13.3 Hz, 2H), 3.08 – 3.04 (m, 2H), 2.95 (d, J = 13.2 Hz, 1H). ^{13}C NMR (100 MHz, CD_3CN, 293 K): δ 154.86, 151.18, 147.31, 140.66, 124.42, 121.22, 79.42, 52.97. Optical spectroscopy (MeCN): 295.9 nm (ε = 908 M^{-1} cm^{-1}), 262 nm (ε = 2094 M^{-1} cm^{-1}). IR (KBr, cm^{-1}): 3507 (w), 3134 (m), 1686 (w), 1611 (w), 1508 (w), 1400 (s), 1385 (s), 1260 (m), 1179 (m), 1096 (w), 1032 (s) 876 (w), 860 (w), 820 (w) 800 (w), 766 (m), 727 (w), 646 (s), 581 (m), 521 (s), 415 (m). MS (ESI): Calcd for $[Zn(Hqp3)]^+$, 427.1113, $[Zn(H_2qp3)(OTf)]^+$, 577.0711; Found, 427.1127, 577.0742. Elemental analysis (crystals): Calcd for $C_{23}H_{24}N_4F_6O_8S_2Zn \cdot 2H_2O$: C, 36.16%; H, 3.69%; N, 7.33%; Found: C, 36.12%; H, 3.74%; N, 7.11%.

4.3 Results

Synthesis

In a prior publication from our laboratory, we reported the synthesis of both the H_4qp2 and H_2qp3 ligands and the chemistry of a Mn(II) complex with H_4qp2.[21] The triflic acid salt of the H_2qp3 ligand, which was the immediate precursor to H_4qp2, was structurally characterized in that report.

Zn(II) complexes with the H_2qp2 and H_2qp3 ligands can be prepared by dissolving a 1:1 mixture of the ligand and $Zn(OTf)_2$ in hot MeCN. Adding diethyl ether to these solutions precipitates $[Zn(H_4qp2)](OTf)_2$ (**2**) and $[Zn(H_2qp3)(H_2O)](OTf)_2$ (**3**) in high yields (>70%) and purities. The compositions were established by both crystallography and elemental analysis. The only challenging aspect about the syntheses is that $Zn(OTf)_2$ is poorly soluble in MeCN, necessitating both the elevated temperature (60 °C) and the lengthy reaction time (16 h). The 1:1 stoichiometry must be strictly observed since any excess $Zn(OTf)_2$ will also precipitate under the isolation conditions and contaminate the desired products. As anticipated, the products are diamagnetic and colorless. The ^{1}H NMR spectra of crystalline samples of both Zn(II) complexes (Figures C1 and C5) contain more features than anticipated from the crystal structures, and each complex appears to exist as a mixture of conformers and/or coordination isomers in solution. Similarly complicated speciation was also noted for $[Zn(H_2qp1)(OTf)](OTf)$ (**1**).[24]

Structural Characterization

The complexes can be crystallized from either $MeOH/CH_2Cl_2$ or MeCN/ether solutions (Figure 4.1). The structures differ substantially from the two Zn(II) complexes crystallized from **1**: $[Zn(H_2qp1)(MeCN)](OTf)_2$ and $[Zn(H_2qp1)(OTf)](OTf)$ in that the quinols are bound directly to the metal center.[24] Both of the new structures feature a 2:1 ratio of triflates to Zn(II)-ligand subunits, suggesting that all of the quinols remain protonated. The C-O bonds range from 1.36 to 1.39 Å,

confirming both that the quinols have not been inadvertently oxidized and that each of the O-H groups remains protonated.[21,22,37]

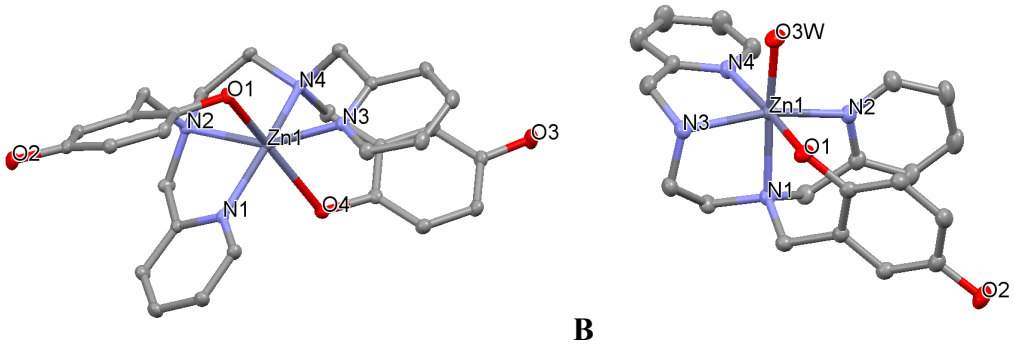

A **B**

Figure 4.1 Thermal ellipsoid plots of (A) $[Zn(H_4qp2)]^{2+}$ and (B) $[Zn(H_2qp3)(H_2O)]^{2+}$. Ellipsoids set at 50% probability. All hydrogen atoms, triflate counteranions, and non-bound solvent molecules have been omitted for clarity.

In the structure of **2**, the H_4qp2 ligand binds in a hexadentate fashion, accounting for all six of the donor atoms in the coordination sphere of the metal ion. Overall, the Zn(II) is chelated in a highly distorted octahedral geometry, with the two quinols *trans* to each other and the two pyridines approximately *cis* to each other. There are two significant distortions from octahedral geometry. First, the bond angle between the two pyridine N-donors, N(1)-Zn(1)-N(3), is 122°; the larger space between the pyridines makes the structure somewhat resemble a pentagonal bipyramid with a missing equatorial vertex. The quinols shift slightly from their ideal octahedral positions towards the gap between the pyridine rings, resulting in a 163° O-Zn(II)-O bond angle. Second, one of the quinols is bound much more weakly than the other, with Zn-O(1) and Zn-O(4) having bond lengths of 2.196 and 2.364 Å, respectively. Each quinol appears to be hydrogen bonded to two triflates. The extensive hydrogen bonding network results in a relatively dense crystal (1.673 g/cm^3). Each quinol is approximately parallel to a pyridine ring, which may suggest aromatic interactions between these groups. The centroids of the aromatic rings are 3.73 Å and 3.89 Å apart, with the pyridine containing N(3) and the quinol containing O(4) being slightly closer together.

The structure of **3** likewise features the quinol-containing ligand coordinating the metal ion to its maximum extent. The Zn(II) center is coordinated in a distorted octahedral geometry by five atoms from H_2qp3 and an oxygen atom from a water molecule. The bond angles around the Zn(II) center do not deviate from the ideal octahedral values as much as they do for **2**. The pyridine rings from the ligand are *cis* to each other; whereas, the bound H_2O is *trans* to one of the amines. As with **2**, the components within the asymmetric unit hydrogen bond extensively with each other, resulting in another dense crystal (1.626 g/cm^3). The non-coordinated OH group in the quinol donates a hydrogen bond to a triflate while the metal-bound OH hydrogen bonds to an outer-sphere molecule of H_2O. The Zn(II)-bound H_2O hydrogen bonds to the second triflate, which is disordered over two positions. The quinol appears to aromatically interact with one of the pyridine rings; the centroids of the quinol and the pyridine ring containing N(2) are 3.59 Å apart.

Table 4.1 Selected crystallographic data for **2** and **3**.

Parameter	$[Zn(H_4qp2)](OTf)_2$ (**2**)	$[Zn(H_2qp3)(H_2O)](OTf)_2$ (**3**)
Formula	$C_{30}H_{30}F_6N_4O_{10}S_2Zn$	$C_{23}H_{27}F_6N_4O_{10}S_2Zn$
MW	850.07	762.97
Crystal system	Triclinic	Monoclinic
Space group	$P\bar{1}$	$P12_1/n1$
a (Å)	11.5601(4)	11.5256(4)
b (Å)	11.9171(4)	12.4789(4)
c (Å)	13.8096(5)	21.6728(7)
α (°)	100.936(2)	90
β (°)	105.707(2)	90.4010(10)
γ (°)	105.978(2)	90
V (Å^3)	1687.37(10)	317.05(18)
Z	2	4
Crystal color	Colorless	Colorless
T (K)	100(2)	110(2)
Reflns collected	57040	93868
Unique reflns	16337	16779
R1 (F, I > 2σ(I))	0.0517	0.0454
wR2 (F^2, all data)	0.1375	0.1256

$R1 = \Sigma \big| |F_o| - |F_c| \big| / \Sigma |F_o|$; $wR2 = [\Sigma w(F_o^2-F_c^2)^2/\Sigma w(F_o^2)^2]^{1/2}$.

Aqueous Solution Characterization

Neither of the solid-state structures of the Zn(II) complexes with H_2qp1 were found to be maintained in water, and the predominant aqueous species for **1** above pH 7 is $[Zn(Hqp1)]^+$, which features a metal-coordinated quinolate.[24] Since **2** and **3** are intended to be used as catalysts for the decomposition of superoxide in aqueous solutions, understanding their behavior in water is essential. We therefore determined the speciation of **2** and **3** in water using potentiometric and spectrophotometric pH titrations (Figures C9-C11).

Table 4.2 Stability constants and pK_a Values for the H_4qp2 and H_2qp3 ligands and their Zn(II) complexes as determined by potentiometric titration at 25 °C.

H_4qp2		**Zn-H_4qp2**	
pK_{L1}[a]	7.18 (±0.03)	pK_{a1}[b]	5.3 (±0.3)
pK_{L2}[a]	4.47 (±0.08)	pK_{a2}[b]	8.5 (±0.3)
H_2qp3		**Zn-H_2qp3**	
pK_{L1}[a]	10.2 (±0.3)	pK_{a1}[b]	5.57 (±0.10)
pK_{L2}[a]	8.19 (±0.05)	pK_{a2}[b]	2.98 (±0.15)
pK_{L3}[a]	5.13 (±0.05)	log K(ZnHqp3)[c]	15.75
pK_{L4}[a]	3.5 (±0.3)	log K(ZnH_2qp3)[c]	11.14
		log K(ZnH_3qp3)	5.93

[a]Ligand pK_a values correspond to the following equilibrium constants:

H_4qp2 $K_{L1} = [(H_4qp2)][H^+]/[(H_5qp2)^+]$, from reference [21].

$K_{L2} = [(H_5qp2)^+][H^+]/[(H_6qp2)^{2+}]$, from reference [21].

H_2qp3 $K_{L1} = [(Hqp3)^-][H^+]/[(H_2qp3)]$, $pK_{L1} = \log\beta_{010} - \log\beta_{-110}$.

$K_{L2} = [(H_2qp3)][H^+]/[(H_3qp3)^+]$, $pK_{L2} = \log\beta_{110} - \log\beta_{010}$.

$K_{L3} = [(H_3qp3)^+][H^+]/[(H_4qp3)^{2+}]$, $pK_{L3} = \log\beta_{210} - \log\beta_{110}$.

$K_{L4} = [(H_4qp3)]^{2+}[H^+]/[(H_5qp3)^{3+}]$, $pK_{L4} = \log\beta_{310} - \log\beta_{210}$.

[b]Metal complex pK_a values correspond to the following equilibrium constants:

Zn-H_4qp2 $K_{a1} = [[Zn(H_3qp2)]^+][H^+]/[[Zn(H_4qp2)]^{2+}]$.

$K_{a2} = [[Zn(H_3qp2)]^+][H^+]/[[Zn(H_2qp2)]]$.

Zn-H_2qp3 $K_{a1} = [[Zn(Hqp3)]^+][H^+]/[[Zn(H_2qp3)]^{2+}]$, $pK_{a1} = \log\beta_{011} - \log\beta_{-111}$.

$K_{a2} = [[Zn(H_2qp3)]^{2+}][H^+]/[[Zn(H_3qp3)^{3+}]]$, $pK_{a12} = \log\beta_{111} - \log\beta_{011}$.

[c]Metal complex stability constants correspond to the following equilibrium constants:

$K(ZnHqp3) = [[Zn(Hqp3)]^+]/[Zn^{2+}][Hqp3^-]$

$K(ZnH_2qp3) = [[Zn(H_2qp3)]^{2+}]/[Zn^{2+}][H_2qp3]$

$K(ZnH_3qp3) = [[Zn(H_3qp3)^{3+}]]/[Zn^{2+}][H_3qp3^+]$

The acid/base chemistry of the H_4qp2 ligand in water was previously described during our characterization of its complex with Mn(II).[21] The Zn(II) complex displays two clear ionization events as the pH increases from 2.5 to 10. These are consistent with pK_a values of 5.3 and 8.5, which we assign to the deprotonation of the two Zn(II)-bound quinols. The major species between pH 7.0 and 7.4 would therefore be $[Zn(H_3qp2)]^+$, where H_3qp2^- is the singly deprotonated form of the ligand. Unfortunately, we could not use these data to obtain stability constants for $[Zn(H_3qp2)]^+$ and [Zn(H_2qp2). The log(β) values for these species do not converge to stable numbers even after extensive attempts to fit the data to a wide variety of models using the speciation program Hyperquad. We had encountered similar difficulties modeling the data for $[Zn(H_2qp1)(OTf)]^+$.[24] The ability to calculate these values requires a substantial amount of the metal to dissociate from the ligand under acidic conditions; this does not appear to happen for either the H_2qp1 systems. Complex **2** is therefore more stable in water than its Mn(II) analogue.

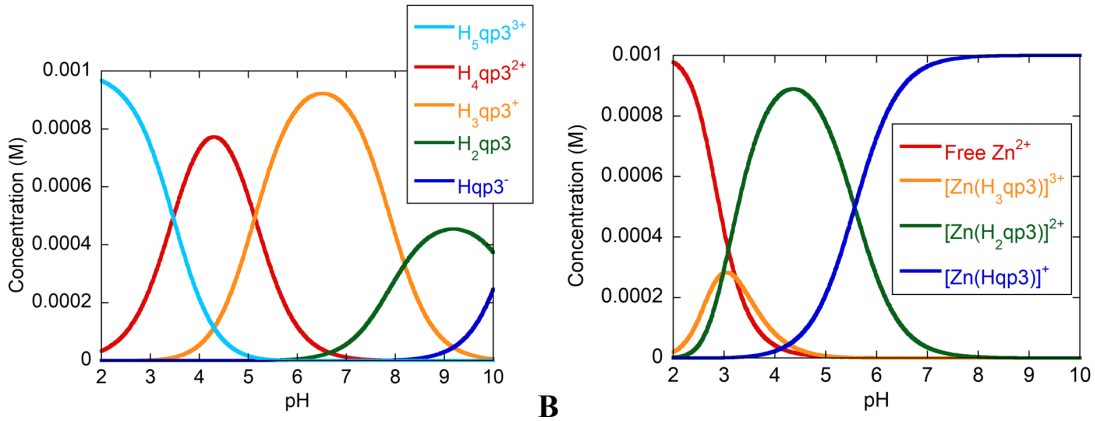

Figure 4.2 Predicted speciation as a function of pH for A) 1.0 mM H_2qp3 and B) a 1:1 mixture of H_2qp3 and $Zn(OTf)_2$ in 100 mM KCl solution.

The H_2qp3 ligand undergoes four ionization events as the pH is increased from 2.5 to 10 (Table 4.2, Figure 4.2A). We have assigned these to four sequential deprotonations of H_5qp3^{3+}. The first three ionization events are associated with pK_a values of 3.5, 5.13, and 8.19 and likely correspond to the

removal of protons from pyridinium and ammonium groups. The 10.2 pK_a value associated with the last ionization event is consistent with the deprotonation of a phenolic OH group, which would convert H_2qp3 into Hqp3$^-$. The error for this value is higher since the Hqp3$^-$ species did not fully form during the titration.

The Zn(II) complex with H_2qp3 appears to be stable above pH 5 (Figure 4.2B), and the pZn calculated for 1.0 mM ligand and 1.0 mM Zn(II) at pH 7.4 is 7.54. Below pH 5, the Zn(II) complex displays two ionization events. The first is assigned to the association/dissociation of Zn(II). We believe that the second ionization event observed with increasing pH corresponds to the deprotonation of $[Zn(H_3qp3)]^{3+}$ to $[Zn(H_2qp3)]^{2+}$. The protonation of the ligand at low pH likely facilitates the loss of the metal ion under acidic conditions. The complex is further deprotonated as the pH rises past 5. The 5.57 pK_a value associated with the third ionization event is consistent with the deprotonation of a Zn(II)-bound quinol.[24] At pH 7 and above, the Zn(II) mostly exists as $[Zn(Hqp3)]^+$.

Electrochemistry

The redox behavior of **2** and **3** in aqueous phosphate solutions buffered to pH 7.0 was analyzed by cyclic voltammetry (CV). The CV for each complex displays a single quasi-reversible feature. For complex **2**, the redox event has $E_{1/2}$ = 195 mV vs. Ag/AgCl and ΔE_p = 208 mV (Figure C11). Complex **3** gives rise to a more reversible redox feature with $E_{1/2}$ = 150 mV vs. Ag/AgCl and ΔE_p = 166 mV (Figure C12).

Antioxidant Activity

Both **2** and **3** were initially screened using the xanthine oxidase/hypoxathine/lucigenin assay[21,22,33,38] and display above-baseline activity (Figure 4.3). The IC_{50} values for the elimination of the lucigenin sensing reaction were found to be within error of each other: 24 (±1) nM for **2** and 27

(±17) nM for **3**. The assay likewise doesn't meaningfully distinguish the antioxidant activities of **2** and **3** from those of the related complexes [Mn(H_4qp2)Br_2] (IC_{50} = 18 nM)[21] and **1** (IC_{50} = 17 nM).[24]

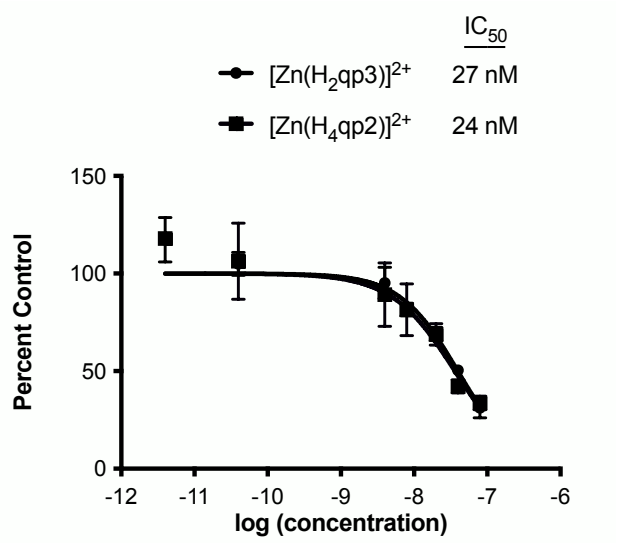

Figure 4.3 Superoxide scavenging effects of **2** and **3**. Superoxide was generated using a hypoxanthine-xanthine oxidase reaction and detected using the chemiluminescent probe lucigenin. Reactions were carried out in 50 mM Tris-HCl (pH 8.0). Data for the various concentrations of Zn(II) complexes are expressed as a percentage of luminescence in the presence of vehicle.

Complexes **2** and **3** were also subjected to the DPPH assay (Figure 4.4), which tests the abilities of compounds to donate hydrogen atoms to 2,2-diphenyl-1-picrylhydrazyl radical hydrate.[34-36,39] In this assay, the production of the hydrazine is confirmed and followed by UV/vis. The IC_{50} values for **2** and **3** were measured to be 8.7 μM and 17.2 μM, respectively, with the H_4qp2 complex being substantially better as an antioxidant. The ascorbic acid standard had an IC_{50} value of 24.2 μM under the same conditions. Other divalent metal complexes with the H_2qp1 and H_4qp2 ligands likewise outperformed ascorbic acid in these measurements by approximately the same extent.[21,22,24]

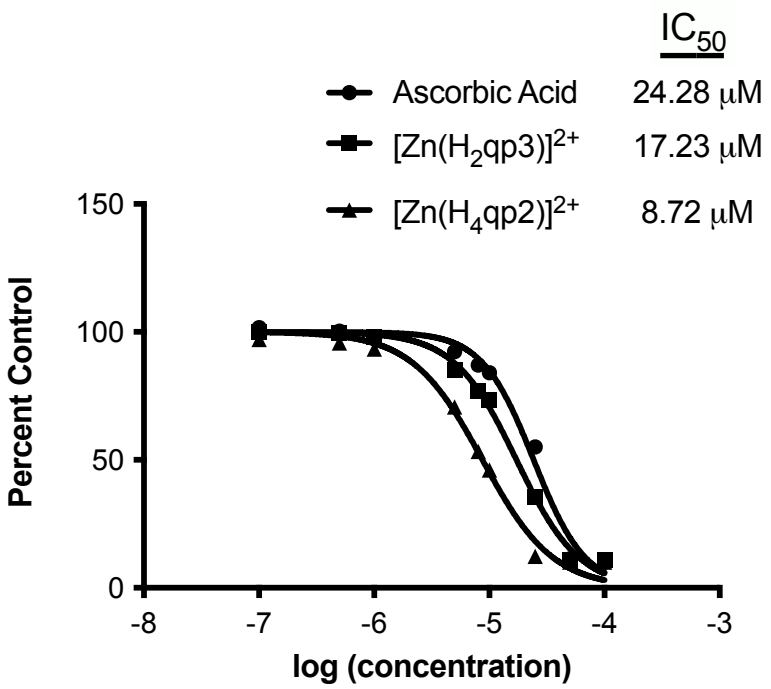

Figure 4.4 DPPH free radical scavenging assay of **2**, **3**, and ascorbic acid. The antioxidants were added to DPPH and incubated in the dark for 30 min at 298 K. Spectroscopic measurements were performed at 517 nm. The data were normalized to the absorbance in the presence of vehicle. All experiments were performed in triplicate and repeated twice.

The aforementioned assays, unfortunately, often provide misleading accounts of the actual reactivity with superoxide due to competing side-reactions between the various components in the reaction mixtures.[12,25,40-43] Consequently, the SOD mimicry was more thoroughly assessed by analyzing the direct reactions between the compounds and KO_2 (Table 4.3). Complex **2** reacts directly with $O_2^{\cdot-}$ and accelerates its decomposition, but compound **3** is not a competent catalyst for superoxide disproportionation (Figure C13).

When mixtures of **3** and KO_2 are analyzed by mass spectrometry, we find *m/z* features consistent with Zn(II)-free oxidized ligand but not any that are consistent with Zn(II) complexes with either H_2qp3 or qp3 (Figure C14). The data suggest that the initial oxidation of **3** by KO_2 to $[Zn(qp3)]^{2+}$ weakens the binding affinity of the ligand enough to destabilize the qp3 complex. Given that free

H_2qp3 by itself cannot catalyze superoxide degradation, we believe that the dissociation of the Zn(II) from the oxidized H_2qp3 ligand halts catalysis.

Table 4.3 Catalytic rate constants, k_{cat} (M^{-1} s^{-1}), measured by stopped-flow kinetics for the direct reactions of **1**, **2**, and **3** with superoxide.

Buffer, pH	**1**[a]	**2**	**3**
60 mM HEPES/MOPS, 7.4	3.4×10^6	1.56×10^7	N.A.
50 mM Phosphate, 7.4	1.9×10^7	2.54×10^7	N.A.

[a]Data from reference [24].

4.4 Discussion

The recently characterized superoxide dismutase (SOD) mimic [Zn(H_2qp1)(OTf)](OTf) (**1**) is highly unusual in that it uses an organic component as the redox partner for the superoxide substrate and lacks a redox-active transition metal ion. In order to determine what structural features are required for functional SOD mimicry for this fundamentally new class of catalysts, we prepared Zn(II) complexes with the quinol-containing H_4qp2 and H_2qp3 ligands (Scheme 4.2). These molecules differ from H_2qp1 in that they either feature a second quinol in place of a pyridine (H_4qp2) or are pentadentate rather than hexadentate (H_2qp3).

The syntheses of [Zn(H_4qp2)]$(OTf)_2$ (**2**) and [Zn(H_2qp3)(H_2O)]$(OTf)_2$ (**3**) are relatively straightforward, and we can readily isolate crystalline samples of both complexes (Figure 4.1). The crystal structures of **2** and **3** differ from those of **1** in that the quinols bind directly to the Zn(II) center.[24] The structural data for **2** suggest that both quinols cannot coordinate tightly to the Zn(II) at the same time, for the Zn-O(4) bond length is much longer than a typical Zn-O bond.[44] Based on this and the other distortions from octahedral geometry, we speculate that the Zn(II) metal center may be too small to be fully chelated by the H_4qp2 ligand. The NMR data for all three complexes are consistent with more than one conformer or coordination isomer existing in solution, suggesting that the metal coordination by H_2qp1, H_4qp2, and H_2qp3 is both flexible and dynamic.

The weaker association of the second quinol with the Zn(II) appears to be maintained when **2** is dissolved in water. The first pK_a is consistent with a phenol ligated to a divalent metal (Table 4.2),[21,24,45] but the second measured pK_a value of 8.5 is much higher than anticipated and approaches the value of 10 expected for a non-metal-bound phenol. Both **2** and **3** appear to be stable in water, and the major species between pH 7.0 and 7.4 are Zn(II) complexes with singly deprotonated H_3qp2^- and $Hqp3^-$ ligands: $[Zn(H_3qp2)]^+$ and $[Zn(Hqp3)]^+$ (Figure 4.2).

Complex **2**, much like **1**, is particularly stable in water, with no metal dissociation observed even at low pH values.[24] The aqueous stabilities of both Zn(II) complexes compare highly favorably to those of the most active small molecule SOD mimics. The Mn(II) porphyrin complex $Mn^{II}Br_8TM$-4-PyP^{4+}, for instance, has been documented to be unstable at neutral pH, and the release of free manganese from the complex has hampered its path to clinical use.[29] Manganese complexes with pentaazamacrocycles represent the other major family of highly active SOD mimics. Arguably the best of these catalysts is M40401, which has a catalytic rate of approximately 1.5×10^9 M^{-1} s^{-1}, but this compound likewise has limited conditional stability in water, with a pMn of 4.7 at pH 7.4.[30,31]

Electrochemically, complexes **2** and **3** resemble **1** in that only a single reduction/oxidation couple is observed by CV (Figures C11 and C12).[24] The ligand structure, however, markedly impacts both $E_{1/2}$ and ΔE_p. The removal of a pyridine ring from the coordination environment increases $E_{1/2}$ from 312 mV vs NHE (**1**) to 347 mV vs NHE (**3**). This structural change also worsens the reversibility, with ΔE_p. increasing from 95 mV (**1**) to 166 mV (**3**). The inclusion of another quinol in the coordination sphere raises $E_{1/2}$ further to 397 mV vs NHE (**3**), and this redox feature is the least reversible of the three observed for the Zn(II)-quinol complexes, with a ΔE_p of 208 mV. The H_4qp2 ligand likewise gave rise to a much less reversible redox event than H_2qp1 when ligated to Mn(II), and the CV features observed for $[Mn(H_4qp2)Br_2]$ in water would be considered irreversible by most.[21,22] The ligand-

derived redox couple seen for [Mn(H_4qp2)Br_2], however, has an $E_{1/2}$ that is less positive than that of [Mn(H_2qp1)(MeCN)]$^{2+}$. Unlike **2**, both of the H_4qp2 quinols appear to tightly coordinate to the larger Mn(II) center in solution, providing an explanation for why the same decrease in $E_{1/2}$ is not observed for the Zn(II) complexes when the H_2qp1 ligand is replaced by H_4qp2.[21] In both **2** and **3**, the $E_{1/2}$ shifts away from the ~300 mV ideal for SOD activity; these shifts and the lesser reversibility could potentially worsen the catalysis of $O_2^{\cdot-}$ degradation.

Both **2** and **3** initially appeared to be competent SOD mimics when analyzed via the xanthine oxidase/hypoxanthine/lucigenin[33] and DPPH assays.[34-36,39] The IC_{50} values from these measurements (Figures 3.2 and 3.3) suggested that their abilities to behave as antioxidants were either comparable or only slightly inferior to those of the related compounds [Mn(H_4qp2)Br_2] and **1**.[21,24] The assay results, however, are misleading. When the direct reactions between the Zn(II) complexes and KO_2 are studied by stopped-flow kinetics methods, the data reveal that **2** is a markedly better catalyst than **1** whereas **3** is not active enough to measurably increase the rate of $O_2^{\cdot-}$ disproportionation above that of the uncatalyzed reaction (Table 4.3).

Complex **2** is approximately five-fold more active in MOPS buffer than **1** is in the comparable HEPES buffer. As with **1**, the catalysis of **2** proceeds more quickly in phosphate solution. The activities of **1** and **2** in phosphate buffered to pH 7.4 are approximately equal, with **2** being just 20% more active than **1**. Complexes **1** and **2** are unique among SOD mimics in that their activities are enhanced, rather than diminished in phosphate buffers.[23,25,26] Given the high prevalence of phosphate in mammalian cells, this represents a substantial advantage.[46,47] That the activity of **2** improves in phosphate buffer suggests that this is a replicable and trademark feature of Zn(II)-quinol SOD mimics and is not just limited to compound **1**.

Curiously, replacing H_2qp1 with H_4qp2 worsens the SOD mimicry of manganese-containing complexes. With the manganese species, the ability of H_4qp2 to deprotonate to a dianionic form (H_2qp2^{2-}) renders its complexes with Mn(II) and Mn(III) less positive than the analogous complexes with Hqp1$^-$. The lesser positive charge hinders the ability of the Mn-H_4qp2 compounds to attract and bind $O_2^{-\cdot}$, thereby decreasing the rate of $O_2^{-\cdot}$ decomposition. The Zn(II)-H_4qp2 system differs from the Mn-H_4qp2 one in that the second quinol cannot approach the metal center as closely (Figure 4.1) which weakens the influence of the metal center on the acid/base properties of the quinol. The Zn(II)-for-Mn(II) substitution thereby raises the pK_a of the second quinol in the coordination complexes from 7.14 (Mn(II))[21] to 8.5 (Zn(II), Table 4.2). The major species for **2** in water at pH 7.4 is consequently cationic [Zn(H_3qp2)]$^+$ rather than [Zn(H_2qp2)].

The charge of the major species for **1** in pH 7.4 water, [Zn(Hqp1)]$^+$, is likewise +1, yet **1** is a less active catalyst, particularly in solutions using sulfonic acid-based buffers.[24] We speculate that the weak interaction between the second H_4qp2 quinol and the Zn(II) makes that particular coordination site on the metal center more accessible to exogenous ligands, such as $O_2^{-\cdot}$. Although H_4qp2 is hexadentate, the inability of the second quinol to attach firmly to Zn(II) gives the ligand some pentadentate character. All of the donor atoms from H_2qp1, conversely, coordinate strongly to the metal center, and this ligand is more strongly hexadentate as a consequence. With the relatively small size of the Zn(II) ion, the H_2qp1 ligand more efficiently blocks the access of $O_2^{-\cdot}$ to the metal center than H_4qp2. The more ready accessibility of the Zn(II) center in **2** leads to faster $O_2^{-\cdot}$ degradation.

The lack of activity for **3** is proposed to result from dissociation of the ligand from the Zn(II) after its initial oxidation by $O_2^{-\cdot}$. The H_2qp3 ligand essentially becomes tetradentate upon two-electron oxidation of the quinolate to a *para*-quinone (qp3). The loss of the strongly coordinating quinolate allows the anions from the MOPS and phosphate buffers to strip the metal ion from the polydentate

ligand; the resultant Zn(II) salts then precipitate from the solution. MS analysis of the reaction mixtures confirms that the reaction with KO_2 produces metal-free oxidized ligand as the major product (Figure C14). The results suggest that this quinol-containing ligand, much like H_2qp1,[24] needs to remain tightly bound to the Zn(II) in order for catalysis to proceed. The observation of oxidized ligand demonstrates that **3** can initially react with $O_2^{\cdot-}$, but the stopped-flow kinetics data suggest that the catalyst does not survive enough turnovers to noticeably impact the rate of $O_2^{\cdot-}$ disproportionation.

Unlike **3**, complex **2** maintains its catalysis after the initial round of oxidation. In addition to providing a readily accessible coordination site for $O_2^{\cdot-}$, the second quinol also serves as a replacement anionic ligand when the first quinol is oxidized to a *para*-quinone. The resultant complex, $[Zn(Hqp2)]^+$, where $Hqp2^-$ is a quinolate/*para*-quinone ligand, is stable enough to persist in water and continue to participate in catalysis, accounting for its higher activity.

4.5 Conclusions

The reactivity of the Zn(II)-H_4qp2 complex **2** demonstrates that the design strategy for SOD mimicry used for the Zn(II)-H_2qp1 complex **1** – using a redox-active ligand in place of a redox-active metal – is generally applicable and is not limited to a single catalyst. The replacement of one of the H_2qp1 pyridines with a quinol improves the activity in aqueous solutions buffered with sulfonic acids five-fold, likely by improving the accessibility of the metal center to $O_2^{\cdot-}$. Complex **2**, like **1**, functions better in phosphate buffer, differentiating these catalysts from manganese-containing SOD mimics and making them more suitable for treating oxidative stress *in vivo*. Complex **3**, conversely, is not a successful SOD mimic due to the lesser stability of its oxidized form $[Zn(qp3)]^{2+}$. The inability of **3** to noticeably impact the rate of superoxide disproportionation demonstrates that merely having a mixture of a Zn(II) salt and a quinol/*para*-quinone compound is not sufficient for catalysis; the redox-active organic component needs to be closely associated with, if not covalently tethered to, the metal center.

Appendix C

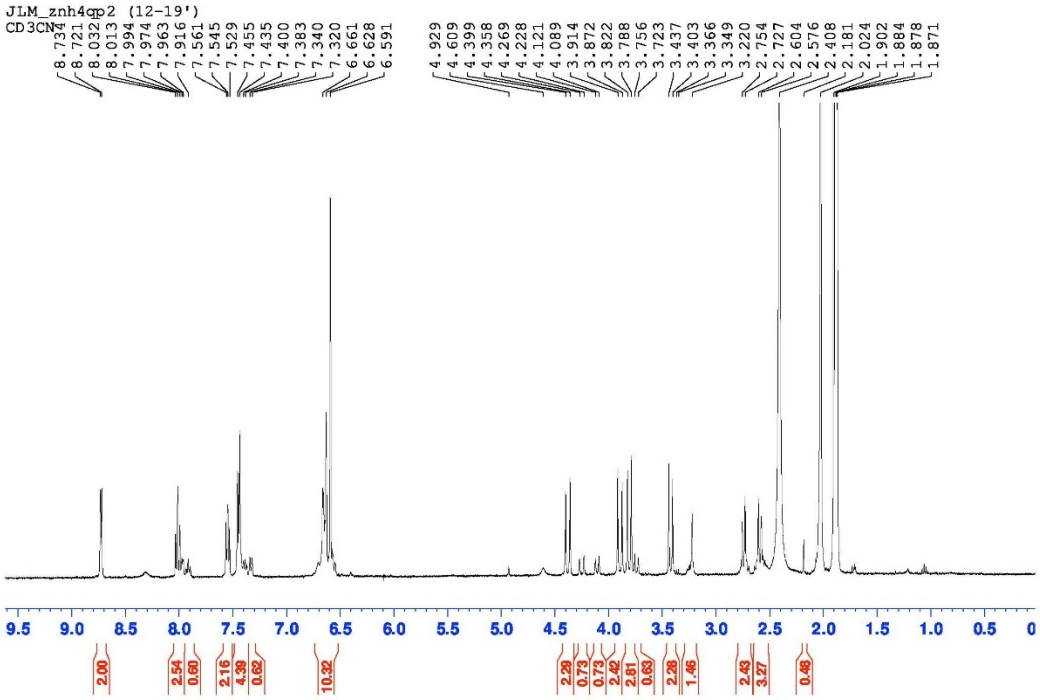

Figure C1. ^{1}H NMR spectrum of a crystalline sample of [Zn(H_4qp2)](OTf)$_2$ (**2**) in CD_3CN (400 MHz, 293 K). Solvent peaks from diethyl ether (1.21, 3.82), water (2.02) and MeCN (1.88) are present.

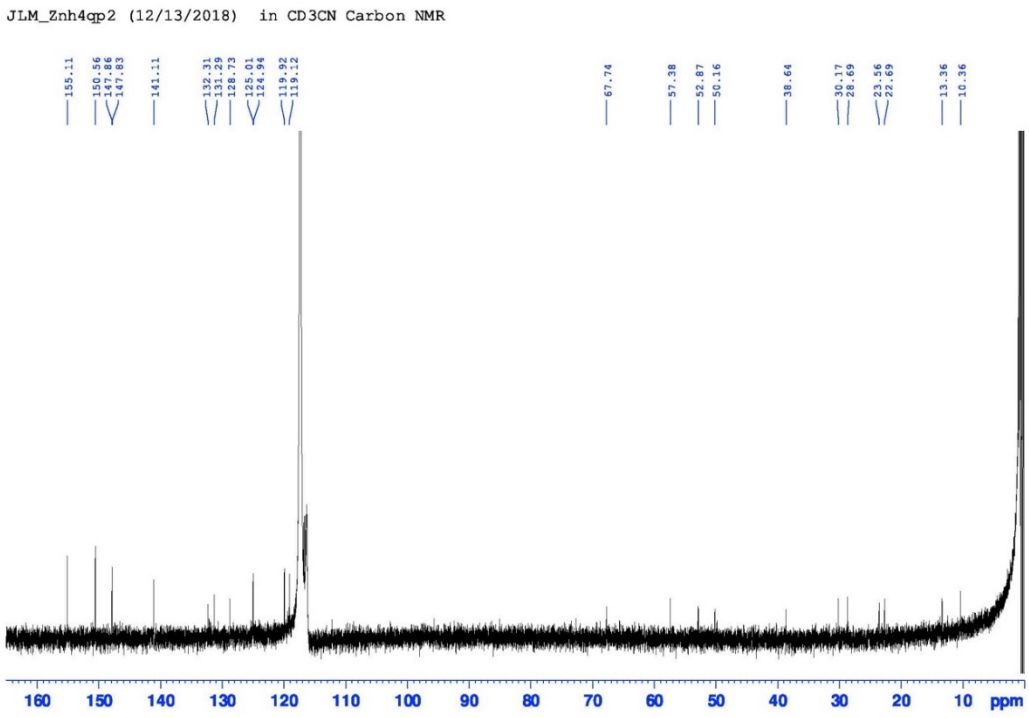

Figure C2. ^{13}C NMR spectrum of a crystalline sample of **2** in CD_3CN (100 MHz, 293 K). Solvent peaks from diethyl ether (13.36, 67.74), MeOH (50.16), and MeCN (117.35) are present.

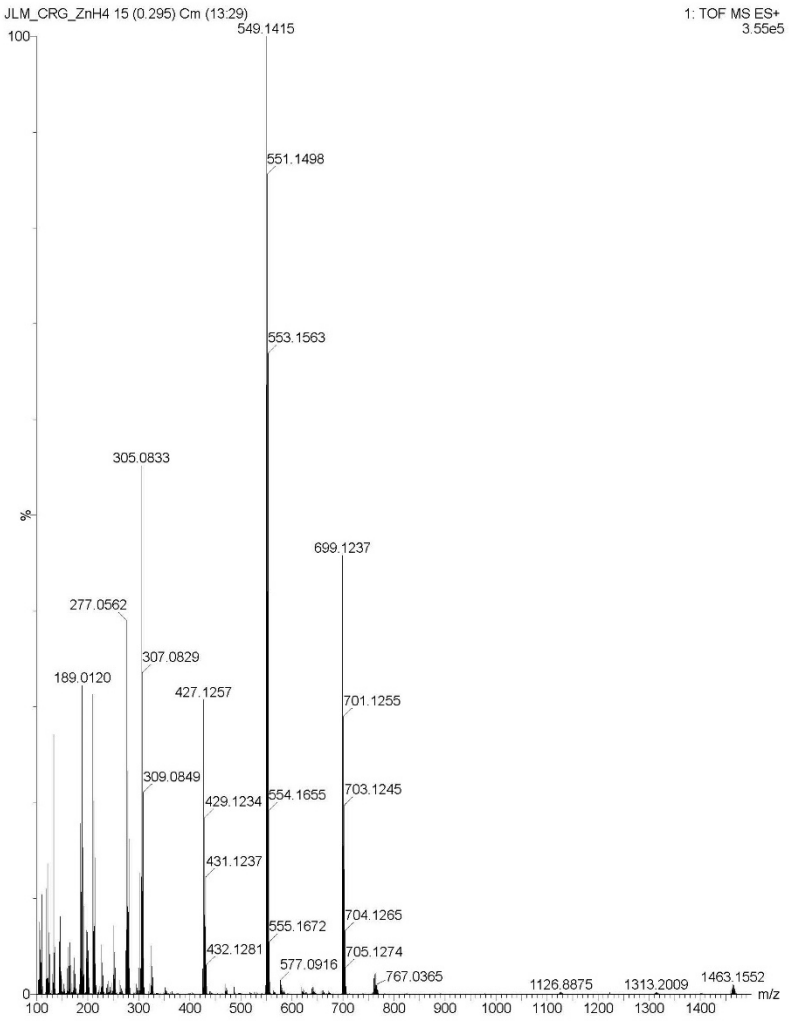

Figure C3. Mass spectrometry (ESI) for [Zn(H4qp2)(OTf)](OTf) (**2**) in MeCN. The *m/z* feature at 549.1415 is assigned to $[Zn(H_3qp2)]^+$ (calculated *m/z* = 549.1481). The feature at 699.1237 is assigned to $[Zn(H_4qp2)(OTf)]^+$ (calculated *m/z* = 699.1079).

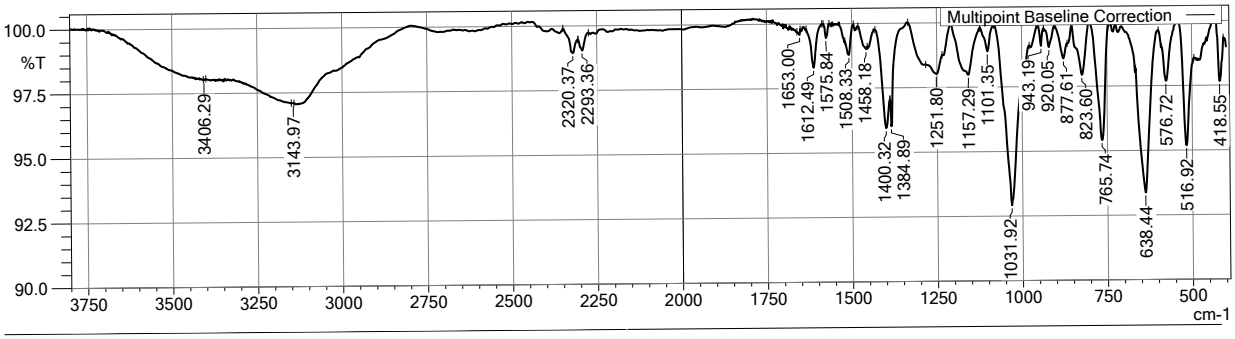

Figure C4. IR spectrum of **2** (KBr).

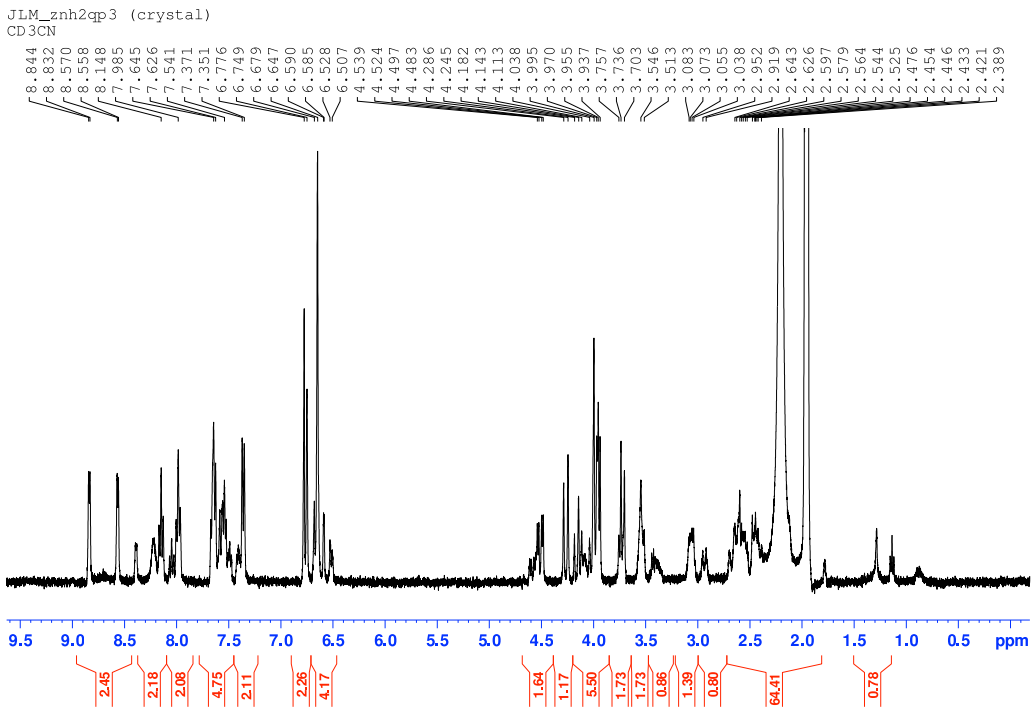

Figure C5. ^{1}H NMR spectrum of a crystalline sample of [Zn(H$_2$qp3)(H$_2$O)](OTf)$_2$ (**3**) in CD$_3$CN (400 MHz, 293 K). Solvent peaks from diethyl ether (1.29, 3.97), water (2.21), and MeCN (1.95) are present.

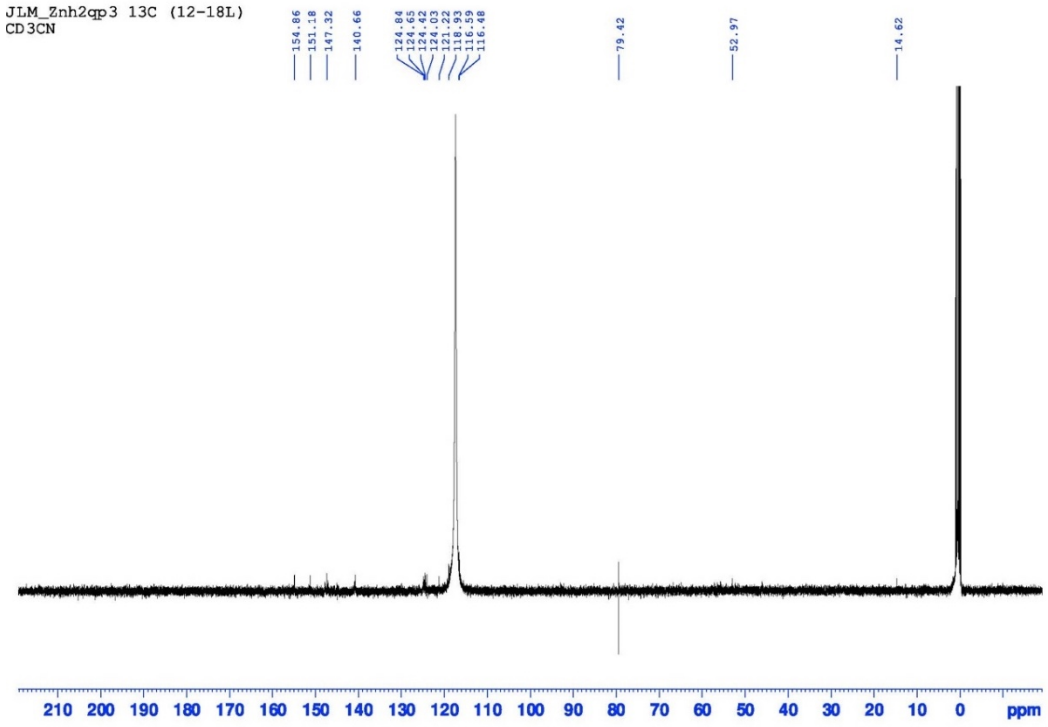

Figure C6. ^{13}C NMR spectrum of a crystalline sample of **3** in CD$_3$CN (100 MHz, 293 K). Solvent peaks from diethyl ether (79.42, 14.62) and MeCN (118.93) are present.

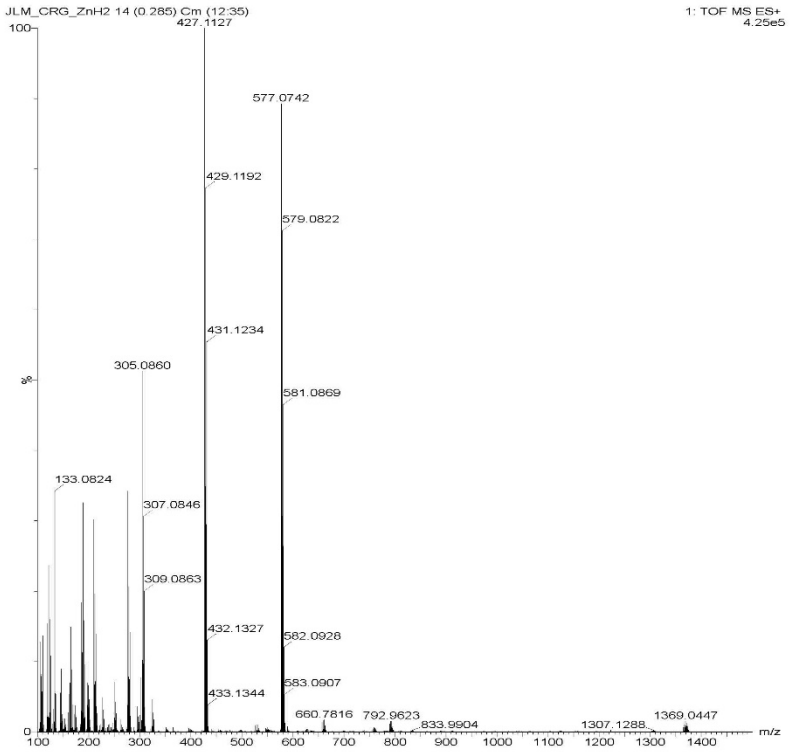

Figure C7. Mass spectrometry (ESI) for **3** in MeCN. The *m/z* feature at 427.1127 is assigned to $[Zn(Hqp3)]^+$ (calculated *m/z* = 427.1113). The feature at 577.0742 is assigned to $[Zn(H_2qp3)(OTf)]^+$ (calculated *m/z* = 577.0711).

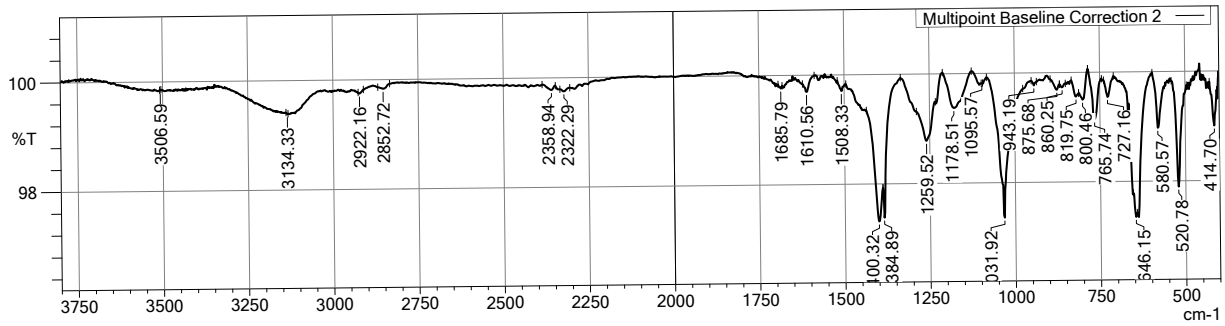

Figure C8. IR spectrum of **3** (KBr).

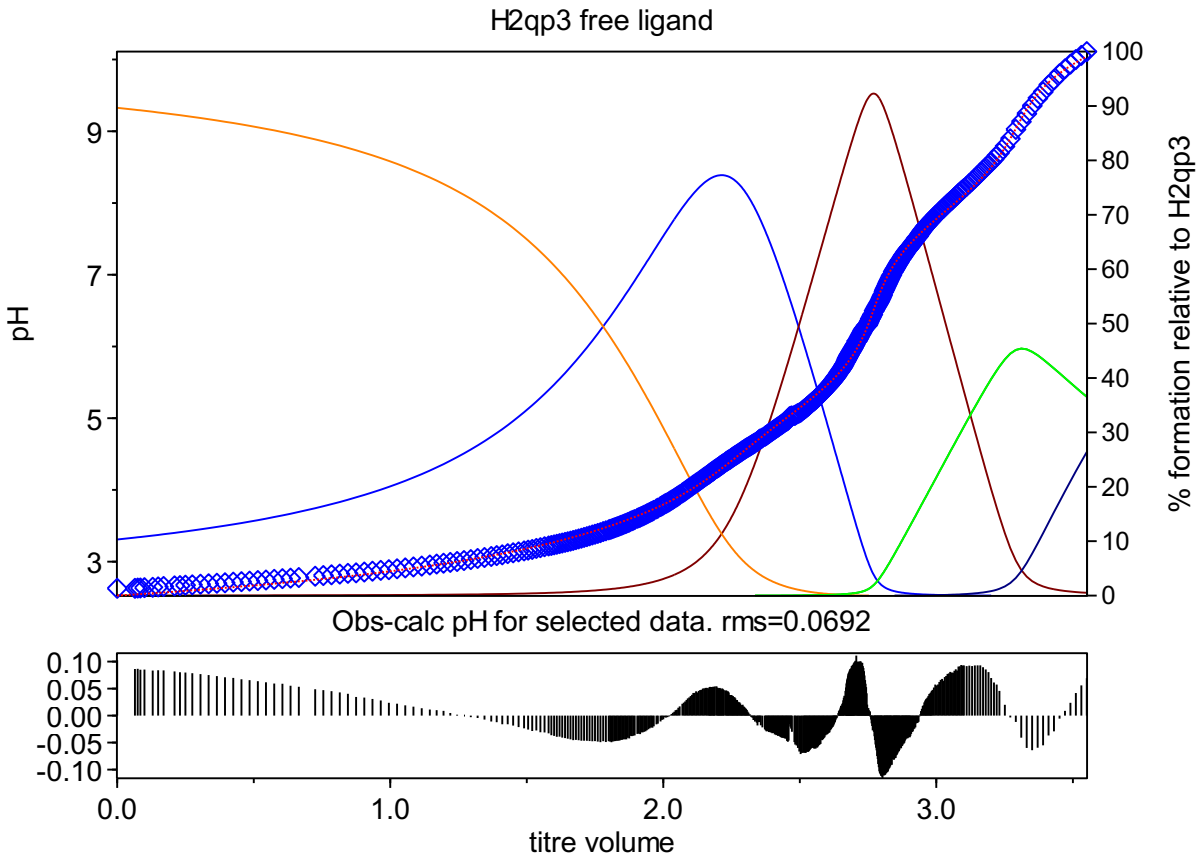

Figure C9. Hyperquad model (red line) overlaid on the experimental data from a potentiometric pH titration (blue) of the H_2qp3 ligand in water. For the titration, 0.1 M KOH was added to an acidic aqueous solution containing 0.1 M KCl and 1.0 mM H_2qp3 at 25 °C under an Argon atmosphere. The residuals for the fit are provided below. The curves represent the formation of $[H_5qp3]^{3+}$ (orange), $[H_4qp3]^{2+}$ (blue), $[H_3qp3]^{+}$ (purple), $[H_2qp3]$ (green), and $[Hqp3]^{-}$ (indigo).

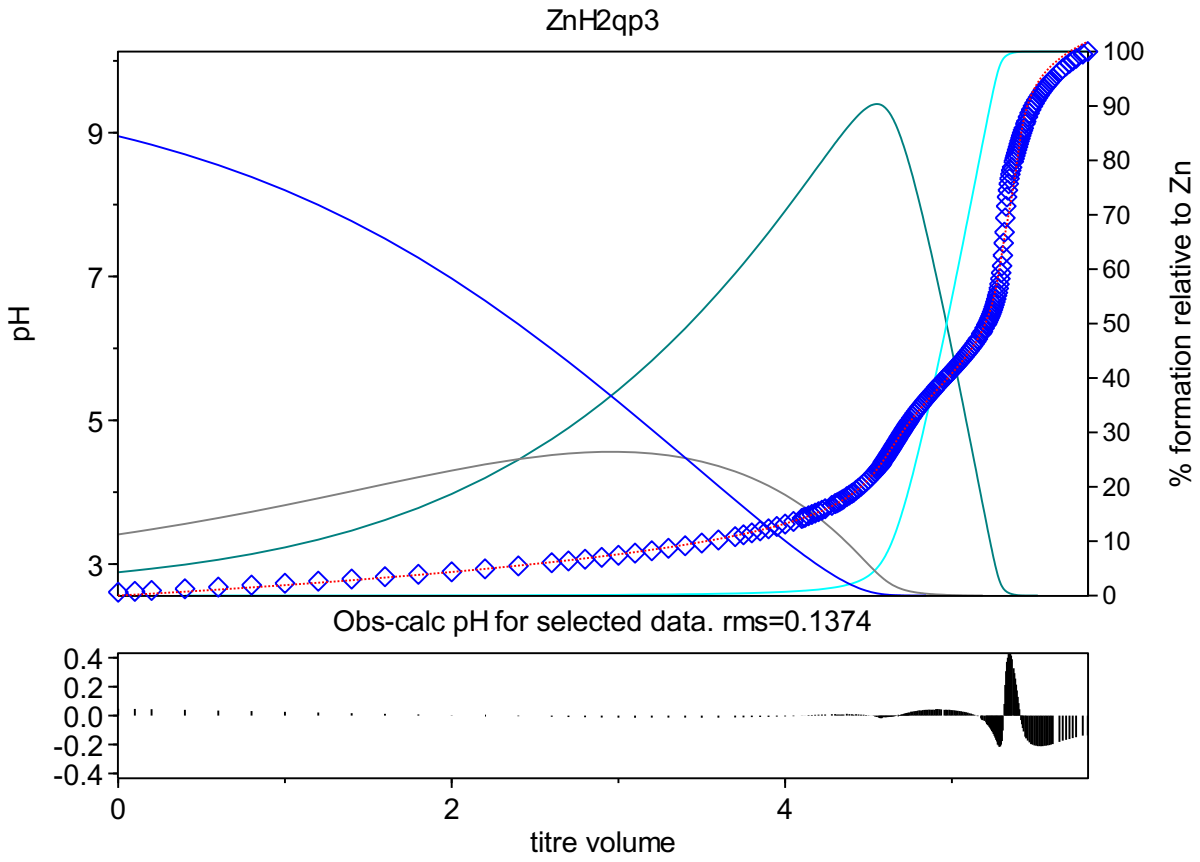

Figure C10. Hyperquad model (red line) overlaid on the experimental data from a potentiometric pH titration (blue) of a 1:1 mixture of $Zn(OTf)_2$ and H_2qp3 ligand in water. For the titration, 0.1 M KOH was added to an acidic aqueous solution containing 0.1 M KCl, 1.0 mM $Zn(OTf)_2$, and 1.0 mM H_2qp3 at 25 °C under an Argon atmosphere. The residuals for the fit are provided below. The curves represent the formation of free Zn(II) (blue), $[Zn(H_3qp3)]^{3+}$ (gray), $[Zn(H_2qp3)]^{2+}$ (pine green), and $[Zn(Hqp3)]^{+}$ (light blue).

Table C1: Parameters for the Hyperquad models used in Figures C9 and C10.

Species	H^+	(H_2qp3)	Zn^{2+}	log(β)	Derived Values
$(Hqp3)^-$	-1	1	0	-10.182 (±0.3)	
(H_2qp3)	0	1	0	0.00	pK_{L1} = 10.2 (±0.3)[a]
$(H_3qp3)^+$	1	1	0	8.1908 (±0.05)	pK_{L2} = 8.19 (±0.05)[a]
$(H_4qp3)^{2+}$	2	1	0	13.3226 (±0.05)	pK_{L3} = 5.13 (±0.05)[a]
$(H_5qp3)^{3+}$	3	1	0	16.7886 (±0.3)	pK_{L4} = 3.5 (±0.3)[a]
$[Zn(Hqp3)]^+$	-1	1	1	5.5659 (±0.05)	log K(ZnHqp3) = 15.75[b]
$[Zn(H_2qp3)]^{2+}$	0	1	1	11.1351 (±0.05)	pK_{a1} = 5.57 (±0.10)[c], log K(ZnH_2qp3) = 11.14[b]
$[Zn(H_3qp3)]^{3+}$	1	1	1	14.1158 (±0.1)	pK_{a2} = 2.98 (±0.15)[c] log K(ZnH_3qp3) = 5.93[b]

[a]Ligand pK_a values correspond to the following equilibrium constants:

$K_{L1} = [(Hqp3)^-][H^+]/[(H_2qp3)]$, $pK_{L1} = \log\beta_{010} - \log\beta_{-110}$.

$K_{L2} = [(H_2qp3)][H^+]/[(H_3qp3)^+]$, $pK_{L2} = \log\beta_{110} - \log\beta_{010}$.

$K_{L3} = [(H_3qp3)^+][H^+]/[(H_4qp3)^{2+}]$, $pK_{L3} = \log\beta_{210} - \log\beta_{110}$.

$K_{L4} = [(H_4qp3)]^{2+}[H^+]/[(H_5qp3)^{3+}]$, $pK_{L4} = \log\beta_{310} - \log\beta_{210}$.

[b]Metal complex stability constants correspond to the following equilibrium constants:

$K(ZnHqp3) = [[Zn(Hqp3)]^+]/[Zn^{2+}][Hqp3^-]$

$K(ZnH_2qp3) = [[Zn(H_2qp3)]^{2+}]/[Zn^{2+}][H_2qp3]$

$K(ZnH_3qp3) = [[Zn(H_3qp3)^{3+}]]/[Zn^{2+}][H_3qp3^+]$

[c]Metal complex pK_a values correspond to the following equilibrium constants:

$K_{a1} = [[Zn(Hqp3)]^+][H^+]/[[Zn(H_2qp3)]^{2+}]$, $pK_{a1} = \log\beta_{011} - \log\beta_{-111}$.

$K_{a2} = [[Zn(H_2qp3)]^{2+}][H^+]/[[Zn(H_3qp3)^{3+}]]$, $pK_{a12} = \log\beta_{111} - \log\beta_{011}$.

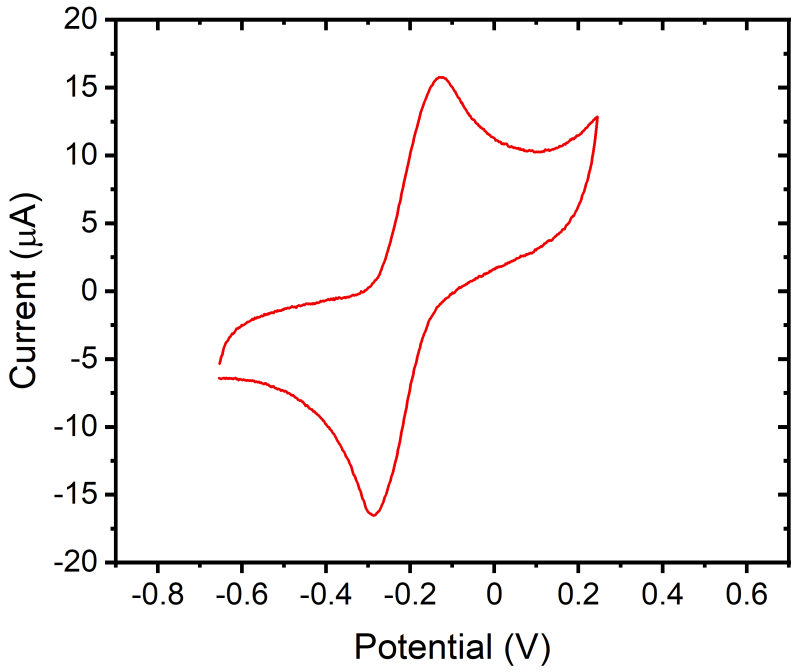

Figure C11. Cyclic voltammetry of 1.0 mM **2** in 0.10 M phosphate buffer (NaH_2PO_4/Na_2HPO_4, pH 7.0). The scan rate was 100 mV/s. $E_{1/2}$ = 196 mV vs. Ag/AgCl (saturated KCl) or 397 mV vs NHE, ΔE_p = 208 mV.

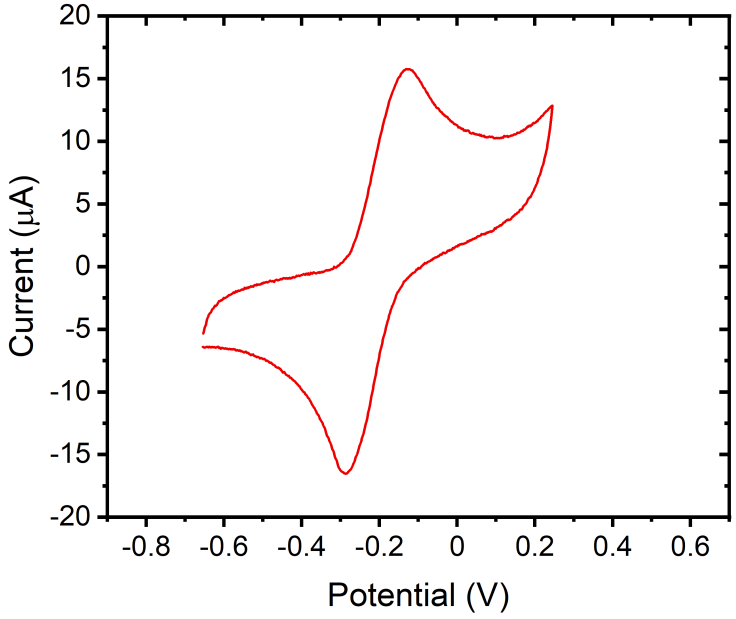

Figure C12. Cyclic voltammetry of 1.0 mM **3** in 0.10 M phosphate buffer (NaH_2PO_4/Na_2HPO_4, pH 7.0). The scan rate was 100 mV/s. $E_{1/2}$ = 150 mV vs. Ag/AgCl (saturated KCl) or 347 mV vs NHE, ΔE_p = 166 mV.

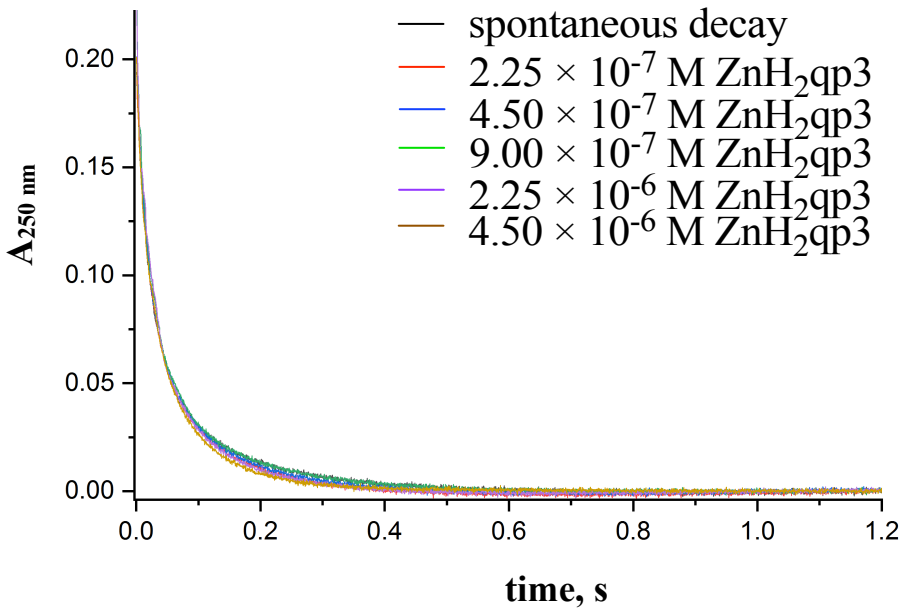

Figure C13. Kinetic traces of superoxide decomposition at 250 nm (60 mM MOPS buffer, pH 7.4 ionic strength of 150 mM) by **3**. The addition of **3** does not have a noticeable impact on the rate of superoxide decay.

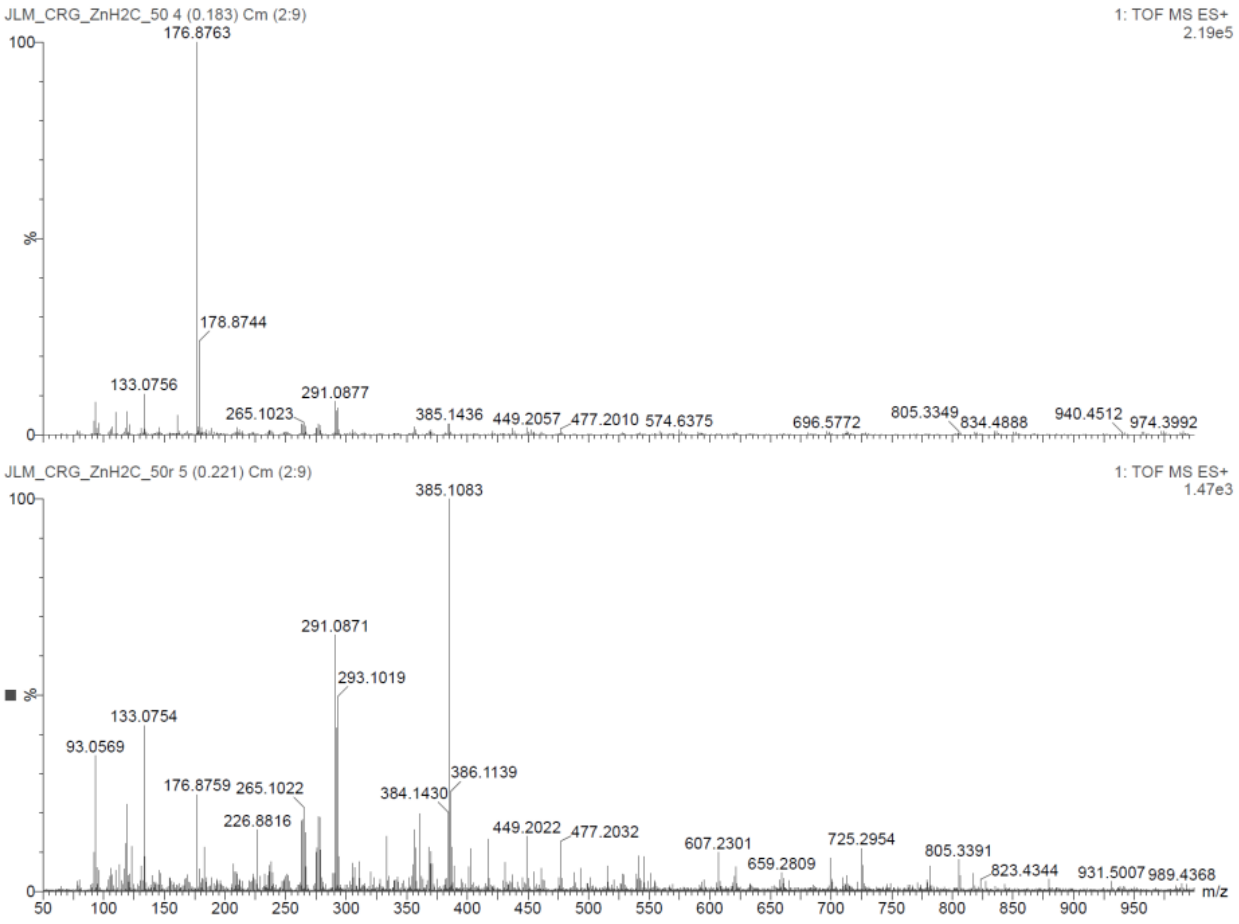

Figure C14. Mass spectrometry analysis of the reaction between **3** and 50 equiv. of KO_2 in carbonate-buffered water (pH 8.1). The 385.1083 *m/z* peak is assigned to the sodium salt of the oxidized *para*-quinone form of the ligand (qp3): $[Na(qp3)]^+$. Note the absence of the 427.1194 *m/z* peak associated with $[Zn(Hqp3)]^+$ and a peak at 213.0517 that would be associated with $[Zn(qp3)]^+$.

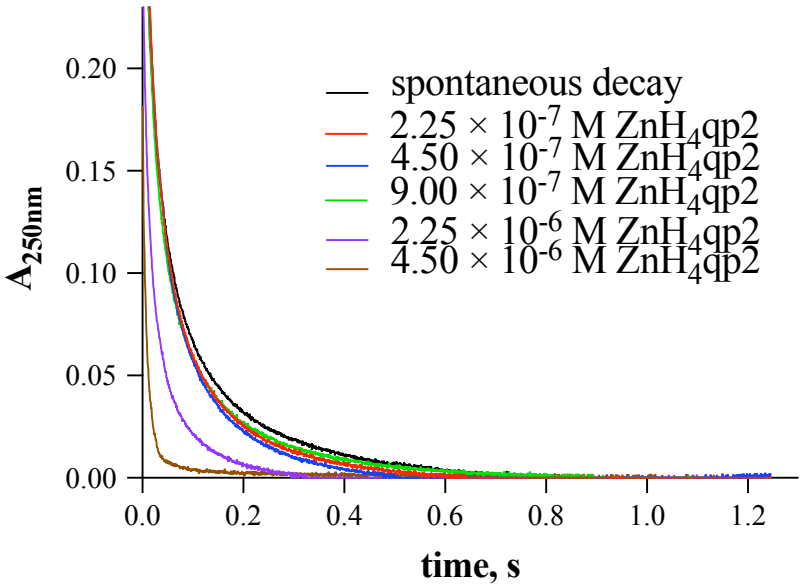

Figure C15. Kinetic traces of superoxide decomposition at 250 nm (50 mM phosphate buffer, pH 7.4 ionic strength of 150 mM) by **2.**

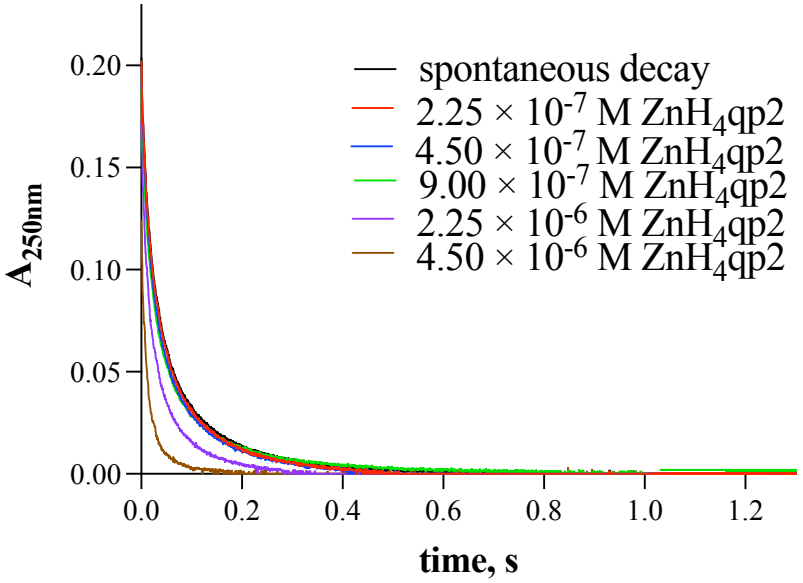

Figure C16. Kinetic traces of superoxide decomposition at 250 nm (60 mM MOPS buffer, pH 7.4 ionic strength of 150 mM) by **2.**

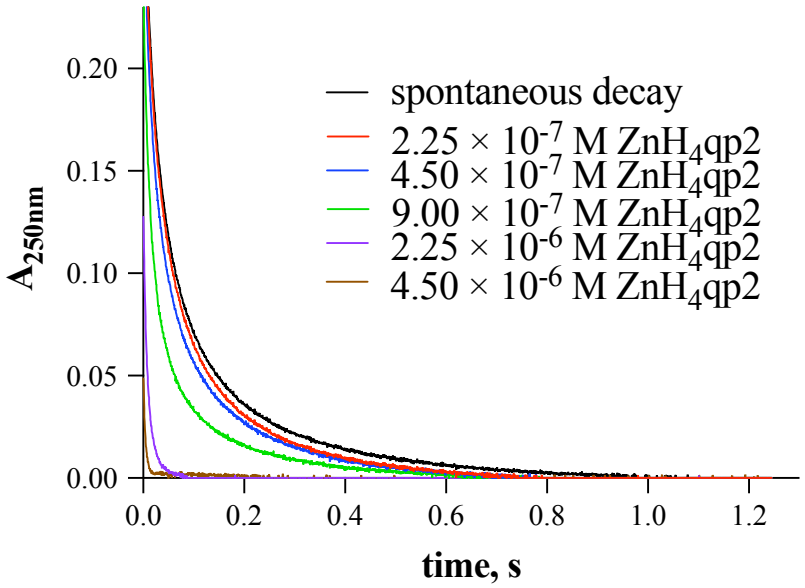

Figure C17. Kinetic traces of superoxide decomposition at 250 nm (60 mM MOPS buffer, pH 7.8 ionic strength of 150 mM) by **2.**

References

(1) Ahmed, M. I.; Gladden, J. D.*; et al. Journal of the American College of Cardiology* **2010**, *55*, 671.

(2) Fearon, I. M.; Faux, S. P. *Journal of Moleuclar and Cellular Cardiology* **2009**, *47*, 372.

(3) Eskici, G.; Axelsen, P. H. *Biochemistry* **2012**, *51*, 6289.

(4) Kinnula, V. L. *Current Drug Targets Inflammation & Allergy* **2005**, *4*, 465.

(5) AbdulSalam, S. F.; Thowfeik, F. S.*; et al. Biochemistry* **2016**, *55*, 5341.

(6) Mosley, R. L.; Benner, E. J.*; et al. Clinical Neuroscience Research* **2006**, *6*, 261.

(7) Laforge, M.; Elbim, C.*; et al. Nature Reviews Immunology* **2020**, *20*, 515.

(8) Abouhashem, A. S.; Singh, K.*; et al. Antioxidants & Redox Signaling* **2020**, *33*, 59.

(9) Riley, D. P.; Weiss, R. H. *Journal of the American Chemical Society* **1994**, *116*, 387.

(10) Riley, D. P.; Schall, O. F. *Adv. Inorganic Chemistry* **2006**, *59*, 233.

(11) Riley, D. P.; Lennon, P. J.*; et al. Journal of the American Chemical Society* **1997**, *119*, 6522.

(12) Riley, D. P. *Chemical Reviews* **1999**, *99*, 2573.

(13) Tovmasyan, A.; Carballal, S.*; et al. Inorganic Chemistry* **2014**, *53*, 11467.

(14) Batinic-Haberle, I.; Reboucas, J. S.*; et al. Antioxidants & Redox Signaling* **2010**, *13*, 877.

(15) Batinic-Haberle, I.; Rajic, Z.*; et al. Free Radical Biology & Medicine* **2011**, *51*, 1035.

(16) Abreu, I. A.; Cabelli, D. E. *Biochimica et Biophysica Acta* **2010**, *1804*, 263.

(17) Robinett, N. G.; Peterson, R. L.*; et al. Journal of Biological Chemistry.* **2018**, *293*, 4636.

(18) Potter, S. Z.; Zhu, H.*; et al. Journal of the American Chemical Society* **2007**, *129*, 4575.

(19) Ellerby, L. M.; Cabelli, D. E.*; et al. Journal of the American Chemical Society* **1996**, *118*, 6556.

(20) Yu, M.; Beyers, R. J.*; et al. Inorganic Chemistry* **2012**, *51*, 9153.

(21) Yu, M.; Ward, M. B.*; et al. Inorganic Chemistry* **2017**, *56*, 2812.

(22) Yu, M.; Ambrose, S. L.*; et al. Journal of the American Chemical Society* **2014**, *136*, 12836.

(23) Kenkel, I.; Franke, A.*; et al. Journal of the American Chemical Society* **2017**, *139*, 1472.

(24) Ward, M. B.; Scheitler, A.*; et al. Nature Chemistry* **2018**, *10*, 1207.

(25) Friedel, F. C.; Lieb, D.*; et al. Journal of Inorganic Biochemistry* **2012**, *109*, 26.

(26) Lieb, D.; Friedel, F. C.*; et al. Inorganic Chemistry* **2013**, *52*, 222.

(27) Irving, H.; Williams, R. J. P. *Journal of the Chemical Society* **1953**, 3192.

(28) Martell, A. E. *Critical Stability Constants*; Plenum Press: New York, NY, 1974.

(29) Batinic-Haberle, I.; Spasojevic, I. In *Porphyrin Science by Women: In 3 Volumes*; World Scientific: 2019, p 197.

(30) Salvemini, D.; Wang, Z.-Q.*; et al. Science* **1999**, *286*, 304.

(31) Aston, K.; Rath, N.*; et al. Inorganic Chemistr y***2001**, *40*, 1779.

(32) Gans, P.; Sabatini, A.*; et al. Talanta* **1996**, *43*, 1739.

(33) McCord, J. M.; Fridovich, I. *Journal of Biological Chemistry* **1969**, *244*, 6049.

(34) Kedare, S. B.; Singh, R. P. *Journal of Food Science and Technology* **2011**, *48*, 412.

(35) Blois, M. S. *Nature* **1958**, *181*, 1199.

(36) Milaeva, E. R.; Shpakovsky, D. B.*; et al. Dalton Transactions* **2013**, *42*, 6817.

(37) Chan, T.-L.; Mak, T. C. W. *Journal of the Chemical Society, Perkin Transactions 2* **1983**, 777.

(38) Iranzo, O. *Bioorganic Chemistry* **2011**, *39*, 73.

(39) Ancerewicz, J.; Migliavacca, E.*; et al. Free Radical Biology & Medicine* **1998**, *25*, 113.

(40) Fridovich, I. *Journal of Biological Chemistry* **1997**, *272*, 18515.

(41) Liochev, S. I. *Chemical Research in Toxicology* **2013**, *26*, 1312.

(42) Riley, D. P.; Rivers, W. J.*; et al. Analytical Biochemistry* **1991**, *196*, 344.

(43) Liochev, S. I.; Fridovich, I. *Archives of Biochemistry and Biophysics* **1997**, *337*, 115.

(44) Shannon, R. D. *Acta Cryst.* **1976**, *A32*, 751.

(45) Gale, E. M.; Mukherjee, S.*; et al. Inorganic Chemistry* **2014**, *53*, 10748.

(46) Bergwitz, C.; Jüppner, H. *Advances in Chronic Kidney Disease* **2011**, *18*, 132.

(47) Bevington, A.; Mundy, K. I.*; et al. Clinical Science* **1986**, *71*, 729.

Chapter 5

Gallium(III) Complex with a Polydentate Quinol-Containing Ligand Displays High Catalase Activity

*This chapter is a revision of a manuscript in preparation by the following authors: Jamonica L. Moore, Julian Oppelt, D. Schwartz, Ivana Ivanović-Burmazović, and Christian R. Goldsmith.

5.1 Introduction

Reactive oxygen species (ROS), such as superoxide ($O_2^{\cdot-}$) and hydrogen peroxide (H_2O_2), are produced when electrons leak from side reactions in cellular processes, such as the mitochondrial electron transport chain or the tricarboxylic acid cycle, or when enzymes that activate dioxygen fail to fully reduce it. Excessive production of ROS results in oxidative stress, a state of aberrant redox homeostasis. Oxidative stress can result in cellular damage and is prevalent in an extensive array of health disorders.[1-6] Although a link between ROS and oxidative stress has been established, how these contribute to the progression of various inflammatory, neurological, and cardiovascular disorders remains unresolved. Although researchers are still understanding how ROS contribute to disease, the development of small molecule antioxidants capable of correcting aberrant oxidative activity is almost certain to benefit modern medicine. One attractive strategy is for the synthetic antioxidant to resemble an enzyme that the body itself uses to regulate ROS concentrations. A small dose of such an antioxidant would alleviate oxidative stress by catalytically degrading one or more sorts of ROS. Investigated antioxidants include functional mimics of superoxide dismutases (SODs), which use either manganese, iron, nickel, or copper to catalyze the degradation of $O_2^{\cdot-}$.[7-13] This process forms H_2O_2, which is more stable than superoxide but nonetheless a strong two-electron oxidant. Although it is certainly not as reactive as $^{\cdot}OH$, high concentrations of H_2O_2 can kill cells by overwhelming protective disproportionation pathways and inducing damaging pathophysiological events. ROS scavengers, such as the metalloenzymes catalase (CAT), glutathione peroxidase and glutathione reductase, assist in controlling the production and/or elimination of ROS. One of the enzymes, CAT, dismutates H_2O_2 through alternating two-electron oxidations and reductions to yield O_2 and H_2O (Scheme 5.1). Although many sequences of catalase exist, in biological systems, enzymes with catalase activity rely on one

of three types of cofactors: heme (iron-porphyrin), a binuclear manganese center, or a binuclear iron center. All cofactors function to catalyze the degradation of H_2O_2.[14-19] Bioinspired mimics of CAT typically resemble one of the two, with most examples being dimanganese complexes.[20,21]

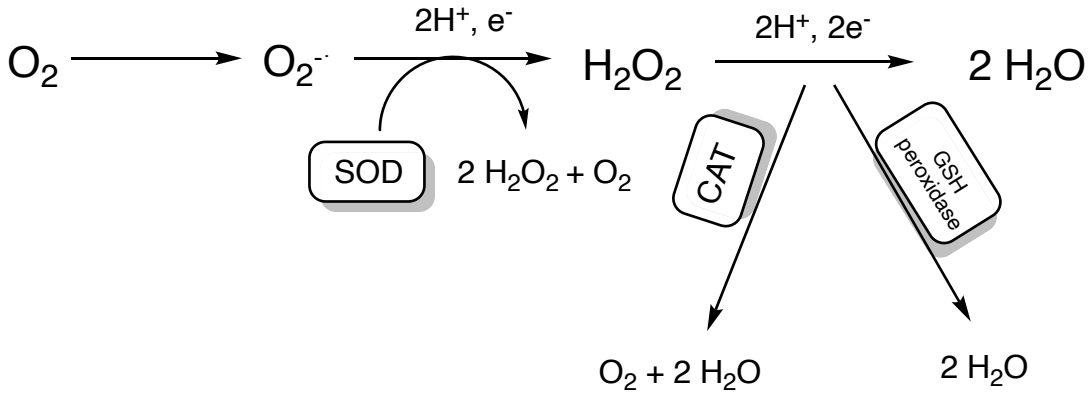

Scheme 5.1 Reduced depiction of oxygen reduction with enzymes involved in ROS elimination and detoxification.

Early research from our laboratory established three Mn(II)-containing magnetic resonance imaging contrast agent sensors for H_2O_2 that could also serve as catalysts for $O_2^{-\cdot}$ degradation.[22-24] Two of these probes contain quinol portions that reversibly oxidize to *para*-quinones upon reaction with excess $O_2^{-\cdot}$ or H_2O_2 (Scheme 5.2).[22,24] Rather than the transition metal being the sole oxidant/reductant, the quinol in the ligands can act as the redox partner for $O_2^{-\cdot}$ disproportionation. Analogous Zn(II) complexes with *N*-(2,5-dihydroxybenzyl)-*N,N',N'*-tris(2-pyridinylmethyl)-1,2-ethanediamine (H_2qp1) and *N,N'*-(2,5-dihydroxybenzyl)-*N,N'*-bis(2-pyridinylmethyl)-1,2-ethanediamine (H_4qp2, Scheme 5.3) are viable catalysts, with activity comparable to Mn-containing SOD mimics.[25,26] Both compounds have enhanced activity in phosphate buffer which distinguishes these from Mn-containing SOD mimics and may make them more suitable for *in vivo* applications.[27-29] Since Zn(II) is redox-inactive, the quinol moiety is necessarily the relevant redox partner for $O_2^{-\cdot}$. The quinol can cycle through three different oxidation states: the starting quinol, quinoxyl radical, and *para*-quinone (Scheme 5.2). The activity of the Zn(II) compounds demonstrates that a redox-active ligand can fulfill the role of a redox-active

transition metal ion in traditional SOD mimicry. Simply mixing quinol and Zn(II) fails to have the same effect; the ligand must remain tightly bound to the metal. The Zn(II) compound with *N*-(2,5-dihydroxybenzyl)-*N,N'*-bis(2-pyridinylmethyl)-1,2-ethanediamine (H_2qp3, Scheme 5.3) is catalytically inactive, and we currently believe that the initial oxidation by superoxide weakens the binding affinity of the ligand enough to dissociate the complex, halting catalysis.

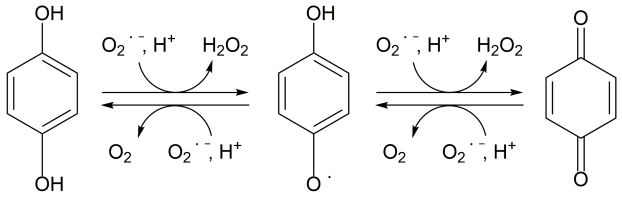

Scheme 5.2 Oxidative states attainable by quinol moiety of ligand.

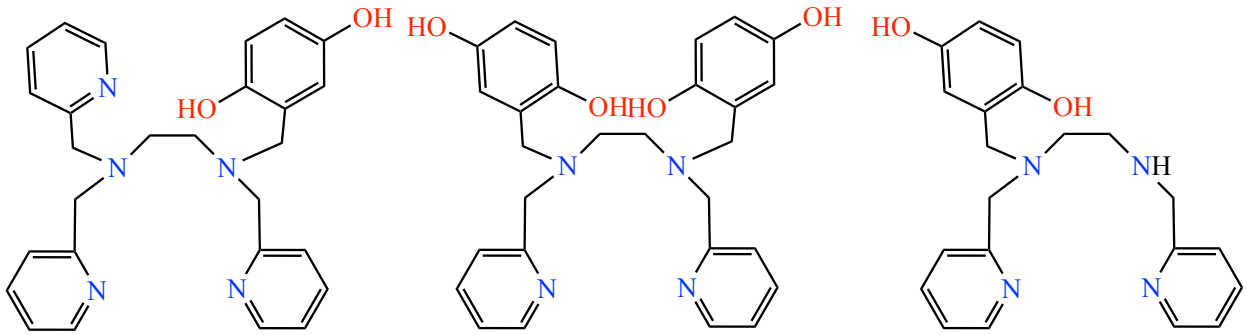

H_2qp1 H_4qp2 H_2qp3

Scheme 5.3 Ligands used to prepare compounds assessed in this study.

Understanding how molecular structure impacts function is an essential prerequisite to the development of even better catalysts for ROS dismutation. With other classes of SOD mimics, more positively charged species tend to be more active due to their ability to better draw in superoxide anions. The charge of the complexes can be readily increased by simply substituting a tricationic metal ion for Zn(II). In the current chapter, we have therefore prepared Ga(III) complexes with H_2qp1, H_4qp2, and H_2qp3.

Initial structural characterization and antioxidant studies were done for all three complexes, but the aqueous chemistry and SOD mimicry were only assessed for the Ga(III) compounds with H_2qp1 and H_2qp3. The Ga(III)-H_2qp1 complex was found to protect cells against H_2O_2 toxicity and was subsequently investigated as a catalase mimic. Although the Ga(III)-H_2qp1 complex (**1**) does not function as an SOD mimic, it appears to be capable of dismutating H_2O_2 to O_2 and water, just like CAT.

5.2 Experimental Section

Materials

All chemicals and solvents were purchased from Sigma-Aldrich and used as received unless otherwise noted. 2,2-Diphenyl-1-picryl-hydrazyl hydrate (DPPH) was supplied by EMD Millipore. All deuterated solvents were bought from Cambridge Isotopes. Diethyl ether (ether) and methanol (MeOH) were bought from Fisher. Methylene chloride (CH_2Cl_2) was purchased from Mallinckrodt Baker. *N*-(2,5-Dihydroxybenzyl)-*N,N',N'*-tris(2-pyridinylmethyl)-1,2-ethanediamine (H_2qp1), *N,N'*-Bis(2,5-dihydroxybenzyl)-*N,N'*-bis(2-pyridinylmethyl)-1,2-ethanediamine (H_4qp2), and *N*-(2,5-dihydroxybenzyl)-*N,N'*-bis(2-pyridinylmethyl)-1,2-ethanediamine (H_2qp3) were previously prepared.[22,24]

Instrumentation

All ^{1}H and ^{13}C NMR spectra were recorded on a 500 MHz or 600 mHz AVANCE Bruker NMR spectrometer. In each spectrum, the reported NMR resonance peak frequencies were referenced to internal standards. Optical data were collected on a Varian Cary 50 spectrophotometer and analyzed using software from the WinUV Analysis Suite. High-resolution mass spectrometry (HR-MS) data were obtained at the Mass Spectrometer Center at Auburn University on a Waters Q-ToF Premier or ThermoFisher Orbitrap Exploris 120 mass spectrometer

via electrospray operated in the positive ion mode. Infrared spectroscopy (IR) data were obtained using attenuated total reflectance Fourier transform infrared ATR-FTIR spectroscopy (Nicolet iS-50 with built-in ATR). For ATR-FTIR measurements, a small amount of solid was placed directly on diamond ATR crystal. Cyclic voltammetry (CV) was performed under N_2 at 294 K using an Gamry 1010E potentiostat or Pine WaveDriver 20 (SN 3716404), a glassy carbon working electrode, a platinum wire auxiliary electrode, and a silver/silver(I) chloride reference electrode. All elemental analyses (C, H, N) were performed by Atlantic Microlabs (Norcross, GA); crystalline samples were dried under vacuum and placed under a N_2 atmosphere prior to shipment.

Potentiometric Titrations

The speciation chemistry of the Ga(III) complexes in water was assessed using a METROHM 765 Dosimat with a jacketed, airtight glass titration vessel. A Mettler Toledo SevenCompact pH meter S220 with pH electrode InLab Routine Pro-ISM was used to determine the pH of the sample solutions during the titrations. The electrode was calibrated before each titration using commercially available standard solutions buffered to pH 4.0, 7.0, and 10.0. All samples were purged with argon prior to analysis and subsequently analyzed under an argon atmosphere at 25 °C. All solution samples were prepared in solutions of 100 mM KCl in deionized Millipore water. The titrations investigating metal-ligand speciation were run with solutions that contained a 1:1 molar mixture of the ligand and $Ga(OTf)_3$. Carbonate-free solutions of 0.10 M KOH and 0.10 M HCl were prepared using argon-saturated deionized Millipore water. Initially, we estimated pK_a values through visual inspection of the data plotted in KaleidaGraph v. 4.0. We subsequently attempted to analyze and fit the data to speciation models using the Hyperquad2006 program.[30]

Analysis of the Antioxidant Properties of the Coordination Complexes

We previously screened the abilities of other coordination complexes to catalytically degrade superoxide using the xanthine oxidase/hypoxanthine/lucigenin assay.[22,24,31] Superoxide was generated *in situ* from a reaction between xanthine and xanthine oxidase. A subsequent reaction between $O_2^{-\cdot}$ and lucigenin provides a spectroscopic signal that can be used to quantify an antioxidant's ability to degrade $O_2^{-\cdot}$. The copper/zinc superoxide dismutase isolated from bovine erythrocytes (0.001-100 U/ml, Calbiochem) served as a positive control. Each assay was carried out in a total volume of 250 μL containing 10 mM PBS (pH 7.4), hypoxanthine (80 μM), xanthine oxidase (0.008 mg/mL or 0.004 U/ml, Calbiochem) and dark-adapted lucigenin (16 μM) in the presence of either the studied Ga(III) complex (0.04 nM – 0.4 mM)) or its vehicle. Reactions were carried out at room temperature and were initiated by the addition of xanthine oxidase to the hypoxanthine-containing solution. Luminescence was measured for ten consecutive reads of 120 s integrations after an initial delay of 3 s. The ten RLU values were averaged, and each concentration was expressed as a percent of RLU produced in the vehicle's presence. Each assay data point was performed in triplicate, and each assay was repeated three times.

We also assessed the antioxidant activities of the Ga(III) complexes through the DPPH assay (DPPH = 2,2-diphenyl-1-picrylhydrazyl radical hydrate).[32-34] In this assay, potential antioxidants are tested for their abilities to donate hydrogen atoms to the radical to generate the corresponding hydrazine. Aqueous solutions of either the Ga(III) complex or ascorbic acid were added to a solution of 0.10 mM DPPH in MeOH, such that the final reaction volume was 0.2 mL. Samples were incubated in the dark for 30 min at room temperature before being spectrophotometrically analyzed on a Molecular Devices Spectramax Plus. The absorbance at 517

nm, the λ_{max} of the hydrazine product, was recorded. Experiments were performed in triplicate and repeated thrice.

Determination of in vitro *SOD Activity via Optical Stopped-Flow Methodology*

The ability of two of the Ga(III) complexes to catalytically degrade superoxide was more thoroughly tested by a direct method using stopped-flow techniques that has been more fully described in prior work from our laboratories.[27] Stopped-flow measurements were performed on a Biologic SFM-400 four syringe stopped-flow system using only the first three syringes and a Berger Ball mixer to minimize mixing effects between aqueous buffered solutions and DMSO solutions of KO_2. A J&M TIDAS S MMS UV/VIS diode array detector (integration time 0.5 ms, 180 nm – 720 nm wavelength) and an Energetiq LDLS ENQ EQ-99-FC laser driven light source were used.

Superoxide solutions were prepared by suspending 220 – 240 mg KO_2 in 20 mL dry DMSO. The suspension was stirred for at least 30 min under inert atmosphere before the suspension was filtered through a PTFE syringe filter (Ø = 0.45 μm) to give a saturated KO_2 solution, which was transferred to the stopped-flow setup. The potential SOD mimics (SODm) were dissolved in aqueous solutions buffered to either pH 7.4 or 8.1. The buffers were prepared from Millipore water and either 4-morpholinepropanesulfonic acid (MOPS) or sodium dihydrogen phosphate. The concentration of the buffer was 60 mM, and the ionic strength was adjusted to 150 mM for each solution through the addition of NaCl. All of the buffered solutions were treated with Chelex 100 sodium exchange resin for at least 24 h before use in order to remove adventitious metal ions. Stock solutions containing 0.10 mM of each tested SODm were prepared in each buffer; if necessary, the stock solution contained 10% DMSO to

ensure that the complexes dissolved fully. The stock solutions were diluted in buffer to give a series of SODm concentrations suitable for the stopped-flow experiments.

Kinetic measurements were performed adding a large excess of superoxide to the putative SOD mimetic: $[O_2^{\cdot-}]$ = 100 – 200 μM, [SODm] = 0.25 – 4.5 μM. The aqueous solution containing the studied Ga(III) complex was mixed in a 9:1 ratio with the superoxide solution in DMSO using a high-density mixer. In each experiment, the concentration of superoxide exceeded that of the zinc-containing catalyst by at least ten-fold to ensure catalytic conditions. All kinetic data were fitted with the program Biokine 32 V4.80. Each k_{obs} value represents an average of at least nine measurements. Each k_{cat} was determined from the slope of k_{obs} vs. [SODm]. All measurements were performed at 21 °C.

Measurements of H_2O_2 Dismutation

The decomposition of H_2O_2 (0.2 – 50 mM) were assessed by noting the changes in $[H_2O_2]$ over time at 240 nm, as described.[35] All measurements contained 50 nM SODm and were analyzed at room temperature in 100 mM phosphate pH 7.0. Catalase activity was analyzed by observing O_2 production over time using a Clark-type O_2-sensitive electrode (Hansatech, Pentney, Norfolk, UK), as described.[35] All reactions contained 10 – 100 nM SODm and were measured at room temperature in 200 mM phosphate buffer, pH 7.0. Data collection was acquired after 20 s, after which H_2O_2 was added to institute O_2 production.

Cytotoxicity Measurements

The cytotoxicity of the Ga(III)-H_2qp1 complex (**1**) and its ability to protect cells against oxidative stress were assessed with H9c2 (rat cardiac) cells. H9c2 cells were obtained from the American Type Culture Collection (Manassas, VA, USA) and grown at 37 °C with 95% humidity and 5% CO_2. Cells were grown in Dulbecco's modified Eagle's medium (DMEM) supplemented

with 10% fetal bovine serum. All experiments were performed at 70−80% confluence. To determine the cytotoxicity of **1**, H9c2 cells were exposed to increasing concentrations of the Ga(III) complex (0.01−1000 μM) or its vehicle in DMEM for 24 h or 48 h. Control wells without the coordination complex antioxidant were incubated under the same conditions. Cell number was assessed by the mitochondrial-dependent reduction of 3-(4,5-dimethylthiazol-2-yl)-2,5-diphenyltetrazolium bromide (MTT) to formazan. The cultures were incubated for 4 h at 37 °C and DMSO was subsequentially added. Formazan production was monitored at 570 nm and 630 nm using a SpectraMax iD5 microplate reader. Cell number was expressed as percentage of the vehicle-treated cells.

The aforementioned method was similarly used to determine the optimum dose of **1** for cytoprotection against H_2O_2-induced oxidative stress. In this procedure H9c2 cells, seeded as previously described, were exposed to three different concentrations of Ga(III) complex (1 – 100 μM) or its vehicle. Cells were then exposed to increasing concentrations of H_2O_2 and incubated for 24 h at 37 °C. Cell number was assessed using the MTT method and processing system as described above.

Syntheses

(*N*–(2,5-dihydroxybenzyl)-*N,N,N'*-tris(2-pyridinylmethyl)-1,2-ethanediamine)gallium(III) triflate ([Ga(H_2qp1)](OTf)$_2$, 1).

The H_2qp1 ligand (266 mg, 0.583 mmol) and Ga(OTf)$_3$ (302 mg, 0.583 mmol) were dissolved in 5 mL of acetonitrile (MeCN) under atmospheric conditions. The solution was stirred for 1 h at room temperature (RT). After this time, ether was gradually added to precipitate the product as a white powder (389 mg, 66%). CH_2Cl_2 was gradually added to a saturated solution of the product in MeOH to yield clumps of needle-like crystals. ^{1}H NMR (500 MHz, CD_3CN, 293

K): δ 8.91 (d, J = 5.2 Hz, 1H), 8.84 (d, J = 5.3 Hz, 1H), 8.30 – 8.27 (td, 1H), 8.10 – 8.06 (td, 1H), 7.88 – 7.84 (td, 1H), 7.82 – 7.78 (m, 2H), 7.61 (t, J = 6.4 Hz, 1H), 7.47 (d, J = 7.9 1H), 7.24 (q , J = 7.8 Hz, 2H), 6.66 (d, J = 5.6 Hz, 1H), 6.47 – 6.40 (m, 3H), 6.28 (d, J = 8.6 Hz, 1H), 4.78 (q, J = 16.3 Hz, 2H), 4.44 (d, J = 18.9 Hz, 1H), 4.29 (d, J = 18.6 Hz, 2H), 3.96 (d, J = 16.3 Hz, 1H), 3.82 (s, 2H), 3.66 (dd, J = 12.4, 2.0 Hz, 1H), 3.26 – 3.14 (m, 3H), 2.77 – 2.71 (td, 1H). ^{13}C NMR (125 MHz, CD_3CN, 293 K): δ 153.72, 152.96, 151.33, 148.89, 147.25, 146.94, 144.4, 143.87, 142.91, 142.36, 127.54, 127.25, 126.18, 125.84, 123.81, 123.00, 122.64, 120.84, 120.1, 118.46, 61.21, 60.91, 59.95, 57.94, 56.02, 54.81. Optical spectroscopy (MeCN, 293 K): 685 nm (ε = 130 M^{-1} cm^{-1}), 510 nm (ε = 150 M^{-1} cm^{-1}), 450 nm (ε = 191 M^{-1} cm^{-1}), 309 nm (ε = 1996 M^{-1} cm^{-1}), 263 nm (ε = 7463 M^{-1} cm^{-1}) 238 nm (ε = 4410 M^{-1} cm^{-1}). FTIR (cm^{-1}): 36003 (w), 3316 (m), 3098 (w), 2958 (w), 1614 (s), 1492 (s), 1435 (w), 1278 (s), 1250 (s), 1219 (s),1147 (s), 1054 (m), 1025 (s), 994 (m), 942 (w), 881 (w), 815 (s), 763 (m), 634 (s), 572 (w), 516 (m). MS (ESI): Calcd for $[Ga(qp1)]^+$, 522.1420, $[Ga(Hqp1)(OTf)]^+$, 672.1024; Found, 522.1385, 672.1042. Elemental analysis (crystals): Calcd for $C_{29}H_{29}N_5F_6O_8S_2Ga$•0.5 MeOH•0.5 Et_2O: C, 43.16%; H, 4.14%; N, 7.99%; Found: 43.18%; H, 4.04%; N, 8.41%.

(*N,N'*-Bis(2,5-dihydroxybenzyl)-*N,N'*-bis(2-pyridinylmethyl)-1,2-ethanediamine)gallium(III) triflate ([Ga(H_4qp2)](OTf)$_3$ 2).

The H_4qp2 ligand (88.9 mg, 0.183 mmol) and $Ga(OTf)_3$ (76.7 mg, 0.164 mmol) were dissolved in 3 mL of MeCN under N_2. The solution was stirred overnight at 85 °C. After this time, the solution was cooled to RT and the solvent was removed. Addition of ether to a saturated solution of MeOH/CH_2Cl_2 yields a white powder (264 mg, 71%). Recrystallization the powder from MeCN/ether yields needle like crystals. ^{1}H NMR (500 MHz, CD_3CN, 293 K): δ 8.86 (d, J = 5.5 Hz, 2H), 8.04 (t, J = 7.7 Hz, 2H), 7.56 (t, J = 6.7 Hz, 2 H), 7.38 (d, J = 7.6 Hz, 5H), 6.53 (d, J

= 8.5 Hz, 2H), 6.45 (s, 2H), 6.36 (t, J = 8.7 Hz, 4H), 4.50 (d, J = 18.5 Hz, 2H), 4.22 (d, J = 18.6 Hz, 2H), 3.91 (d, J = 13.6 Hz, 2H), 3.76 (d, J = 13.3 Hz, 2H), 3.15 (t, J = 9.5 Hz, 2H), 2.88 (d, J = 9.4 Hz, 2H). ^{13}C NMR (125 MHz, CD_3CN, 293 K): δ 207.18, 155.84, 153.64, 148.30, 147.76, 142.48, 125.63, 123.55, 121.03, 120.59, 61.94, 58.02, 56.04. Optical spectroscopy (MeCN, 293 K): 680 nm (ε = 146 M^{-1} cm^{-1}), 509 nm (ε = 199 M^{-1} cm^{-1}), 445 nm (ε = 288 M^{-1} cm^{-1}), 309 nm (ε = 689 M^{-1} cm^{-1}), 263 nm (ε = 863 M^{-1} cm^{-1}), 238 nm (ε = 1386 M^{-1} cm^{-1}). FTIR (cm^{-1}): 3350 (m), 1610 (m), 1490 (s), 1440 (m), 1240 (s), 1225 (s), 1179 (s), 1027 (s), 942 (w), 866 (w), 804 (m), 772 (w), 719 (w), 643 (s), 5800 (m), 518 (m). MS (ESI): Calcd for $[Ga(H_2qp2)]^+$, 553.1366; Found, 553.1151. Elemental analysis (crystals): Calcd for $C_{31}H_{30}N_4F_9O_{13}S_3Ga$•1.5 H_2O: C, 35.71%; H, 3.19%; N, 5.37%; Found: 35.57%; H, 3.19%; N, 5.42%.

(*N*-(2,5-dihydroxybenzyl)-*N,N'*-bis(2-pyridinylmethyl)-1,2-ethanediamine)gallium(III)] triflate ([Ga(H_2qp3)](OTf)$_3$, 3).

The H_2qp3 ligand (216 mg, 0.594 mmol) and gallium(III) triflate ($Ga(OTf)_3$, 307 mg, 0.594 mmol) were dissolved in 3 mL of MeCN under N_2. The solution was stirred for 4 h at RT. Ether was added to the reduced solution to deposit the product as a yellow crystalline powder (510 mg, 98% yield). Slow diffusion of ether in saturated solution of MeCN yields fine needle crystals. ^{1}H NMR (500 MHz, CD_3CN, 293 K): δ 8.93 (d, J = 6.8 Hz, 1H) 8.63 (d, J = 5.8 Hz, 1H), 8.26 (td, J = 9.7, 1.9 Hz, 1H), 8.09 (td, J = 9.7, 1.8 Hz, 1H), 7.78 – 7.73 (m, 2H), 7.65 (t, J = 7.9 Hz, 1H), 7.41 (d, J = 9.6 Hz, 1H), 6.53 – 6.50 (m, 2H), 6.34 – 6.31 (m, 2H), 4.73 – 4.51 (m, 2H), 4.44 (d, J = 23.2 Hz, 1H), 4.27 – 4.19 (m, 2H), 4.03 (d, J = 16.2 Hz, 1H), 3.91 (b, 1H), 3.01 (b, 2H), 2.86 (b, 1H), 2.67 (b, 1H). ^{13}C NMR (125 MHz, CD_3CN, 293 K): δ 146.31, 143.74, 143.40, 126.57, 126.20, 125.51, 61.14, 55.07. Optical spectroscopy (MeCN, 293 K): 683 nm (ε = 161 M^{-1} cm^{-1}), 509 nm (ε = 297 M^{-1} cm^{-1}), 448 nm (ε = 410 M^{-1} cm^{-1}), 310 nm (ε = 2053 M^{-1} cm^{-1}), 263 nm (ε =

7130 M^{-1} cm^{-1}), 237 nm (ε = 4744 M^{-1} cm^{-1}). FTIR (cm^{-1}): 3147 (m), 2925 (m), 1617 (m), 1574 (w), 1492 (s), 1451 (s), 1354 (w), 1302 (s), 1237 (s), 1213 (s), 1154 (s) 1076 (w), 1045 (w), 1024 (s) 877 (w), 801 (m), 758 (m), 726 (w), 633 (s), 572 (m), 514 (m). MS (ESI): Calcd for $[Ga(Hqp3)]^{2+}$, 431.0998, $[Ga(H_2qp3)(OTf)]^{3+}$, 581.0602; Found, 431.0742, 581.0547. Elemental analysis (crystals): Calcd for $C_{24}H_{24}N_4F_9O_{11}S_3Ga$•0.5 Et_2O: C, 34.00%; H, 3.18%; N, 6.10%; Found: C, 33.99%; H, 3.25%; N, 5.79%.

5.3 Results

Synthesis

Prior publications from our laboratory reported the synthesis of the H_2qp1, H_4qp2, and H_2qp3 ligands along with the chemistry of the Mn(II) complexes with H_2qp1 and H_4qp2.[22,24] Zn(II) complexes with the three ligands were also prepared and subsequently characterized.[25,26]

Ga(III) complexes with the ligands can be prepared by dissolving a 1:1 mixture of the ligand and $Ga(OTf)_3$ in hot or room temperature MeCN. The addition of ether to saturated solutions or reconstituted solutions in MeOH/CH_2Cl_2 yields compounds $[Ga(H_2qp1)](OTf)_2$ (**1**), $[Ga(H_4qp2)](OTf)_3$ (**2**), and $[Ga(H_2qp3)](OTf)_3$ (**3**). Highly crystalline samples of the compounds can be obtained in yields exceeding 70%. The compositions were established by elemental analysis, as structural analysis of the compounds is impeded by the morphology of the crystals. Varying the crystal-growing conditions has thus far failed to improve the suitability of the crystals for diffraction. Compounds **1** and **3** are easier to synthesize; **2** is less accessible due to the poor solubility of H_4qp2 in MeCN. The successful synthesis of **2** requires both an elevated temperature (85 °C) and a lengthy reaction time (16 h).

As anticipated, all products are diamagnetic and faintly colored yellow or white solids. The ^{1}H NMR spectra of crystalline samples of all Ga(III) complexes (Figures D1, D5 and D9) feature

slight deviations from expected the structural composition, suggesting the complexes exist as a mixture of conformers and/or coordination isomers in solution. Similarly complicated speciation was also noted for [Zn(H_2qp1)(OTf)](OTf)[26] and the Zn(II) complexes with H_4qp2 and H_2qp3.

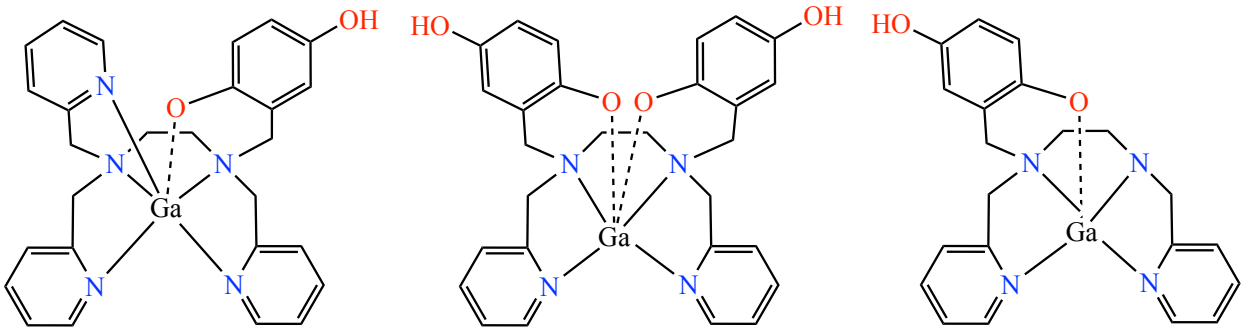

[Ga(H_2qp1)](OTf)$_2$ (**1**) [Ga(H_4qp2)](OTf)$_3$ (**2**) [Ga(H_2qp3)](OTf)$_3$ (**3**)

Figure 5.1 Structural representation of prepared Ga(III) complexes assessed in this study.

Aqueous Solution Characterization

The Ga(III) catalysts are intended to be used to degrade ROS in aqueous solutions. Ascertaining the stability and speciation of the complexes is therefore vital. Consequently, we determined the speciation of **1**, **2**, and **3** in water using potentiometric and spectrophotometric pH titrations. For this chapter only the preliminary results for **1** and **3** will be shared; the data for **2** are still being collected and refined.

The acid/base chemistry of the ligand set in water was previously described.[24-26] Aqueous preliminary studies of Ga(III) complexes, with H_2qp1 or H_2qp3, reveal two clear ionization events as the pH increases from 2.5 to 10. The H_2qp1 system has pK_a values of 4.4 and 8.5, which we tentatively assign to the (de)protonation of the two hydroxy groups on the quinol. The pK_a value of 4.4 suggests the major species between pH 7.0 and 7.4 would be $[Ga(Hqp1)]^{2+}$, where $Hqp1^-$ is the conjugate base of the ligand. The H_2qp3 system has pK_a values of 3.1 and 8.4. Similar to the

H_2qp1 system these values tentatively correspond to the (de)protonation of the two hydroxy groups on the quinol (Table 5.1).

Table 5.1 Preliminary pK_a values for the H_2qp1 and H_2qp3 ligands and their Ga(III) complexes as determined by potentiometric titration at 25 °C.

H_2qp1		**Ga-H_2qp1**	
pK_{L1}[a]	4.72 (±0.08)	pK_{a1}[b]	4.4
pK_{L2}[a]	7.24 (±0.03)	pK_{a2}[b]	8.5
H_2qp3		**Ga-H_2qp3**	
pK_{L1}[a]	10.2 (±0.3)	pK_{a1}[b]	3.2
pK_{L2}[a]	8.19 (±0.05)	pK_{a2}[b]	8.4
pK_{L3}[a]	5.13 (±0.05)		
pK_{L4}[a]	3.5 (±0.3)		

[a]Ligand pK_a values correspond to the following equilibrium constants:

H_2qp1 $K_{L1} = [(H_3qp1)^+][H^+]/[(H_4qp1)^{2+}]$, from reference [26].

$K_{L2} = [(H_2qp1)][H^+]/[(H_3qp1)^+]$, from reference [26].

H_2qp3 $K_{L1} = [(Hqp3)^-][H^+]/[H_2qp3]$, from reference [25].

$K_{L2} = [H_2qp3][H^+]/[(H_3qp3)^+]$, from reference [25].

$K_{L3} = [(H_3qp3)^+][H^+]/[(H_4qp3)^{2+}]$, from reference [25].

$K_{L4} = [(H_4qp3)^{2+}][H^+]/[(H_5qp3)^{3+}]$ from reference [25].

[b]Metal complex pK_a values correspond to the following equilibrium constants:

Ga-H_2qp1 $K_{a1} = [[Ga(Hqp1)]^{2+}][H^+]/[[Ga(H_2qp1)]^{3+}]$.

$K_{a2} = [[Ga(qp1)]^+][H^+]/[[Ga(Hqp1)^{2+}]]$.

Ga-H_2qp3 $K_{a1} = [[Ga(Hqp3)]^{2+}][H^+]/[[Ga(H_2qp3)]^{3+}]$.

$K_{a2} = [[Ga(qp3)]^+][H^+]/[[Ga(Hqp3)^{2+}]]$.

The pK_a assignments are consistent with the spectroscopic changes detected in spectrophotometric titrations (Figure D13). Below pH 7 the species displays no observable changes. Above pH 7, the slight shoulder at 237 nm disappears and 263 nm band is enhanced. The 310 nm band undergoes a bathochromic shift to 410 nm, indicative of protonation consistent with intraligand electronic transition for a phenolate.[36] This suggests the complex exists as $[Ga(Hqp1)]^{2+}$ and potentially undergoes another chemical change as the pH rises indicated by hypochromic shift of 410 nm to 352 nm. Similar spectroscopic changes are noted for the H_2qp3 system (Figure D14). Analysis of the spectral features of **2** could predict similar aqueous behavior, however detailed potentiometric and spectrometric studies have yet to be performed.

Unfortunately, we could not use these data to obtain accurate speciation models. The log(β) values for these species did not converge to stable values even after extensive attempts to fit the data to a wide variety of models using the speciation program Hyperquad. We had encountered similar difficulties modeling the data for $[Zn(H_2qp1)(OTf)]^+$ and $[Zn(H_4qp2)](OTf)_2$.[25,26] The sole conclusion that we can make is that the complexes appear to be very stable in water.

Electrochemistry

The redox behavior of **1**, **2**, and **3** in aqueous phosphate solutions buffered to pH 7.0 was analyzed by cyclic voltammetry (CV). The CV for each complex displays two irreversible reduction-oxidation couples. For complex **1**, the species has a redox event of $E_{1/2}$ = 209 mV vs. Ag/AgCl (ΔE_p = 308 mV) and an event of $E_{1/2}$ = 343 mV vs. Ag/AgCl (ΔE_p = 442 mV) (Figure D15). Complex **2** features redox couples at $E_{1/2}$ = 250 mV vs. Ag/AgCl (ΔE_p = 403 mV) and another with $E_{1/2}$ = 319 mV vs. Ag/AgCl (ΔE_p = 363 mV) (Figure D16). Complex **3** gives rise to redox events with $E_{1/2}$ = 261 mV vs. Ag/AgCl (ΔE_p = 348 mV) and $E_{1/2}$ = 192 mV vs. Ag/AgCl (ΔE_p = 354 mV) (Figure D17).

Antioxidant Activity

All complexes are initially screened using the DPPH assay which tests the abilities of compounds to donate hydrogen atoms to 2,2-diphenyl-1-picrylhydrazyl radical hydrate.[32-34,37] The conversion of DPPH to its non-radical hydrazine form is assessed and monitored by UV/vis. The IC_{50} values for **1**, **2**, and **3** were measured to be 23 μM, 30 μM and 17 μM, respectively (Figure 5.2). The ascorbic acid standard had an IC_{50} value of 25 μM under the same conditions. Previously isolated divalent metal complexes with the H_2qp1, H_4qp2, and H_2qp3 ligands likewise outperformed ascorbic acid in these measurements by approximately the same extent.[22,24-26]

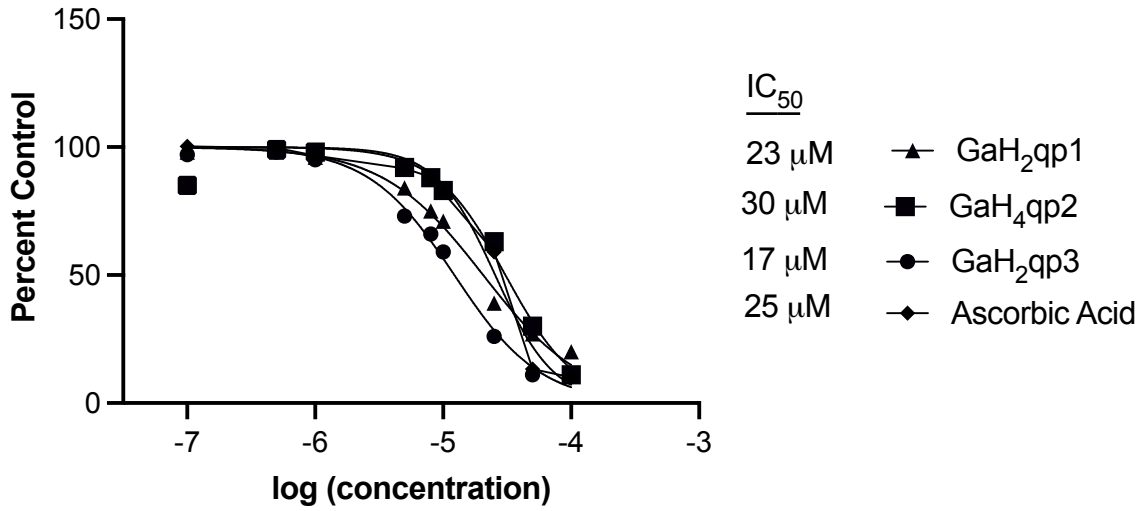

Figure 5.2 DPPH free radical scavenging assay of **1**, **2**, **3**, and ascorbic acid. The antioxidants were added to DPPH and incubated in the dark for 30 min at 298 K. Spectroscopic measurements were performed at 517 nm. The data were normalized to the absorbance in the presence of vehicle. All experiments were performed in triplicate and repeated twice.

The abilities of complexes **1** and **3** to mimic SOD were initially gauged using an established procedure that uses xanthine oxidase/hypoxanthine to generate $O_2^{\cdot-}$ and a chromophore lucigenin probe to detect it.[22,24,31,38] Both complexes display above-baseline activity (Figure 5.3). The IC_{50} values for the elimination of the lucigenin sensing reaction were found to be within error of each other: 28 (±0.01) nM for **1** and 27 (±0.3) μM for **3**. Similar values were reported for [Zn(H_2qp1)(OTf)](OTf) (IC_{50} = 17 nM), [Zn(H_4qp2)](OTf)$_2$ (IC_{50} = 8 nM), and [Zn(H_2qp3)(H_2O)](OTf)$_2$ (IC_{50} = 17 nM). As stated in prior chapters, the reported IC_{50} values do not accurately depict the relative catalytic efficiencies of the mimics.

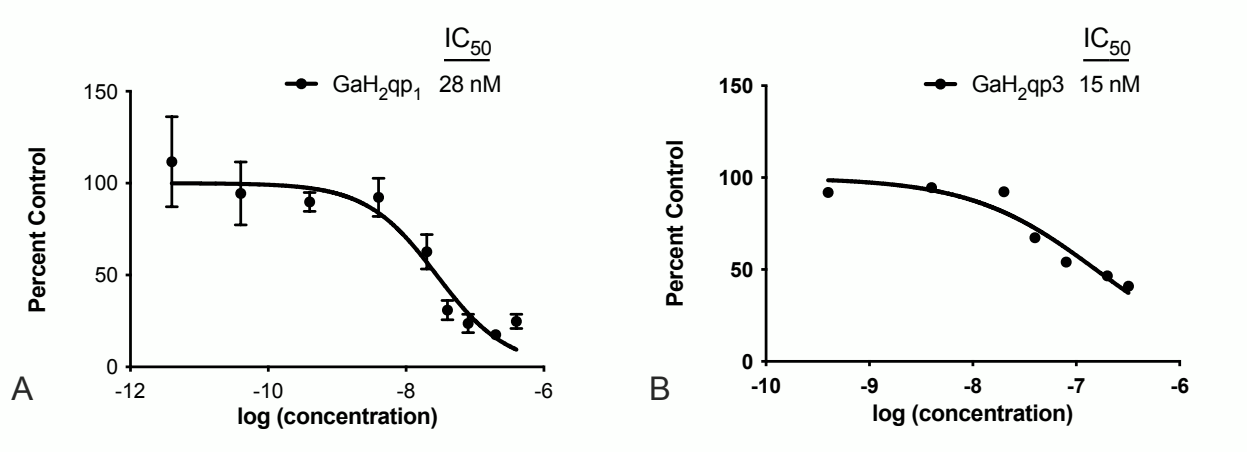

Figure 5.3 Superoxide scavenging effects of A) **1** and B) **3**. Superoxide was generated using a hypoxanthine- xanthine oxidase reaction and detected using the chemiluminescent probe lucigenin. Reactions were carried out in 10 mM PBS (pH 7.4). Data for the various concentrations of Ga(II) complexes are expressed as a percentage of luminescence in the presence of vehicle.

The aforementioned assays often provide misleading accounts of the actual reactivity with superoxide due to competing side-reactions between the various components in the reaction mixtures.[27,39-42] The reactivity can be more thoroughly analyzed by measuring the direct reactions between SODm and KO_2. Surprisingly, stopped-flow analysis demonstrates that both complexes **1** and **3** are inefficient catalysts for superoxide disproportionation (Figure D18). The rates of superoxide degradation in these experiments are identical within error to that of the uncatalyzed reaction, and the gallium has no impact on the rate of decomposition.

The similarly inert $[Zn(H_2qp3)(H_2O)](OTf)_2$ was found to quickly degrade upon reaction with superoxide, with the dissociation of the metal from the ligand halting activity. Mass spectrometry analysis of **1** and **3** with KO_2, conversely, suggests that both Ga(III) complexes, even with the less highly chelating H_2qp3, remain intact. The data exhibit major *m/z* values features that correspond to Ga(III) complexes with deprotonated ligands (Figure D19 and D20). We currently hypothesize that the coordination of the tricationic metal ion renders the quinols in the ligand less

susceptible to oxidation and that superoxide cannot quickly oxidize these groups as in the Zn(II) complexes.

Cytotoxicity and Cytoprotection Studies

Cytotoxicity studies were initially performed for complex **1**, [Zn(H_2qp1)(OTf)](OTf), and [Zn(H_4qp2)](OTf)$_2$. For the purposes of this study, only compound **1** will be highlighted. The Zn(II) compounds are viable SOD mimics and are non-toxic below 0.1 mM. Complex **1** is similarly non-toxic, and concentrations below 0.1 mM of **1** by itself does not worsen the viability of H9c2 cells (Figure 5.4A). Subsequentially all compounds were analyzed for their ability to protect against H_2O_2-induced stress. Only **1** shows a notable dose-dependent effect against H_2O_2-induced toxicity. Based on the demonstrated protection against cell death with increasing concentrations of oxidant, 100 μM was determined to be the optimum dose for cytoprotection against cellular induced toxicity (Figure 5.4B – Figure 5.4D)

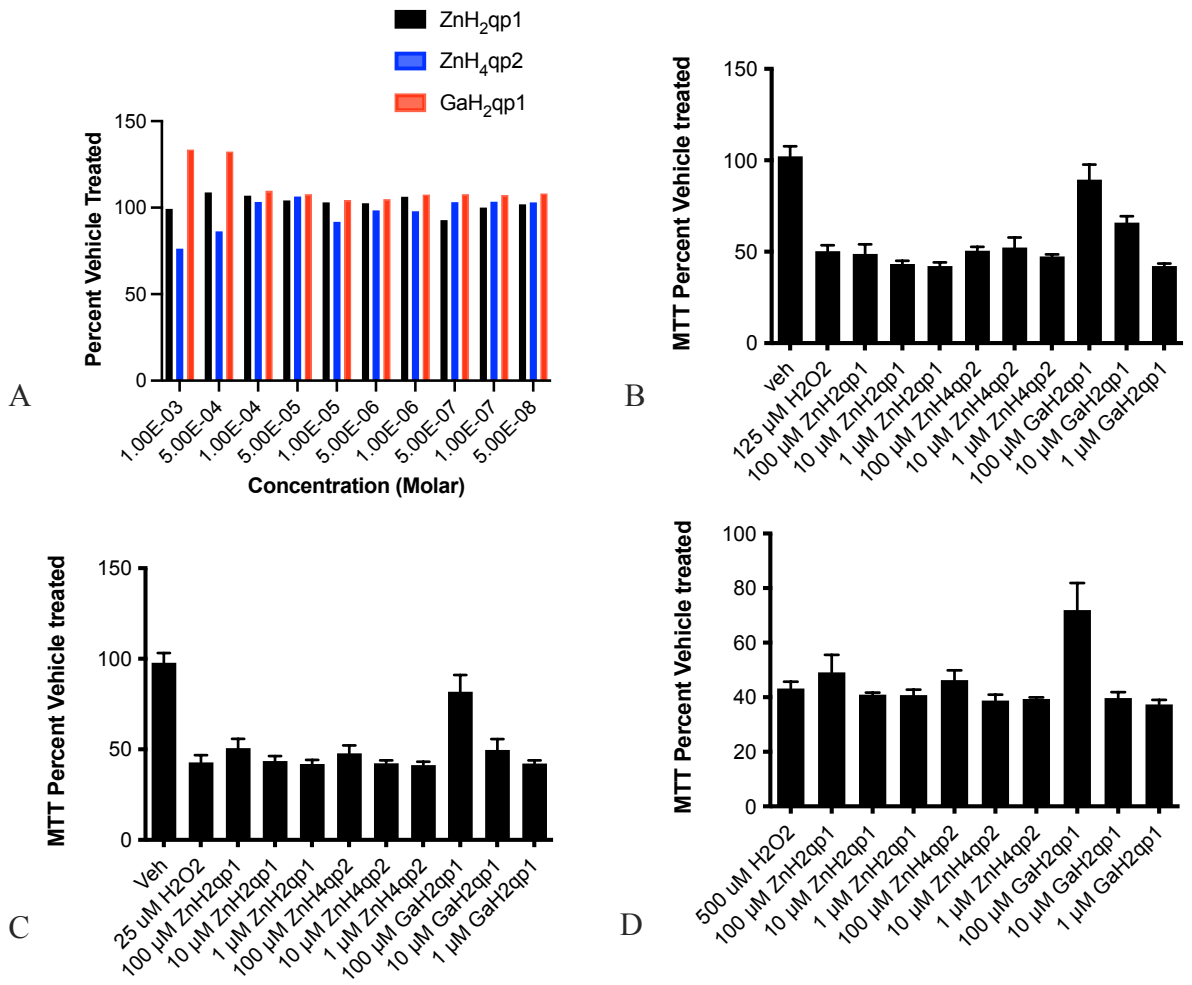

Figure 5.4 H9c2 cell viability studies of A) cytotoxicity and B) cytoprotective effects of 1, [Zn(H_2qp1)(OTf)](OTf), and [Zn(H_4qp2)](OTf)$_2$.

Analysis of H_2O_2 Dismutation

The ability of **1** to dismutate H_2O_2 into O_2 and H_2O was assessed by two methods: a) monitoring the decrease of [H_2O_2] by UV/vis at 240 nm[43] and b) measuring the rate of O_2 production using a Clark-type electrode. The rate of H_2O_2 consumption was substantially higher when monitored by UV/vis (Table 5.2 and Figure D21 and D22). The discrepancy between the spectrophotometric and polarigraphic measurements suggests that the photophysical properties of **1** may influence activity readings at 240 nm and produce fluctuations in obtained values. This issue

has been observed with previous CAT mimics.[44] Thus, the values obtained for O_2 production are anticipated to be the more reliable of the two data sets.

Table 5.2 Catalase kinetic parameters for rates of H_2O_2 decomposition and O_2 evolution k_{cat} (s^{-1}) and k_{cat}/K_m (M^{-1} s^{-1}) . Unless indicated all values are measured with O_2 polarography.

	k_{cat} (s^{-1})	k_{cat}/K_m (M^{-1} s^{-1})	*Ref*
[Ga(H_2qp1)](OTf)$_3$	1.9×10^{3}[a]	5.8×10^{6}[a]	This work
	6.4	2.4×10^{2}	This work
[Mn^{III}(2-OHsalpn)]$_2$	10.1	9.9×10^{2}	[45]
[Mn(bpia)(OAc)]$_2^{2+}$	0.23	1.1	[46]
CAT *T. Thermophilus*	2.6×10^{5}	3.1×10^{6}	[47]
Heme CAT	3.8×10^{7}[b]	3.5×10^{7}[b]	[48]

[a] *Rates assessed by H_2O_2 decomposition.*
[b] *Rates assessed using rapid-flow two-mixer method.*

5.4 Discussion

Two Zn(II) complexes, [Zn(H_2qp1)(OTf)](OTf) and [Zn(H_4qp2)](OTf)$_2$, were recently characterized as superoxide dismutase (SOD) mimics. These displayed the highest reported SOD activities for compounds that lack redox-active metals as well as a unique enhancement in catalysis in phosphate solutions. Ga(III) complexes with quinol-containing ligands were prepared to probe how increasing the positive charge impacts functional SOD mimicry. We prepared Ga(III) complexes with the quinol-containing H_2qp1, H_4qp2, and H_2qp3 ligands (Scheme 5.3). Ga(III), like Zn(II), is redox-inactive and coordinates readily to N-donor ligands. Other tricationic metal centers tend to be much more oxophilic, and most would not be anticipated to form stable complexes with these ligands.

The syntheses of [Ga(H_2qp1)](OTf)$_2$ (**1**), [Ga(H_4qp2)](OTf)$_3$ (**2**), and [Ga(H_2qp3)](OTf)$_3$ (**3**) are straightforward, and the products can be obtained as needle-like crystals. Multiple crystallization conditions were attempted but were unable to yield suitable crystals for single-crystal X-ray diffraction. Structural characterization was instead performed using elemental

analysis, NMR, and MS. Complex **1** differs from **2** and **3** in that only two triflate anions are present per metal center, indicating the presence of another unidentified anionic molecule, specifically the singly deprotonated $Hqp1^-$ ligand. The NMR data for all three suggest the more than one conformer or coordination isomer exist in solution, which is consistent with what was seen for previously characterized Zn(II) complexes with these ligands.[25,26]

The electrochemistry of complexes **1** – **3** differ substantially from analogous Mn(II) and Zn(II) complexes. The previously studied Zn(II) compounds each gave rise to a single ligand-derived reduction/oxidation event around ~300 mV vs NHE, the ideal value for superoxide dismutation. [25,26] With the Ga(III) complexes, we instead see two highly irreversible events for each complex, with the initial oxidations being substantially less favorable. We assign the first redox event to the oxidation of the quinol to a quinoxyl radical and the second to the oxidation of the radical to the *para*-quinone. We believe that this is sufficient to shift the thermodynamic favorability for ligand oxidation outside the range that would allow rapid catalytic reactions with $O_2^{-\cdot}$.

Initial analysis of **1** - **3** by the DPPH assay indicates all complexes can serve as hydrogen atom donors.[32-34,37] The xanthine oxidase/hypoxanthine/lucigenin assay[31] suggested that **1** and **3** could also dismutate superoxide. However, interpretation of the assay results is complicated as neither complex appears to react directly with $O_2^{-\cdot}$ when the direct reactions between the Ga(III) complexes and KO_2 are followed by stopped-flow kinetic methods. The lack of activity is unusual; most of our compounds with positive results on the SOD assay have been able to impact the rate of superoxide decomposition. Based on the results, we surmise that the coordination of the tricationic metal center renders the oxidation events less favorable than those seen for dicationic

metals, such as Zn(II) and Mn(II). As a consequence, the Ga(III) complexes cannot be as readily oxidized by superoxide, precluding catalysis.

Toxicity measurements indicate that **1** has no long-term (48 h) impact on the viability of H9c2 cells at concentrations ≤ 100 μM. Complex **1**, however, can protect these cells against H_2O_2. The Zn(II) analog, despite its established SOD mimicry, was unable to do so under the same conditions. The ability to protect these cells against cytotoxic concentrations of H_2O_2 suggests that **1** could instead be active as a catalase mimic. The Ga(III) complex indeed converts H_2O_2 to O_2; the data are consistent with the following preliminary rate constants: k_{cat}/K_m = (6.4 ± 1.2) M^{-1} s^{-1} and k_{cat} = (2.4 ± 0.4) × 10^2 s^{-1}. The k_{cat} value should be considered a lower limit; the concentrations of H_2O_2 evaluated did not permit a close approach to the asymptotic behavior of saturation needed to confidently assign this value.

Most catalase mimics contain mono- or dinuclear Mn(II) centers. Although catalytically active, these small molecule mimics tend be several orders of magnitude slower than native dimanganese and heme catalases.[49,50] Our complex is still much slower than these enzymes, but to the best of our knowledge, is more reactive than any other reported small mononuclear mimic of CAT.[49] Additionally, **1** is singular in that it does not contain a redox-active transition metal, instead relying on a redox-active organic component for its catalase activity.

5.5 Conclusion

We can successfully obtain Ga(III) complexes with redox-active quinol-based ligands. The addition of a tricationic metal to the series seemingly shifts the electrochemical properties enough to preclude them from catalytic degrading $O_2^{\cdot-}$. Despite the lack of SOD mimicry, preliminary results show that complex **1** can protect cells against H_2O_2. This result encouraged us to assess its ability to disproportionate H_2O_2 into O_2 and water. Preliminary measurements show that we do in fact have a

catalytically active mimic of CAT. Future studies will proceed to examine the cytoprotective and CAT properties of **2** and **3**.

Appendix D

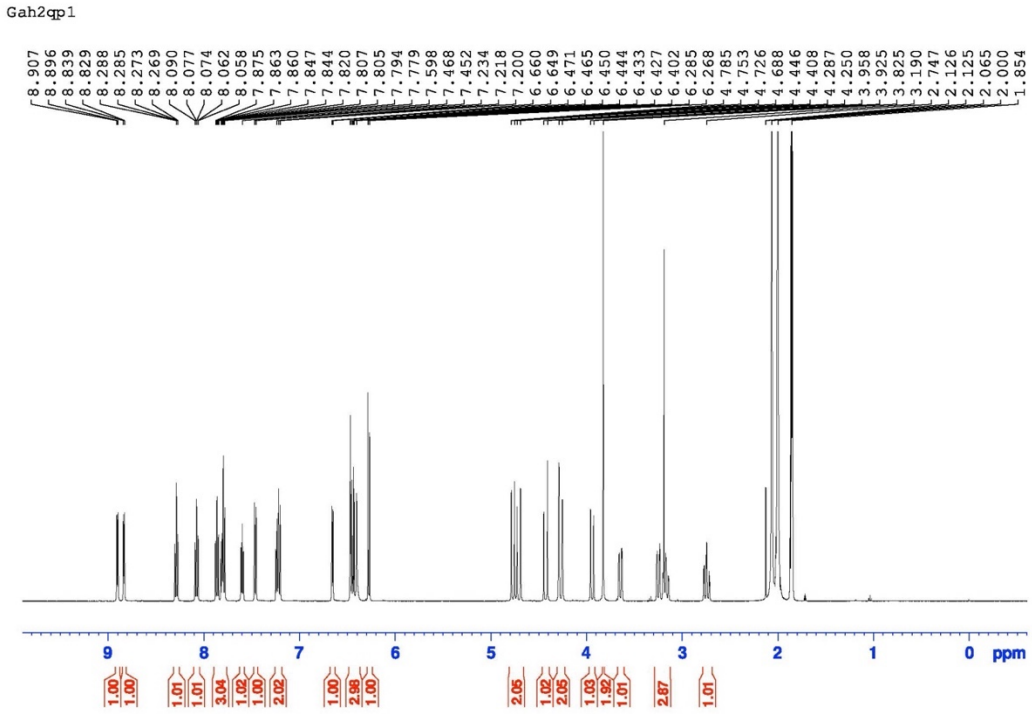

Figure D1. ^{1}H NMR spectrum of a crystalline sample of [Ga(H_2qp1)](OTf)$_2$ (**1**) in CD_3CN (500 MHz, 293 K). Solvent peaks from diethyl ether (3.82), water (2.00) and MeCN (1.85) are present.

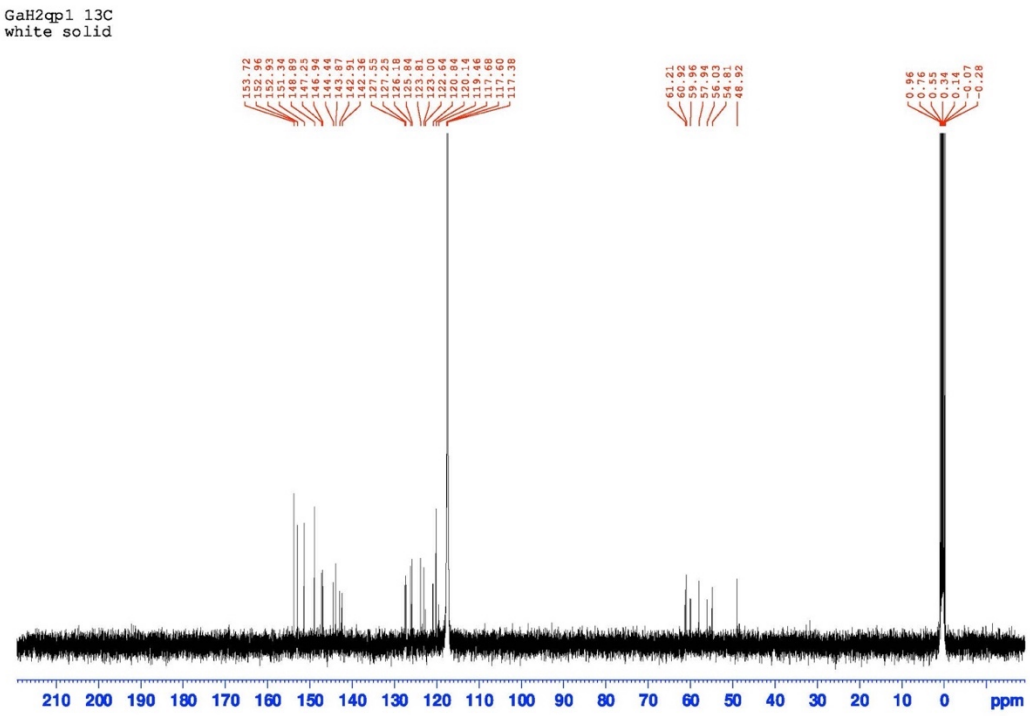

Figure D2. ^{13}C NMR spectrum of a crystalline sample of **1** in CD_3CN (125 MHz, 293 K). Solvent peaks from MeCN (117.60) are present.

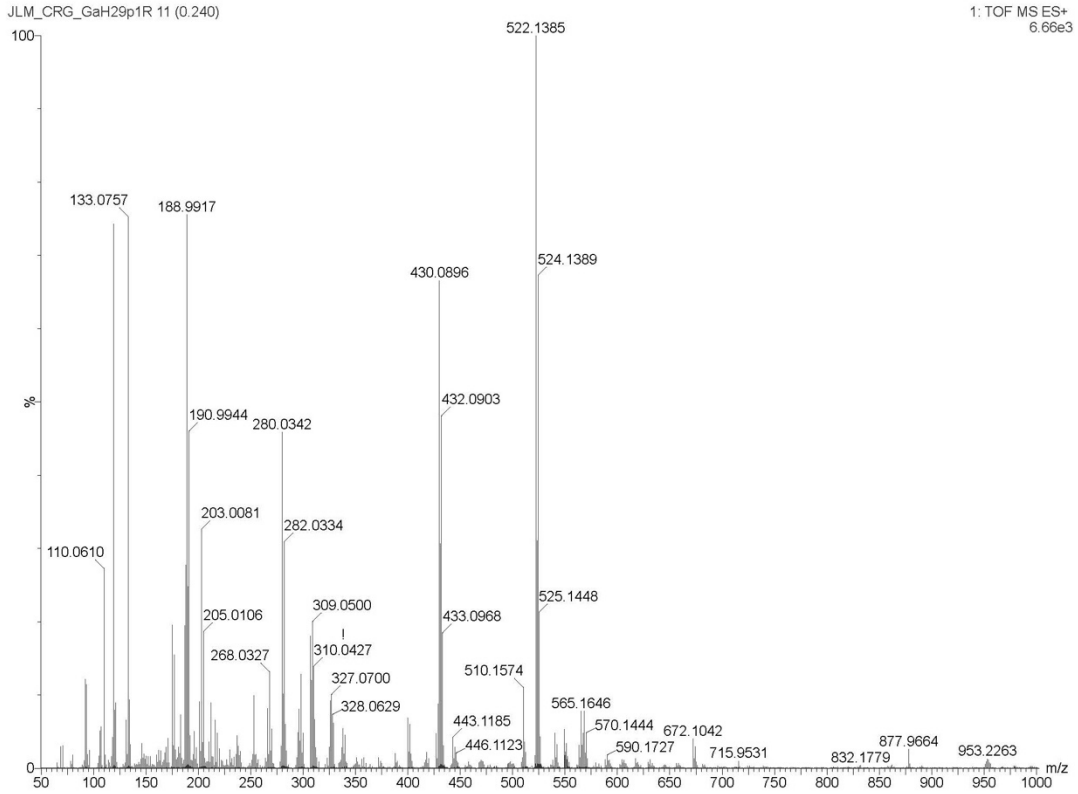

Figure D3. Mass spectrometry (ESI) for [Ga(H2qp1)](OTf)2 (**1**) in MeCN. The *m/z* feature at 522.1385 is assigned to $[Ga(qp1)]^+$ (calculated *m/z* = 522.1420). The feature at 672.1024 is assigned to $[Ga(Hqp1)(OTf)]^+$ (calculated *m/z* = 672.1024).

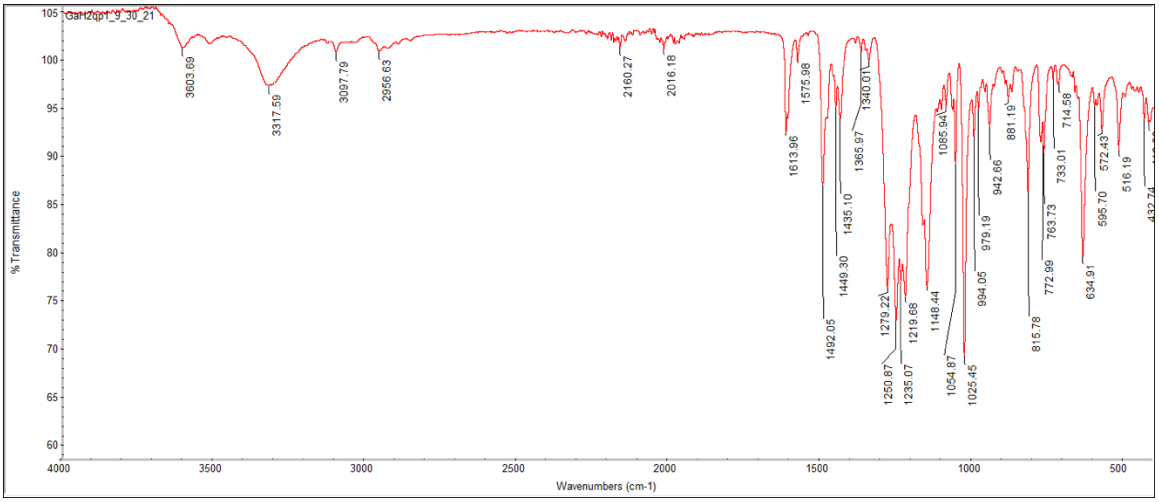

Figure D4. FTIR absorption spectrum of **1**.

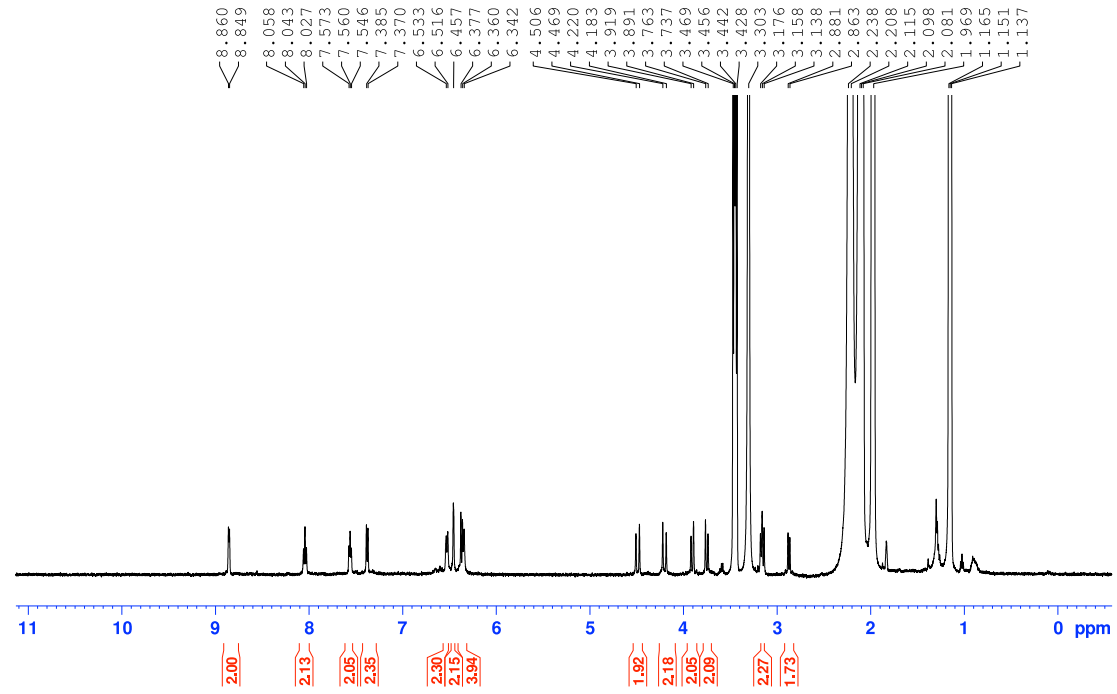

Figure D5. ^{1}H NMR spectrum of a crystalline sample of [Ga(H$_4$qp2)](OTf)$_3$ (**2**) in CD$_3$CN (500 MHz, 293 K). Solvent peaks from diethyl ether (1.16, 3.30, 3.44), water (2.11) and MeCN (1.99) are present.

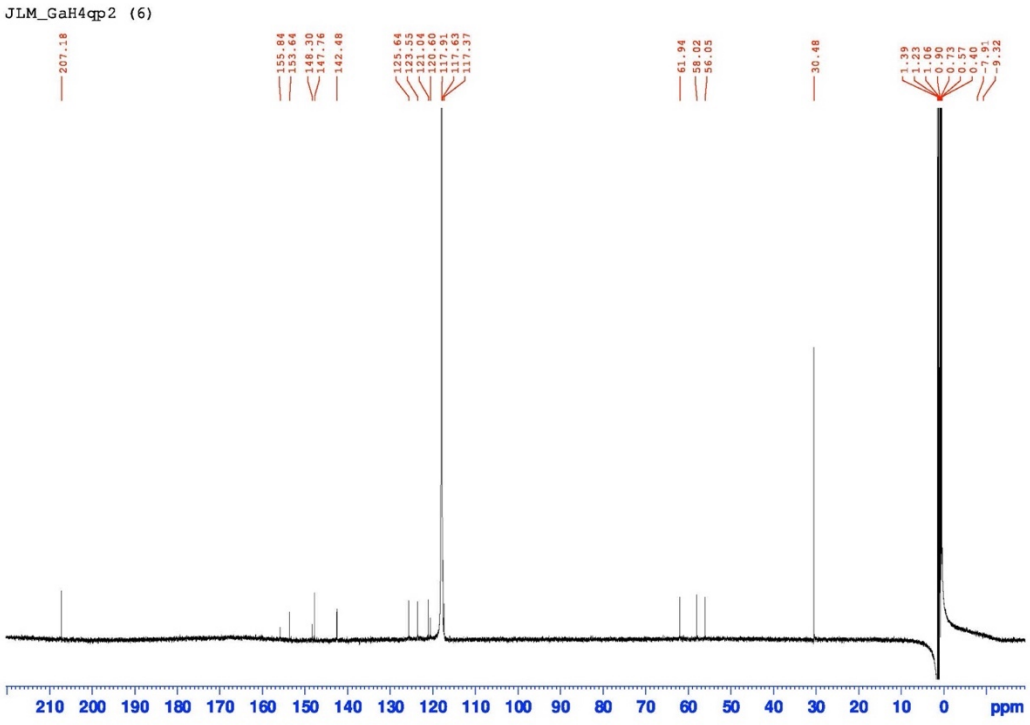

Figure D6. ^{13}C NMR spectrum of a crystalline sample of **2** in CD_3CN (125 MHz, 293 K). Solvent peaks from MeCN (1.39, 117.63) and "grease" (30.48) are present.

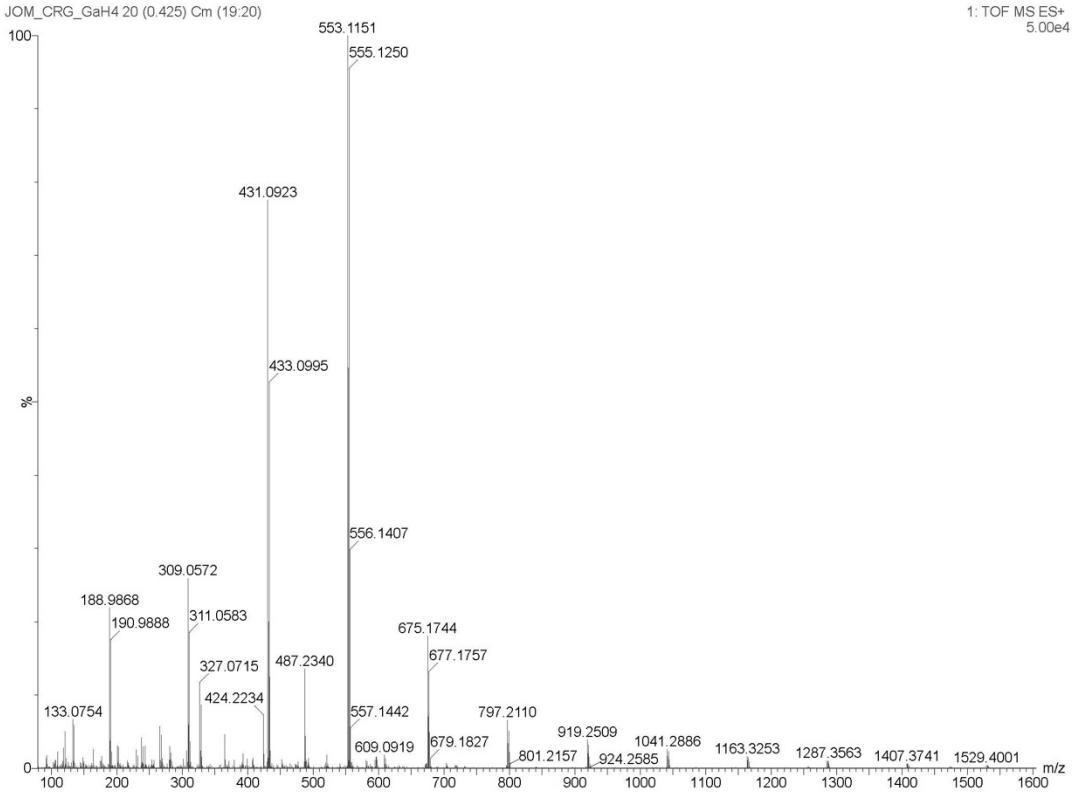

Figure D7. Mass spectrometry (ESI) for $[Ga(H_4qp2)](OTf)_3$ (**2**) in MeCN. The *m/z* feature at 553.1151 is assigned to $[Ga(H_2qp2)]^+$ (calculated *m/z* = 553.1366).

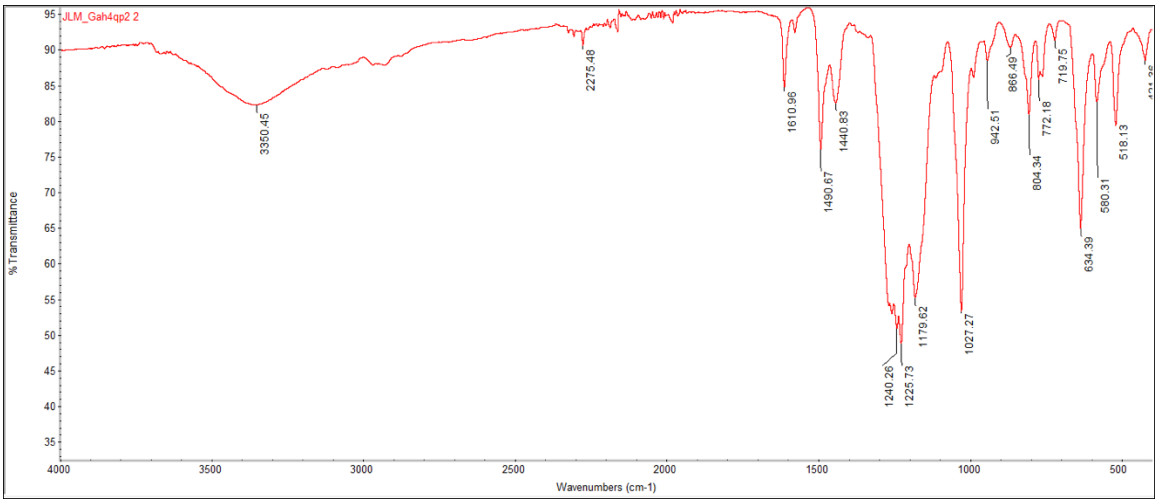

Figure D8. FTIR absorption spectrum of **2**.

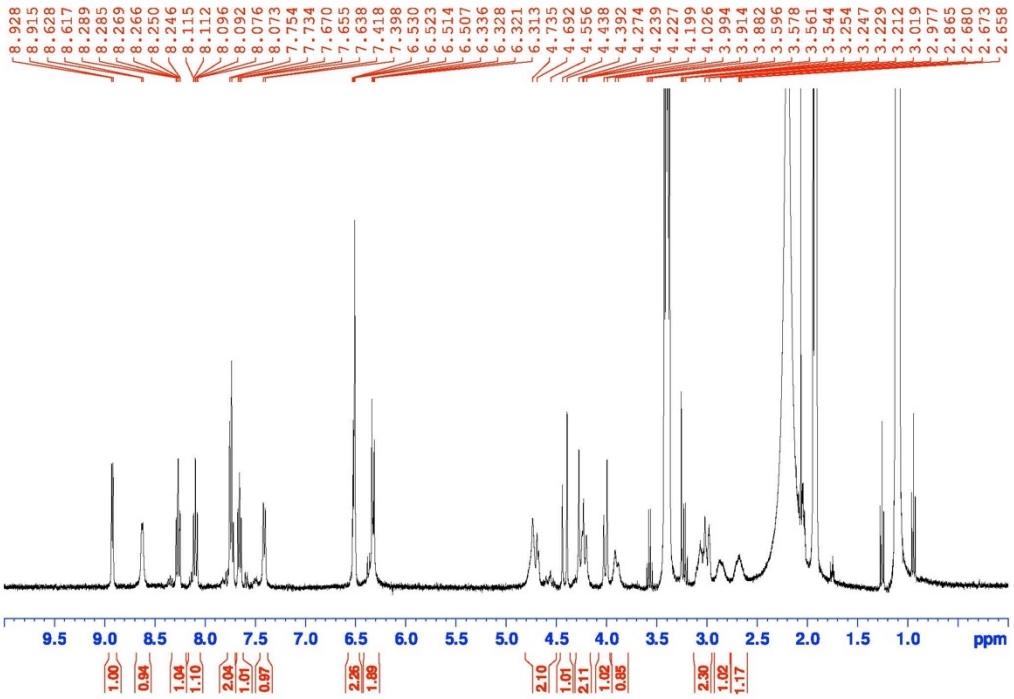

Figure D9. ^{1}H NMR spectrum of a crystalline sample of [Ga(H_2qp3)](OTf)$_3$ (**3**) in CD_3CN (500 MHz, 293 K). Solvent peaks from diethyl ether (1.10, 3.40), water (2.19) and MeCN (1.92) are present.

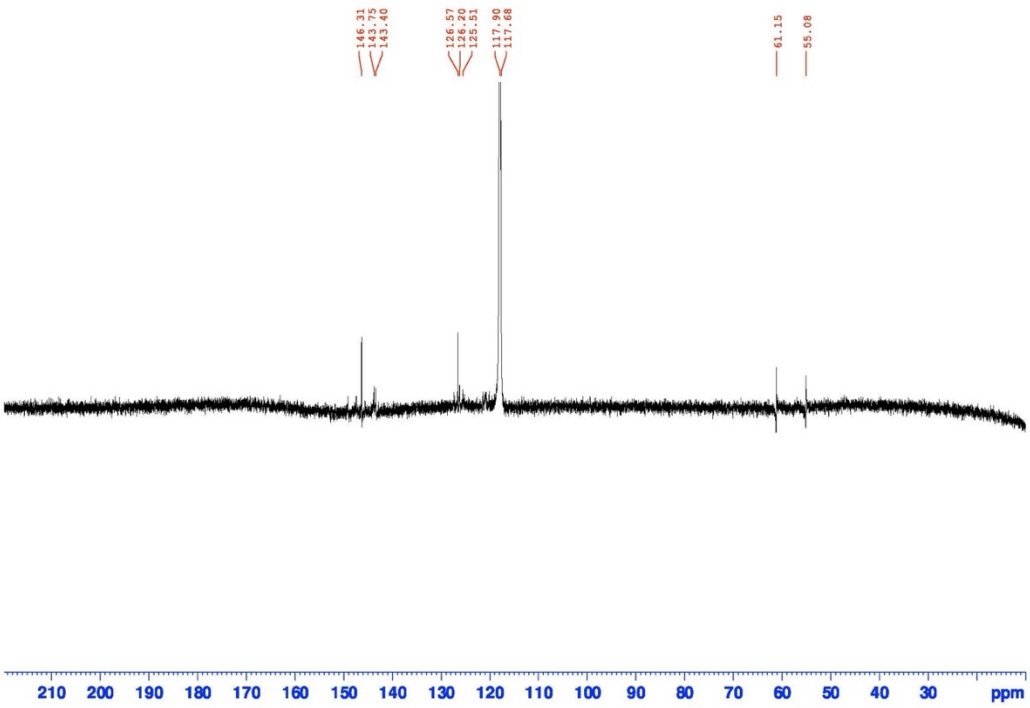

Figure D10. ^{13}C NMR spectrum of a crystalline sample of **3** in CD_3CN (125 MHz, 293 K). A solvent peak from MeCN (117.68) is present.

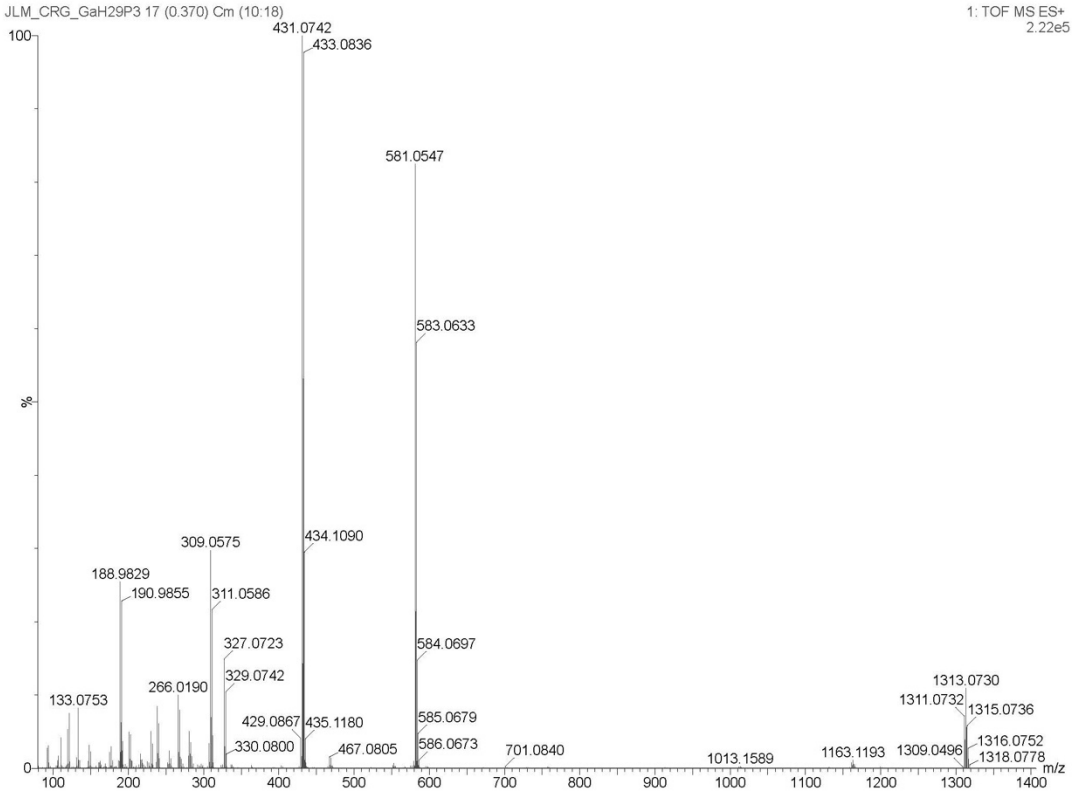

Figure D11. Mass spectrometry (ESI) for $[Ga(H_2qp3)](OTf)_3$ (**3**) in MeCN. The *m/z* feature at 431.0998 is assigned to $[Ga(Hqp3)]^{2+}$ (calculated *m/z* = 431.0998). The feature at 581.0547 is assigned to $[Ga(H_2qp3)(OTf)]^{3+}$ (calculated *m/z* = 581.060).

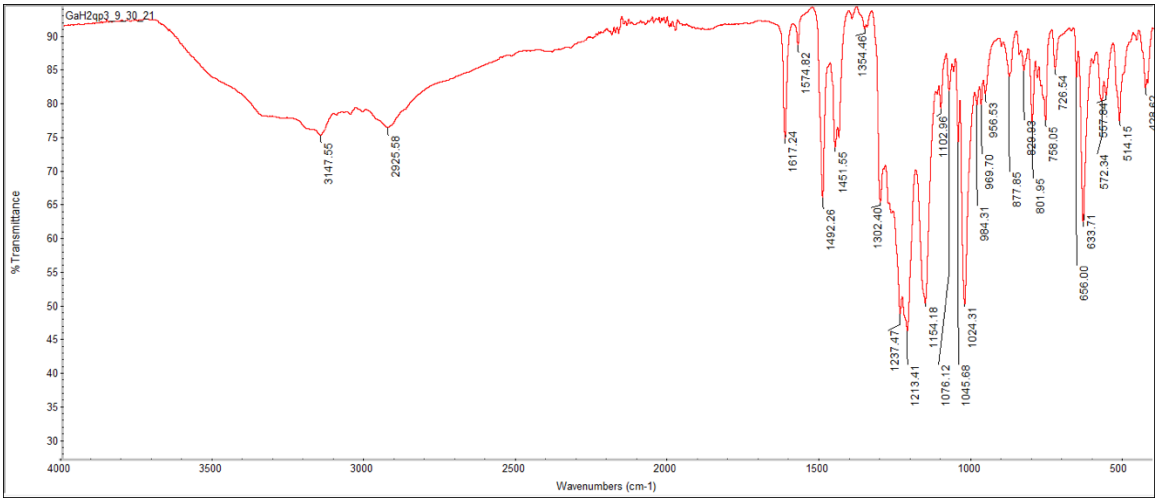

Figure D12. FTIR absorption spectrum of **3**.

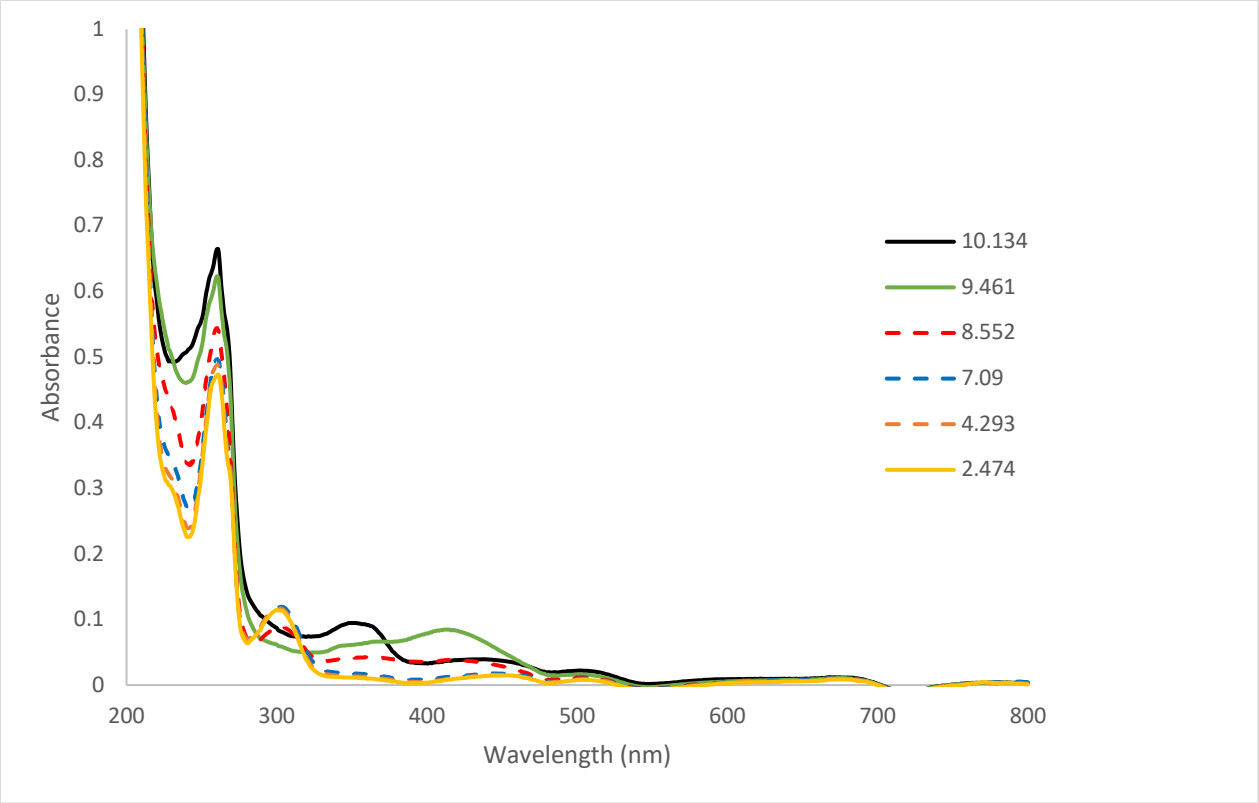

Figure D13. Spectrophotometric pH titration data for **1** in aqueous solution. The data were acquired at 294 K with a 1.0 cm pathlength. The concentration of **1** was 0.10 mM. The pH was controlled through the addition of 1.0 M KOH and 1.0 M HCl solutions.

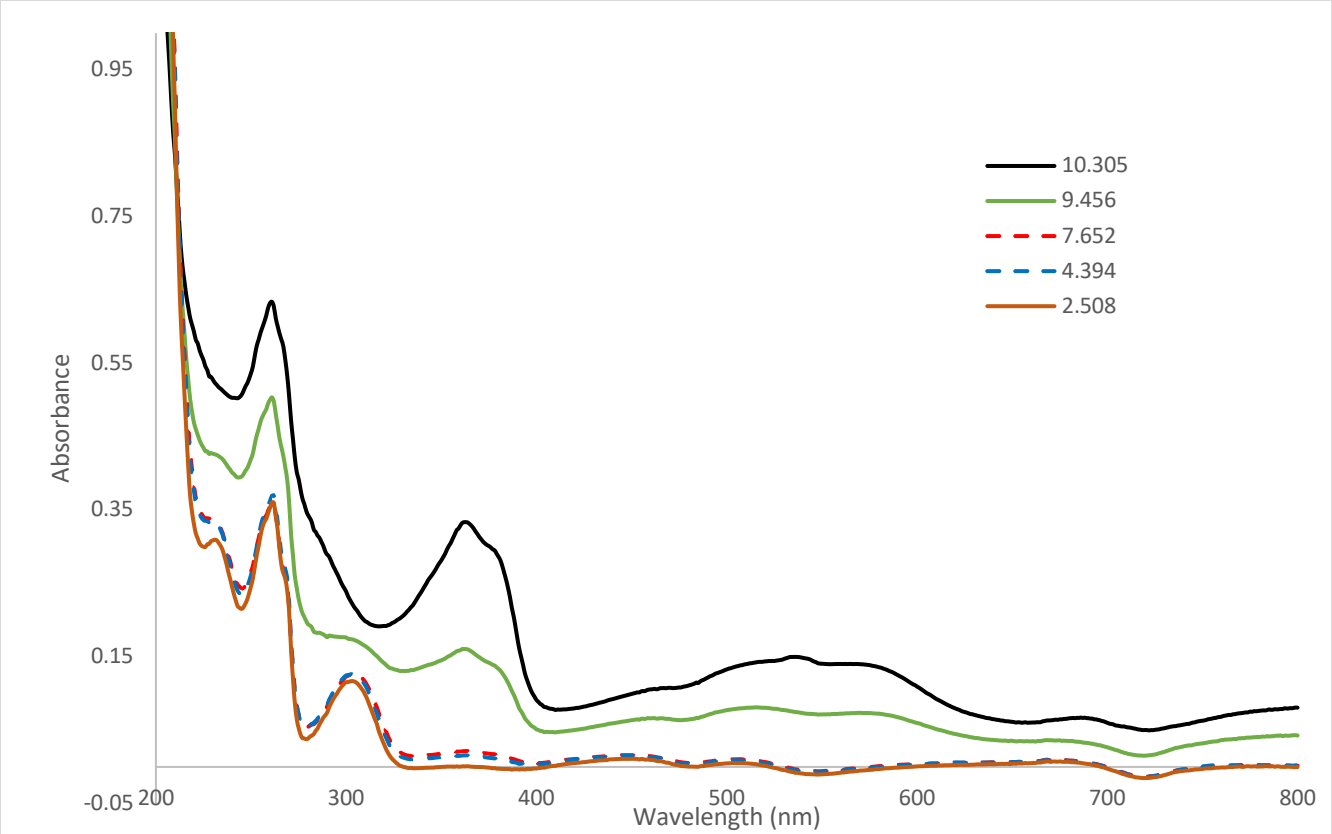

Figure D14. Spectrophotometric pH titration data for **3** in aqueous solution. The data were acquired at 294 K with a 1.0 cm pathlength. The concentration of **3** was 0.10 mM. The pH was controlled through the addition of 1.0 M KOH and 1.0 M HCl solutions.

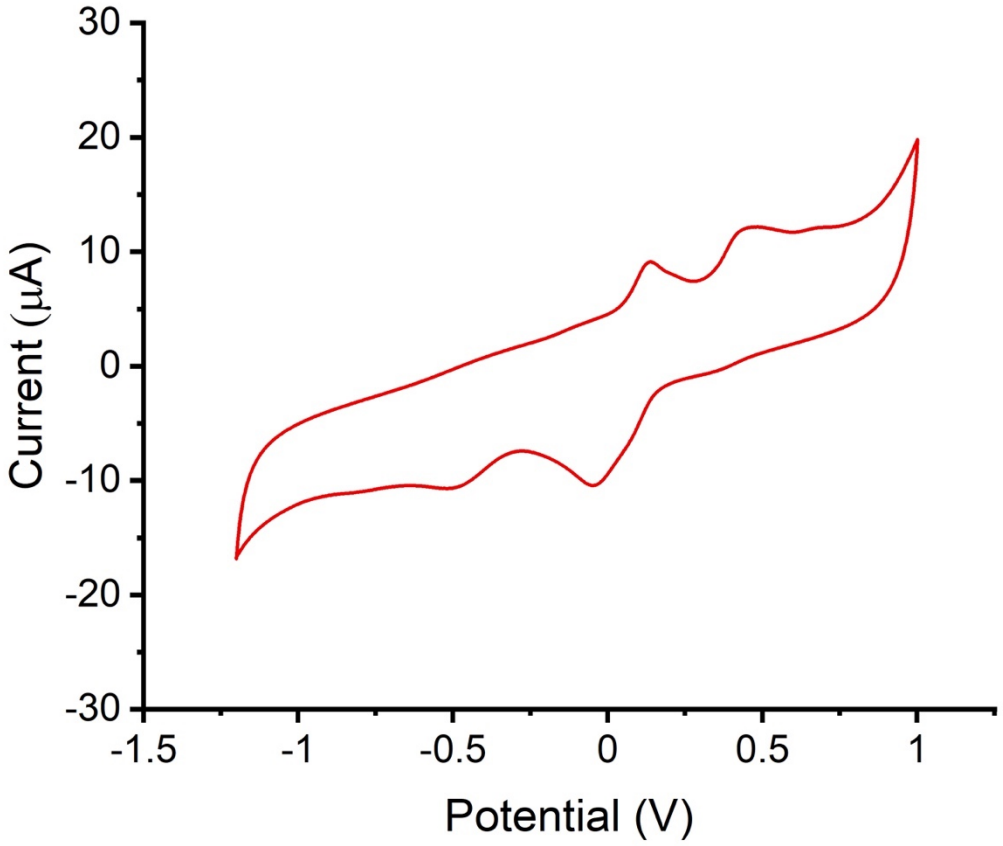

Figure D15. Cyclic voltammetry of 1.0 mM **1** in 0.10 M phosphate buffer (NaH_2PO_4/Na_2HPO_4, pH 7.2). The scan rate was 100 mV/s. Two redox features: $E_{1/2}$ = 209 mV vs. Ag/AgCl (saturated KCl) or 406 mV vs NHE, ΔE_p = 308 mV and $E_{1/2}$ = 343 mV vs. Ag/AgCl (saturated KCl) or 540 mV vs NHE, ΔE_p = 442 mV.

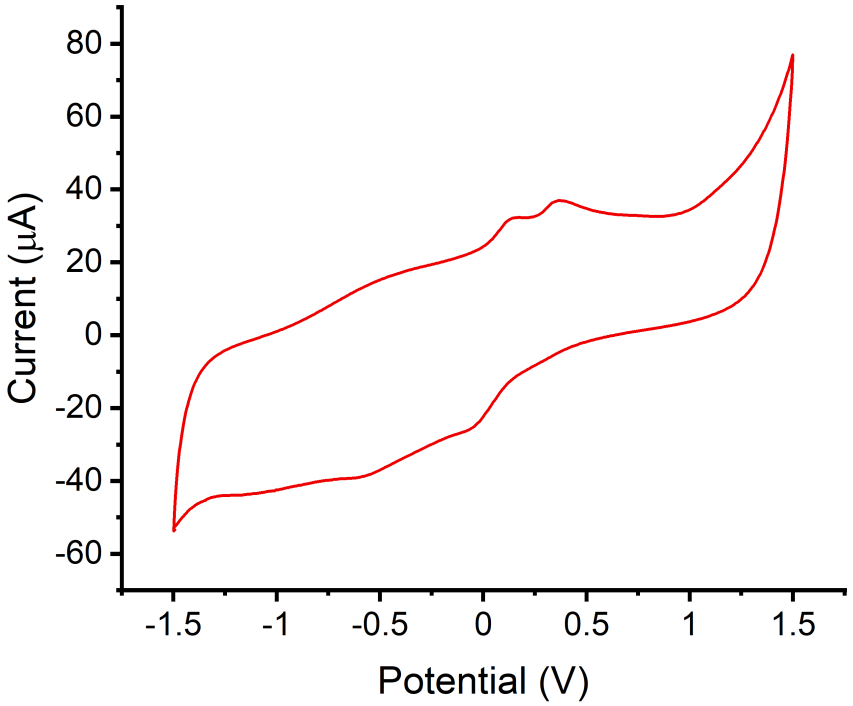

Figure D16. Cyclic voltammetry of 0.5 mM **2** in 0.10 M phosphate buffer (NaH_2PO_4/Na_2HPO_4, pH 7.0). The scan rate was 100 mV/s. Two redox features: $E_{1/2}$ = 250 mV vs. Ag/AgCl (saturated KCl) or 447 mV vs NHE, ΔE_p = 403 mV and $E_{1/2}$ = 319 mV vs. Ag/AgCl (saturated KCl) or 516 mV vs NHE, ΔE_p = 363 mV.

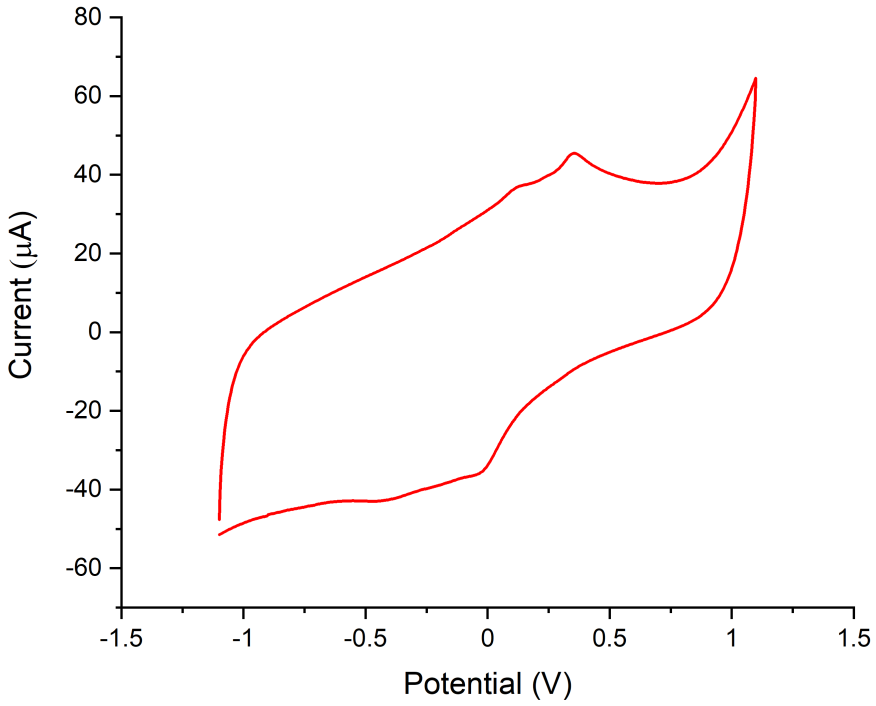

Figure D17. Cyclic voltammetry of 1.0 mM **3** in 0.10 M phosphate buffer (NaH_2PO_4/Na_2HPO_4, pH 7.0). The scan rate was 100 mV/s. Two redox features: $E_{1/2}$ = 265 mV vs. Ag/AgCl (saturated KCl) or 348 mV vs NHE, ΔE_p = 462 mV and $E_{1/2}$ = 192 mV vs. Ag/AgCl (saturated KCl) or 389 mV vs NHE, ΔE_p = 354 mV.

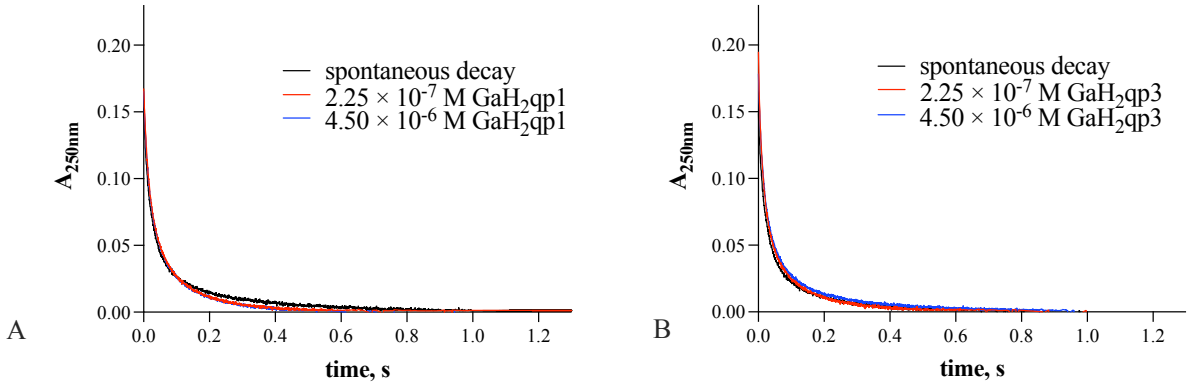

Figure D18. Kinetic traces of superoxide decomposition at 250 nm (60 mM MOPS buffer, pH 7.4 ionic strength of 150 mM) by A) **1** and B) **3**. The addition of either **1** or **3** does not have a noticeable impact on the rate of superoxide decay.

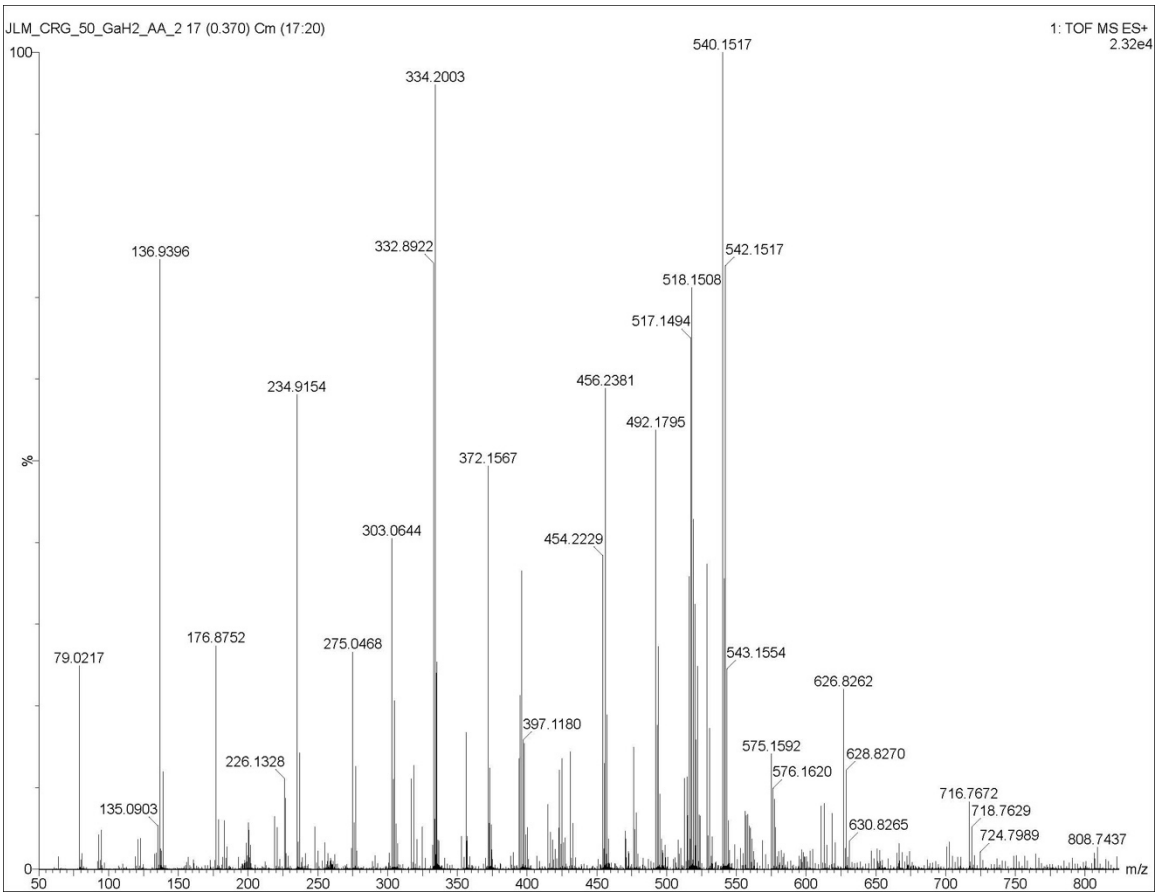

Figure D19. Mass spectrometry analysis of the reaction between **1** and 50 equiv. of KO_2 in carbonate-buffered water (pH 8.1). The 540.1517 *m/z* peak is assigned to the oxygenated benzylic carbon of the quinol form complex: $[Ga(H_2qp1\text{-}OH)]^{3+}$.

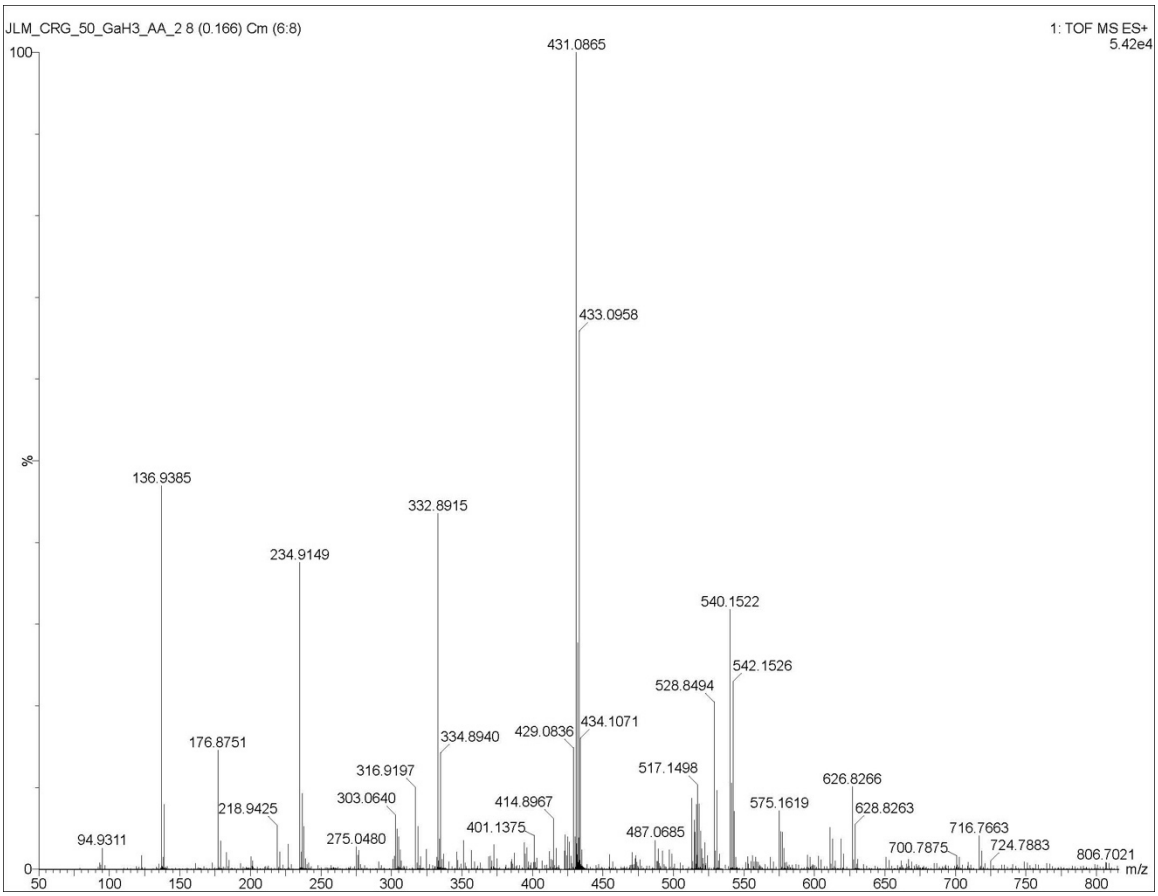

Figure D20. Mass spectrometry analysis of the reaction between **3** and 50 equiv. of KO_2 in carbonate-buffered water (pH 8.1). The 431.0865 *m/z* peak is assigned to the quinolates form of complex: $[Ga(Hqp3)]^{2+}$.

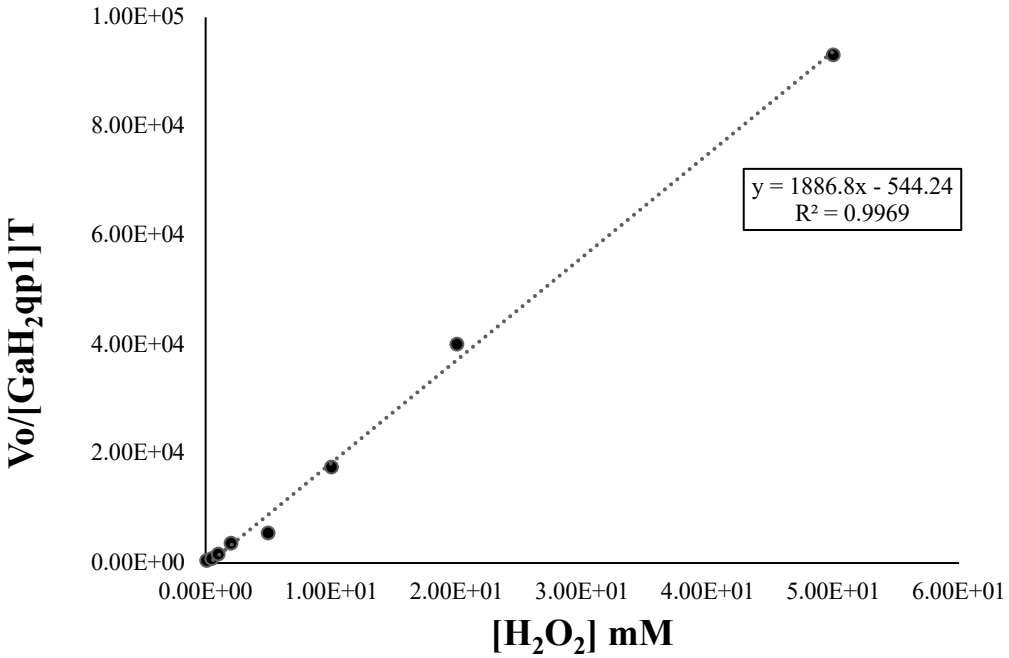

Figure D21. Extent of H_2O_2 consumption monitored by decrease in absorbance at 240 nm. Determination of catalase-like activity of **1** was acquired from dependence of initial rates on concentration of H_2O_2. Experiment performed at 25 ± 1 ℃ in 100 mM phosphate buffer, pH 7.0.

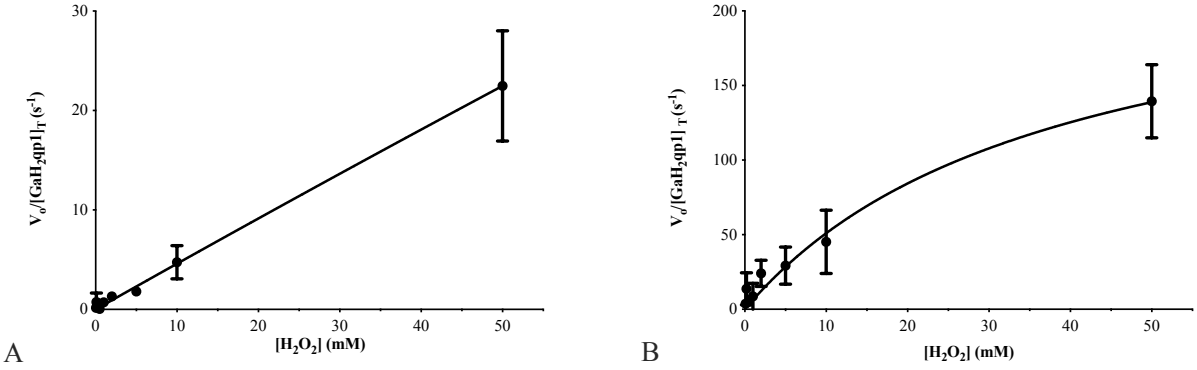

Figure D22. Catalase activity of **1** measured by O_2 production in presence of varying H_2O_2 concentrations. Kinetic parameters were calculated from non-linear least squares fitting, as described.[34] Experiment performed with A) 10 nM or B) 100 nM at 25 ± 1 ℃ in 200 mM phosphate buffer, pH 7.0.

References

(1) AbdulSalam, S. F.; Thowfeik, F. S.*; et al. Biochemistry* **2016**, *55*, 5341.

(2) Ahmed, M. I.; Gladden, J. D.*; et al. Journal of the American College Cardiology* **2010**, *55*, 671.

(3) Eskici, G.; Axelsen, P. H. *Biochemistry* **2012**, *51*, 6289.

(4) Fearon, I. M.; Faux, S. P. *Journal of Molecular and Cellular Cardiology* **2009**, *47*, 372.

(5) Kinnula, V. L. *Current Drug Targets Inflammation & Allergy* **2005**, *4*, 465.

(6) Mosley, R. L.; Benner, E. J.*; et al. Clinical Neuroscience Research* **2006**, *6*, 261.

(7) Abreu, I. A.; Cabelli, D. E. *Biochimica et Biophysica Acta* **2010**, *1804*, 263.

(8) Batinic-Haberle, I.; Rajic, Z.*; et al. Free Radical Biology and Medicine* **2011**, *51*, 1035.

(9) Batinić-Haberle, I.; Rebouças, J. S.*; et al. Antioxidants & Redox Signaling* **2010**, *13*, 877.

(10) Riley, D. P.; Lennon, P. J.*; et al. Journal of the American Chemical Society* **1997**, *119*, 6522.

(11) Riley, D. P.; Schall, O. F. *Advances in Inorganic Chemistry* **2006**, *59*, 233.

(12) Riley, D. P.; Weiss, R. H. *Journal of the American Chemical Society* **1994**, *116*, 387.

(13) Tovmasyan, A.; Carballal, S.*; et al. Inorganic Chemistry* **2014**, *53*, 11467.

(14) Murthy, M. R. N.; Reid, T. J.*; et al. Journal of Molecular Biology* **1981**, *152*, 465.

(15) Theorell, H.; Ehrenberg, A. *Archives of Biochemistry and Biophysics* **1952**, *41*, 462.

(16) Barynin, V.; Grebenko, A. *DOKLADY AKADEMII NAUK SSSR* **1986**, *286*, 461.

(17) Delwiche, E. *Journal of Bacteriology* **1961**, *81*, 416.

(18) Johnston, M.; Delwiche, E. *Journal of Bacteriology* **1965**, *90*, 352.

(19) Ma, Z.; Strickland, K. T.*et al The Journal of Biological Chemistry* **2018**, *293*, 1590.

(20) Signorella, S.; Hureau, C. *Coordination Chemistry Reviews* **2012**, *256*, 1229.

(21) Signorella, S.; Palopoli, C.*; et al. Coordination Chemistry Reviews* **2018**, *365*, 75.

(22) Yu, M.; Ambrose, S. L.*; et al. Journal of the American Chemical Society* **2014**, *136*, 12836.

(23) Yu, M.; Beyers, R. J.*; et al. Inorganic Chemistry* **2012**, *51*, 9153.

(24) Yu, M.; Ward, M. B.*; et al. Inorganic Chemistry* **2017**, *56*, 2812.

(25) Moore, J. L.; Scheitler, A.*; et al. Thesis Work Chapter 4* **2022**.

(26) Ward, M. B.; Scheitler, A.*; et al. Nature Chemistry* **2018**, *10*, 1207.

(27) Friedel, F. C.; Lieb, D.*; et al. Journal of Inorganic Biochemistry* **2012**, *109*, 26.

(28) Kenkel, I.; Franke, A.*; et al. Journal of the American Chemical Society* **2017**, *139*, 1472.

(29) Lieb, D.; Friedel, F. C.*; et al. Inorganic Chemistry* **2013**, *52*, 222.

(30) Gans, P.; Sabatini, A.*; et al. Talanta* **1996**, *43*, 1739.

(31) McCord, J. M.; Fridovich, I. *Journal of Biological Chemistry* **1969**, *244*, 6049.

(32) Blois, M. S. *Nature* **1958**, *181*, 1199.

(33) Kedare, S. B.; Singh, R. P. *Journal of Food Science and Technology.* **2011**, *48*, 412.

(34) Milaeva, E. R.; Shpakovsky, D. B.*; et al. Dalton Transactions* **2013**, *42*, 6817.

(35) Ndontsa, E. N.; Moore, R. L.*; et al. Archives of biochemistry and biophysics* **2012**, *525*, 215.

(36) Gale, E. M.; Mukherjee, S.*; et al. Inorg. Chem.* **2014**, *53*, 10748.

(37) Ancerewicz, J.; Migliavacca, E.*; et al. Free Radical Biology and Medicine* **1998**, *25*, 113.

(38) Iranzo, O. *Bioorganic Chemistry* **2011**, *39*, 73.

(39) Fridovich, I. *Journal of Biological Chemistry* **1997**, *272*, 18515.

(40) Liochev, S. I. *Chem. Res. Toxicol.* **2013**, *26*, 1312.

(41) Riley, D. P.; Rivers, W. J.*; et al. Analytical Biochemistry* **1991**, *196*, 344.

(42) Riley, D. P. *Chemical Reviews* **1999**, *99*, 2573.

(43) Beers, R. F., Jr.; Sizer, I. W. *Journal of Biological Chemistry* **1952**, *195*, 133.

(44) Costa, R. O.; Ferreira, S. S.*; et al. Frontiers in Chemistry* **2018**, *6*.

(45) Gelasco, A.; Bensiek, S.*; et al. Inorganic Chemistry* **1998**, *37*, 3301.

(46) Signorella, S.; Rompel, A.*; et al. Inorganic Chemistry* **2007**, *46*, 10864.

(47) Shank, M.; Barynin, V.*; et al. Biochemistry* **1994**, *33*, 15433.

(48) Ogura, Y. *Archives of Biochemistry and Biophysics* **1955**, *57*, 288.

(49) Coulibaly, K.; Thauvin, M.*; et al. Inorganic Chemistry* **2021**, *60*, 9309.

(50) Tovmasyan, A.; Maia, C. G. C.*; et al. Free Radical Biology and Medicine* **2015**, *86*, 308.